

BINDING OF HYDROGEN SULFIDE TO BIOLOGICALLY RELEVANT
SCAFFOLDS: METAL SYSTEMS AND NON-COVALENT BINDING

by

MATTHEW DAVID HARTLE

A DISSERTATION

Presented to the Department of Chemistry and Biochemistry
and the Graduate School of the University of Oregon
in partial fulfillment of the requirements
for the degree of
Doctor of Philosophy

December 2016

DISSERTATION APPROVAL PAGE

Student: Matthew David Hartle

Title: Binding of Hydrogen Sulfide to Biologically Relevant Scaffolds: Metal Systems and Non-covalent Binding

This dissertation has been accepted and approved in partial fulfillment of the requirements for the Doctor of Philosophy degree in the Department of Chemistry and Biochemistry by:

Victoria DeRose	Chairperson
Michael Pluth	Advisor
Darren Johnson	Core Member
Bruce Branchaud	Core Member
Benjamin Young	Institutional Representative

and

Scott L. Pratt	Dean of the Graduate School
----------------	-----------------------------

Original approval signatures are on file with the University of Oregon Graduate School.

Degree awarded December 2016

© 2016 Matthew David Hartle
This work is licensed under a Creative Commons
Attribution-SareAlike (United States) License.



DISSERTATION ABSTRACT

Matthew David Hartle

Doctor of Philosophy

Department of Chemistry and Biochemistry

December 2016

Title: Binding of Hydrogen Sulfide to Biologically Relevant Scaffolds: Metal Systems and Non-Covalent Binding

Hydrogen Sulfide (H_2S) is an important biologically produced gasotransmitter along with carbon monoxide (CO) and nitric oxide (NO). Unlike CO and NO, the bioinorganic chemistry of H_2S reactivity with biologically relevant metal centers remains underinvestigated. To address this gap, several model bio(in)organic complexes were used to understand the ligation and reaction chemistry of H_2S , including phthalocyanine, protoporphyrin IX, tetraphenyl porphyrin, and a pyridine diimine zinc complex. In addition to being a reactive gasotransmitter, the hydrosulfide anion (HS^-) has been found to be an important biological anion.

Studies with readily available cobalt and zinc phthalocyanines in organic solution illustrated the importance of protonation state in the ligation and redox chemistry of H_2S and highlighted the need for an organic-soluble source of HS^- . To address this need, we developed a simple method to prepare tetrabutylammonium hydrosulfide (NBu_4SH). Using NBu_4SH , we expanded the knowledge of H_2S reaction chemistry to encompass a significantly larger set of biologically relevant metals beyond iron using the protoporphyrin IX scaffold, revealing three principle reaction pathways: binding, no response, or reduction and binding.

Iron in biology is of particular importance given its role in oxygen transport in hemoglobin. The swamp-dwelling bivalve *L. Pectinata* hemoglobin 1 (Hb1) transports H₂S, via ligation to heme, to symbiotic bacteria. The stabilization of H₂S in Hb1 is believed to be from one of the following: a protected pocket, hydrogen bonding with a proximal glutamate residue, or a complex combination of these or other factors. By using Collman's "Picket-Fence" porphyrin to isolate the protected pocket model, we determined that a protected pocket alone is insufficient to account for H₂S stabilization on Hb1. This realization led to an examination of hydrogen bonding in the secondary coordination sphere of a zinc complex.

Finally, we explored the role of HS⁻ as a biologically relevant anion using a bis(ethynylaniline) supramolecular receptor. We determined that rather than covalently modifying the receptor molecule, HS⁻ was bound in the pocket, similar to bacterial anion transport channel.

This dissertation includes previously published co-authored material.

CURRICULUM VITAE

NAME OF AUTHOR: Matthew David Hartle

GRADUATE AND UNDERGRADUATE SCHOOLS ATTENDED:

University of Oregon, Eugene, OR
Colorado School of Mines, Golden, CO

DEGREES AWARDED:

Doctor of Philosophy, Chemistry, 2016, University of Oregon
Bachelor of Science, Chemistry, 2012, Colorado School of Mines

AREAS OF SPECIAL INTEREST:

Space and Planetary Science and Engineering, Colorado School of Mines

PROFESSIONAL EXPERIENCE:

Biomass Compositional Analyst, National Renewable Energy Laboratory
National Bioenergy Center, Golden, CO, 07/2011-08/2012

RPP Intern, National Renewable Energy Laboratory Integrated Applications
Center, Golden, CO, 07/2011-08/2011

Physical Sciences Technician, United States Naval Observatory Alternate Master
Clock, Schriever Air Force Base, CO, 06/2009-08/2009

GRANTS, AWARDS, AND HONORS:

Graduate Student Award for Excellence in the Teaching of Chemistry, University
of Oregon, 2016

Graduate Student Award for Excellence in the Teaching of Chemistry, University
of Oregon, 2013

Outstanding Chemistry Service Award, Colorado School of Mines, 2012

Outstanding Achievement Award in Analytical Chemistry, Colorado School of
Mines, 2011

Eagle Scout, Boy Scouts of America, 2008

Colorado School of Mines Medal of Achievement in Math and Science, Colorado School of Mines, 2007

PUBLICATIONS:

Matthew D. Hartle, Samantha K. Sommer, Stephen R. Dietrich, Michael D. Pluth. “Chemically Reversible Reactions of Hydrogen Sulfide with Metal Phthalocyanines” *Inorg. Chem.* **2014**, 53(15), 7800-7802. (Cover Article)

Michael D. Pluth, Shannon W. Boettcher, George V. Nazin, Ann L. Greenaway, Matthew D. Hartle. “Collaboration and Near-Peer Mentoring as a Platform for Sustainable Science Education Outreach” *J. Chem. Educ.* **2015**, 92(4) 625-630.

Michael D. Pluth, T. Spencer Bailey, Matthew D. Hammers, Matthew D. Hartle, Hillary A. Henthorn, Andrea K. Steiger. “Natural Products Containing Hydrogen Sulfide Releasing Moieties” *Synlett.* **2015**, 26(19) 2633-2643.

Matthew D. Hartle, Daniel J. Meininger, Lev N. Zakharov, Zachary J. Tonzetich, Michael D. Pluth. “NBu₄SH provides a convenient source of HS⁻ soluble in organic solution for H₂S and anion-binding research” *Dalton Trans.* **2015**, 44(46) 19782-19785.

Matthew D. Hartle, Jim S. Prell, Michael D. Pluth. “Spectroscopic Investigations into the Binding of Hydrogen Sulfide to Synthetic Picket-Fence Porphyrins.” *Dalton Trans.* **2016**, 45(11) 4843-4853.

Matthew D. Hartle, John D. Gilbertson, Michael D. Pluth. “Stabilization of Zn(II) Hydrosulfide Complex Utilizing a Hydrogen-Bond Accepting Ligand.” *Chem. Commun.* **2016**, 52(19) 7680-7682.

Matthew D. Hartle, Michael D. Pluth. “A practical guide to working with H₂S at the interface of chemistry and biology” *Chem. Soc. Rev.* **2016**, DOI: 10.1039/C6CS00212A.

Matthew D. Hartle, Ryan J. Hansen, Blakely W. Tresca, Samuel S. Praker, Lev N. Zakharov, Michael D. Pluth, Michael M. Haley, Darren W. Johnson. “A Synthetic Supramolecular Receptor for Hydrosulfide Anion” *Angew. Chemie. Int. Ed.* **2016**, 55(38) 11480-11484.

Matthew D. Hartle, McKinna R. Tillotson, Michael D. Pluth. “Spectroscopic Investigation of the Reaction of Metallo-protoporphyrins with Hydrogen Sulfide” *Journal of Inorganic Biochemistry*. Submitted.

ACKNOWLEDGMENTS

Thank you to my Ph.D. advisor, Dr. Michael Pluth, for the excellent help during my time at the University of Oregon. From the first day on campus, Dr. Pluth has helped me define my goals, explore the different opportunities of chemistry, and serve as an excellent mentor and guide. Thank you, Dr. Victoria DeRose, my thesis chair, and authority for understanding the theoretical and practical application of EPR spectroscopy to metal systems. Thank you as well to Dr. Darren Johnson, a committee member who pushed me to look outside my research at entrepreneurship and understand how innovations in research could be applied to the market. I would also thank Dr. Bruce Branchaud, whose insights in committee meetings and classes lead to my thorough understanding of organic chemistry. Thank you, Dr. Benjamin Young, for participation in my dissertation committee. I would also like to thank Dr. Jim Prell for help with mass spectrometry experiments, Dr. Zack Tonzetich and Dr. Daniel Meinger for the assist in synthesizing NBu₄SH, Dr. John Gilbertson and Maria Delgado for inspiration and material to study secondary coordination sphere interactions, Dr. Lev Zakharov for solving many crystal structures, and Dr. Michael Strain for the NMR instrumentation and allowing me to use liquid helium for the EPR. Finally, I would like to acknowledge Mrs. Suzanne Tibbits, my AP Chemistry teacher who first inspired me to pursue chemistry.

I would especially like to thank the graduate students who have made my research path so memorable. Dr. Leticia Montoya, Dr. Samantha Sommer, Dr. Jackie McGrath, Dr. Matt Hammers, Dr. Spence Bailey, Hillary Henthorn, Dan Seidenkranz, Andrea Steiger, Matt Cerda, Ryan Hanson, and Annie Greenaway.

I would like to acknowledge the contribution of my undergraduate mentees in particular. Sterling, McKinna, Sam, and Wyatt, your collective creativity, tenacity, and desire to understand the challenging research problems facing you inspired me to work harder and find the answers to many of the probing questions you asked.

I must also emphatically thank my wife, who stood by me during the stressful times and supported me during the struggle. You are amazingly talented, and an inspiring mother. Thank you, my dear daughter, as well; your innocent exploration of the world was an unending source of joy. Thank you, mom and dad, for your support and teasing whenever I came close to "squishy" science.

I would like to acknowledge the financial assistance from the National Institutes of Health, (R00-GM092970 to Dr. Pluth, R01-GM087398 to Dr Johnson and Dr. Haley), National Science Foundation (CHE-1454747 to Dr. Pluth, CHE-1255570 to Dr. Gilbertson), the Welch Foundation (AX-1772 to Dr. Tonzetich), the Oregon Medical Research Foundation (to Dr. Pluth), the Dreyfus Foundation (to Dr. Pluth), the Sloan Foundation (to Dr. Pluth), the University of Oregon Department of Chemistry 2013 Graduate Student Award for Excellence in the Teaching of Chemistry, and Dr. Ronald Swisher for the funds available for the 2016 Graduate Student Award for Excellence in the Teaching of Chemistry. The NMR facilities at the University of Oregon are supported by NSF (CHE-0923589, CHE-1427987).

Finally, I would like to acknowledge the support of all those who I forgot to add to this dissertation. Looking at this list of my support web, I realize the work of obtaining a Ph.D. or conducting quality scientific research, cannot occur in a vacuum, and I am grateful to all those who have assisted in my work.

I dedicate this dissertation to my most beautiful wife, who has taken this incredible, yet often stressful journey with me.

TABLE OF CONTENTS

Chapter	Page
I. A PRACTICAL GUIDE TO WORKING WITH H ₂ S AT THE INTERFACE OF CHEMISTRY AND BIOLOGY.....	1
Preface.....	1
Introduction.....	1
Properties and Enzymatic Production of H ₂ S.....	3
Practical Handling and Safety Considerations.....	5
Interactions with the Sulfane-Sulfur Pool.....	7
Methods for Modulating H ₂ S Levels.....	9
KO Mouse Models.....	9
RNA Knockdown Methods.....	10
Small-Molecule Inhibitors.....	11
Enzymatic Stimulators.....	12
Small-Molecule H ₂ S Donors.....	13
H ₂ S Detection and Quantification.....	16
Quantification Methods.....	17
Detection Methods.....	19
Conclusions and Outlook.....	22
Bridge.....	23
II. CHEMICALLY REVERSIBLE REACTIONS OF HYDROGEN SULFIDE WITH METAL PHTHALOCYANINES.....	25
Preface.....	25
Introduction.....	26
Results and Discussion.....	27

Chapter	Page
Conclusion	32
Bridge.....	32
Experimental.....	33
Materials and Methods.....	33
Spectroscopic Methods.....	34
General procedure for UV-vis spectroscopic studies.....	34
General procedure for NMR studies.....	34
General Procedure for Job Plot Experiments.....	35
III. TETRABUTYLAMMONIUM HYDROSULFIDE PROVIDES A CONVENIENT SOURCE OF HS ⁻ SOLUBLE IN ORGANIC SOLUTION FOR H ₂ S AND ANION-BINDING RESEARCH.....	36
Preface.....	36
Introduction.....	37
Results and Discussion	38
Conclusion	42
Bridge.....	42
Experimental.....	43
Materials and Methods.....	43
Spectroscopic Methods.....	43
X-ray crystallography details.....	44
Synthetic procedure for NBu ₄ SH.....	44
IV. SPECTROSCOPIC INVESTIGATION OF THE REACTION OF METALLO- PROTOPORPHYRINS WITH HYDROGEN SULFIDE	46
Preface.....	46
Introduction.....	46

Chapter	Page
Results and Discussion	48
Metal PPIX complexes that bind sulfide	49
Metal PPIX complexes that are reduced by sulfide.....	54
Metal PPIX complexes that show no reaction with sulfide	58
Conclusion	58
Bridge.....	59
Experimental.....	60
Materials and Methods.....	60
Spectroscopic methods.....	60
General procedure for UV-vis spectroscopic studies.....	61
General procedure for NMR studies.....	61
General Procedure for H ₂ S gas studies.....	62
General procedure for EPR studies:.....	62
Preparation and use of Zinc Amalgam.....	62
Removal of Sn ^{IV} (PPIX)Cl ₂ chlorides.....	62
V. SPECTROSCOPIC INVESTIGATIONS INTO THE BINDING OF HYDROGEN SULFIDE TO SYNTHETIC PICKET-FENCE PORPHYRINS	63
Preface.....	63
Introduction.....	64
Results and Discussion	67
Reaction of Fe ^{II} (TPivPP)(N-MeIm) ₂ with sulfide.....	68
Reactivity of Fe ^{III} (TPivPP)Br with sulfide.....	71
Oxygen sensitivity of [Fe ^{II} (TPivPP)(SH)] ⁻	73
NMR Reactivity of Picket-fence Complexes with sulfide.....	75

Chapter	Page
Reaction of Fe(TPP) with sulfide.	76
Sulfide Binding Affinities.....	77
Mass Spectrometry.....	80
Conclusion	82
Bridge.....	83
Experimental.....	84
Materials and Methods.....	84
Spectroscopic Methods.	85
General procedure for UV-Vis spectroscopic studies.....	85
General procedure for NMR studies.	86
General procedure for mass spectrometry studies.	86
General procedure for Evans' Method magnetic susceptibility measurements.....	86
Synthesis of Cr(OAc) ₂ and Cr(acac) ₂	87
Synthesis of iron porphyrin complexes.....	87
5,10,15,20-tetrakis(2-nitrophenyl)porphyrin (H ₂ TNPP).....	88
5,10,15,20-tetrakis(2-aminophenyl)porphyrin (H ₂ TAPP).	89
Separation of all-cis-H ₂ TAPP.	90
(all-cis)-5,10,15,20-tetrakis[2-(2,2-dimethylpropionamido)phenyl] porphyrin (H ₂ TPivPP).....	90
Bromo {(all-cis)-5,10,15,20-tetrakis-[2-(2,2- dimethylpropionamido)phenyl]porphyrinato(2-)}-iron(III), (Fe(TPivPP)Br).....	91
Bis(N-methylimidazole)[all-cis)-5,10,15,20-tetrakis-[2-(2,2- dimethylpropionamido)phenyl]porphyrinato(2-)]-iron(II) (Fe(TPivPP) (N-MeIm) ₂).	92

Chapter	Page
VI. STABILIZATION OF A ZINC(II) HYDROSULFIDO COMPLEX UTILIZING A HYDROGEN-BOND ACCEPTING LIGAND.....	94
Preface.....	94
Introduction.....	94
Results and Discussion	96
Conclusion	101
Bridge.....	101
Experimental.....	102
General considerations.....	102
Spectroscopic Methods.....	103
UV-Vis Titrations.....	103
NMR experiments.....	104
Determination of excess Zinc in Zn(didpa)Cl ₂	104
VII. A SYNTHETIC SUPRAMOLECULAR RECEPTOR FOR HYDROSULFIDE ANION	105
Preface.....	105
Introduction.....	105
Results and Discussion	109
Conclusion	115
Summary.....	116
Experimental.....	117
Materials and Methods.....	117
Spectroscopic Methods.....	117
General procedure for UV-Vis titrations.....	118
General procedure for NMR titrations.....	118

Chapter	Page
X-ray crystallography	118
APPENDICES	120
A. SUPPORTING INFORMATION: CHEMICALLY REVERSIBLE REACTIONS OF HYDROGEN SULFIDE WITH METAL PHTHALOCYANINES.....	120
B. SUPPORTING INFORMATION: TETRABUTYLAMMONIUM HYDROSULFIDE PROVIDES A CONVENIENT SOURCE OF HS- SOLUBLE IN ORGANIC SOLUTION FOR H ₂ S AND ANION- BINDING RESEARCH.....	128
C. SUPPORTING INFORMATION: SPECTROSCOPIC INVESTIGATION OF THE REACTION OF METALLO- PROTOPORPHYRINS WITH HYDROGEN SULFIDE	134
D. SUPPORTING INFORMATION: SPECTROSCOPIC INVESTIGATIONS INTO THE BINDING OF HYDROGEN SULFIDE TO SYNTHETIC PICKET-FENCE PORPHYRINS.....	146
E. SUPPORTING INFORMATION: STABILIZATION OF A ZINC(II) HYDROSULFIDO COMPLEX UTILIZING A HYDROGEN-BOND ACCEPTING LIGAND.....	167
F. SUPPORTING INFORMATION: A SYNTHETIC SUPRAMOLECULAR RECEPTOR FOR HYDROSULFIDE ANION	177
VIII. REFERENCES CITED.....	201

LIST OF FIGURES

Figure	Page
1. Figure I-1. Enzymatic H ₂ S production pathways. CSE: cystathionine γ -lyase; CBS: cystathionine β -synthase; CAT: cysteine aminotransferase; DAO: D-aminoacid oxidase; 3-MST: 3-mercaptopyruvate sulfurtransferase. Grey boxes indicate common substrates for H ₂ S-producing enzymes.	5
2. Figure I-2. Selected common CSE and CBS inhibitors with associated IC ₅₀ values.	11
3. Figure II-1(a) UV-Vis titration of ZnPc (6.3 μ M in THF, black) with NaSH (0.25 equiv. increments of 8 mM in DMSO up to 5 equiv.). (b) ¹ H NMR (600 MHz, THF- <i>d</i> ₈) spectra of 600 μ M ZnPc (top, black), 600 μ M ZnPc with 2 equiv. of KOH in DMSO- <i>d</i> ₆ (middle, green), and 600 μ M ZnPc with 2 equiv. of NaSH in DMSO- <i>d</i> ₆ (bottom, blue).....	29
4. Figure II-2. UV-Vis spectra of ZnPc (2 μ M in THF, black) treated with 10 equiv. of NaSH in DMSO (red). Treatment with 10 equiv. of AcOH regenerates the original ZnPc spectrum. This system can be cycled numerous times (inset).	30
5. Figure II-3. UV-Vis titration showing the reduction of CoPc (7 μ M in THF, black) to [Co(I)Pc] ⁻ (red) by NaSH (21.7 mM in DMSO in 1 equiv. increments up to 10 equiv.)	31
6. Figure II-4. UV-vis spectra of CoPc (7 μ M in THF, black trace, blue cuvette) after treatment with 10 equiv. of NaSH in DMSO (red trace, green cuvette). Subsequent exposure to atmospheric oxygen regenerates CoPc. The inset shows changes in the Q-band, corresponding to three cycles of treatment with HS ⁻ followed by exposure to air.	32
7. Figure III-1. Top: Quantification of the HS ⁻ content in NBu ₄ SH. Bottom: Titration of NBD-Cl with NBu ₄ SH to confirm HS ⁻ stoichiometry. UV-Vis spectra of 66 μ M NBD-Cl treated with 0.05 increments of NBu ₄ SH with 3 min. incubation between scans. Conditions: 50 mM PIPES, 100 mM KCl, pH 7.4, and 37 °C.	39
8. Figure III-2. Left: ORTEP diagram of NBu ₄ SH. Thermal ellipsoids are drawn at the 50% probability level. Hydrogens omitted for clarity. Right: Schematic of the intermolecular CH-anion hydrogen bonding interactions. Full crystallographic details are available in Appendix B.	40
9. Figure III-3. Cyclic voltammogram of NBu ₄ SH (2 mM) at a 3 mm glassy carbon disk electrode in acetonitrile. Scan rate is 50 mV/s and the supporting electrolyte is 0.1 M NBu ₄ PF ₆	41

10. Figure IV-1. Metal protoporphyrin IX scaffold and possible H ₂ S/HS ⁻ reaction pathways.	49
11. Figure IV-2. (a) Schematic representation of the reaction of ZnPPIX with HS ⁻ . (b) Titration of ZnPPIX (1.8 μM in THF) with NBu ₄ SH (73 equiv.); inset: Q-band region of the spectrum.	50
12. Figure IV-3. (a) Labeled structure of ZnPPIX. ¹ H NMR spectra of ZnPPIX (3.6 μM, THF- <i>d</i> ₈) before (b) and after (c) addition of 23 equiv. of NBu ₄ SH.....	51
13. Figure IV-4. (a) Schematic representation of Cr ^{III} (PPIX)Cl reaction with HS ⁻ . (b) Titration of CrPPIX (2.4 μM in THF) with NBu ₄ SH (26 equiv.); inset: Q-band region of the spectrum.	52
14. Figure IV-5. (a) Schematic for the addition of HS ⁻ to SnPPIX. (b) SnPPIX (4.95 μM) in THF before (black) and after (red) bubbling with H ₂ S(g) for 5 minutes. (c) Titration of SnPPIX (4.95 μM) with NBu ₄ SH in THF. The starting SnPPIX spectrum (black) shows a Soret band at 403 nm, which transitions to a new Soret band at 407 nm (red) in route to the final absorbance at 410 nm (blue). Inset: Absorbances at 403 and 428 nm as a function of [HS ⁻].	54
15. Figure IV-6. (a) Schematic for the reactivity of MnPPIX with HS ⁻ . (b) Titration of Mn ^{III} PPIX (9.6 μM in THF, black) with NBu ₄ SH (14 equiv., blue), proceeding through going through a Mn ^{II} PPIX intermediate (red). (c) Titration of Mn ^{II} PPIX (10.3 μM, red) with NBu ₄ SH (3.6 equiv., blue).	56
16. Figure IV-7. Continuous wave EPR spectra (1:2 DMSO:CH ₂ Cl ₂ , 5 K) of (a) Mn ^{II} PPIX (5 mM), (b) Mn ^{II} PPIX upon addition of 6.5 equiv. of NBu ₄ SH. (c) Mn ^{III} (PPIX)Cl (2 mM), (c) Mn ^{III} (PPIX)Cl upon addition of 8.2 equiv. of NBu ₄ SH. Spectra simulated with EasySpin are in red.	58
17. Figure V-1. Model Fe(II) and Fe(III) scaffolds used to study sulfide binding. The hydrophobic pocket in picket-fence porphyrin systems (1-3) provides a distinct ligand environment from the parent tetraphenyl porphyrin systems (4-6). ...	68
18. Figure V-2. (a) Titration of 3 (black) with 0.25 equiv. increments of NBu ₄ SH leads to clean conversion to [Fe(TPivPP)(SH)] ⁻ , 7 , (red). Conditions: MePh solution of 10.8 μM 3 with 367 μM <i>N</i> -methylimidazole titrated with 10 equiv. of NBu ₄ SH in 1:9 MeCN:MePh. (b) Titration of 3 (black) with 0.25 equiv. increments of NBu ₄ SH leads to clean conversion to 7 (red). Conditions: DMF solution of 5.2 μM 3 with 36.5 μM <i>N</i> -methylimidazole titrated with 10 equiv. of NBu ₄ SH in DMF. All titrations were performed under anaerobic conditions with sufficient time to allow for complete reaction between aliquot additions.	70

19. **Figure V-3.** Titration of **2** (black) with 0.25 equiv. increments of NBu₄SH leads to conversion to **7** (red) after disaggregation of the porphyrin (blue). Conditions: MePh solution of 5.7 μM **2** titrated with 5 equiv. of NBu₄SH in a 1:9 MeCN:MePh solution. All titrations were performed under anaerobic conditions with sufficient time to allow for complete reaction between aliquot additions..... 71
20. **Figure V-4.** (a) Titration of **1** (black) with 0.25 equiv. increments of NBu₄SH leads to reduction of Fe(III) to Fe(II) (blue trace shows 0.75 equiv. NBu₄SH) followed by binding of HS⁻ to form **7** (red). Conditions: MePh solution of 20 μM **1** with 69 μM *N*-methylimidazole titrated with 3 equiv. of NBu₄SH in 1:9 MeCN:MePh. (b) Titration of **1** (black) with 0.25 equiv. increments of NBu₄SH leads to reduction of Fe(III) to Fe(II) (blue trace shows 0.5 equiv. NBu₄SH) followed by binding of HS⁻ to form **7** (red). Conditions: DMF solution of 12 μM **1** with 80 μM *N*-methylimidazole titrated with 5 equiv. of NBu₄SH. 73
21. **Figure V-5.** Exposure of **3** to atmospheric oxygen leads to conversion to **7**. Titration of **7** (blue) with 0.25 equiv. increments of NBu₄SH leads to irreversible oxidation (red, 20 equiv. and green, 220 equiv.). Conditions: MePh solution of 5.6 μM **3** and 192 μM *N*-methylimidazole, exposed to atmosphere for 5 minutes, followed by purging headspace for 10 minutes with N₂, and titrated with NBu₄SH in a 1:39 acetonitrile-MePh solution. 74
22. **Figure V-6.** ¹H NMR (600 MHz, toluene-d₈) spectra of **1** (4 mM, black), **3** (4 mM, blue) and **7** (red) in CD₃CN. The spectrum of **7** was recorded after addition of 5 equiv. of NBu₄SH to either **1** or **3**. 75
23. **Figure V-7.** (a) Titration of **6** (black) with 0.25 equivalent increments of NBu₄SH to form **8** (red). Conditions: MePh solution of 3.8 μM **6** with 35 μM *N*-methylimidazole titrated with 10 equivalents of NBu₄SH. (b) Titration of **4** (black) with 0.25 increments of NBu₄SH leads to reduction of Fe^{III} to Fe^{II} (**6**) (blue trace shows 0.75 equiv. NBu₄SH) followed by binding of HS⁻ to form **8** (red). Conditions: DMF solution of 4.5 μM **4** with 30 μM *N*-methylimidazole titrated with 10 equivalents NBu₄SH. 77
24. **Figure V-8.** A competitive continuous variation plot of **3** and NBu₄SH supports 1:1 binding. Conditions: Total concentration: 11.1 μM in 1:9 MePh:MeCN solution with 0.33 mM *N*-methylimidazole. The molar ratio of Fe was varied from 0.1 to 1 and the absorbance was corrected for the concentration of *N*-methylimidazole..... 79

25. **Figure V-9.** (a) Mass spectrum of **3** with 15 equiv. of NBu₄SH added in THF results in formation of **2** (blue) and **7** (red), [Fe^{II}(TPivPP) – H⁺]⁻ and [Fe(TPivPP)(SH)]⁻ respectively. (b) Mass spectrum of **1** with 15 equiv. of NBu₄SH added in THF results in the formation of **2** (blue) and **7** (red), [Fe^{II}(TPivPP) – H⁺]⁻ and [Fe(TPivPP)(SH)]⁻ respectively. (c) Mass spectrum of **6** with 15 equiv. of NBu₄SH added in THF results in formation of **5** (blue) and **8** (red), which ionize as [Fe^{II}(TPP) – H⁺]⁻ and [Fe^{II}(TPP)(SH) – H⁺]⁻ respectively. (d) Mass spectrum of **4** with 15 equiv. of NBu₄SH added in THF results in formation of **5** (blue) and **8** (red), which ionize as [Fe^{II}(TPP) – H⁺]⁻ and [Fe^{II}(TPP)(SH) – H⁺]⁻ respectively. Conditions: electrospray in negative ion mode with [Fe] = 1 mM in THF with 15 equiv. NBu₄SH added in 1:1 THF-acetonitrile. 81
26. **Figure VI-1.** Titration of Zn(didpa)Cl₂ (87.3 μM, CH₂Cl₂, black) with NBu₄SH (0.1 equiv. increments up to 6 equiv., red). The inset shows the Job plot of **1** with NBu₄SH in MeCN at a total concentration of 420 μM. The observed break is consistent with 1:1 binding. 97
27. **Figure VI-2.** ¹H NMR spectra of **1** (11.8 mM in CD₃CN) before (top, black) and after (bottom, red) addition of 1.5 equiv. of NBu₄SH. Peaks denoted with a (*) correspond to the NBu₄⁺ counterion. 98
28. **Figure VI-3.** Variable temperature ¹H NMR spectra of 11.4 mM Zn(didpa)Cl₂, and 1.5 equiv. NBu₄SH in CD₃CN. Cooling to -35 °C results in sharpening and an upfield shift of the broad SH peak to 11.05 ppm. See Figure E-9 for an expanded spectrum of the SH peak. 99
29. **Figure VI-4.** ¹H NMR spectrum of 10.3 mM **1** (black), upon addition of 1.5 equiv. of NBu₄SH (red) is characteristic for **2**. Addition of 20 equiv. of NBu₄Cl produces the spectrum characteristic of the Cl⁻ adduct. 100
30. **Figure VII-1.** (a) Protein structure of HSC (PDB:3TDX) showing five individual channels with the bound anion represented as a yellow sphere. (b) Enlargement of the binding pocket showing short contacts to His (2.980 Å), Thr (3.010 Å), Leu (3.725 Å) and Val (3.619 and 4.610 Å). Non-interacting helices are excluded for clarity. (c) Synthetic receptors **1-3**. 107
31. **Figure VII-2.** (a) Scheme showing HS⁻ host-guest equilibrium. (b) Representative UV-Vis difference titration of NBu₄SH with 10 μM **2** in CH₃CN and fit to a 1:1 binding isotherm (inset). (c) ¹H NMR spectra of a titration of 0.988 mM **1** with NBu₄SH in 10% DMSO-*d*₆/CD₃CN. 111
32. **Figure VII-3.** (a) Reversibility reaction scheme. (b) ¹H NMR spectrum of a 1.0 mM solution of **1** in 10% DMSO-*d*₆/CD₃CN. (c) Treatment with 2 equiv. of NBu₄SH. (d) Addition of 4 equiv. Zn(OAc)₂. Each inset shows the ¹³C {¹H} resonances corresponding to the alkyne region of **1**. 114

33. Figure VII-4. ORTEP representation showing selected hydrogen bond distances. Atoms are drawn at the 50% probability level. Hydrogens not interacting with the bound HS ⁻ are removed for clarity.	115
34. Figure A-1. UV-vis titration data of 3.0 mL of 10 μM CoPc with 2.8 mM [NBu ₄][BH ₄] in 5.9 μL aliquots in THF showing reduction of CoPc to [CoPc] ⁻ . The band at 320 nm observed in the [NBu ₄][BH ₄] titration is consistent with formation of borane-THF complex.	121
35. Figure A-2. Job plot of ZnPc and NaSH in 1:1 THF:DMSO following the absorbance at 426 nm.	121
36. Figure A-3. Job plot of CoPc and NaSH in 1:1 THF:DMSO following the absorbance at 467 nm.	122
37. Figure A-4. ¹ H NMR spectrum of ZnPc in THF- <i>d</i> ₈	123
38. Figure A-5. ¹ H NMR spectrum of ZnPc in THF- <i>d</i> ₈ with 2 equiv. of NaSH in DMSO- <i>d</i> ₆	124
39. Figure A-6. ¹ H NMR spectrum of ZnPc in THF- <i>d</i> ₈ with 2 equiv. of KOH in DMSO- <i>d</i> ₆	125
40. Figure A-7. ¹ H NMR spectrum of 0.136 mM CoPc in 750 μL of THF- <i>d</i> ₈ with 40 μL of added DMSO- <i>d</i> ₆	126
41. Figure A-8. ¹ H NMR spectrum of 0.136 mM [Co(I)Pc] ⁻ in 750 μL of THF- <i>d</i> ₈ with 40 μL of 22.6 mM NaSH (8.8 equiv.) in DMSO- <i>d</i> ₆ added. The change in the Pc resonances from a broad singlet to well defined peaks is consistent with a change from paramagnetic Co(II) to diamagnetic Co(I).	127
42. Figure B-1 ¹ H (600 MHz, CD ₃ CN) NMR spectrum of NBu ₄ SH.	129
43. Figure B-2. ¹³ C{ ¹ H} (151 MHz, CD ₃ CN) NMR spectrum of NBu ₄ SH.	129
44. Figure B-3. ¹ H NMR spectra demonstrating that H ₂ S is not sufficiently nucleophilic to react with BnCl. Only upon deprotonation to form HS ⁻ does nucleophilic attack on BnCl occur. a) A saturated solution of H ₂ S gas in CD ₃ CN. b) Addition of BnCl does not result in any reaction. c) Addition of NEt ₃ (TEA) to deprotonated H ₂ S generates HS ⁻ , which is quickly trapped by BnCl to form Bn ₂ S.	130
45. Figure B-4. ¹ H NMR spectrum of the reaction of NBu ₄ SH with BnCl to form Bn ₂ S and BnSH. Unlike in Figure B-3, no added base is required for this reaction to occur. Bottom: NBu ₄ SH in CD ₃ CN. Top: Addition of 3 equiv. of BnCl.	131
46. Figure B-5. FTIR (ATR, neat) spectrum of NBu ₄ SH.	132

47. Figure B-6. FTIR (ATR, neat) spectrum of NaSH.	132
48. Figure C-1. Titration of ZnPPIX (1.8 μ M) with NBu ₄ SH (30 equiv.) followed by titration with AcOH (30 equiv.) in THF.	135
49. Figure C-2. Treatment of ZnPPIX (2.4 μ M, black) with NBu ₄ SH (80 equiv., blue) followed by exposure to the atmosphere for 15 minutes (purple) in THF.	135
50. Figure C-3. Treatment of ZnPPIX (2.3 μ M) with NBu ₄ OAc (20 equiv.) in THF.	136
51. Figure C-4. Treatment of ZnPPIX (2.5 μ M) with DBU (890 equiv.) followed by NBu ₄ SH (30 equiv.) in THF.	136
52. Figure C-5. Treatment of ZnPPIX (2.6 μ M) with dicyclohexylamine (4.5 equiv.) in THF.	136
53. Figure C-6. ZnPPIX binding isotherm and associated fit for titration data shown in Figure 2b. Data points related to the deprotonation of carboxylic acid moieties removed (first equivalent), as they did not show significant spectral change.	137
54. Figure C-7. Treatment of Cr ^{III} (PPIX)Cl (2.4 μ M, red) with NBu ₄ SH (26 equiv., blue) in THF, followed by AcOH (50 equiv., orange). Note: The reverse reaction was kinetically slow.	138
55. Figure C-8. Treatment of Cr ^{III} (PPIX)Cl (2.4 μ M, black) with NBu ₄ SH (25 equiv., blue) in THF followed by exposure to the atmosphere for 30 minutes (red).	138
56. Figure C-9. Cr ^{III} (PPIX)Cl binding isotherm and associated fit for titration data shown in Figure 4b. Data points corresponding to deprotonation (1 st equiv.) showed no spectral change and were removed before fitting.	138
57. Figure C-10. Treatment of Sn ^{IV} PPIX (6 μ M) with Cl ⁻ (25 equiv.) in THF.	139
58. Figure C-11. Treatment of Sn ^{IV} PPIX (3.9 μ M, red) with NBu ₄ SH (20 equiv., blue) followed by addition of triflic acid (1 μ L, black) in THF.	139
59. Figure C-12. Treatment of Sn ^{IV} PPIX (5.5 μ M, red) with NBu ₄ OAc (20 equiv., blue) in THF.	139
60. Figure C-13. Treatment of Sn ^{IV} PPIX (5.4 μ M, red) with DBU (200 equiv., black) in THF.	140
61. Figure C-14. Treatment of Sn ^{IV} PPIX (6 μ M, red) with dicyclohexylamine (11 equiv., black) in THF.	140

62. Figure C-15. Treatment of Mn ^{III} PPIX (9.6 μM, red) with NBu ₄ SH (15 equiv., blue) followed by AcOH (40 equiv., purple) in THF	141
63. Figure C-16. Treatment of Mn ^{II} PPIX (7.7 μM, black) with NBu ₄ SH (4 equiv., red) followed by AcOH (40 equiv., blue) in THF.	141
64. Figure C-17. Treatment of Mn ^{II} PPIX (7.7 μM, black) with NBu ₄ SH (4 equiv., red) followed by exposure to the atmosphere for 60 minutes (blue) in THF	141
65. Figure C-18. Treatment of Mn ^{III} PPIX (10 μM, black) with NBu ₄ OAc (20 equiv., red) in THF.	142
66. Figure C-19. Treatment of Mn ^{II} PPIX (6.4 μM, red) with DBU (1 μL, black) in THF.	142
67. Figure C-20. Treatment of Mn ^{II} PPIX (10 μM, red) with dicyclohexylamine (50 equiv., blue), followed by addition of NBu ₄ SH (30 equiv., black) in THF.....	142
68. Figure C-21. Treatment of Mn ^{III} PPIX (7.5 μM, red) with CoCp ₂ (1.5 equiv., black) in THF.	143
69. Figure C-22. Mn ^{II} PPIX binding isotherm and associated fit for titration data shown in Figure 6b after complete conversion to Mn ^{II} (PPIX).	143
70. Figure C-23. Continuous wave EPR spectra (DMSO/CH ₂ Cl ₂ , 7 K) of (a) Cr ^{III} (PPIX) (2 mM), (b) Cr ^{III} (PPIX)SH upon addition of 20.4 equiv. of NBu ₄ SH.	144
71. Figure D-1. ¹ H (600 MHz, DMSO- <i>d</i> ₆) NMR spectrum of H ₂ TNPP.....	148
72. Figure D-2. UV-Vis spectrum of H ₂ TNPP in DMF.....	148
73. Figure D-3. FTIR (ATR, neat) spectrum of H ₂ TNPP.....	149
74. Figure D-4. ¹ H (600 MHz, CDCl ₃) NMR spectrum of H ₂ TAPP.....	149
75. Figure D-5. ¹³ C{ ¹ H} (151 MHz, CDCl ₃) NMR spectrum of H ₂ TAPP.....	150
76. Figure D-6. UV-Vis spectrum of H ₂ TAPP in CHCl ₃	150
77. Figure D-7. FTIR (ATR, neat) spectrum of H ₂ TAPP.....	150
78. Figure D-8. ¹ H (600 MHz, CDCl ₃) NMR spectrum of H ₂ TPivPP.....	151
79. Figure D-9. ¹³ C{ ¹ H} (151 MHz, CDCl ₃) NMR spectrum of H ₂ TPivPP.	152
80. Figure D-10. ¹ H- ¹ H COSY NMR spectrum of H ₂ TPivPP.....	153

81. Figure D-11. ^1H - ^{13}C HMQC NMR spectrum of H_2TPivPP	154
82. Figure D-12. ^1H - ^{13}C HMBC NMR spectrum of H_2TPivPP	155
83. Figure D-13. UV-Vis spectrum of H_2TPivPP in CHCl_3	155
84. Figure D-14. FTIR (ATR, neat) spectrum of H_2TPivPP	156
85. Figure D-15. ^1H (600 MHz, toluene- d_8) NMR spectrum of $\text{Fe}(\text{TPivPP})\text{Br}$	156
86. Figure D-16. UV-Vis spectrum of $\text{Fe}(\text{TPivPP})\text{Br}$ in CHCl_3	157
87. Figure D-17. FTIR (ATR, neat) spectrum of $\text{Fe}(\text{TPivPP})\text{Br}$	157
88. Figure D-18. Comparison of the UV-Vis spectra of different species in the metalation reaction for $\text{Fe}(\text{TPivPP})\text{Br}$ in CHCl_3	157
89. Figure D-19. Full electrospray negative ion mode mass spectrum of $\text{Fe}(\text{TPivPP})\text{Br}$	158
90. Figure D-20. Area of interest for negative ion mode mass spectrum of $\text{Fe}(\text{TPivPP})\text{Br}$ including the isotopic distribution of the observed and calculated peaks.	158
91. Figure D-21. Area of interest for negative ion mode mass spectrum of $\text{Fe}(\text{TPivPP})\text{Br}$ including the isotopic distribution of the observed and calculated peaks.	158
92. Figure D-22. ^1H (600 MHz, toluene- d_8) NMR spectrum of $\text{Fe}(\text{TPivPP})$	159
93. Figure D-23. UV-Vis spectrum of $\text{Fe}(\text{TPivPP})(\text{Im})_2$ (10.8 μM) in toluene with 33-fold excess of <i>N</i> -methyl imidazole.	159
94. Figure D-24. FTIR (ATR, neat) spectrum of $\text{Fe}(\text{TPivPP})$	160
95. Figure D-25. Full negative ion mode mass spectrum of $\text{Fe}(\text{TPivPP})(\text{Im})$	160
96. Figure D-26. Area of interest for negative ion mode mass spectrum of $\text{Fe}(\text{TPivPP})(\text{Im})$ including the isotopic distribution of the observed and calculated peaks.	160
97. Figure D-27. UV-Vis spectrum of representative oxygen binding of $\text{Fe}(\text{TPivPP})(\text{Im})_2$ (23 μM) in toluene.	161
98. Figure D-28. ^1H (600 MHz, toluene- d_8) NMR Spectrum of $\text{Fe}(\text{TPivPP})(\text{SH})$ after reaction with $\text{Fe}(\text{TPivPP})\text{Br}$	161
99. Figure D-29. ^1H (600 MHz, toluene- d_8) NMR spectrum of $\text{Fe}(\text{TPivPP})(\text{SH})$ after reaction with $\text{Fe}(\text{TPivPP})$	162

100. Figure D-30. ^1H (600 MHz, toluene- d_8) NMR spectra of different Fe species and the reaction results with NBu_4SH .	162
101. Figure D-31. UV-Vis of the starting and final product for NMR titrations.	163
102. Figure D-32. Representative UV-Vis titration data (in toluene) and residual (inset).	163
103. Figure D-33. Negative ion mode mass spectrum of $\text{Fe}(\text{TPivPP})(\text{Im})_2$ with 15 equiv. of NBu_4SH in THF.	163
104. Figure D-34. Negative ion mode mass spectrum of $\text{Fe}(\text{TPivPP})\text{Br}$ with 15 equiv. of NBu_4SH .	164
105. Figure D-35. Negative ion mode mass spectrum of $\text{Fe}(\text{TPP})(\text{Im})_2$ with 15 equiv. of NBu_4SH .	164
106. Figure D-36. Negative ion mode mass spectrum of $\text{Fe}(\text{TPP})\text{Cl}$ with 15 equiv. of NBu_4SH .	164
107. Figure D-37. Negative ion mode mass spectrum of the degradation product of $\text{Fe}(\text{TPivPP})(\text{Im})_2$ treated with 15 equiv. of NBu_4SH and exposed to the atmosphere.	165
108. Figure D-38. (a) Mass spectrum of 3 after addition of 15 equiv. of NBu_4SH in THF shows the formation of 2 (blue) and 7 (red). (b) Mass spectrum of 6 after addition 15 equiv. of NBu_4SH in THF shows the formation of 5 (blue) and 8 (red). In both cases, increasing the collisional energy results in a decrease in the peak intensity corresponding to the SH-ligated iron complex with respect to the unligated porphyrin. The decrease in (b) is greater than that of (a), consistent with sulfur bound inside the pocket of the porphyrin.	166
109. Figure E-1. Titration of a 88 μM solution of $\text{Zn}(\text{didpa})\text{Cl}_2$ in MeCN (black) with NBu_4SH added in 0.1 equiv. increments up to 1.5 equiv. (red). The titration was continued up to 5 equiv. (blue) of NBu_4SH , which results in a spectrum primarily dominated by the absorption of free HS^- , which has an absorbance at 273 nm (inset) in MeCN. Attempts to fit this data to a 1:1 or 1:2 binding model were unsuccessful due to overlapping peaks.	168
110. Figure E-2. Titration of a 87 μM solution of $\text{Zn}(\text{didpa})\text{Cl}_2$ in MeCN (black) with sodium butylthiolate added in 0.3 equiv. increments up to 6 equivalents (red). Further increase in the spectrum at 250 nm is due to sodium butane thiolate (blue). The spectrum of sodium butylthiolate is shown in the inset for comparison. Attempts to fit this data to a 1:1 or 1:2 binding model were unsuccessful.	168

111. **Figure E-3.** Titration of a 88 μM solution of $\text{Zn}(\text{didpa})\text{Cl}_2$ in MeCN with NBu_4Cl added in 0.1 equiv. increments of NBu_4Cl up to 13.6 equivalents (red). Inset shows the binding isotherm at 282 nm with fit of $4,440 \pm 15 \text{ M}^{-1}$. Residuals are assigned to the right y-axis. 169
112. **Figure E-4.** Titration of 175 μM solution of $\text{Zn}(\text{didpa})\text{Cl}_2$ in DCM with NBu_4Cl added in 0.1 equiv. increments of NBu_4Cl up to 4.0 equivalents (red). Inset shows the binding isotherm at 263 nm and was unable to be fit due to its sinusoidal nature. The apparent induction behavior could be due to chloride binding free zinc (see methods); however, removal of these initial points does not provide reasonable fits to a 1:1 or 1:2 model. 169
113. **Figure E-5.** NOESY spectrum of 11.6 mM $\text{Zn}(\text{didpa})\text{Cl}_2$, and 18.9 mM NBu_4SH (1.6 equiv.) in CD_3CN recorded at -35°C . The spectra were recorded with a 2.0 s relaxation delay and a 0.4 s mixing time. The largest observed peak is an exchange peak with residual water. 170
114. **Figure E-6.** ^1H NMR spectra of $\text{Zn}(\text{didpa})\text{Cl}_2$ (5.8 mM in CD_3CN) before (top, black spectrum) and after (bottom, red spectrum) addition of 5.7 equiv. of NBu_4Cl . The (*) correspond to NBu_4^+ 171
115. **Figure E-7.** ^1H NMR spectra of **1** (11.8 mM in CD_3CN before (top, black) and after (bottom, red) addition of 1.5 equiv. of NBu_4SH . Peaks denoted with (*) correspond to the NBu_4^+ counterion. (reprint of figure 2) 172
116. **Figure E-8.** Variable temperature ^1H NMR spectra of 11.4 mM $\text{Zn}(\text{didpa})\text{Cl}_2$, and 1.5 equiv. NBu_4SH in CD_3CN . Cooling to -35°C results in sharpening and an upfield shift of the broad SH peak to 11.05 ppm. See Figure S6 for an expanded view of the SH peak. 173
117. **Figure E-9.** ^1H NMR spectra of 11.4 mM $\text{Zn}(\text{didpa})\text{Cl}_2$, and 16.7 mM NBu_4SH (1.5 equiv.) in CD_3CN showing the SH resonance upon cooling. All spectra were measured with a 5 second relaxation delay. 174
118. **Figure E-10.** ^1H NMR spectra of 10.3 mM **1** (black) at 25°C . Addition of 1.5 equivalents NBu_4SH at 25°C (red). Addition of 20 equiv. of NBu_4Cl at 25°C (blue). 174
119. **Figure E-11.** ^1H NMR spectra of 2.63 mM $\text{Zn}(\text{}^i\text{PrPDI})\text{Cl}_2$ and 4.85 mM NBu_4SH in CD_3CN . Formation of a white precipitate was observed during addition of the first two equivalents of sulfide. 175
120. **Figure E-12.** Job plot of $\text{Zn}(\text{didpa})\text{Cl}_2$ with NBu_4Cl in MeCN at an overall concentration of 412 μM . The break is consistent with a 1:1 binding event. The plot was corrected for 6.0% excess zinc as determined by addition of TPEN by subtraction of that percentage from the mol ratio of zinc as described in the experimental details above. 176

121. **Figure E-13.** Titration of Zn(didpa)Cl₂ (85.5 μM, CH₂Cl₂, black) with tetramethylammonium hydroxide pentahydrate (0.1 equiv. increments up to 3 equivalents, red). The inset shows the Job plot of **1** with tetramethylammonium hydroxide pentahydrate in MeCN at a total concentration of 413 μM. The break is consistent with 1:1 binding. 176
122. **Figure F-1.** Binding isotherm for HS⁻ titration of **1** in 10% DMSO-*d*₆/CD₃CN determined by ¹H NMR spectroscopy. ¹H NMR stacked plot of **1** (0.988 mM) titrated with NBu₄SH (0-13 equiv., bottom to top) in 10% DMSO-*d*₆/CD₃CN. 178
123. **Figure F-2.** Binding isotherm for Cl⁻ titration of **1** in 10% DMSO-*d*₆/CD₃CN determined by ¹H NMR spectroscopy. ¹H NMR stacked plot of **1** (0.649mM) titrated with NBu₄Cl (0-49 equiv., bottom to top) in 10% DMSO-*d*₆/CD₃CN..... 179
124. **Figure F-3.** Binding isotherm for HS⁻ titration of **2** in 10% DMSO-*d*₆/CD₃CN determined by ¹H NMR spectroscopy. ¹H NMR stacked plot of **2** (0.681 mM) titrated with NBu₄SH (0-27 equiv., bottom to top) in 10% DMSO-*d*₆/CD₃CN. 180
125. **Figure F-4.** Binding isotherm for Cl⁻ titration of **2** in 10% DMSO-*d*₆/CD₃CN determined by ¹H NMR spectroscopy. ¹H NMR stacked plot of **2** (1.04 mM) titrated with NBu₄Cl (0-24 equiv., bottom to top) in 10% DMSO-*d*₆/CD₃CN..... 181
126. **Figure F-5.** Binding isotherm for HS⁻ titration of **3** in 10% DMSO-*d*₆/CD₃CN determined by ¹H NMR spectroscopy. ¹H NMR stacked plot of **3** (0.864 mM) titrated with NBu₄SH (0-20 equiv., bottom to top) in 10% DMSO-*d*₆/CD₃CN. 182
127. **Figure F-6.** Binding isotherm for Cl⁻ titration of **3** in 10% DMSO-*d*₆/CD₃CN determined by ¹H NMR spectroscopy. ¹H NMR stacked plot of **3** (0.904 mM) titrated with NBu₄Cl (0-34 equiv., bottom to top) in 10% DMSO-*d*₆/CD₃CN..... 183
128. **Figure F-7.** UV-Vis titration of **1** with HS⁻ in MeCN. HS⁻ was incrementally added to a 10.3 μM solution of **1**. Inset: Representative curve at 333 nm: black dots are data collected, line is experimental fit, and red dots are residuals, corresponding to the right (red) axis. 185
129. **Figure F-8.** UV-Vis titration of **1** with Cl⁻ in MeCN. Cl⁻ was incrementally added to a 10.3 μM solution of **1**. Inset: Representative curve at 343 nm: black dots are data collected, line is experimental fit, and red dots are residuals, corresponding to the right (red) axis. 187
130. **Figure F-9.** UV-Vis titration of **2** with HS⁻ in MeCN. HS⁻ was incrementally added to a 10.6 μM solution of **2**. Inset: Representative curve at 360 nm: black dots are data collected, line is experimental fit, and red dots are residuals, corresponding to the right (red) axis. 189

131. **Figure F-10.** UV-Vis titration of 2 with Cl^- in MeCN. Cl^- was incrementally added to a 10.6 μM solution of 2. Inset: Representative curve at 355 nm: black dots are data collected, line is experimental fit, and red dots are residuals, corresponding to the right (red) axis. 191
132. **Figure F-11.** UV-Vis titration of 3 with HS^- in MeCN. HS^- was incrementally added to a 10.7 μM solution of 3. Inset: Representative curve at 333 nm: black dots are data collected, line is experimental fit, and red dots are residuals, corresponding to the right (red) axis. 193
133. **Figure F-12.** UV-Vis titration of 3 with Cl^- in MeCN. Cl^- was incrementally added to a 10.8 μM solution of 3. Inset: Representative curve at 350 nm: black dots are data collected, line is experimental fit, and red dots are residuals, corresponding to the right (red) axis. 195
134. **Figure F-13.** a, $^{13}\text{C}\{^1\text{H}\}$ NMR spectrum of a 2.318 mM solution of 1 with addition of 10 equivalents of NBu_4SH . ^{13}C NMR (151 MHz, CD_3CN) δ 154.97, 153.56, 144.98, 138.51, 136.94, 133.28, 130.71, 128.86, 128.70, 126.68, 123.21, 121.14, 121.08, 113.72, 111.92, 93.85, 86.89. b, $^{13}\text{C}\{^1\text{H}\}$ NMR spectrum of a 2.318 mM solution of 1. ^{13}C NMR (151 MHz, CD_3CN) δ 155.36, 153.07, 144.98, 138.39, 134.64, 132.68, 131.76, 129.06, 128.87, 127.03, 123.48, 121.03, 119.81, 114.05, 111.26, 93.80, 86.60. 196
135. **Figure F-14.** a ^1H NMR spectrum of a 1.5 mM solution of 3. b ^1H NMR spectrum of a 1.5 mM solution of 3 with 150 mM solution of 1,8-diazabicyclo[5.4.0]undec-7-ene (DBU). This results in the disappearance of urea protons NH_b and NH_c , as well as upfield shifting of remaining aryl protons. c 1.5 mM of 3 with 3.74 mM of NBu_4SH . Spectrum of the host-guest complex bears a marked difference to the deprotonated host. 197
136. **Figure F-15.** ORTEP representation of the crystal structure of 1 and NBu_4SH , showing short contacts to the NBu_4 counterion. Non-coordinating hydrogen atoms omitted for clarity. 199
137. **Figure F-16.** Overlay of the X-ray crystal structures of 1 bound to Cl^- and HS^- . Non-coordinating hydrogen atoms omitted for clarity. In the images, the hydrosulfide structure is represented in red with a yellow anion, while the chloride structure is represented in blue with a green anion. The RMS distance between the two structures is 0.184 Å. A, top view of the two structures overlaid. B, side view looking toward the phenyl core through the anions. 200

LIST OF TABLES

Table	Page
1. Table III-1. Comparison of the solubility of NaSH and NBu ₄ SH in different solvents.	42
2. Table IV-1. EPR parameters for Mn(PPIX) species.	58
3. Table V-1. Comparison of HS ⁻ binding constants for Fe-porphyrin systems.	80
4. Table VII-1. HS ⁻ and Cl ⁻ Binding Parameters in Hosts 1-3	113
5. Table A-1. Parameters for ZnPc Job Plot in 1:1 THF:DMSO.	122
6. Table A-2. Parameters for CoPc Job Plot in 1:1 THF:DMSO.	122
7. Table C-1. Summary of Results.	135
8. Table D-1. Table of porphyrin compounds and absorbances.	166
9. Table F-1. Titration of 1 with HS ⁻ . (Stock [HS ⁻] = 19.99 mM)	178
10. Table F-2. Titration of 1 with Cl ⁻ . (Stock [Cl ⁻] = 44.59 mM)	179
11. Table F-3. Titration of 2 with HS ⁻ . (Stock [HS ⁻] = 25.40 mM)	180
12. Table F-4. Titration of 2 with Cl ⁻ . (Stock [Cl ⁻] = 35.04 mM)	181
13. Table F-5. Titration of 3 with HS ⁻ . (Stock [HS ⁻] = 23.7 mM)	182
14. Table F-6. Titration of 3 with Cl ⁻ . (Stock [Cl ⁻] = 43.35 mM)	183
15. Table F-7. Titration of 1 with HS ⁻	184
16. Table F-8. Titration of 1 with Cl ⁻	186
17. Table F-9. Titration of 2 with HS ⁻	188
18. Table F-10. Titration of 2 with Cl ⁻	190
19. Table F-11. Titration of 3 with HS ⁻	192
20. Table F-12. Titration of 3 with Cl ⁻	194
21. Table F-13. Crystal data and structure refinement for 1 + HS ⁻	198

LIST OF SCHEMES

Scheme	Page
1. Scheme I-1. (a) Cold cyanolysis detection/quantification of sulfane sulfur. (b) General strategy for tag-switch labelling of protein persulfides.....	9
2. Scheme I-2. Common motifs for small-molecule H ₂ S donors. (a) Organic polysulfides, (b) Cysteine-activated H ₂ S donors, (c) Cysteine-activated H ₂ S donors with N-SH motifs, (d) Hydrolysis-based donors, and (e) Anethole 1,2-dithiole-3-thione (ADT) derived donors.....	15
3. Scheme I-3. (a) Methylene blue (MB) and (b) monobromobimane (mBB) methods for H ₂ S quantification.....	18
4. Scheme I-4. Common motifs in reaction-based probes for H ₂ S, including reactions based on (a) reduction, (b) nucleophilic attack, and (c) metal precipitation.	22
5. Scheme II-1. Reaction of ZnPc with HS ⁻ and reversibility with acid.....	30
6. Scheme II-2. Reaction of CoPc with HS ⁻ and subsequent oxidation.....	32
7. Scheme V-1. Overall reactivity of the Fe ^{III/II} (TPivPP) scaffold with H ₂ S, HS ⁻ , and O ₂	83
8. Scheme VI-1. Reaction of Zn(didpa)Cl ₂ (1) with NBu ₄ SH to generate hydrosulfide adduct 2	96
9. Scheme VI-2. Reaction of 3 with NBu ₄ SH shows decomposition, demonstrating the importance of the H-bond acceptor in 2	101
10. Scheme D-1. Synthesis of Fe(TPivPP)(Im) ₂	147

CHAPTER I

A PRACTICAL GUIDE TO WORKING WITH H₂S AT THE INTERFACE OF CHEMISTRY AND BIOLOGY

Published as Hartle, M. D. and Pluth M. D. “A practical guide to working with H₂S at the interface of chemistry and biology.” *Chem. Soc. Rev.* **2016** DOI:10.1039/c6cs00212a. This is a co-authored literature review with M. D. Pluth. This chapter is a general introduction to the currently available tools for studying hydrogen sulfide at the interface of chemistry and biology.

Preface

Hydrogen sulfide (H₂S) is the most recently accepted endogenously produced gasotransmitter and is now implicated in a variety of physiological functions. This chapter provides a background on H₂S chemical biology and highlights practical considerations, pitfalls, and best practices in the field. Practical handling and safety considerations for working with this reactive biomolecule and basic roles of H₂S biogenesis and action are presented. Experimental methods for modulating H₂S levels, including enzymatic knockout, RNA silencing, enzymatic inhibition, and use of small molecule H₂S donors are also highlighted. Complementing H₂S modulation techniques, we also highlight current strategies for H₂S detection and quantification.

Introduction

Hydrogen sulfide (H₂S) has emerged as an important biological signaling molecule that plays diverse roles in human health and physiology. Despite its long history as a toxic gas and environmental pollutant, H₂S now joins nitric oxide (NO) and carbon monoxide (CO) as a gasotransmitter – a small, enzymatically generated, gaseous

molecule with a tightly regulated metabolism that impacts physiological functions.¹⁻⁴ The innate chemical properties of H₂S, including its redox activity, acidity, and high nucleophilicity, allow for reaction with different cellular targets as part of its signaling capacity. By comparison, disentangling this chemistry is in many ways more complicated to that of NO and CO.⁵ Misregulation of endogenous H₂S is implicated in diverse physiological processes, including blood pressure regulation, immune response, and long term potentiation, as well as various diseases in the neuronal, gastrointestinal, circulatory, and endocrine systems.² Aligned with our rapidly expanding understanding of biological H₂S, new and impactful investigative tools for elucidating its genesis, translocation, and action have emerged and continue to be an active and fruitful research area.

By contrast to biological studies focused on NO and CO, H₂S-focused investigations are often faced with unique experimental challenges – some of which are due to the recent emergence of H₂S chemical biology and others from the innate physical properties of H₂S. For example, although CO, NO, and H₂S are all gasses, common gas detection techniques, such as gas chromatography (GC) and chemiluminescence detectors provide robust methods for detection and quantification for CO and NO, respectively, whereas similar techniques have not been widely developed for H₂S. The different protonation states of H₂S, and its interaction with the redox-active biological sulfur pool, make analysis by GC or other common analytical methods challenging. Similarly, reaction-based imaging techniques, as well as synthetic donor scaffolds, are often more complicated than similar systems for NO or CO. Despite these challenges, recent studies have suggested the potential interplay between the biological chemistry of H₂S and NO^{3,6} as well as CO,⁴ thus highlighting the interconnectivity of these three gaseous molecules.

These interactions, as well as those with H₂S and reactive sulfur, oxygen, and nitrogen species (RSONS) highlight the complexity of the biological landscape in which H₂S is involved, and the synergistic relationship of H₂S to other important and reactive small molecules in biology.

In this chapter, we highlight key points regarding H₂S chemical biology and provide a brief survey of accessible tools and methods for H₂S research at the interface of chemistry and biology. Our goal is not to provide a comprehensive overview of all investigative tools for H₂S research, but rather to highlight currently available classes of tools and to provide important considerations to help guide new researchers into the rapidly developing field of H₂S chemical biology.

Properties and Enzymatic Production of H₂S

H₂S is a weak acid with a first pK_a of 7.0, and a second pK_a, corresponding to the deprotonation of hydrosulfide anion (HS⁻) of >14.¹ Under physiological conditions, HS⁻ constitutes about 80% of the speciation, neutral H₂S about 20%, and dianionic S²⁻ less than 1%.¹ The HS⁻ and H₂S protonation states provide water-solubility and lipophilicity, respectively, and HS⁻ is a potent nucleophile that can react with different electrophilic cellular targets including RSONS. Additionally, the different protonation states afford different metal-ligation and redox properties. The complex redox landscape of biological sulfur, with oxidation states ranging from -2 in H₂S to +6 in SO₄²⁻, means that H₂S/HS⁻ can be readily oxidized to other biologically-relevant reactive sulfur species. Indeed, the redox-labile / sulfane-sulfur pool may provide an important method of sulfide storage and transport, but also may provide new signaling pathways distinct from those associated with H₂S alone (vide infra).⁷

Enzymatic H₂S biosynthesis stems primarily from cystathionine- γ -lyase (CSE), cystathionine- β -synthase (CBS), and 3-mercaptopyruvate sulfurtransferase (3-MST) / cysteine aminotransferase (CAT). In each of these pathways, the sulfur atom incorporated into H₂S is derived from the sulfhydryl group of homocysteine (Hcy) or L-cysteine (L-Cys). Details of these pathways have been recently reviewed in significant detail and are summarized briefly here (Figure I-1).¹⁻⁴ CSE catalyzes the formation of H₂S and homolanthionine from 2 equiv. of Hcy, but can also work in concert with CBS to convert Hcy and Cys to H₂S and cystathionine. CBS can also catalyze the condensation of Hcy with Serine (Ser) to generate cystathionine and H₂O. Upon reaction with CSE, cystathionine is converted back to L-Cys with concomitant formation of homoserine. This generated Cys can either participate in the above pathways, can be hydrolyzed to Ser and H₂S by CBS or CSE, or can be condensed with a second equivalent of Cys by the same two enzymes to form lanthionine and H₂S. Cysteine is also a viable substrate for CAT, which generates 3-mercaptopyruvate (3-MP), which is then converted to pyruvate, NH₃, and H₂S by 3-MST. The 3-MST pathway also accounts for H₂S formed from D-Cys, which is first converted to 3-mercaptopyruvate by DAO.

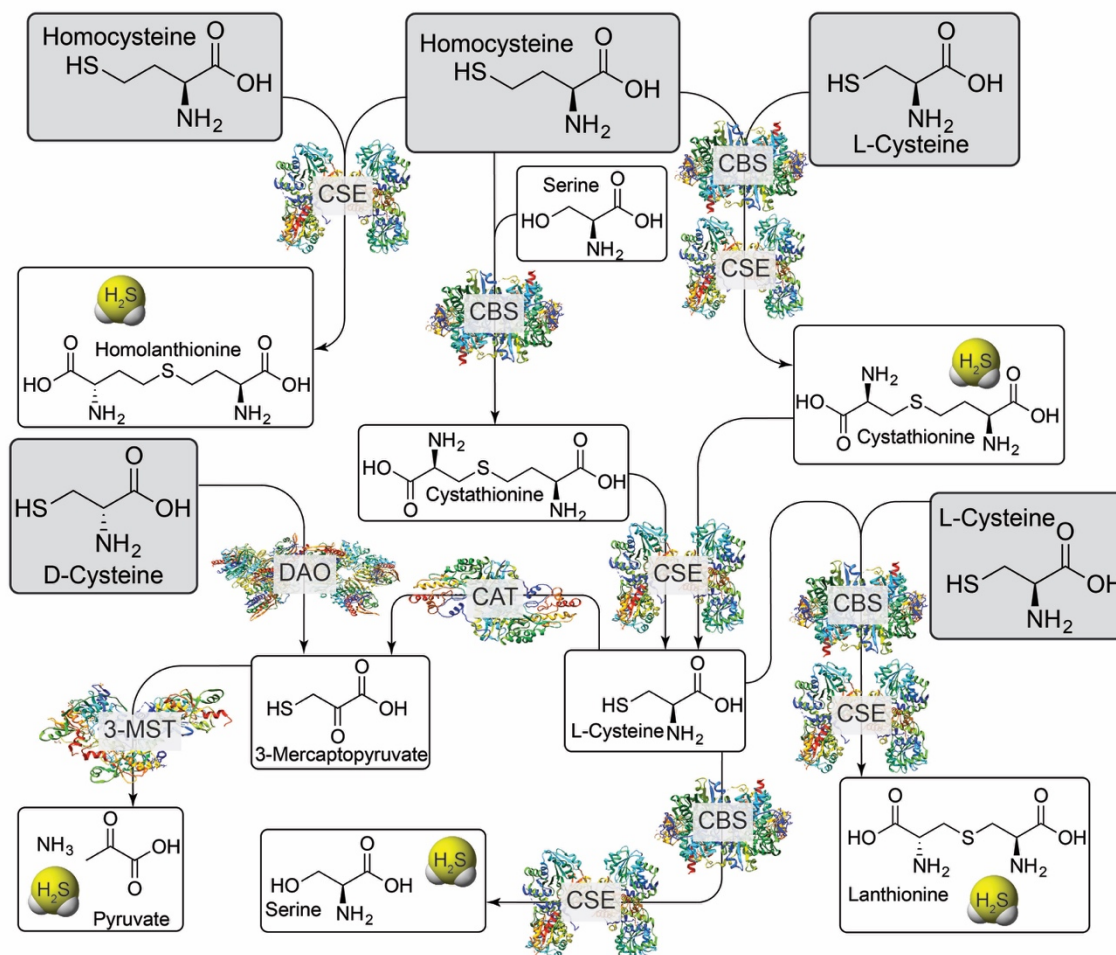


Figure I-1. Enzymatic H₂S production pathways. CSE: cystathionine γ -lyase; CBS: cystathionine β -synthase; CAT: cysteine aminotransferase; DAO: D-aminoacid oxidase; 3-MST: 3-mercaptopyruvate sulfurtransferase. Grey boxes indicate common substrates for H₂S-producing enzymes.

Practical Handling and Safety Considerations

Hydrogen sulfide is a highly toxic gas, and adequate care must be given when handling H₂S gas, sulfide salts, and synthetic H₂S donors. Although the characteristic rotten egg odor is detectable as low as 0.01 ppm in air, odor alone should never be used as the primary method of safety monitoring. Rapid olfactory fatigue results upon exposure to concentrations greater than 100 ppm but also after continuous exposure to significantly lower levels. H₂S concentrations as low as 20 ppm cause eye and lung

irritation, 300-500 ppm levels result in serious eye damage, and 700 ppm or higher levels can result in unconsciousness, respiratory failure, and death.⁸ The combination of high toxicity with rapid olfactory fatigue necessitates handling in a well ventilated fume hood equipped with an H₂S alarm, which detects H₂S gas and typically reports in the 5-10 ppm range, especially when using H₂S gas directly or quantities of sulfide salts sufficient to provide a potentially toxic response.⁹ It is also practical, both from a safety and odor-mediation standpoint, to quench any H₂S-containing solutions after use. Such quenching can be readily accomplished by preparation and use of a Zn²⁺ quenching solution, which rapidly reacts with free sulfide to generate insoluble ZnS. This quenching slurry can be prepared by adding 30 g Zn(OAc)₂, 9 g sodium citrate, and 12 g NaOH to 1 L of H₂O.⁸

For experiments involving aqueous sulfide solutions, it is often more practical to use sulfide salts, such as NaSH or Na₂S, rather than H₂S gas directly. Despite their convenience, the commercial purity of NaSH or Na₂S is often poor, and many samples contain significant quantities of elemental sulfur or polysulfides.^{5,10-11} In general, sulfide salts should be free-flowing white powders – any inclusion of yellow or other highly colored impurities should signal to the user that the sample does not have the appropriate purity and should be discarded. Because of the propensity of H₂S/HS⁻ to oxidize, especially in the presence of trace metal ions and oxygen, H₂S solutions should be prepared in anaerobic buffer under a blanket of nitrogen or argon in clean, metal-free, glass- or plastic-ware. Such solutions should also be prepared in septum-sealed vials to prevent significant loss from H₂S volatilization and also to enable easy transfer of sulfide solutions via gas-tight syringe. Because of this volatility and potential for oxidation, it is

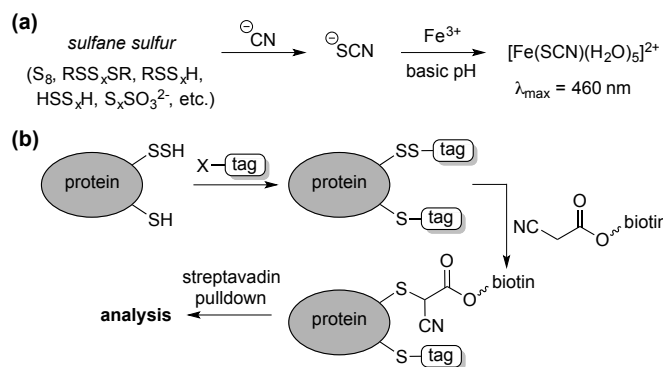
most practical to prepare sulfide-containing solutions immediately prior to use rather than to re-use solutions from previous experiments.

Interactions with the Sulfane-Sulfur Pool

Complementing the signaling roles of biological H_2S , significant evidence suggests that sulfane-sulfur compounds, such as polysulfides, persulfides, and other sources of reductant-labile sulfur, play important biochemical roles.^{7,10-11} The term “sulfane sulfur” refers to a sulfur atom with formally six valence electrons and no charge (S^0), which is bound to one or more sulfur atoms.¹² Upon reaction with cellular reductants or thiols, sulfane-sulfur compounds can release sulfide, thus providing a convenient source of H_2S storage. Additionally, sulfane-sulfur species have distinct chemical reactivities that may contribute to additional modes of action. For example, persulfides (RSSH) are more nucleophilic than the corresponding thiols, and S-persulfidation of nucleophilic Cys residues in enzymes is known to modify enzymatic activity.¹ As completely inorganic species, hydropolysulfides (HSS_xH) are also important sulfane-sulfur species, as evidenced by a recent report demonstrating that 3-MST not only generates H_2S , but also H_2S_3 .¹⁰ The use of small molecule persulfides and persulfide-releasing motifs as H_2S donors (vide infra) and as model systems is quickly providing more information on persulfide reactivity and its role in the intricate chemistry of RSONS.¹³ Although isolated persulfides are typically unstable in solution and have not yet found utility in biochemical investigations, caged persulfides, which release persulfides upon hydrolysis or reaction with nucleophiles, or persulfides generated in-situ from reaction of GSSG with HS^- , have been used to investigate different roles of persulfides in reactive sulfur species regulation and action.¹⁴

One of the most basic methods for sulfane-sulfur detection and quantification is the cold cyanolysis assay, which utilizes the reaction of sulfane sulfur atoms with CN^- at basic pH to form thiocyanate (SCN^-). Addition of excess ferric iron results in the formation of $[\text{Fe}(\text{SCN})(\text{H}_2\text{O})_5]^{2+}$, which can be readily detected and quantified by the characteristic absorbance at 460 nm (Scheme I-1a).¹⁵ In practice, the cold cyanolysis method is usually used for purified proteins or samples in simple matrices and cannot differentiate between individual components, such as persulfides and polysulfides, in the sulfane-sulfur pool.

One significant limitation of the cold cyanolysis method is that persulfides are not differentiated from polysulfides or other sulfane-sulfur sources. As a step toward addressing this challenge, a tag-switch method to detect and assay persulfides was recently reported (Scheme I-1b).¹⁶ In this method, all sulfhydryl groups, both from thiols (-SH) and persulfides (-SSH) are labelled with an electrophile, such as methylsulfonyl benzothiazole (MSBT), to generate the corresponding benzothiazole thioether and disulfide, respectively. Importantly, the resultant benzothiazole disulfide remains reactive toward specific carbon-based nucleophiles, allowing for conjugation with biotin tags. The biotinylated proteins can then be subjected to streptavidin pulldown and detection by standard Western blot or mass spectrometric techniques.¹⁶ Complementing these strategies, selective reaction-based fluorescent probes for polysulfides and sulfane sulfur have been reported and are the subject of a recent review.² These, as well as other emerging tools, are poised to help differentiate between the genesis of H_2S and other reactive polysulfides.



Scheme I-1. (a) Cold cyanolysis detection/quantification of sulfane sulfur. (b) General strategy for tag-switch labelling of protein persulfides.

Methods for Modulating H₂S Levels

The ability to modulate cellular H₂S levels provides a cornerstone for investigating the actions of H₂S in biology. Such control can be achieved by selective knockout and/or knockdown of H₂S-producing enzymes, use of small-molecule competitive inhibitors or stimulators, or by administration of synthetic H₂S donors. In model cell lines and organisms, supplementation with exogenous H₂S can often provide protection (or rescue) from various (patho)physiological disease states associated with abnormal H₂S biosynthesis. These insights suggest that synthetic H₂S donors may not only provide important chemical tools for understanding biological H₂S, but may also offer viable therapeutic potential for diseases associated with H₂S misregulation.

KO Mouse Models.

Selective knockout (KO) of CSE, CBS, or 3-MST in different cell lines has been utilized in specific investigations (*vide infra*), but the development of KO mouse models has provided a more broad platform on which to study the impacts of reduced enzymatic H₂S generation.¹⁷ Homozygous CBS^{-/-} KO in mice results in severe developmental growth problems, and few of the mice live past 4 weeks of age.¹⁸ The heterozygous CBS^{+/-} KOs exhibit better viability and present hyperhomocysteinemia (high levels of

homocysteine in the blood) but have not been used extensively in H₂S-related investigations.¹⁸ By contrast, the CSE^{-/-} mouse model¹⁹ has found significantly more utility in H₂S-related investigations, including studies on the role of H₂S in blood pressure regulation, angiogenesis, and neurodegeneration, as well as many other studies. A second CSE^{-/-} mouse model exhibiting somewhat different phenotypes was also subsequently developed and used as an animal model for cystathionemia.²⁰ Homozygous 3-MST^{-/-} mice have been developed more recently and may also provide a useful animal model for H₂S-related investigations.²¹ As a whole, the availability of KO mouse models provide a key tool in studying the impacts of H₂S in contextually-rich biological environments and overcome some of the limitations of small molecule inhibitors or sulfide donors (vide infra).

RNA Knockdown Methods.

In addition to enzyme KO methods, gene knockdown by RNA interference (RNAi) methods has been used to silence CSE, CBS, and 3-MST. Importantly, these methods often provide a simpler approach to overcome the limitation of animal models or small-molecule inhibitors, and also offer a complementary approach for other enzyme modulation experiments. For example, small interfering RNA (siRNA) methods have been used to silence CSE and CBS.²² Unlike small-molecule inhibitors for 3-MST (vide infra), siRNA methods aimed at this enzyme have proven efficacious in reducing H₂S production, leading to important insights into mitochondrial electron transport and cellular bioenergetics.²³

Small-Molecule Inhibitors.

Small-molecule competitive inhibitors of H₂S-producing enzymes are commonly used to decrease H₂S synthesis in studies using isolated enzymes or cell culture models. On the basis of this widespread use, significant efforts have been made to discover or develop potent enzymatic inhibitors for CBS, CSE, and 3-MST. Although these studies have provided a useful suite of compounds for partial inhibition of H₂S-producing enzymes, identifying inhibitors with specificity for one enzyme over another and low inhibitory constant (K_i) values remains a significant challenge.

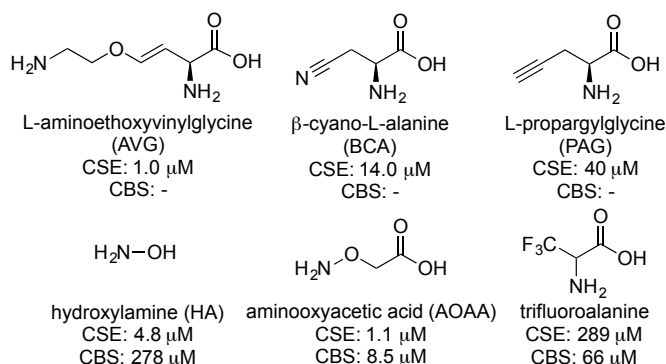


Figure I-2. Selected common CSE and CBS inhibitors with associated IC₅₀ values.

Commonly-used CSE inhibitors with IC₅₀ < 1 mM are L-aminoethoxyvinylglycine (AVG, 1 μM), β-cyano-L-alanine (BCA, 14 μM), and propargylglycine (PAG, 40 μM) (Figure I-2).^{17,24} Each of these inhibitors also affect other proximal phosphate (PLP)-dependent enzymes at mM concentrations, making it likely that off-target inhibition is observed at practical concentrations. Inhibition of CBS has proven significantly more challenging, with fewer inhibitors with IC₅₀ < 1 mM identified. Hydroxylamine (HA, 278 μM), aminoxyacetic acid (AOAA, 8.52 μM), and trifluoroalanine (66 μM) are among the most commonly used competitive inhibitors for

CBS,²⁴ but none of these show marked selectivity for CBS over CSE. Recent studies have used high-throughput screening methods, often in combination with H₂S fluorescent probes (vide infra), to identify CBS inhibitors. Such screens have identified new lead compounds with good IC₅₀ values in the low micromolar range, but many hits have not been compared directly with commonly-used inhibitors and their selectivity for CBS over CSE remains to be fully elucidated. Similar to the challenges with developing selective CBS inhibitors, selective inhibition of 3-MST has been unsuccessful to date.¹⁷ Given the overall difficulty in selectively inhibiting individual H₂S producing enzymes, the identification and development of new inhibitors for H₂S-producing enzymes is needed. Such inhibitors, if selective and functional at pharmacologically-reasonable concentrations, would provide important research tools for modulating cellular H₂S levels.

Enzymatic Stimulators.

Complementing methods to reduce H₂S synthesis using small-molecule inhibitors, H₂S synthesis can also be increased by use of different enzymatic stimulators. The most common of such methods is use of S-adenosylmethionine (AdoMet), an allosteric activator of CBS, to increase enzymatic H₂S production.²⁵⁻²⁷ In addition to CBS, CSE stimulation has also been demonstrated using cytokines and endotoxins, such as tumor necrosis factor α (TNF- α) or lipopolysaccharides (LPS), involved in immune response.²⁸⁻
²⁹ By contrast to CBS and CSE stimulation, common stimulators of 3-MST are not readily available and remain an active area of research.

Small-Molecule H₂S Donors.

Complementing methods to modulate endogenous H₂S synthesis, the ability to increase endogenous H₂S levels using exogenous sulfide sources provides an important research and pharmacological tool for studying the roles of biological H₂S. Commonly-used sources of exogenous H₂S include inorganic salts, such as NaSH and Na₂S, as well as small-molecule synthetic donors. Although NaSH and Na₂S provide convenient sources of sulfide, the large dose of H₂S released upon addition to buffer does not match the slower, continuous, enzymatic production characteristic of endogenous H₂S synthesis. Additionally, the large bolus of H₂S often results in a toxicological response and is quickly oxidized/metabolized by the cellular environment. Motivated by these limitations, researchers have developed slow-release sulfide donors that better mimic the gradual H₂S release of enzymatic synthesis. As our understanding of sulfide biology continues to evolve, one common observation is that slow-releasing H₂S donors often elicit different cellular responses than inorganic sulfide salts.³⁰ For example, sulfide salts and slow-releasing donors have been shown to be pro- and anti-inflammatory, respectively, in different models of inflammation, including sepsis.³⁰ These differences highlight the importance of experimental design when using different sulfide sources, but also highlight the potential pharmacological importance of such slow-releasing donors. Here we provide a brief overview of the most commonly-used donor motifs along with their sulfide release mechanisms when known. We also refer interested readers to recent reviews on this topic.^{14,31-32}

Some of the most simple sulfide-donating motifs are organic polysulfides, which are often found in natural products. For example, diallyltrisulfide (DATS), isolated from

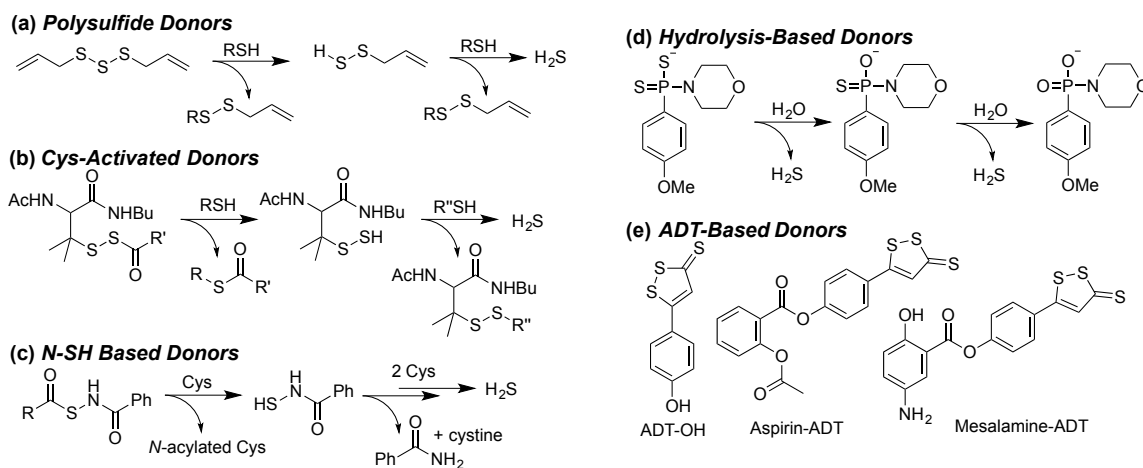
garlic and other alliums, is a commonly used donor molecule, and other organic polysulfides such as varacin have also been implicated in H₂S release.³³ Because polysulfides are electrophilic, attack by GSH or other thiols results in formation of an intermediate persulfide, which after a second reaction with GSH releases H₂S (Scheme I-2a).³⁴ Although DATS is the most commonly-used polysulfide donor, it is likely that other small molecule polysulfides are also potential platforms for H₂S release.

Inspired by disulfide exchange chemistry, chemists have also developed H₂S donors that are activated by nucleophilic attack by endogenous thiols.¹⁴ For example, protection of the thiol in penicillamine derivatives with an acyldisulfide results in persulfide formation after nucleophilic attack by Cys (Scheme I-2b).³⁵ Once the persulfide is released, reaction with a second thiol generates a stable disulfide and extrudes H₂S. Application of such donors to the treatment of myocardial ischemia/reperfusion (MI/R) injury in murine models results in reduced circulating levels of MI/R biomarkers suggesting these and similar donor motifs exhibit cardiac protection, and may have potential therapeutic applications.³⁵⁻³⁶

Operating by similar Cys-activated H₂S release mechanisms, donors containing N-mercapto (N-SH) motifs also generate a persulfide intermediate en route to H₂S release (Scheme I-2c).³⁷ In these donors, thiol exchange between Cys and the donor generates an S-acylated Cys intermediate, which undergoes native chemical ligation to rearrange to N-acylated Cys and an N-mercaptobenzamide intermediate. This N-SH compound reacts with Cys to generate Cys persulfide, which reacts with a second equivalent of thiol to release H₂S. The rate of H₂S release from these scaffolds can be tuned by the addition of electron donating or withdrawing groups on the scaffold. Additionally, new H₂S-donating

materials activated by thiol activation are also emerging, indicating the potential viability of this strategy for incorporation into therapeutics such as wound dressing to encourage angiogenesis.^{4,38}

In addition to donor activation by nucleophilic attack of thiols, other common donor constructs are activated by hydrolysis. For example, one of the most commonly used synthetic donors, GYY4137,³⁹ is a phosphino-dithioate derived from Lawson's reagent. GYY4137 undergoes slow hydrolysis in water to release H₂S (Scheme I-2d), although the efficiency of sulfide release remains low.⁴⁰ The rate of hydrolysis is pH dependent and slow at physiological pH, contrasting the rapid release of H₂S by inorganic salts. For example, treatment of precontracted aortic rings with NaSH results in relaxation in 20 to 30 seconds, whereas GYY4137 treatment requires nearly 10 minutes to achieve similar relaxation.⁴¹



Scheme I-2. Common motifs for small-molecule H₂S donors. (a) Organic polysulfides, (b) Cysteine-activated H₂S donors, (c) Cysteine-activated H₂S donors with N-SH motifs, (d) Hydrolysis-based donors, and (e) Anethole 1,2-dithiole-3-thione (ADT) derived donors.

Another common class of H₂S donors is based on 1,2-dithiole-3-thiones, with the most often used being 5-(4-hydroxyphenyl)-3H-1,2-dithiole-3-thione (ADT-OH) (Scheme I-2e).⁴² Although the mechanism of H₂S release from these scaffolds remains to be fully elucidated, one benefit of this donor motif is the ease with which it can be tethered to different molecules through ester or hydrolytically-stable amide linkages.⁴³ For example, linkage of a triphenylphosphonium cation imparts mitochondrial targeting for AP39, whereas ligation to common non-steroidal anti-inflammatory drugs (NSAIDs) has resulted in significant reduction in GI damage scores.⁴² The use of ADT derivatives in NSAID applications highlight the potential therapeutic action of H₂S donors,⁴² however, insights into the H₂S release mechanism from such donors is poised to make significant impacts into our understanding of the therapeutic action of these donor motifs.

All of the above donor motifs provide sources of sulfide in aqueous solution, but researchers interested in H₂S/HS⁻ using biomimetic compounds in organic solvents also have access to organic-soluble sources of sulfide. In practice, H₂S gas is sufficiently soluble in organic solutions for most investigations, however NaSH or Na₂S are generally insoluble in organic solvents. To aid in such investigations, we have recently reported simple method to prepare organic-soluble sources of HS⁻, such as NBu₄SH.⁴⁴ Such compounds offer a convenient source of HS⁻ in organic solution, enabling the separation of HS⁻ from H₂S in different bio(in)organic model studies, which is otherwise not possible in aqueous solution.

H₂S Detection and Quantification

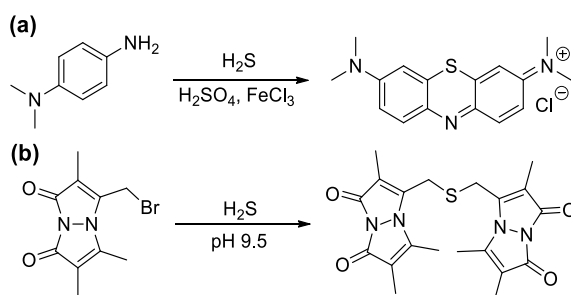
Coincident with the increased biological importance of H₂S, new methods for H₂S quantification and detection are rapidly emerging. Ranging from binary presence/absence

tests based on the formation of PbS from Pb^{II} salts to complex molecular architectures aimed at real-time H₂S detection, analytical methods of H₂S determinations comprise an important area of H₂S research. We highlight here general classes of analytical tools for H₂S research and describe their general benefits and pitfalls. On the basis of the rapid expansion of new methods for H₂S detection and quantification, as well as revisions and refinements of current methods, we refer the interested reader to a number of recent reviews on these topics.⁴⁵⁻⁴⁶

Quantification Methods.

Commonly used sulfide quantification methods typically require sample homogeneity, which is straightforward for biological fluids such as blood or serum, but significantly more complicated for naturally heterogeneous samples such as those from cell or tissue culture experiments. Spectrophotometric methods such as the methylene blue (MB) assay have constituted one of the classical methods of H₂S quantification. This method leverages the FeCl₃-catalyzed electrophilic aromatic substitution of p-dimethylamino aniline with sulfide to form MB, which has a characteristic absorbance at 670 nm and allows for sulfide quantification (Scheme I-3a). Despite its widespread use, recent studies have demonstrated that the detection limit of the MB assay for sulfide is only 2 μM rather than previously-reported lower values, making it insufficiently sensitive to differentiate between sulfide levels in normal versus CSE^{-/-} mice.⁴⁷ Furthermore, the MB method is performed under highly acidic conditions, which can result in sulfur extraction from other biological sources and diminishes the accuracy of sulfide levels measured with this method. Researchers new to the field of sulfide quantification will notice the large number of past studies using the MB method but are cautioned when

comparing H₂S levels measured with this method, especially when more accurate contemporary methods are available. For example, the monobromobimane (mBB) method, which utilizes the reaction of two equivalents of mBB with H₂S under basic conditions to generate fluorescent sulfide dibimane (SdB), enables quantification of H₂S by fluorescence HPLC with a detection limit of 2 nM (Scheme I-3b).⁴⁷ Because mBB reacts with both H₂S and thiols, separation of the fluorescent signals by HPLC is required for quantification. Despite this limitation, a significant benefit of this method is that workflows have been developed to analytically separate the free, reductant-labile / sulfane-sulfur, and acid-labile sulfide pools, enabling more detailed investigations across distributions in complex systems.⁴⁷ Additionally, the mBB method has been used more recently to also detect and quantify different poly- and persulfides, providing analytical information about these important reactive sulfur species.⁴⁸



Scheme I-3. (a) Methylene blue (MB) and (b) monobromobimane (mBB) methods for H₂S quantification.

Complementing spectrophotometric H₂S quantification methods are other analytical tools, such as sulfide selective electrodes. These tools can provide both the ability to quantify H₂S, based on a calibration curve, and provide real-time H₂S detection in solution. Readers interested in the differences in available sulfide electrodes are referred to a recent review focused on this topic.⁴⁵ In general, sulfide electrodes employ

an ion-selective membrane that allows H₂S permeability for solution-based measurements. In the solution phase of the electrode, a strongly basic environment allows the dianionic sulfide ion to reduce Fe(CN)₆³⁻ to Fe(CN)₆⁴⁻, which is subsequently re-oxidized at the platinum electrode to produce a current relative to H₂S concentration. One advantage of sulfide electrodes is that they can be used directly in mammalian tissues;⁴⁵ however, these electrodes cannot provide sub-cellular resolution of sulfide generation, storage, or transport. Even so, sulfide electrodes provide a convenient, time-resolved method for sulfide quantification or detection.⁴⁵

Detection Methods.

The development, refinement, and application of reaction-based probes for H₂S detection has expanded rapidly in the last few years. Such scaffolds typically couple various H₂S-selective reactions with different chromophores to generate a colorimetric or fluorescence response. Because of this design strategy, such methods are irreversible and the resultant methods measure accumulated probe activation rather than real-time H₂S dynamics. Despite these limitations, such constructs offer the potential to provide significantly higher spatiotemporal resolution than current H₂S quantification methods and also provide access to live cell and tissue imaging experiments. The predominant strategy for developing reaction-based probes for H₂S has been to utilize a fluorescence-quenching group on a fluorophore that can be modified or removed selectively by H₂S. As is common with most small molecule fluorescent probes, different detection strategies exhibit somewhat different selectivity patterns and each strategy may be better suited for certain types of investigations. The interested reader is referred to recent reviews on different aspects of reaction-based H₂S probe development.⁴⁶

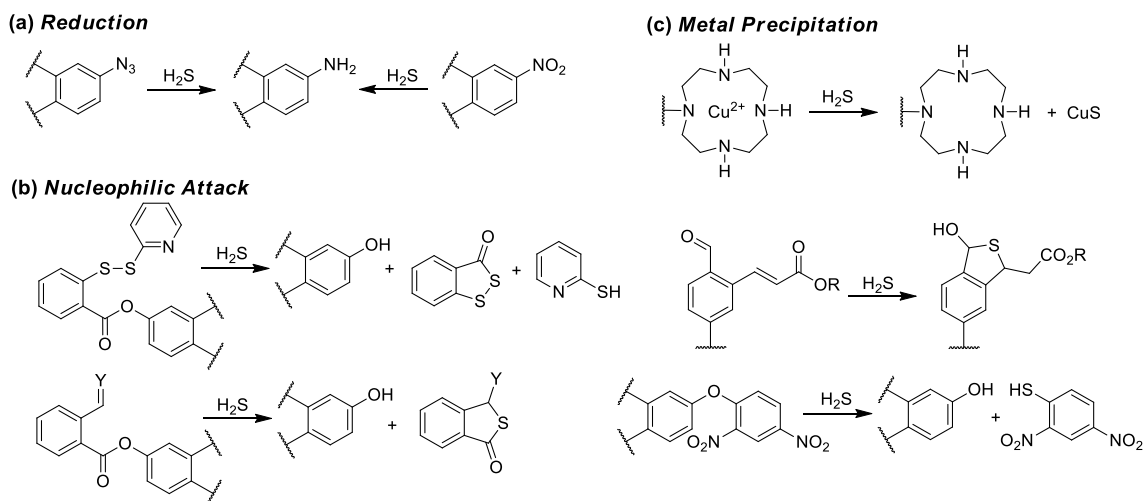
The most common reaction-based detection strategy to date is H₂S-mediated azide (R-N₃) reduction (Scheme I-4a).⁴⁶ Based on the ease of appending azides onto fluorogenic scaffolds, over 70 papers in the last few years described H₂S-detecting scaffolds using an azide to generate turn-on fluorescent probes (Scheme I-4a).⁴⁹⁻⁵¹ Reduction of other oxidized nitrogen functional groups, such as nitro groups, has also been utilized for H₂S detection.⁵¹ For most fluorophores, the azide moiety quenches fluorescence by a push-pull energy transfer mechanism, although other quenching mechanisms are also possible. Although the selectivity of azides for reduction by H₂S rather than biological thiols is predominantly empirical, most azide-based probes provide good to excellent selectivity for H₂S over other RSONS. A recent mechanistic investigation established that HS⁻ is the active species involved in H₂S-mediated probe activation, and that sulfide is oxidized to sulfane sulfur, such as HSS⁻, during azide reduction.⁵²

Further leveraging the high nucleophilicity of HS⁻, a variety of H₂S sensing strategies have been developed in which sulfide attacks an electrophilic, fluorescence-quenching protecting group appended on a fluorophore. Such scaffolds generally rely on the ability of H₂S to participate in two sequential nucleophilic reactions to remove or modify the group. One benefit of this strategy is that it imparts inherent selectivity because thiols, which can only participate in one nucleophilic attack, are unable to remove the protecting group.⁴⁶ One consequence of this selectivity, however, is that in many cases thiols can react with the electrophilic scaffolds, thus effectively consuming the probe prior to reaction with H₂S. This general strategy for H₂S sensing has been used

to attack activated disulfides, α - β -unsaturated ketones, and activated benzylic electrophiles (Scheme I-4b).⁵³⁻⁵⁶

In addition to exploiting the high nucleophilicity of HS^- for sensing, the high metallophilic nature of sulfur has also been exploited.⁵⁷ For example, ligation of a paramagnetic metal ion, such as Cu^{2+} , to a fluorescent molecule results in fluorescence quenching. Subsequent reaction with H_2S results in CuS formation and precipitation, thus releasing the fluorophore and producing a turn-on response. This strategy is inherently selective for sulfide over other biological thiols, but depending on the ligand characteristics may also be prone to metal reduction and release by cellular reductants or thiols, or exchange of the quenching paramagnetic metal ion with more prevalent diamagnetic ions like Zn^{2+} .

Beyond H_2S , polysulfides and persulfides are quickly becoming reactive sulfur species of interest. In addition to contributing to the biological chemistry associated with H_2S , it is likely that these sulfane-sulfur species provide signaling pathways distinct to those associated with sulfide. Aligned with this importance, reaction-based probes for polysulfides and other sulfane-sulfur sources are now beginning to emerge.⁵⁸⁻⁶⁰ The development and refinement of these, as well as other, tools appear poised to provide complementary information on the different pools of biological sulfide and further inform on the role of H_2S and sulfane-sulfur in the RSONS landscape.



Scheme I-4. Common motifs in reaction-based probes for H₂S, including reactions based on (a) reduction, (b) nucleophilic attack, and (c) metal precipitation.

Conclusions and Outlook

Hydrogen sulfide is an increasingly important biological molecule joining NO and CO as a key signaling agent and adding a new level of complexity to the RSONS landscape. Importantly, many of the unanswered questions in the field lay at the interface of chemistry and biology, thus requiring collaborative investigations and innovation to develop, refine, and apply new investigative tools in this rapidly expanding area of research. Key challenges include developing selective inhibitors of H₂S producing enzymes, generating new classes of sulfide donors that do not consume cellular thiols for activation or that can be programmed to release H₂S in response to certain stimuli, and refining H₂S imaging methods so that they do not irreversibly consume sulfide. As researchers progress toward these goals, the toolbox of available methods for studying biological H₂S will continue to grow and become more accessible to researchers in adjacent fields (such as NO or CO biochemistry, redox biology, and pharmacology), thus broadening the potential impact of H₂S-related investigations in these diverse scientific communities.

Bridge

The last few decades have witnessed the acceptance of other small molecule gases, namely carbon monoxide (CO), and nitric oxide (NO), with hydrogen sulfide (H₂S), as important endogenously produced gaseous signaling molecules involved in physiological functions including smooth muscle relaxation, neurotransmission, and vasoregulation.^{26,61} Beyond the study of H₂S in biology from a visualization and modulation standpoint, the interaction between heme-containing metalloproteins and gas molecules plays a significant role in biological systems. In addition to being a strong reductant, highly metallophilic, and oxygen sensitive, H₂S exists in various protonation states at physiological pH, thus complicating whether H₂S or HS⁻ is the active species when reacting with bioinorganic centers.⁶² To begin understanding the different interaction of H₂S and HS⁻ toward different biological targets, we chose to investigate the differential reactivity between the diprotic (neutral) and monoprotic (monoanionic) forms of sulfide toward different model complexes. Chapter II highlights the preference of simple metalloporphyrin derivatives to react with the monoanionic HS⁻ over H₂S.

Each chapter contains previously published or will be published co-authored material. Chapter I was co-authored with Dr. Michael Pluth. Chapter II was co-authored with Dr. Michael Pluth, Dr. Samantha Sommer, and Stephen Dietrich. Chapter III was co-authored with Dr. Daniel Meininger, Dr. Lev Zakharov, Dr. Zachary Tonzetich, and Dr. Michael Pluth. Chapter IV was co-authored by McKinna Tillotson and Dr. Michael Pluth. Chapter V was co-authored by Dr. James Prell and Dr. Michael Pluth. Chapter VI was co-authored by Maira Delgado, Dr John Gilbertson, and Dr. Michael Pluth. Chapter VII was co-authored by Ryan Hansen, Dr. Blakely Tresca, Sam Praker, Dr. Lev

Zakharov, Dr. Michael Haley, Dr. Michael Pluth, Dr. Darren Johnson. Specific contributions can be identified in the opening paragraph of each chapter.

CHAPTER II

**CHEMICALLY REVERSIBLE REACTIONS OF HYDROGEN SULFIDE WITH
METAL PHTHALOCYANINES**

Published as Hartle M. D., Sommer, S. K., Dietrich, S. R., and Pluth M. D. “Chemically Reversible Reactions of Hydrogen Sulfide with Metal Phthalocyanines” *Inorg. Chem.* **2014** 53(15) 7800-7802. The experimental work was performed by me, with preliminary experiments by S. R. Dietrich under the direction of S. K. Sommer. M. D. Pluth provided experimental design advice and editorial assistance. Associated content can be located in Appendix A.

Preface

Hydrogen sulfide (H₂S) is an important signaling molecule that exerts action on various bioinorganic targets. Despite this importance, few studies have investigated the differential reactivity of the physiologically-relevant H₂S and HS⁻ protonation states with metal complexes. In this chapter, we investigate the distinct reactivity of H₂S and HS⁻ with Zn(II) and Co(II) phthalocyanine (Pc) complexes and highlight the chemical reversibility and cyclability of each metal. ZnPc reacts with HS⁻, but not H₂S, to generate [ZnPc-SH]⁻, which can be converted back to ZnPc by protonation. CoPc reacts with HS⁻, but not H₂S, to form [Co(I)Pc]⁻, which can be reoxidized to CoPc by air. Taken together, these results demonstrate the chemically reversible reaction of HS⁻ with metal Pc complexes and highlight the importance of H₂S protonation state in understanding the reactivity profile of H₂S with biologically relevant metal scaffolds.

Introduction

Hydrogen sulfide (H_2S) is an endogenously-produced molecule that plays important and diverse roles in both vasoregulation and neurotransmission, as well as other physiological processes.^{1,19,26,61,63-68} As a gaseous small molecule signaling agent, endogenous H_2S joins NO and CO as a gasotransmitter, and all three mediate important functions through action on bioinorganic targets.^{1,26,61,68} Unlike NO and CO, however, H_2S exists in different protonation states at physiological pH, which can facilitate lipid and water solubility in the diprotic (H_2S) and monoanionic (HS^-) forms, respectively. Furthermore, the redox potential, nucleophilicity, and tendency to form insoluble metal salts also vary with H_2S protonation state, thus complicating reactivity with transition-metal centers.⁶⁵ Despite its widespread importance, the coordination chemistry of H_2S with bio-inspired transition-metal scaffolds remain underexplored by comparison to CO and NO.⁶⁹ Although H_2S binding to Ru- and Fe-based complexes have been reported,⁶⁹⁻⁷⁴ investigations of isolated porphyrinoid scaffolds remain limited.⁷⁵⁻⁷⁸ Motivated by the growing interest in the biochemical functions of H_2S and lack of information on the differential reactivity of H_2S and HS^- in bioinorganic contexts, we report here the differential reactivity of H_2S and HS^- toward metal phthalocyanine (Pc) complexes and highlight the chemically reversible reactions of HS^- with these platforms.

Phthalocyanines are planer, aromatic porphyrin derivatives that have been used previously as models of bioinorganic reactivity including the reversible binding of NO, CO, and O_2 to heme mimics⁷⁹ and the reduction of CO.⁸⁰ Metal Pc complexes have characteristic UV-Vis spectroscopic signatures⁸¹ including the Q-band (600-700 nm), which provides information on the oxidation state and binding modes of the central metal

ion, as well as the B-band (300-400 nm), and window region (400-550 nm), which provide information about bound ligands and metal oxidation state.⁸² Based on these characteristics, as well as solubility⁸¹ and redox properties,⁸² we viewed ZnPc and CoPc as promising initial platforms on which to investigate the differential reactivity of H₂S and HS⁻ with redox inactive and active metal complexes.

Results and Discussion

Due to its redox inactivity, we reasoned that treatment of ZnPc with H₂S or HS⁻ would result in metal ligation rather than metal-based redox chemistry. To probe such reactivity, we titrated ZnPc in THF with H₂S gas (up to 100 equiv. or by bubbling for 15 min.) but failed to observe any reaction by UV-Vis spectroscopy. By contrast, titration of ZnPc in THF with NaSH dissolved in DMSO resulted in clean conversion to a new species as evidenced by a 5 nm bathochromic shift of the Q-band, appearance of a broad absorbance centered at 410 nm, and well-anchored isosbestic points at 329, 381, and 667 nm (Figure II-1a). Control experiments titrating ZnPc in THF with DMSO, H₂O, KOH in DMSO, H₂S in DMSO, or S₈ failed to change the ZnPc UV-Vis spectrum. Addition of aqueous NaSH to ZnPc in THF resulted in identical reactivity to the DMSO experiments, suggesting that the availability of weakly-acidic protons does not influence the reactivity. Similarly, addition of [NBu₄][BH₄], a stronger reductant than H₂S or HS⁻,⁸³ failed to change the UV-Vis spectrum of ZnPc, suggesting that HS⁻-mediated reduction of the metal or ligand was not occurring. To probe the binding stoichiometry, we constructed a Job plot by monitoring changes in absorbance as a function of the ZnPc and NaSH molar ratios, which resulted in data consistent with 1:1 binding (Figure A-2). Taken together

with the above experiments, these studies suggest formation of a $[\text{ZnPc-SH}]^-$ adduct upon treatment of ZnPc with HS^- .

To confirm that HS^- was binding to the Zn(II) center and not reacting with the Pc ring directly, we used ^1H NMR spectroscopy to investigate changes in the Pc resonances upon reaction with NaSH. Treatment of ZnPc in $\text{THF-}d_8$ with 2 equiv. of NaSH in $\text{DMSO-}d_6$ resulted in an upfield shift in the Pc ^1H NMR resonances from 9.59 and 8.20 ppm to 9.41 and 8.06 ppm, respectively (Figure II-1b). Furthermore, the dd splitting pattern of the Pc ring is maintained upon treatment with NaSH, indicating that C4 rotational symmetry is preserved. This symmetry preservation precludes the possibility of HS^- nucleophilic addition or $\text{HS}\cdot$ radical addition into the Pc ring because such addition would lower the overall symmetry of the complex and subsequently increase the complexity of the coupling. Treatment of ZnPc in $\text{THF-}d_8$ with two equiv. of KOH in $\text{DMSO-}d_6$ failed to change the ^1H NMR spectrum of ZnPc significantly, indicating that the changes in chemical shift upon treatment of ZnPc with HS^- were not simply derived from acid-base chemistry (Figure II-1b).

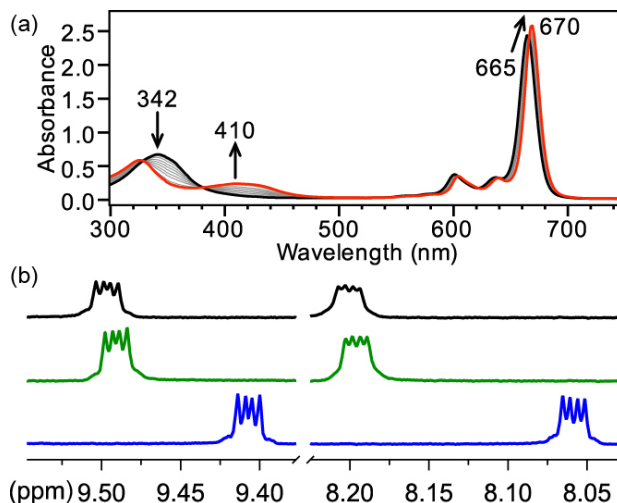
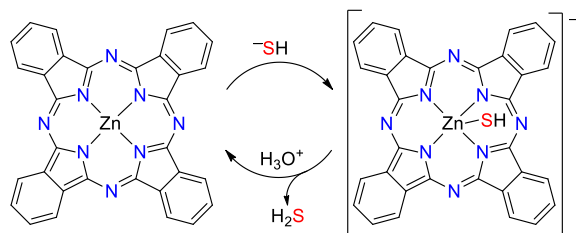


Figure II-1(a) UV-Vis titration of ZnPc (6.3 μM in THF, black) with NaSH (0.25 equiv. increments of 8 mM in DMSO up to 5 equiv.). (b) ^1H NMR (600 MHz, $\text{THF-}d_8$) spectra of 600 μM ZnPc (top, black), 600 μM ZnPc with 2 equiv. of KOH in $\text{DMSO-}d_6$ (middle, green), and 600 μM ZnPc with 2 equiv. of NaSH in $\text{DMSO-}d_6$ (bottom, blue).

Because ZnPc binds HS^- but not H_2S , we reasoned that bound HS^- should be acid labile, thus allowing for chemically reversible coordination of HS^- by addition of a suitable proton source (Scheme II-1). To test this hypothesis and to demonstrate the chemically reversible binding of HS^- to ZnPc, we first generated $[\text{ZnPc-SH}]^-$ in situ by treating ZnPc in THF with 10 equiv. of NaSH in DMSO and then added an equimolar amount of AcOH. As predicted, the characteristic spectral features of $[\text{ZnPc-SH}]^-$ at 410 and 670 nm reverted to the 342 and 665 nm absorbances corresponding to the parent ZnPc (Figure II-2). Further addition of NaSH in DMSO regenerated the 410 and 670 nm $[\text{ZnPc-SH}]^-$ spectral features (Scheme II-1).*

* The solution becomes naturally buffered, so each addition of NaSH or AcOH required more equivalents.



Scheme II-1. Reaction of ZnPc with HS⁻ and reversibility with acid.

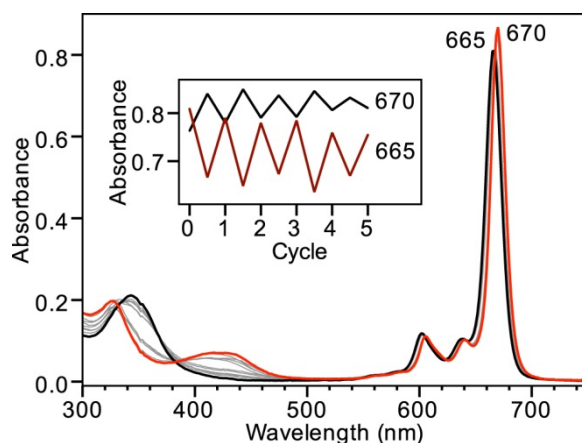


Figure II-2. UV-Vis spectra of ZnPc (2 μ M in THF, black) treated with 10 equiv. of NaSH in DMSO (red). Treatment with 10 equiv. of AcOH regenerates the original ZnPc spectrum. This system can be cycled numerous times (inset).

Having established that redox inactive ZnPc binds HS⁻ but not H₂S, we next investigated the reactions of HS⁻ and H₂S with a redox active CoPc. We chose CoPc due to its well-defined and readily-monitored redox states of blue Co(II)Pc and green [Co(I)Pc]⁻.⁸⁴⁻⁸⁵ Paralleling the chemistry observed for ZnPc, CoPc does not react with H₂S gas (up to 100 equiv. or by bubbling for 15 min.). Titration of CoPc in THF with NaSH in DMSO, however, resulted in a significant bathochromic shift of the Q-band from 656 to 697 nm, emergence of a broad absorbance at 467 nm centered in the window region, and well-anchored isosbestic points at 316, 370, 555, and 676 nm (Figure II-3). These new absorbances match the reported spectrum of [Co(I)Pc]⁻,⁸⁴ and also match the spectrum of [Co(I)Pc]⁻ generated from CoPc and [NBu₄][BH₄] (Figure A-1). A Job plot

constructed by monitoring the absorbance at 467 nm as function of the CoPc and HS⁻ molar ratio is consistent with a 1:1 reaction of CoPc with HS⁻ (Figure A-3). This reaction stoichiometry, as well as previous work using CoPc to oxidize thiolates to disulfides, is consistent with initial oxidation of HS⁻ to HSSH with potential conversion to further oxidation products.⁸⁶⁻⁹⁰

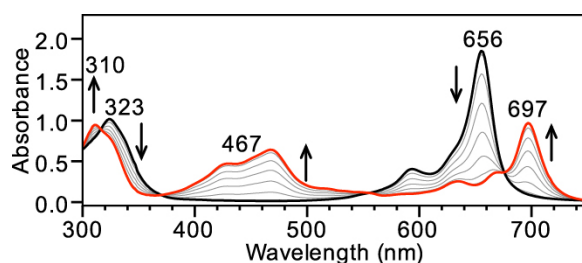
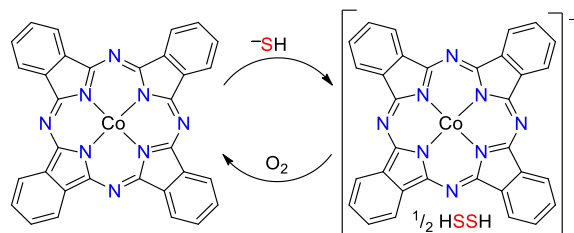


Figure II-3. UV-Vis titration showing the reduction of CoPc (7 μ M in THF, black) to [Co(I)Pc]⁻ (red) by NaSH (21.7 mM in DMSO in 1 equiv. increments up to 10 equiv.)

Based on the observed HS⁻-mediated reduction of CoPc, we reasoned that the observed reactivity could be reversed by oxidation with atmospheric oxygen to generate a chemically-reversible and cycleable system. To demonstrate this redox cycling, we first treated a THF solution of CoPc with 10 equiv. of NaSH under N₂ to generate [Co(I)Pc]⁻ and then exposed the solution to air, which resulted in rapid oxidation back to the parent CoPc (Figure II-4). Subsequent addition of NaSH regenerates [Co(I)Pc]⁻. If protected from O₂ and under an N₂ atmosphere, the [Co(I)Pc]⁻ product is stable and does not spontaneously revert to CoPc. Unlike ZnPc, this chemically-reversible reaction with HS⁻ results in a color change that can be easily detected by the naked eye (Figure II-4, inset), highlighting the potential for future use in chemically-reversible colorimetric HS⁻ detection (Scheme II-2).



Scheme II-2. Reaction of CoPc with HS^- and subsequent oxidation.

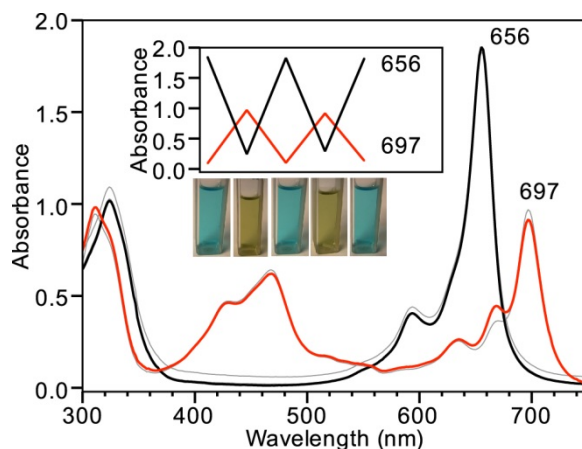


Figure II-4. UV-vis spectra of CoPc ($7 \mu\text{M}$ in THF, black trace, blue cuvette) after treatment with 10 equiv. of NaSH in DMSO (red trace, green cuvette). Subsequent exposure to atmospheric oxygen regenerates CoPc. The inset shows changes in the Q-band, corresponding to three cycles of treatment with HS^- followed by exposure to air.

Conclusion

Taken together, these studies with ZnPc and CoPc demonstrate the differential reactivity of HS^- and H_2S toward metal centers and highlights how these changes in a protonation state can be used to generate chemically-reversible HS^- ligation. Additionally, these examples of chemical reversibility clarify the fundamental reaction chemistry of porphyrin-derived scaffolds with H_2S and expand the fundamental understanding of how H_2S interacts with biologically relevant metal scaffolds.

Bridge

This chapter highlighted the different reactions of HS^- and H_2S toward metal phthalocyanines. Because of the low solubility of NaSH in non-polar organic solvents,

we needed to use DMSO stock solutions of HS^- for our investigations. Unfortunately, DMSO is a highly polar solvent and can also act as a competitor for hydrogen bonding systems and metal ligation. To address these challenges and provide a means for conducting biomimetic investigations involving HS^- in organic solution, we sought to develop a simple method to prepare an organic-soluble form of HS^- , which we describe in Chapter III.

Experimental

Materials and Methods.

All manipulations were performed under an inert atmosphere using standard Schlenk techniques or an Innovative Atmospheres N_2 -filled glove box. Metal phthalocyanines (ZnPc, CoPc) were purchased from Strem Chemicals and used as received. Anhydrous sodium hydrogen sulfide (NaSH) was purchased from Strem Chemicals and handled under nitrogen. Hydrogen sulfide gas was purchased from Sigma Aldrich and transferred through a custom-built stainless steel transfer line to a glass storage bulb prior to use. *Note:* Hydrogen sulfide and its salts are highly toxic and should be handled carefully to avoid exposure. Spectroscopic grade THF was degassed by sparging with argon followed by passage through a Pure Process Technologies solvent purification system to remove water and stored over 4Å molecular sieves. THF- d_8 was purchased from Cambridge Isotope Laboratories and vacuum transferred from sodium/benzophenone ketyl, subjected to three freeze-pump-thaw cycles, and stored in an inert atmosphere glove box over 4Å molecular sieves. $[\text{NBu}_4][\text{BH}_4]$ was purchased from TCI and used as received. Glacial acetic acid was purchased from EMD Chemicals and used as received. Anhydrous DMSO was purchased from EMD Chemicals, degassed

using four freeze-pump-thaw cycles, and stored in an inert atmosphere glove box over 4Å molecular sieves. Phthalocyanine stock solutions were prepared in dry THF and stored in amber vials at -20 °C in an inert atmosphere glove box until immediately prior to use.

Spectroscopic Methods.

UV-vis measurements were acquired on an Agilent Cary 100 UV-Vis spectrophotometer equipped with a QNW dual cuvette temperature controller at 25.00 ± 0.05 °C. All spectroscopic samples were prepared under an inert atmosphere in septum-sealed cuvettes obtained from Starna Scientific. NMR spectra were acquired on a Bruker Avance-III-HD 600 spectrometer with a Prodigy multinuclear broadband CryoProbe at 25.0 °C. Chemical shifts are reported in parts per million (δ) and are referenced to residual protic solvent resonances.

General procedure for UV-vis spectroscopic studies.

In a glove box, the phthalocyanine stock solutions were diluted to the desired concentration and 3.0 mL of the resultant solution was transferred to a septum-sealed cuvette and removed from the glove box. Non-phthalocyanine reagents were prepared approximately 10^5 times more concentrated than the phthalocyanine to provide minimal dilution during the study. NaSH, H₂S, and other reagents were added to the septum-sealed cuvettes by gas-tight syringe. Titration studies were performed using 0.25 equiv. increments unless otherwise noted.

General procedure for NMR studies.

In a glove box, 3.0 mL of a ZnPc stock solution (0.60 mM in THF-*d*₈) was prepared and 1.0 mL added to three septum-capped NMR tubes. Stock solutions of NaSH and KOH (35.6 mM in DMSO-*d*₆) were prepared, and 17 μ L of each stock solution was

added to two of the NMR tubes using a gas-tight syringe. A control experiment using 17 μL $\text{DMSO-}d_6$ was also performed.

General Procedure for Job Plot Experiments

A 183 μM stock solution of ZnPc in 1:1 THF:DMSO was prepared in a glove box. Aliquots of various volumes were added to septum-capped air-tight cuvettes in the glove box. A 183 μM stock solution of NaSH in 1:1 THF:DMSO was prepared outside of the glove box using standard Schlenk technique. Each of the ZnPc cuvettes was diluted to 3 mL total volume with NaSH solution maintaining a total cuvette concentration of 183 μM , and the UV-vis spectra was immediately taken for all fractions. The job plot was constructed by following 427 nm across all concentrations.

A 38 μM stock solution of CoPc in 1:1 THF:DMSO was prepared in a glove box. Aliquots of various volumes were added to septum-capped air-tight cuvettes in the glovebox. A 39 μM stock solution of NaSH in 1:1 THF:DMSO was prepared outside of the glovebox using standard Schlenk technique. Each of the CoPc cuvettes was diluted to 3 mL total volume with NaSH solution maintaining a total cuvette concentration of 38 μM , and the UV-vis spectra was immediately taken for all fractions. The job plot was constructed by following 467 nm across all concentrations.

CHAPTER III

TETRABUTYLAMMONIUM HYDROSULFIDE PROVIDES A CONVENIENT SOURCE OF HS⁻ SOLUBLE IN ORGANIC SOLUTION FOR H₂S AND ANION-BINDING RESEARCH

Published as Hartle M. D., Meininger, D. J., Zakharov, L. N., Tonzetich, Z. J., and Pluth M. D. "NBu₄SH Provides a Convenient Source of HS⁻ Soluble in Organic Solution for H₂S and Anion-Binding Research" *Dalton Transactions*. **2015** 44(46) 19782-19785. The experimental work was performed by me, cyclic voltammetry was performed by D. J. Meininger, and crystallography was performed by L. N. Zakharov. I wrote the majority of the manuscript and Z. J. Tonzetich and M. D. Pluth provided editorial advice. Associated content can be located in Appendix B.

Preface

Hydrogen sulfide (H₂S) has gained significant interest within the scientific community due to its expanding roles in different (patho)physiological processes. Despite this importance, the chemical mechanisms by which H₂S exerts its action remain under investigated. Biomimetic investigations in organic solution offer the potential to clarify these mechanisms and to delineate the differential reactivity between H₂S and HS⁻; however, such studies are hampered by the lack of readily-available sources of HS⁻ that are soluble in organic solution. In this chapter, we present a simple method for preparing analytically pure tetrabutylammonium hydrosulfide (NBu₄SH), which we anticipate will be of significant utility to researchers in the H₂S and anion-binding communities.

Introduction

Hydrogen sulfide (H_2S), although historically recognized for its toxicity and roles in geochemistry, is now accepted to have broad biological importance and is implicated in physiological processes ranging from vasodilation to neurotransmission.¹ This recent surge of interest in the biomedical and pharmacological roles of H_2S has resulted in the need for versatile sulfide sources amenable to use under different experimental conditions. For example, most aqueous studies have used inorganic salts, such as NaSH or Na_2S , to generate sulfide solutions. Slow-releasing H_2S donor molecules, however, have emerged as promising alternatives with better pharmacological profiles due to their slow, continuous release by comparison to the large bolus of sulfide released by inorganic salts.^{14,31-32,91} In contrast to their utility in aqueous solution, NaSH and Na_2S salts are generally insoluble in organic solvents, and slow-release H_2S donors are often much less efficacious in organic solution. Moreover, slow-release H_2S donors can also generate side-products other than H_2S , thus complicating precise reactivity studies under controlled conditions. One benefit of using organic solutions to investigate $\text{H}_2\text{S}/\text{HS}^-$ reaction chemistry with bio(in)organic models, such as transition metals^{62,71,75,77,92-94} or reactive sulfur species,⁹⁵⁻⁹⁹ is that such constructs enable differentiation of H_2S reactivity from that of HS^- , which is otherwise challenging in protic media. For example, we have previously demonstrated that HS^- and H_2S react differently with Zn and Co phthalocyanine complexes.⁶² Furthermore, HS^- is a significantly more potent nucleophile than H_2S , resulting in different reactivity toward common electrophiles (Figure B-3, B-4). Although H_2S is readily available and soluble in organic solutions, simple sources of HS^- that are soluble in common organic solvents remain scarce. Based on the growing need

for such organic-soluble sources of the hydrosulfide ion, we describe a simple method of preparing and characterizing NBu₄SH in this chapter.

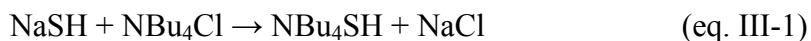
Use of tetraalkylammonium cations to enhance the solubility of HS⁻ in organic solution has been cited since the 1960s, however most reported syntheses rely on in situ salt generation or reaction of H₂S gas with tetraalkylammonium hydroxides.¹⁰⁰ Such preparative methods introduce complications involving removal of the water by-product in the case of hydroxide precursors,¹⁰¹ and limit the reaction scale in cases where H₂S gas is employed.¹⁰² Additionally, compounds prepared in this fashion suffer from limited product characterization, and previously-available commercial sources of NBu₄SH were not of analytical purity. To provide a convenient source of HS⁻ soluble in organic solution, we chose to prepare NBu₄SH by simple anion exchange chemistry.* Additionally, NBu₄⁺ is the most common counterion used for host-guest anion binding studies in organic solution, which to date have focused primarily on halides and oxoanions but have omitted investigations with HS⁻.¹⁰³

Results and Discussion

We found that simply stirring NBu₄Cl with NaSH in MeCN for several days resulted in an efficient cation exchange, allowing for isolation of analytically-pure NBu₄SH after removal of solvent and washing with Et₂O (eq. III-1). Complete Cl⁻ exchange was confirmed by elemental analysis. The resultant NBu₄SH product provides a characteristic S-H stretch at 2550 cm⁻¹ by IR spectroscopy (Figure B-5), which is similar to the 2540 cm⁻¹ S-H stretch observed for NaSH under identical conditions (Figure B-4).

* During the review of this paper, a recent report of HS⁻-containing organic liquids was reported. See: L. H. Finger, F. Wohde, E. I. Grigoryev, A. K. Hansmann, R. Berger, B. Roling, and J. Sundermeyer *Chemical Communications* **2015**, 51(90), 16169-16172.

Additionally, ^1H NMR spectroscopy in anhydrous CD_3CN revealed a resonance at -3.85 ppm corresponding to the sulfur-bound hydrogen atom, which broadens significantly upon addition of proton sources, such as water. T1 measurements of the resonance at -3.85 demonstrated a slow relaxation of 14 s.



Supporting the purity of NBu_4SH , we titrated with 4-chloro-7-nitrobenzo[d][1,2,3]oxadiazole (NBD-Cl) with NBu_4SH to analyze the sulfur content. Treatment of NBD-Cl with HS^- initially forms NBD_2S , which is then converted to NBD-SH upon further reaction with HS^- (Figure III-1). The final NBD-SH product of the titration has a characteristic absorbance at 534 nm, allowing for facile quantification of the sulfide content of NBu_4SH .¹⁰⁴

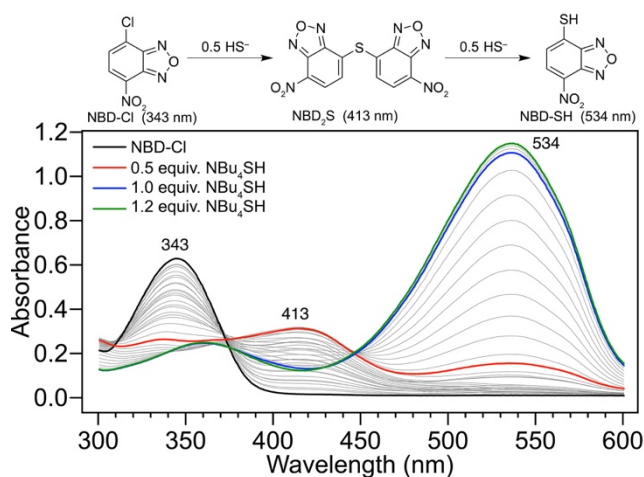


Figure III-1. Top: Quantification of the HS^- content in NBu_4SH . Bottom: Titration of NBD-Cl with NBu_4SH to confirm HS^- stoichiometry. UV-Vis spectra of $66 \mu\text{M}$ NBD-Cl treated with 0.05 increments of NBu_4SH with 3 min. incubation between scans. Conditions: 50 mM PIPES, 100 mM KCl, pH 7.4, and 37°C .

We further verified the identity of NBu₄SH by X-ray diffraction using single crystals grown by the slow diffusion of heptane into a toluene solution of NBu₄SH containing a drop of MeCN. Solution of the diffraction data confirmed the molecular structure of NBu₄SH, which crystallized in C2/c (Figure III-2, CCDC 1421021). Under these crystallization conditions, residual electron density corresponding to 0.5 equiv. of toluene within the asymmetric unit was observed. The solid-state structure also revealed six short contacts ranging from 2.74–2.92 Å from the sulfur atom to the α - and β -hydrogens of NBu₄⁺. These intermolecular interactions are consistent with C-H hydrogen bonding to the anions¹⁰⁵ and suggest that NBu₄SH may provide a useful anionic source of HS⁻ of significant interest for the anion-binding community.¹⁰⁶⁻¹⁰⁹ The availability of an organic solvent-soluble HS⁻ source will hopefully enable investigations into the reversible binding of this important analyte in synthetic receptors, thus potentially leading to new reversible sensing platforms for H₂S and HS⁻.

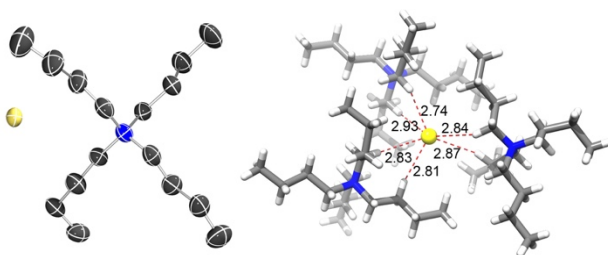


Figure III-2. Left: ORTEP diagram of NBu₄SH. Thermal ellipsoids are drawn at the 50% probability level. Hydrogens omitted for clarity. Right: Schematic of the intermolecular CH-anion hydrogen bonding interactions. Full crystallographic details are available in Appendix B.

Given the well-defined nature of NBu₄SH in organic solvent, we elected to investigate its electrochemical properties in acetonitrile. Displayed in Figure III-3 is the cyclic voltammogram of NBu₄SH at a glassy carbon electrode. The compound

demonstrates an irreversible oxidation wave at -0.365 V (vs Fc/Fc⁺) consistent with facile oxidation to polysulfide species.¹¹⁰⁻¹¹¹ The return reduction wave is greatly attenuated, most likely as a consequence of subsequent chemical reactions involving the oxidized sulfur species.

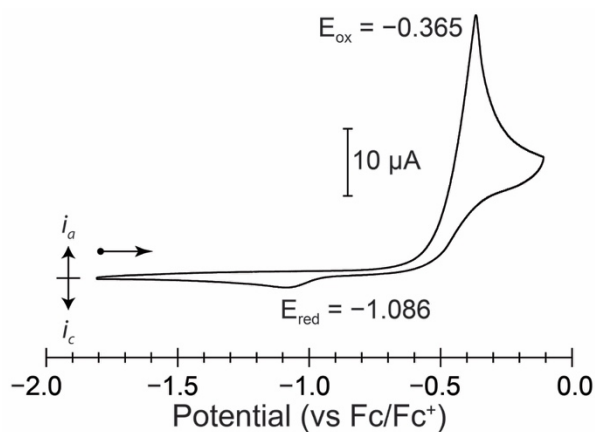


Figure III-3. Cyclic voltammogram of NBu₄SH (2 mM) at a 3 mm glassy carbon disk electrode in acetonitrile. Scan rate is 50 mV/s and the supporting electrolyte is 0.1 M NBu₄PF₆.

To highlight the diverse solubility of NBu₄SH, we compared the solubility of this sulfhydryl source with that of NaSH in various solvents (Table III-1). As expected, NBu₄SH is soluble in a significantly broader range of organic solvents than NaSH, thus highlighting its utility as a source of organic-soluble HS⁻.

Table III-1. Comparison of the solubility of NaSH and NBu₄SH in different solvents.

	NaSH	NBu ₄ SH		NaSH	NBu ₄ SH
H ₂ O	Yes	Yes	DMF	Sparingly	Yes
MeOH	Yes	Yes	DMA	Sparingly	Yes
CH ₂ Cl ₂	No	Yes	DMSO	*	*
CHCl ₃	No	*	Acetone	No	Yes
THF	No	Yes	Toluene	No	Sparingly
MeCN	No	Yes	Hexanes	No	No

*Some reactivity with solvent observed.

Conclusion

In summary, we provide a simple method to prepare and characterize NBu₄SH, a source of HS⁻ that is soluble in many organic solvents. We anticipate that this convenient hydrosulfide source will be of significant utility for the field of bioorganic and bioinorganic H₂S chemistry and will also provide a new analyte of interest for the community interested in anion binding mediated by host-guest supramolecular interactions.

Bridge

Having established a method for the synthesis and characterization of analytically pure HS⁻ in organic solution, we turned our attention to understanding how hydrogen sulfide reacts with different common metal-containing motifs in biology. The study of porphyrin complexes, in particular, provide a relatively simple system for investigating the ligation and redox properties of hydrogen sulfide with bioinorganic model complexes. Iron porphyrin compounds have received the most attention,^{77,112-113} while other important metal porphyrin complexes remain absent. In Chapter IV, we survey a range of metal protoporphyrin IX complexes, classifying their reaction into three categories:

unreactive toward H_2S and HS^- , binding of H_2S or HS^- , or reduction followed by binding of H_2S or HS^- .

Experimental

Materials and Methods.

All manipulations were performed under an inert atmosphere using standard Schlenk techniques or an Innovative Atmospheres N_2 -filled glove box unless otherwise noted. All chemicals were used as received. Tetrabutylammonium chloride was purchased from Sigma-Aldrich. NaSH (anhydrous) was purchased from Strem chemicals and handled under nitrogen. *Note:* Hydrogen sulfide and its salts are highly toxic and should be handled carefully to avoid exposure. Spectroscopic grade acetonitrile was degassed by sparging with argon followed by passage through a Pure Process Technologies solvent purification system to remove water and stored over 4Å molecular sieves in an inert atmosphere glove box. Acetonitrile- d_3 was purchased from Cambridge Isotope laboratories and distilled from calcium hydride, deoxygenated by three freeze-pump-thaw cycles, and stored in an inert atmosphere glove box.

Spectroscopic Methods.

UV-Vis measurements were acquired on an Agilent Cary 100 UV-Vis spectrophotometer equipped with a QNW dual cuvette temperature controller at 25.00 ± 0.05 °C. All spectroscopic samples were prepared under an inert atmosphere in septum-sealed cuvettes obtained from Starna Scientific. NMR spectra were acquired on a Bruker Avance-III-HD 600 spectrometer with a Prodigy multinuclear broadband cryoProbe at 25.0 °C. Chemical shifts are reported in parts per million (δ) and are referenced to residual solvent resonances. IR spectra were acquired on a Thermo Scientific Nicolet

6700 spectrometer equipped with a diamond crystal Smart ATR Attachment. Cyclic voltammetry was performed at 25 °C on a CH Instruments 620D electrochemical workstation. A 3-electrode set-up was employed comprising a glassy carbon working electrode, platinum wire auxiliary electrode, and a silver quasi-reference electrode. Triply recrystallized NBu₄PF₆ was used as the supporting electrolyte. All electrochemical data were referenced externally to the ferrocene/ferrocenium couple at 0.00 V.

X-ray crystallography details.

Diffraction intensities for NBu₄SH were collected at 173(2) K on a Bruker Apex2 CCD diffractometer using CuK_α source, $\lambda = 1.54178 \text{ \AA}$. The space group was determined based on systematic absences. Absorption corrections were applied by SADABS.¹¹⁴ The structure was solved by direct methods and Fourier techniques and refined on F^2 using full matrix least-squares procedures. The H atoms for the NBu₄⁺ cation were refined in calculated positions using the rigid group model. The H atom in the HS⁻ anion was not explicitly located. The solvent molecule (toluene) was disordered around an inversion center and was not involved in specific intermolecular interactions, therefore was treated by SQUEEZE.¹¹⁵ Corrections of the X-ray data by SQUEEZE results in a change of 232 electron/cell, which matches well with the expected value of 200 electron/cell for four toluene molecules in the full unit cells. All calculations were performed by the Bruker SHELXTL (v. 6.10) package.⁹⁸

Synthetic procedure for NBu₄SH.

In an inert atmosphere glove box, NaSH (1.0 g, 18 mmol, acquired from Strem Chemicals) and NBu₄Cl (4.93 g, 17.7 mmol) were added to a 250 mL round bottom flask, after which 100 mL of anhydrous, degassed MeCN was added. (Note: The commercial

purity of many NaSH sources is poor, and use of high purity NaSH is essential for preparation of NBu₄SH. Additionally, should complete anion exchange not occur, a 2 equiv. excess of NaSH can be used to facilitate full exchange.) The flask was sealed with a septum and electrical tape and stirred for 3 days. The yellow-brown solution was filtered under an inert atmosphere, and the solvent was removed under vacuum. The resultant solid was washed with Et₂O until a white solid was obtained, which was dried under vacuum to yield 2.6 g (53%) of NBu₄SH. The product is very hygroscopic and should be protected from atmospheric water and oxygen to prevent hydration or unwanted oxidation. The HS⁻ content can be conveniently determined by titration with NBD-Cl as described previously for NaSH.¹⁰⁴ FTIR (ATR, neat) cm⁻¹: 2960 (s, C-H), 2870 (m, C-H), 2550 (w, S-H); ¹H NMR (600 MHz, CD₃CN) δ: 3.16-3.10 (m, 8H), 1.61 (p, J = 7.9 Hz, 8H), 1.35 (h, J = 7.4 Hz, 8H), 0.96 (t, J = 7.4 Hz, 12H), -3.85 (s, 1H); ¹³C{¹H} NMR (151 MHz, CD₃CN) δ 59.3, 24.4, 20.3, 13.8; Calcd. for C₁₆H₃₇NS: C, 69.75; H, 13.54; N, 5.08; S, 11.64. Found: C, 70.22; H, 13.23; N, 5.23; S, 11.46; Cl, 0.00.

CHAPTER IV

**SPECTROSCOPIC INVESTIGATION OF THE REACTION OF METALLO-
PROTOPORPHYRINS WITH HYDROGEN SULFIDE**

Submitted for publication as Hartle M. D., Tillotson, M. R., and Pluth M. D. “Spectroscopic investigation of the reaction of metallo-protoporphyrins with hydrogen sulfide” *Journal of Inorganic Biochemistry* **2016**. Experimental design and EPR spectroscopy work was performed by me, all other experimental work completed by M. R. Tillotson. I wrote the manuscript and M. D. Pluth provided editorial advice. Associated content can be located in Appendix C.

Preface

Hydrogen sulfide (H₂S) is the most recently discovered gasotransmitter molecule joining nitric oxide and carbon monoxide. In addition to being biologically important small gases, these gasotransmitters also provide distinct modes of reactivity with biomimetic metal complexes. The majority of previous investigations on the reactivity of H₂S with bioinorganic models have focused on Fe-based porphyrin systems, whereas investigations with other metals remains underinvestigated. To address this gap, we report here an examination of the reactions of H₂S, HS⁻, and S₈ with Mg^{II}, Cu^{II}, Co^{II}, Zn^{II}, Cr^{II}, Sn^{IV}, and Mn^{II/III} protoporphyrins.

Introduction

Hydrogen sulfide (H₂S) is a malodorous and toxic gas, but also plays important roles in biology alongside nitric oxide (NO) and carbon monoxide (CO) as an endogenously produced gasotransmitter.^{1,116} Each of these gasotransmitters has significantly different physicochemical properties and exerts different actions on

biological targets, but all share postulated roles in neurotransmission and vasorelaxation.^{6,19,21,117} Additionally, each gasotransmitter exhibits rich coordination chemistry, suggesting that bioinorganic molecules may constitute major targets.^{62,118-122} For example, CO is widely used to probe structure in heme protein active sites because of its strong ligand back-bonding interaction which affords detailed information about the presence of other proximal ligands.¹²² By contrast, NO reaction with bioinorganic targets often results in metal nitrosyl formation or translation to oxidized forms of NO, including NO⁺ or NO₂.¹²³⁻¹²⁴ Given this rich bioinorganic chemistry of NO and CO, it is likely that H₂S also provides diverse reactions with bioinorganic targets. Furthermore, the redox activity of both NO and H₂S suggests that metals may provide an important regulatory platform for interconversion between different redox states of these gasotransmitters.^{1,116} Although both NO and CO benefit from significant previous work focusing on the coordination chemistry of these important ligands,^{119-120,122,125-126} significantly fewer investigations have focused on the reaction of H₂S with bioinorganic scaffolds.

H₂S is metallophilic, nucleophilic, acidic (pK_a = 7), and reducing; all of which complicate the potential modes of reactivity with bioinorganic targets.¹¹⁶ For example, demetallation,¹²⁷ covalent modification of ligand scaffolds,¹²⁸ acid/base equilibria,⁷¹ metal reduction,^{62,75} and binding of H₂S/HS^{-75,112,129} have all been observed. Additionally, differentiating the observed reactivity of H₂S from HS⁻ in water remains a significant challenge, whereas investigations in organic solution enable clear delineation of how the different protonation states contribute to observed reactivity.⁴⁴ Based on the importance of heme iron in biological systems, the majority of investigations on H₂S reactivity have focused on iron-based systems, although tin, gallium, and manganese

porphyrins have also been investigated.¹³⁰⁻¹³² Recent iron-based investigations have encompassed various synthetic porphyrins,^{70,75,77,112,132} protein-based systems,^{121,128,133-134} microperoxidase (MP11) oligopeptides,¹³⁵ and cyclodextrin-bound hemes.⁹⁴ To expand these investigations to include other metal complexes, we report here the investigation of the reactivity of H₂S/HS⁻ with Mg^{II}, Cu^{II}, Zn^{II}, Sn^{IV}, Cr^{III}, Co^{II}, and Mn^{III/II} protoporphyrin IX (PPIX) complex to better establish the fundamental reactivity of each of these metals with sulfide species (Figure IV-1). Together, these compounds represent a broad spectrum of metals, reduction potentials, and biologically relevant targets for understanding the chemistry of H₂S in biological systems.

Results and Discussion

To investigate the reaction of different sulfide species with metal protoporphyrins, we used H₂S and NBu₄SH (an organic-soluble source of HS⁻) in THF to isolate the individual protonation states.⁴⁴ We expected that the reaction of the various metal protoporphyrins with sulfide (H₂S or HS⁻) would result in three possible outcomes: no reaction, H₂S/HS⁻ coordination, and/or metal reduction (Figure IV-1). We hypothesized that protoporphyrins housing redox-inactive or fully oxidized metal ions, such as Mg^{II}, Zn^{II}, and Sn^{IV}, would be either unreactive or would bind sulfide. By contrast, Cu^{II}, Cr^{III}, Mn^{III}, and Co^{II} are all redox active, and HS⁻ is expected to reduce Mn^{III} or Cu^{II} on the basis of accessible redox potentials.^{62,136-138}

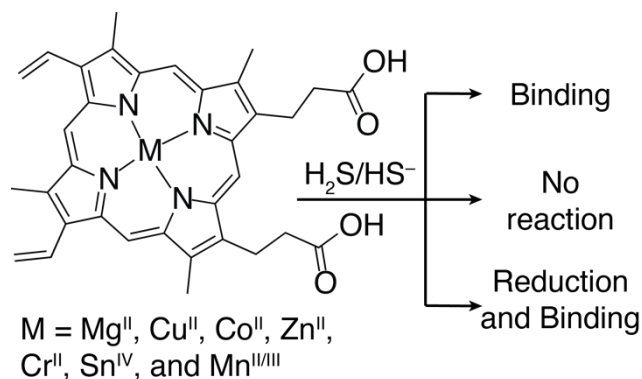


Figure IV-1. Metal protoporphyrin IX scaffold and possible H₂S/HS⁻ reaction pathways.

Metal PPIX complexes that bind sulfide

ZnPPIX.

Titration of NBu₄SH into a THF solution of ZnPPIX resulted in clean conversion to a new species as evidenced by a shift in the Soret band from 413 nm to 441 nm, with a well-anchored isobestic point at 425 nm (Figure IV-2b). The two Q-bands at 544 and 582 nm also coalesce into a single peak at 563 nm with a small shoulder at 602 nm, proceeding through well-anchored isobestic points at 523, 552, 572 and 590 nm. The titration data fits a 1:1 binding isotherm, producing a K_a for HS⁻ binding of 17500 ± 700 M⁻¹ (Figure C-6).¹³⁹ By contrast, bubbling H₂S or addition of S₈ to a THF solution of ZnPPIX failed to produce a change in the UV-Vis spectrum. The two carboxylic acids of ZnPPIX have pK_a values (in water) of 6.3 and 9.4,¹⁴⁰ suggesting that HS⁻ (pK_b = 7.4) should deprotonate one, but not both, of the carboxylic acids to generate [Zn(PPIX)SH]²⁻. Treatment of ZnPPIX with excess 1,8-diazabicyclo[5.4.0]undec-7-ene (DBU) or dicyclohexylamine (Cy₂NH) resulted in deprotonation of one carboxylate and generated a final spectrum consistent with ligation of a nitrogen base (Figure C-4 and C-5).¹⁴¹⁻¹⁴³ Addition of excess HS⁻ to the nitrogen base ligated spectrum cleanly generated the [Zn(PPIX)SH]²⁻ spectrum observed previously. Treatment of ZnPPIX with NBu₄OAc

failed to produce significant changes in the spectrum, suggesting that the deprotonated carboxylate on the PPIX ligand was not coordinating to metal centers in solution (Figure C-3). Taken together, the NBu_4OAc and $\text{DBU}/\text{Cy}_2\text{NH}$ studies suggest that deprotonation of the carboxylic acid moieties does not significantly change the spectrum of metal PPIX scaffolds, and that the final product formed from the addition of HS^- is $[\text{Zn}(\text{PPIX})\text{SH}]^{2-}$.

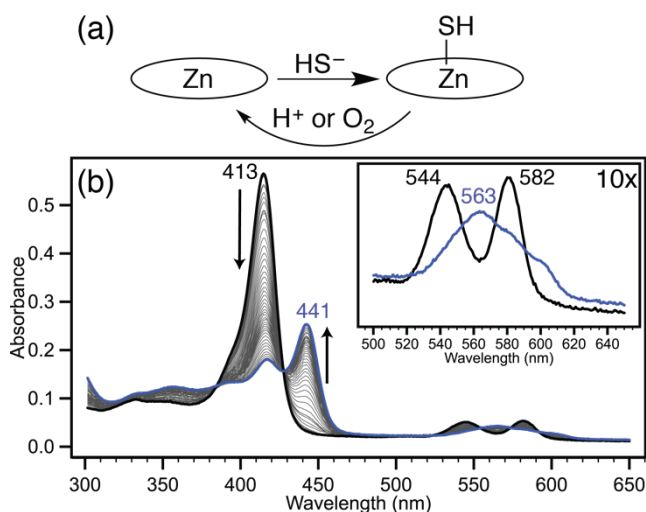


Figure IV-2. (a) Schematic representation of the reaction of ZnPPIX with HS^- . (b) Titration of ZnPPIX ($1.8 \mu\text{M}$ in THF) with NBu_4SH (73 equiv.); inset: Q-band region of the spectrum.

To further establish HS^- binding, rather than covalent modification of the PPIX scaffold, we measured the ^1H NMR spectrum of both free and hydrosulfide bound ZnPPIX (Figure IV-3). Upon addition of NBu_4SH to a 3.6 mM solution of ZnPPIX in $\text{THF-}d_8$, we observed a small upfield shift in the terminal alkene ($2\beta\text{c}$, $2\beta\text{t}$, $4\beta\text{c}$, $4\beta\text{t}$) protons and a shift of the meso (α , β , γ , δ) protons.¹⁴⁴ We note that the splitting pattern of the alkene and meso protons remain constant, indicating no covalent modification of the electrophilic positions of the porphyrin scaffold. By contrast, the methylene protons (6α , 7α , 6β , and 7β) split, indicating differentiation of the top and bottom faces of the

porphyrin and rotational restriction of the ethylene spacers (6α , 7α , 6β , and 7β) on the NMR time-scale, resulting from an internal hydrogen bond between the carboxylate / carboxylic acid moieties. We were unable to observe the sulfhydryl hydrogen in $[\text{Zn}(\text{PPIX})\text{SH}]^{2-}$ by ^1H NMR spectroscopy.

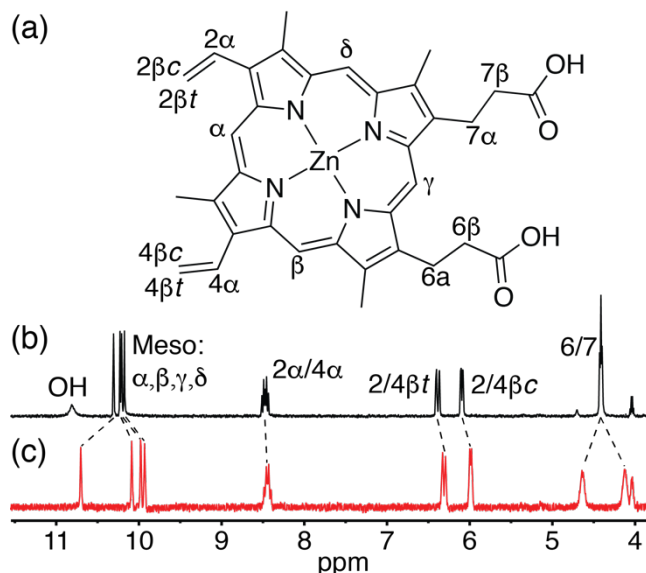


Figure IV-3. (a) Labeled structure of ZnPPIX. ^1H NMR spectra of ZnPPIX ($3.6 \mu\text{M}$, $\text{THF-}d_8$) before (b) and after (c) addition of 23 equiv. of NBu_4SH .

We reasoned that because ZnPPIX bound HS^- but not S_8 or H_2S , that addition of acid would protonate the Zn-SH resulting in release of H_2S gas and regeneration of the ZnPPIX spectrum. Similarly, oxidation of the bound hydrosulfide ligand should also regenerate the parent spectrum. Consistent with these hypotheses, exposure of $[\text{Zn}(\text{PPIX})\text{SH}]^{2-}$ to acetic acid resulted in immediate regeneration of the original ZnPPIX UV-Vis spectrum (Figure C-1). Similarly, exposure of $[\text{Zn}(\text{PPIX})\text{SH}]^{2-}$ to atmospheric oxygen results in HS^- oxidation and also regenerates the parent ZnPPIX/ $[\text{ZnPPIX}]^-$ UV-Vis spectrum, likely forming polysulfide species (Figure C-2).

Cr^{III}PPIX.

Titration of Cr(PPIX)Cl (Figure IV-4b) with NBu₄SH reduced the intensity of the Soret band at 435 nm in the UV-Vis spectrum and resulted in formation of a broad shoulder at 480 nm. Although Cr(PPIX)Cl is redox active, the observed changes in the UV-Vis spectrum are similar to those observed for thiolate binding to Cr^{III}PPIX, suggesting HS⁻ binding, rather than reduction to Cr^{II}.¹⁴⁵ The addition of DBU or Cy₂NH to deprotonate the carboxylic acids in Cr(PPIX)Cl failed to change the UV-Vis spectrum, suggesting that the observed spectral changes from HS⁻ addition were not merely due to deprotonation. As in the case of Zn^{II}PPIX, Cr(PPIX)Cl was inert toward H₂S gas or S₈.¹⁴⁶ The UV-Vis titration data of HS⁻ addition to Cr(PPIX)Cl fit cleanly to a 1:1 binding model, with a K_a of $8600 \pm 300 \text{ M}^{-1}$ (Figure C-9).¹³⁹

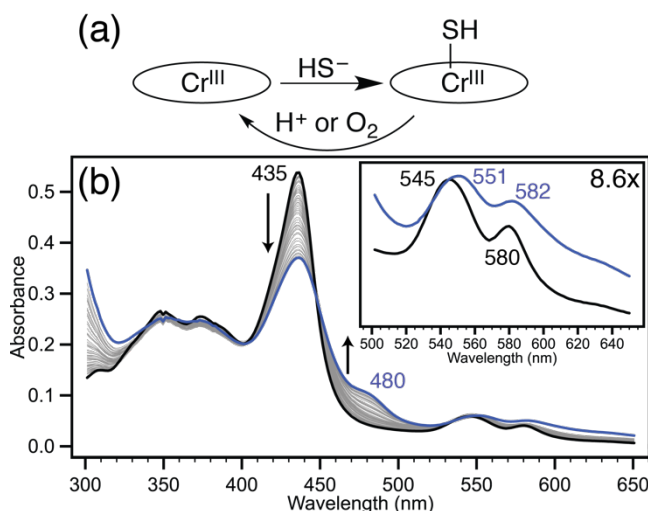


Figure IV-4. (a) Schematic representation of Cr^{III}(PPIX)Cl reaction with HS⁻. (b) Titration of CrPPIX (2.4 μM in THF) with NBu₄SH (26 equiv.); inset: Q-band region of the spectrum.

Based on the results from ZnPPIX, we reasoned that Cr(PPIX)Cl could be regenerated by protonation of the ligated HS⁻ by AcOH or by oxidation of the bound HS⁻

by atmospheric oxygen. As expected, treatment of Cr(PPIX)SH with AcOH protonated the bound HS⁻ to form H₂S and dissociate from the porphyrin, and atmospheric O₂ resulted in HS⁻ oxidation to polysulfide and regeneration of the parent Cr^{III}PPIX complex (Figure C-7 and C-8). These studies suggest that Cr and Zn porphyrin scaffolds undergo similar reaction chemistry.

Sn^{IV}PPIX.

In contrast to the observed Zn^{II} and Cr^{III} chemistry with HS⁻/H₂S, Sn^{IV}(PPIX)Cl₂ displayed significantly different reactivity. To generate free binding sites, Sn^{IV}(PPIX)Cl₂ was treated with AgPF₆ and filtered to generate [Sn^{IV}(PPIX)]²⁺ (Figure C-10). Bubbling H₂S through a THF solution of [Sn^{IV}PPIX]²⁺ produced a bathochromic shift in the solet band from 403 to 407 nm, consistent with H₂S binding to form [Sn^{IV}(PPIX)(H₂S)]²⁺ (Figure IV-5b). [Sn^{IV}PPIX]²⁺ also reacts with NBu₄SH in THF to produce a decrease and bathochromic shift in the solet band from 403 to 410 nm (Figure IV-5c), with consecutive isosbestic points at 410 and 428 nm, respectively. Plotting the concentration of HS⁻ vs. the absorbances at 428 or 403 nm show several distinct chemical processes, which include initial deportation of one of the carboxylic acids, followed by HS⁻ binding to Sn, and finally deprotonation of the acidic Sn-SH proton.¹³⁰ Similarly, initial carboxylic acid deprotonation using DBU or Cy₂NH (Figure C-12 through C-14), followed by addition of excess HS⁻ also resulted in formation of the [Sn^{IV}(PPIX)(S)]⁻ spectrum. Due to the range of species in solution with overlapping peaks, we were unable to obtain a binding constant for sulfide to Sn^{IV}PPIX. Acidification of the bound hydrosulfide species produced the [Sn^{IV}(PPIX)(H₂S)]²⁺ spectrum (Figure C-11), which

could not be modified by sparging with dry N₂ or opening the cuvette to atmospheric oxygen, suggesting the that formation of [Sn^{IV}(PPIX)(H₂S)]²⁺ is irreversible.

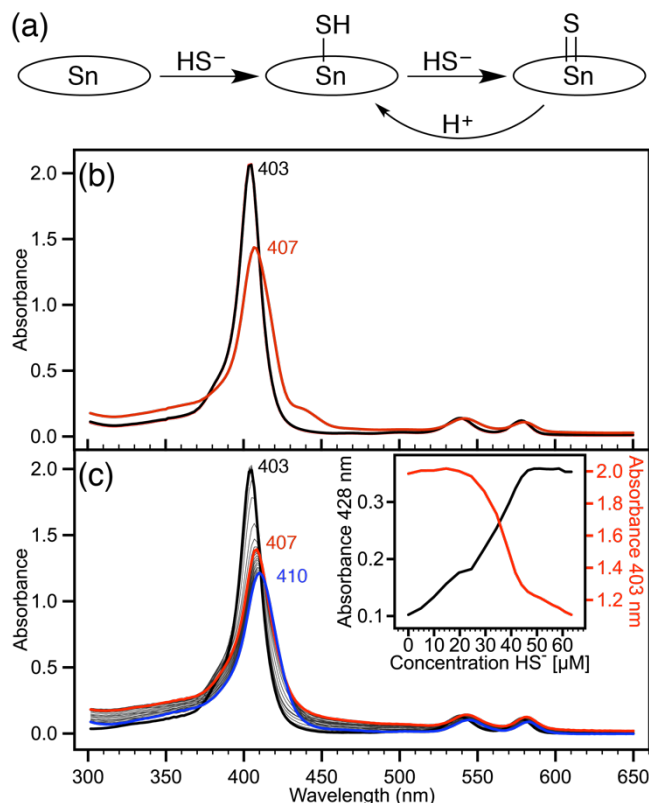


Figure IV-5. (a) Schematic for the addition of HS⁻ to SnPPIX. (b) SnPPIX (4.95 μM) in THF before (black) and after (red) bubbling with H₂S(g) for 5 minutes. (c) Titration of SnPPIX (4.95 μM) with NBu₄SH in THF. The starting SnPPIX spectrum (black) shows a Soret band at 403 nm, which transitions to a new Soret band at 407 nm (red) in route to the final absorbance at 410 nm (blue). Inset: Absorbances at 403 and 428 nm as a function of [HS⁻].

Metal PPIX complexes that are reduced by sulfide.

Mn(PPIX)Cl.

Upon titration of Mn^{III}(PPIX)Cl with NBu₄SH, the UV-Vis spectrum was cleanly converted to reduced Mn^{II}PPIX, as evidenced by a decrease in the peaks at 366 and 462 nm and concomitant increase at 430 nm (Figure IV-6b).¹⁴⁷⁻¹⁴⁸ Further addition of NBu₄SH resulted in further spectral changes, producing a final spectrum similar to that

obtained after addition of various thiolates to Mn^{II} porphyrins,¹⁴⁷⁻¹⁴⁸ suggesting sulfide binding to the Mn^{II} product. This outcome was confirmed by titration of authentic Mn^{II}PPIX (Figure C-21) with NBu₄SH (Figure IV-6c), which was fit to a 1:1 binding isotherm to afford a K_a for HS⁻ binding of $23000 \pm 2000 \text{ M}^{-1}$ (Figure C-22).¹³⁹ Bubbling H₂S or adding S₈ to a solution of Mn^{III}(PPIX)Cl or Mn^{II}PPIX did not change the UV-Vis spectrum. Similarly, the addition of DBU or Cy₂NH did not change the spectrum for either Mn^{III}PPIX or Mn^{II}PPIX (Figure C-18 through C-20). Similar to the chemistry observed for ZnPPIX and Cr^{III}PPIX, the addition of AcOH results in protonation and release of the bound HS⁻ to regenerate Mn^{II}PPIX and H₂S (Figure C-15 and C-16). Exposure of Mn^{II}(PPIX)(SH) to atmospheric oxygen resulted in the partial reversion to Mn^{III}(PPIX)Cl, with some degradation (Figure IV-6a and C-17). The sequence of HS⁻ first reducing the central metal of a porphyrin complex, followed by ligation of HS⁻ has been observed in other iron porphyrin systems.^{75,77,112}

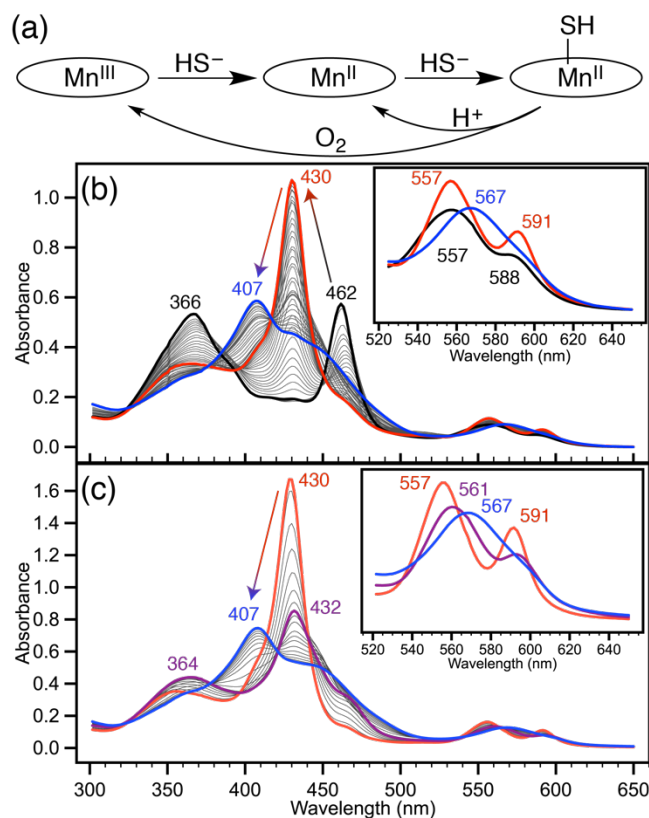


Figure IV-6. (a) Schematic for the reactivity of MnPPIX with HS⁻. (b) Titration of Mn^{III}PPIX (9.6 μ M in THF, black) with NBu₄SH (14 equiv., blue), proceeding through going through a Mn^{II}PPIX intermediate (red). (c) Titration of Mn^{II}PPIX (10.3 μ M, red) with NBu₄SH (3.6 equiv., blue).

To further characterize the reactivity of HS⁻ with Mn protoporphyrins, we used EPR spectroscopy to investigate sulfide ligation. Frozen solutions of Mn^{II}PPIX in 1:2 DMSO:DCM at 5 K of provided a typical high spin ($S = 5/2$) axial spectrum with two observable resonances at $g_{\perp} = 6.9$ and $g_{\parallel} = 2.14$ (Figure IV-7a). The g_{\perp} value shows six lines, characteristic of hyperfine coupling to the nuclear spin (I) of 5/2 for Mn. These features are similar to other high-spin Mn porphyrin systems reported with $g_{\perp} \approx 6$ and $g_{\parallel} \approx 2$.¹⁴⁹⁻¹⁵¹ Using the simulation package EasySpin¹⁵²⁻¹⁵³ we estimated the zero-field splitting (zfs) parameters D and E (Table 1), which correspond to the axial and rhombic components, respectively, and hyperfine coupling constants (A) to the Mn nucleus.^{150,153}

The Mn^{II}PPIX provided values of 0.00043 and 0.00045 cm⁻¹ for D and E, respectively. These are comparable to values for other Mn porphyrin systems and reflect an axial field.¹⁴⁹⁻¹⁵¹ The ⁵⁵Mn nuclear hyperfine coupling constants are also consistent with reported values, with A_x ≈ A_y = 0.021 cm⁻¹ and A_z = 0.0087 cm⁻¹.¹⁴⁹⁻¹⁵¹ The addition of excess HS⁻ to Mn^{II}PPIX resulted in the hyperfine coupling becoming more resolved and a small change in g-values to g_⊥ = 7.21 and g_∥ = 2.14 (Figure IV-7b) that we have assigned to Mn^{II}(PPIX)(SH). The values for D and E were simulated to be 0.00016 cm⁻¹ and 0.0015 cm⁻¹, respectively, indicating a more distorted axial system. These zfs parameters are smaller than mono-halogenated iron and manganese porphyrins, and are consistent with HS⁻ ligation.¹⁴⁹⁻¹⁵¹ Also, because HS⁻ has a stronger field strength than Cl⁻ in the spectrochemical series,¹⁵⁴ the observed axial spectrum with lower E/D ratio than for Cl⁻ is consistent with HS⁻ ligation. In addition, this indicates an increase in the distortion and loss of planarity in the porphyrin ring, as observed in sulfide-bound iron porphyrin complexes.^{70,75,77,155} In contrast, diamagnetic Mn^{III}(PPIX)Cl is EPR silent (Figure IV-7a). The addition of excess HS⁻ displayed a nearly identical spectrum to that of the Mn^{II}(PPIX)SH.

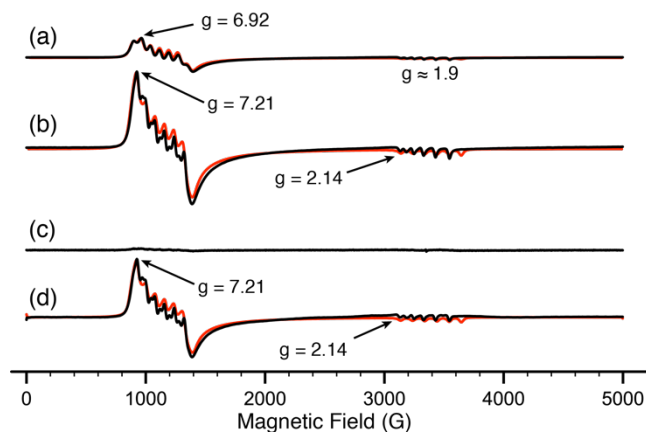


Figure IV-7. Continuous wave EPR spectra (1:2 DMSO:CH₂Cl₂, 5 K) of (a) Mn^{II}PPIX (5 mM), (b) Mn^{II}PPIX upon addition of 6.5 equiv. of NBu₄SH. (c) Mn^{III}(PPIX)Cl (2 mM), (d) Mn^{III}(PPIX)Cl upon addition of 8.2 equiv. of NBu₄SH. Spectra simulated with EasySpin are in red.

Table IV-1. EPR parameters for Mn(PPIX) species.

	Spin	g_x^a	g_y^a	g_z^a	T(K)	D^b	E^b	A_x^b	A_y^b	A_z^b	$\lambda(E/D)$
Mn ^{II} (PPIX)	5/2	6.2	5.7	1.97	5	0.43	0.45	21.7	20.7	8.8	1.05
Mn ^{II} (PPIX)(SH) ^c	5/2	6.2	5.7	1.97	5	0.16	1.49	22.5	21.0	9.3	9.19
Mn ^{II} (PPIX)(SH) ^d	5/2	6.2	5.7	1.97	5	0.16	1.48	22.4	21.0	9.3	9.43

^a Estimated using EasySpin ^b Values in dam^{-1} ^c From Mn^{II}(PPIX) ^d From Mn^{III}(PPIX)Cl

Metal PPIX complexes that show no reaction with sulfide

The addition of NBu₄SH, H₂S gas, or S₈ to Mg^{II}PPIX or Cu^{II}PPIX failed to produce changes in the UV-Vis spectra, suggesting that Mg^{II}PPIX and Cu^{II}PPIX are inert to these sulfur sources. Finally, treatment of Co^{II}PPIX, prepared by stirring commercially available Co^{III}(PPIX)Cl with Zn amalgam, showed no change in the UV-Vis spectrum when treated with NBu₄SH, H₂S gas, or S₈.

Conclusion

We have investigated the chemical reactivity of hydrogen sulfide with a series of metal protoporphyrin complexes by UV-Vis, NMR, and EPR spectroscopies. We found

that $\text{Mg}^{\text{II}}\text{PPIX}$, $\text{Cu}^{\text{II}}\text{PPIX}$, and $\text{Co}^{\text{II}}\text{PPIX}$ to not react with $\text{H}_2\text{S}(\text{g})$, HS^- , or S_8 . In contrast, $\text{Zn}^{\text{II}}\text{PPIX}$, $\text{Cr}^{\text{III}}(\text{PPIX})\text{Cl}$, and $\text{Sn}^{\text{IV}}\text{PPIX}$ simply bind HS^- , with $\text{Sn}^{\text{IV}}\text{PPIX}$ also showing binding of $\text{H}_2\text{S}(\text{g})$. We also found that HS^- binding to the ZnPPIX and $\text{Cr}^{\text{III}}\text{PPIX}$ systems is chemically reversible by addition of acid or exposure to atmospheric oxygen, whereas $\text{Sn}^{\text{IV}}\text{PPIX}$ reacts with $\text{H}_2\text{S}/\text{HS}^-$ irreversibly to generate $[\text{Sn}^{\text{IV}}(\text{PPIX})(\text{S})]^-$. Finally, addition of HS^- to $\text{Mn}^{\text{III}}(\text{PPIX})\text{Cl}$ resulted in reduction to Mn^{II} followed by HS^- binding, similar to the observed reactivity of synthetic Fe porphyrins. Taken together, these results provide a consistent platform to understand the reaction and coordination chemistry of $\text{H}_2\text{S}/\text{HS}^-$ with different bioinorganic targets.

Bridge

Having established the various reactive pathways with non-iron protoporphyrin complexes, we shifted our focus to explore iron porphyrins in more depth. While *H. Sapien* hemoglobin and myoglobin are covalently modified at the periphery of the porphyrin ring when exposed to H_2S , the bivalve *L. Pectinata*, a resident of sulfide-rich swamps, is capable of transporting H_2S with hemoglobin 1 (Hb1). There are several possible mechanisms by which H_2S is stabilized within the binding pocket of Hb1, including hydrogen bonding from a proximal glutamate residue, a hydrophobic and protected pocket, or other more complex interactions working in tandem. We choose to isolate and study the protected pocket aspect by using Collman's "Picket-Fence" porphyrin as described in Chapter V.

Experimental

Materials and Methods.

All manipulations were performed under an inert atmosphere using standard Schlenk techniques or an Innovative Atmospheres N₂-filled glove box unless otherwise noted. All chemicals used as received unless otherwise noted. Hydrogen sulfide gas was purchased from Praxair and transferred through a custom-built stainless steel transfer line. Stock solutions of each protoporphyrin (Frontier Scientific) were prepared in dry DMSO and stored in an inert atmosphere glove box until immediately before use. Sulfur (S₈) purchased from Fischer Scientific. Tetrabutylammonium acetate (NBu₄OAc) and dicyclohexylamine purchased from TCI chemicals. 1,8-Diazabicyclo[5.4.0]undec-7-ene (DBU), HgCl₂, zinc powder, and AgPF₆ purchased from Sigma-Aldrich. Acetic acid and hydrochloric acid were purchased from EMD Chemicals. *p*-Toluenesulfonic acid purchased from STREM. Tetrabutylammonium hydrosulfide (NBu₄SH) was synthesized as previously reported.⁴⁴ *Note: hydrogen sulfide and its salts are highly toxic and should be handled carefully to avoid exposure.* Spectroscopic grade MeCN and THF degassed by sparging with argon followed by passage through a Pure Process Technologies solvent purification system to remove water and stored over 4 Å molecular sieves in an inert atmosphere glove box. DMSO-*d*₆, CD₂Cl₂, and CD₃CN were purchased from Cambridge Isotopes, dried with CaH₂, distilled or vacuum transferred, exposed to three freeze-pump-thaw cycles, and stored over 4 Å molecular sieves in an inert atmosphere glove box.

Spectroscopic methods.

UV-Vis measurements were acquired on an Agilent Cary 100 UV-Vis spectrophotometer equipped with a QNW dual cuvette temperature controller at 25.00 ±

0.05 °C. All spectroscopic samples prepared under an inert atmosphere in septum-sealed cuvettes obtained from Starna Scientific. NMR spectra were acquired on a Brüker Avance-III-HD 600 spectrometer with a Prodigy multinuclear broadband cryoProbe at 25.0 °C. X-band continuous wave (cw) electron paramagnetic resonance (EPR) measurements were carried out on a Brüker Elexsys E500 EPR spectrometer equipped with an ER049X bridge at a microwave frequency of 9.46 GHz using a liquid nitrogen cooling system. The EPR spectra were measured at 77 K with a modulation amplitude of 5 Gauss, a modulation frequency of 100 kHz, and a microwave power of 21.4 mW. The EPR spectra were simulated using the EasySpin package.¹⁵²

General procedure for UV-vis spectroscopic studies.

Protoporphyrin (PPIX) stock solutions diluted to the desired concentration by addition of 3.0 mL of THF in a septum-sealed cuvette. Non-porphyrin reagents were prepared approximately 10^3 times more concentrated than the porphyrin to provide minimal dilution during addition. NBu_4SH and other reagents added to the septum-sealed cuvettes by gas-tight syringe. $\text{H}_2\text{S}(\text{g})$ bubbled via a custom-built stainless steel transfer line. Binding constants (K_a) were determined from UV-Vis titration data and fit a 1:1 model using the Thordarson program.¹³⁹

General procedure for NMR studies.

A 1 mM stock solution of the desired porphyrin prepared in a 50/50 DMSO- d_6 /CD₃CN mixture in a septum-capped NMR tube. A stock solution of NBu_4SH (1 M in CD₃CN) was prepared, and five equiv. were added to the NMR tube using a gas-tight syringe.

General Procedure for H₂S gas studies.

Protoporphyrin stock solutions were diluted to the desired concentration by addition of 3.0 mL of THF in a septum-sealed cuvette and removed from the glove box. H₂S gas bubbled through the cuvette for one minute. Reversibility of H₂S addition evaluated by bubbling the cuvette with N₂ for 1 minute.

General procedure for EPR studies:

A 5 mM stock solution of protoporphyrin in 1:3 DMSO:CH₂Cl₂ was prepared. Stock solutions of NBu₄SH (1 M in CH₃CN) were prepared, and 30 equiv. added to the EPR tube using a gas-tight syringe. All tubes were placed under an argon atmosphere to prevent oxygen exposure.

Preparation and use of Zinc Amalgam.

HgCl₂ (0.2 g, 0.8 mmol) was dissolved in a dilute 0.1M aqueous solution of HCl. Powdered zinc (1g, 15 mmol), freshly washed with concentrated HCl, was quickly added while stirring for 10 to 15 minutes while crushing clumps. The mixture was filtered and washed with H₂O, EtOH, and Et₂O before being transferred to a glove box. For metal reductions, 2.5 equiv. of the 5% zinc amalgam added to Mn^{III}PPIX, 1.5 mL of DMSO added, and the reaction mixture stirred for 15 minutes. The resultant precipitate was filtered to afford the Mn^{II}PPIX stock solution.

Removal of Sn^{IV}(PPIX)Cl₂ chlorides.

AgPF₆ (2.5 equiv.) was added to Sn(PPIX)Cl₂ in the absence of light, after which three mL of DMSO added, and the reaction mixture stirred for 15 minutes. The resultant solution was filtered to afford the stock solution of chloride-free Sn^{IV}PPIX.

CHAPTER V

SPECTROSCOPIC INVESTIGATIONS INTO THE BINDING OF HYDROGEN

SULFIDE TO SYNTHETIC PICKET-FENCE PORPHYRINS

Published as Hartle M. D., James S. Prell, and Michael D. Pluth. "Spectroscopic investigations into the binding of hydrogen sulfide to synthetic picket-fence porphyrins" *Dalton Transactions* **2016** 45(11) 4843-4853. The experimental work was performed by me and J. S. Prell collected mass spectrometry data. The majority of the manuscript is written by me, with editorial assistance from M. D. Pluth. Associated content can be found in Appendix D.

Preface

The reversible binding of hydrogen sulfide (H_2S) to hemeprotein sites has been attributed to several factors, likely working in concert, including the protected binding pocket environment, proximal hydrogen bond interactions, and iron ligation environment. To investigate the importance of a sterically-constrained, low-polarity environment on sulfide reactivity with heme centers, we report here the reactivity of H_2S and HS^- with the picket-fence porphyrin system. Our results indicate that the picket-fence porphyrin does not bind H_2S in the ferric or ferrous state. By contrast, reaction of the ferric scaffold with HS^- results in reduction to the ferrous species, followed by ligation of one equivalent of HS^- , as evidenced by UV-vis, NMR spectroscopy and mass spectrometry studies. Measurement of the HS^- binding affinities in the picket-fence or tetraphenyl porphyrin systems revealed identical binding. Taken together, these results suggest that the low-polarity, sterically-constrained environment alone is not the primary contributor for stabilization of ferric $\text{H}_2\text{S}/\text{HS}^-$ species in model systems, but that other interactions,

such as hydrogen bonding, must play a critical role in facilitation of reversible interactions in ferric hemes.

Introduction

Interactions between heme-containing metalloproteins and gas molecules play important roles in biological systems. For example, dioxygen (O_2) ligation to Myoglobin (Mb) and Hemoglobin (Hb) constitutes a critical mechanism of oxygen transport associated with aerobic respiration.¹⁵⁶ Consistent with the importance of a protected binding pocket, not only to provide protection for the bound O_2 but also to prevent unwanted μ -oxo bridged dimer formation, preparation and use of the all-*cis*-tetra-pivaloylamide-*ortho*-substituted phenyl porphyrin (“picket-fence porphyrin”) by Collman and co-workers provided the first example of reversible O_2 binding to a synthetic heme model almost 40 years ago.¹⁵⁷⁻¹⁵⁸

In addition to O_2 , the last few decades have witnessed the acceptance of other small molecule gases, namely carbon monoxide (CO), nitric oxide (NO), and hydrogen sulfide (H_2S), as important endogenously-produced gaseous signaling molecules involved in physiological functions including smooth muscle relaxation, neurotransmission, and vasoregulation.^{26,61} Extending the use of the picket-fence porphyrin model beyond O_2 -binding investigations, treatment with CO leads to irreversible heme-CO formation and inhibition of O_2 binding, both of which are consistent with the effects of CO poisoning.¹⁵⁸ Similarly, the reaction of NO and related oxidized species including nitrite (NO_2^-) has also been investigated in the picket-fence porphyrin, leading to a greater understanding of steric interactions involved in the heme-mediated oxidation of NO to NO_2^- .¹⁵⁹⁻¹⁶² For example, reaction of atmospheric oxygen in pyridine with heme-nitrosyl produces a

stable bis-ligated NO_2^- adduct in which the pocket-bound NO_2^- is stabilized by a weak hydrogen bond to one of the amides in the porphyrin scaffold.^{118,162} Despite the important insights gained from use of the picket-fence porphyrin model to investigate O_2 , CO , and NO interactions with heme centers, analogous investigations with H_2S remain absent.

Hydrogen sulfide is the most recently discovered endogenously produced gasotransmitter, with identified roles in diverse aspects of biological signaling and human health.¹⁻² Adding to the challenges of unravelling this important biomolecule, H_2S exhibits more complex reactivity than that of NO or CO . In addition to being a good reductant, highly metallophilic, and oxygen sensitive, H_2S exists in various protonation states at biological pH, thus complicating whether H_2S or HS^- is the active species when reacting with bioinorganic centers.^{62,134,163} One of the first recognized reactions of sulfide with heme iron was sulfheme formation, in which the periphery of the porphyrin is irreversibly modified by sulfide in the presence of an oxidant, such as H_2O_2 , iron hydroperoxo, or iron(IV) oxo species.^{121,128,164-166} The resulting compound is characterized by a green color and dominant absorption band near 620 nm in ferrous Mb.^{165,167-168} Sulfheme formation reduces the affinity for other gasses at the heme center, as evidenced by a 2500- and 1500-fold reduction in O_2 and CO affinity, respectively.¹⁶⁴⁻¹⁶⁶ By contrast to the detrimental effects of sulfheme formation, $\text{H}_2\text{S}/\text{HS}^-$ binds reversibly to heme centers in many organisms that live in sulfide-rich environments, such as the HbI center of the *Lucina Pectinata* clam found in sulfide-rich mangrove swamps.¹⁶⁹⁻¹⁷⁰ The reversible binding of sulfur to hemeprotein sites has been attributed to several factors, likely working in concert, including the protected binding pocket environment and

proximal glutamate residue forming a hydrogen bond with bound sulfide, and iron ligation environment.^{128,169-170}

As a whole, investigations of sulfide with synthetic hemes have focused on relatively simple porphyrin platforms. In one of the first such studies, Scheidt and co-workers reported the structure of an iron hydrosulfido complex from a tetra(methoxyphenyl)porphyrin system in 1984.⁷⁰ Studies by Collman and co-workers aimed at reactions of sulfide with a cytochrome c oxidase model renewed the field in 2012.^{63,78} Recent investigations into heme/sulfide interactions have included work on the binding of HS⁻ to open-faced ferrous porphyrin complexes⁷⁵ and use of silyl-protected sulfur species to overcome Fe-SH instabilities.⁷⁷ The importance of distal histidine/pyridine coordination has also been investigated using a microperoxidase and a cyclodextrin-functionalized porphyrin system; both of which suggest that distal ligation is important for stable ferric hydrosulfido formation.^{94,135} As a whole, these investigations have focused on open-faced synthetic porphyrins, which do not probe effects such as a protected binding site or the importance of proximal hydrogen bonding interactions. Motivated by the utility of the picket-fence porphyrin in investigating and understanding O₂,¹⁵⁸ CO,^{158,171-172} and NO^{162,173-175} reactivity with synthetic heme systems, we sought to extend the utility of this model compound to investigate whether the presence of a protected binding pocket alone would be sufficient to bind H₂S or HS⁻. In addition, we hypothesized that the low-polarity pocket in the picket fence porphyrin system could provide useful insight into the different factors impacting bound sulfide stability in synthetic heme centers.

Results and Discussion

To investigate the chemistry of H₂S with synthetic heme platforms and to determine whether protected axial binding environments affect H₂S/HS⁻ binding, we chose to use the “picket-fence porphyrin” (PFP) model because of its protected axial cavity. Furthermore, the PFP model allows for direct sulfide binding comparison in both low and high polarity solvents, as well as with the parent tetraphenyl porphyrin (TPP) complexes, which lack the axial pocket.

We prepared the picket-fence porphyrin as described in the literature using minor modifications (see Experimental Section) to afford isomerically-pure all-cis ligand (Figure V-1). To compare the charge and the importance of axial ligands, we prepared Fe^{III}(TPivPP)Br (**1**), imidazole-free Fe^{II}(TPivPP) (**2**), and Fe^{II}(TPivPP)(N-MeIm)₂ (**3**).^{158,176-177} To compare the results of these protected systems, we also used the parent TPP complexes Fe^{III}(TPP)Cl (**4**), Fe^{II}(TPP) (**5**), and Fe^{II}(TPP)(N-MeIm)₂ (**6**). Although such model compounds are only soluble in organic solvents, the broad solubility in solvents ranging from toluene to DMF provides the unique opportunity to investigate the role of solvent polarity in concert with the protected PFP pocket. Additionally, the ability to isolate different protonation states of sulfide using H₂S gas or organic-soluble NBu₄SH allows for differentiation of H₂S versus HS⁻ reactivity, which is otherwise not possible in aqueous systems.^{*44,178-179}

* Although most protein-based H₂S/heme investigations have assumed that HS⁻ is the active sulfide species at physiological pH, sulfide binding in Mb decreases in alkaline solution. This observation suggests that H₂S may be the active species or that pH changes significantly influence the protonation state of important residues that stabilize sulfide binding interactions. (Kraus, D. W.; Wittenberg, J. B. *J. Biol. Chem.* **1990**, 265, 16043-16053 and Brittain, T.; Yosaatmadja, Y.; Henty, K. *IUBMB Life* **2008**, 60, 135-138.)

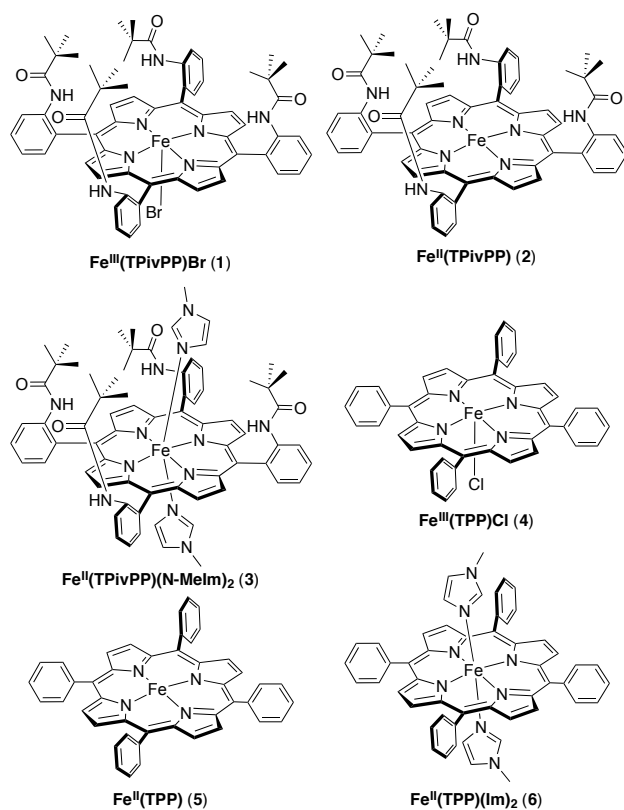


Figure V-1. Model Fe(II) and Fe(III) scaffolds used to study sulfide binding. The hydrophobic pocket in picket-fence porphyrin systems (**1-3**) provides a distinct ligand environment from the parent tetraphenyl porphyrin systems (**4-6**).

Reaction of Fe^{II}(TPivPP)(N-MeIm)₂ with sulfide.

To determine the reactivity of different sulfide sources with Fe(II) picket-fence systems, we first treated toluene solutions of **3** with stoichiometric as well as saturated solutions of H₂S gas. In all experiments, excess *N*-methylimidazole (N-MeIm) was present to ensure blockage of the bottom face of **3**. No changes in the UV-Vis or NMR spectra of **3** were observed upon treatment with H₂S, suggesting that H₂S does not bind to the ferrous system. Similarly, treatment with elemental sulfur (S₈) failed to change the UV-Vis spectrum of **3**. Treatment of **3** in toluene (Figure V-2a) with tetrabutylammonium hydrosulfide (NBu₄SH), an organic-soluble source of HS⁻,⁴⁴ results in clean formation of [Fe^{II}(TPivPP)(SH)]⁻ (**7**), as evidenced by a bathochromic shift of

the Soret band from 429 to 419 nm with a concomitant reduction in intensity and appearance of a shoulder at 455 nm. Additionally, the principle Q-band absorbance of **3** at 534 nm decreased in intensity with the associated formation of new bands at 534, 578, and 620 nm (Figure V-2a, inset). Similar spectroscopic changes in the Soret band, including the shoulder near 450 nm, have been observed previously in the binding of HS⁻ to Fe^{II}(octaethylporphyrinate) (Fe^{II}(OEP)), Fe^{II}(tetra-p-methoxyphenylporphyrinate) (Fe^{II}(p-MeOPP)), and Fe^{II}(tetramesitylporphyrinate) (Fe^{II}(TMP)).⁷⁵

Because both the binding pocket of **3** and toluene (2.38) have low dielectric constants we also investigated whether a solvent with a higher dielectric, such as DMF (38.25), would lead to similar observed reactivity with HS⁻. Much like in toluene, treatment of a DMF solution of **3** with H₂S gas or S₈ failed to produce spectral changes, however treatment with NBu₄SH resulted in a bathochromic shift of the Soret band from 443 to 419 nm, with concurrent appearance of a shoulder at 455 nm (Figure V-2b). The Q-band region of the spectrum also parallels the observed reactivity in toluene with new absorbances at 538, 575, and 621 nm corresponding to **7**. As observed in toluene, conversion of **3** to **7** proceeds cleanly, with well-anchored isosbestic points at 428 and 457 nm. The identical reactivity between NBu₄SH in toluene and DMF suggests that the sulfide bound in the PFP cavity of **3** is unaffected by changes to bulk solvent polarity.

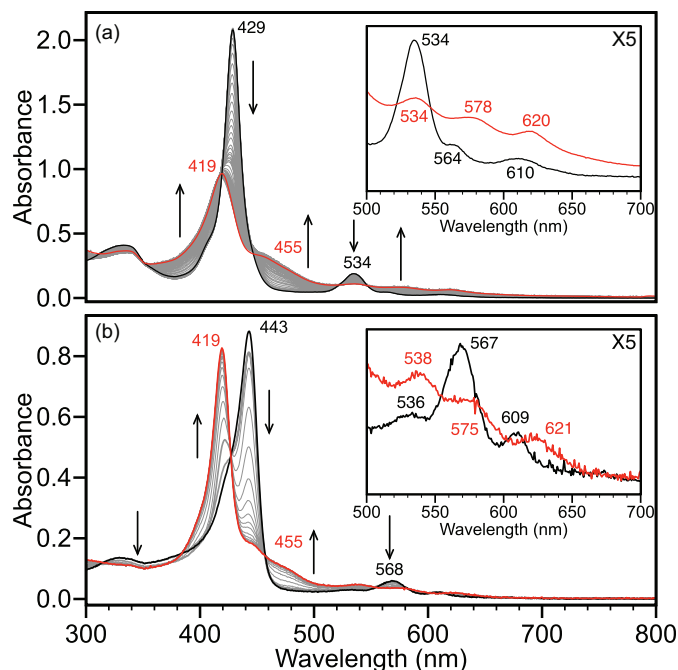


Figure V-2. (a) Titration of **3** (black) with 0.25 equiv. increments of NBu_4SH leads to clean conversion to $[\text{Fe}(\text{TPivPP})(\text{SH})]^-$, **7**, (red). Conditions: MePh solution of $10.8 \mu\text{M}$ **3** with $367 \mu\text{M}$ *N*-methylimidazole titrated with 10 equiv. of NBu_4SH in 1:9 MeCN:MePh. (b) Titration of **3** (black) with 0.25 equiv. increments of NBu_4SH leads to clean conversion to **7** (red). Conditions: DMF solution of $5.2 \mu\text{M}$ **3** with $36.5 \mu\text{M}$ *N*-methylimidazole titrated with 10 equiv. of NBu_4SH in DMF. All titrations were performed under anaerobic conditions with sufficient time to allow for complete reaction between aliquot additions.

To confirm that excess imidazole was not impacting HS^- binding, we prepared imidazole-free $\text{Fe}^{\text{II}}(\text{TPivPP})$ (**2**). Addition of 0.25 equiv. of NBu_4SH to **2** in toluene in the absence of *N*-methylimidazole resulted in splitting of the Soret band from 414 nm to new peaks at 445 and 419 nm (Figure V-3), which is consistent with disaggregation of the porphyrin.[†] Further addition of HS^- cleanly converts the split Soret band to a final

[†] An alternative possibility is that two porphyrins are coming together to form a μ -sulfido bridged complex through initial sulfide binding to the bottom face of the porphyrin. Although we are unaware of μ -sulfido species in similar systems, the μ -oxo bridged $\text{Fe}(\text{III})$ PFP exhibits a single, well-resolved band at 408 nm. (J. P. Collman, R. R. Gagne, T. R. Halbert, J. C. Marchon and C. A. Reed, *J. Am. Chem. Soc.*, **1973**, 95, 7868-7870.) In addition, the parent $\text{Fe}(\text{II})$ (TPP) (Cheng, L.; Powell, D. R.; Khan, M. A.; Richter-Addo, G. B. *Chem. Commun.* **2000**, 2301-2302.) exhibits a split Soret band at 418 and 443 nm for the unligated species, and single absorbance at 409 nm is associated with the μ -oxo bridged species. (Conradie, J.; Ghosh, A. *Inorg. Chem.* **2006**, 45, 4902-4909.)

absorbance at 419 nm and results in three Q-bands at 534, 577, and 621 nm, all of which match the spectrum generated from reaction of **3** with NBu_4SH (Figure V-2a), suggesting that the imidazole is not bound in the final product. Formation of a five-coordinate, SH-ligated product is also consistent with previous work with $\text{Fe}^{\text{II}}(\text{OEP})$, $\text{Fe}^{\text{II}}(\text{p-MeOPP})$, and $\text{Fe}^{\text{II}}(\text{TMP})$.⁷⁵ In addition, no reaction was observed when *N*-methylimidazole-free **2** was treated with H_2S and S_8 , suggesting that *N*-methylimidazole does not out-compete sulfide binding. When taken together with the previous experiments using **3**, as well as the observation that addition of *N*-methylimidazole at the end of the titration does not significantly alter the spectrum, these results suggest that the presence of *N*-methylimidazole does not interfere with sulfide binding to the iron center.^{158,180}

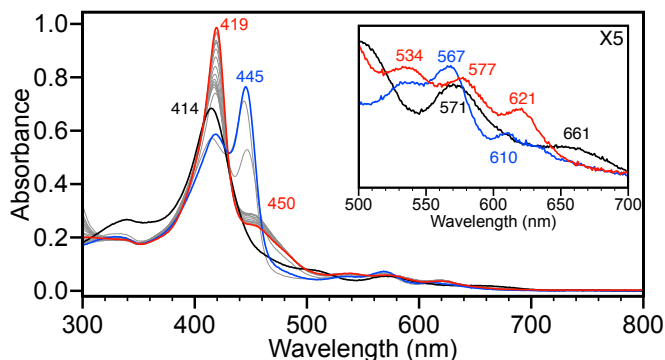


Figure V-3. Titration of **2** (black) with 0.25 equiv. increments of NBu_4SH leads to conversion to **7** (red) after disaggregation of the porphyrin (blue). Conditions: MePh solution of $5.7 \mu\text{M}$ **2** titrated with 5 equiv. of NBu_4SH in a 1:9 MeCN:MePh solution. All titrations were performed under anaerobic conditions with sufficient time to allow for complete reaction between aliquot additions.

Reactivity of $\text{Fe}^{\text{III}}(\text{TPivPP})\text{Br}$ with sulfide.

Based on our results with **2** and **3**, we expected that treatment of ferric **1** with HS^- would result in initial reduction from Fe^{III} to Fe^{II} producing various oxidized polysulfide species, followed by HS^- binding to form **7**. As expected, titration of **1** in toluene with

NBu₄SH initially produces a spectrum similar to that of **3** with an increase in intensity of the Soret band and a bathochromic shift from 419 nm to 429 nm, and also a shift in the Q-band from 510 to 534 nm (Figure V-4a). Further addition of NBu₄SH produces a spectrum identical to that of **7**, consistent with initial reduction of Fe^{III} to Fe^{II}, followed by binding of HS⁻ to form [Fe^{II}(TPivPP)(SH)]⁻. Identical reactivity was observed in DMF solution, which upon titration of **1** with NBu₄SH (Figure V-4b) produced a spectrum similar to that of **3** with Q-band peaks at 536, 567, and 609 nm. Further addition of NBu₄SH produces an identical spectrum to **7** with a Soret band at 419 nm, a prominent shoulder at 455 nm, and Q-band peaks at 538, 575, and 621 nm. Similar to the ferrous system, treatment of **1** in MePh or DMF, in the presence or absence of *N*-methylimidazole, with S₈ failed to produce any changes in the UV-Vis spectrum. In addition to reactivity with HS⁻, we reasoned that the protected binding pocket in the PFP could potentially allow for observation of bound H₂S to the ferric scaffold; however, addition of stoichiometric H₂S or a saturated H₂S solution to **1** in the presence or absence of *N*-methylimidazole failed to produce any changes in the UV-vis spectrum in either toluene or DMF.

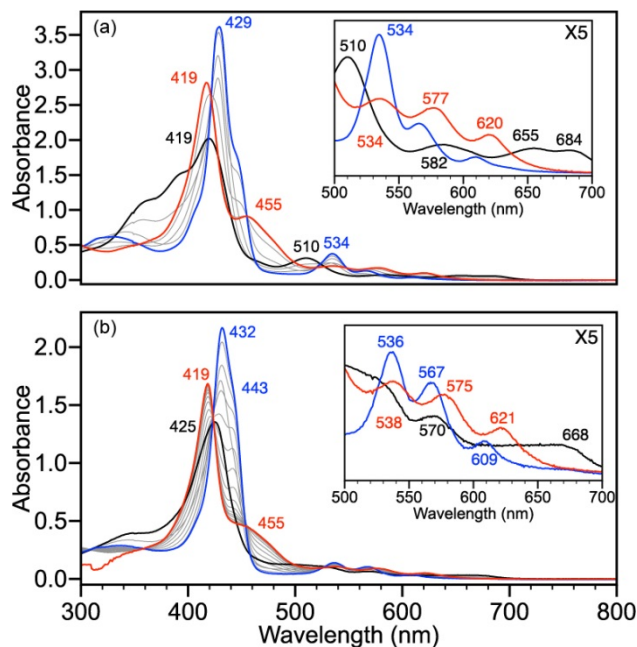


Figure V-4. (a) Titration of **1** (black) with 0.25 equiv. increments of NBu₄SH leads to reduction of Fe(III) to Fe(II) (blue trace shows 0.75 equiv. NBu₄SH) followed by binding of HS⁻ to form **7** (red). Conditions: MePh solution of 20 μM **1** with 69 μM *N*-methylimidazole titrated with 3 equiv. of NBu₄SH in 1:9 MeCN:MePh. (b) Titration of **1** (black) with 0.25 equiv. increments of NBu₄SH leads to reduction of Fe(III) to Fe(II) (blue trace shows 0.5 equiv. NBu₄SH) followed by binding of HS⁻ to form **7** (red). Conditions: DMF solution of 12 μM **1** with 80 μM *N*-methylimidazole titrated with 5 equiv. of NBu₄SH.

Oxygen sensitivity of [Fe^{II}(TPivPP)(SH)]⁻.

Unlike the TPP systems, the Fe^{II}(TPivPP)(*N*-MeIm)₂ scaffolds can bind O₂ reversibly, thus providing a unique opportunity to directly investigate the interaction of HS⁻ and O₂ at the heme center. Compound **3** readily binds O₂, either by exposure of **3** to the atmosphere or by direct injection of O₂, and the presence of Fe(TPivPP)(O₂)(*N*-MeIm) (**9**) is characterized by a decrease in intensity and hypsochromic shift of the Soret band from 429 to 427 nm with a concomitant attenuation and bathochromic shift of the Q-band from 534 to 540 nm (Figure V-5).¹⁵⁸ To remove any excess O₂, the headspace of the cuvette was purged with dry N₂ prior to NBu₄SH addition. Upon treatment of **9** with NBu₄SH in toluene, the intensity of the porphyrin absorbances are attenuated with an

increased baseline absorbance, suggesting the formation of particulates in the solution. Additionally, an increase in absorbance at 320 nm is observed, which is consistent with formation of sulfur oxidation and polysulfide formation.¹⁸¹⁻¹⁸⁴ Treatment of **3** with NBu₄SH to form **7**, followed by exposure to the atmosphere afforded the same reactivity. These data suggest that the porphyrin ring is irreversibly oxidized in the presence of oxygen and HS⁻, matching earlier observations of irreversible oxidation O₂-bound PFP compounds in the presence of acids.¹⁵⁸ Mass spectrometric data of the oxidized product showed a peak at 1160.4010 m/z, which matches the exact mass (1160.4097 m/z) and isotope pattern of addition of three O₂ molecules to the PFP system, consistent with porphyrin oxidation.[‡]

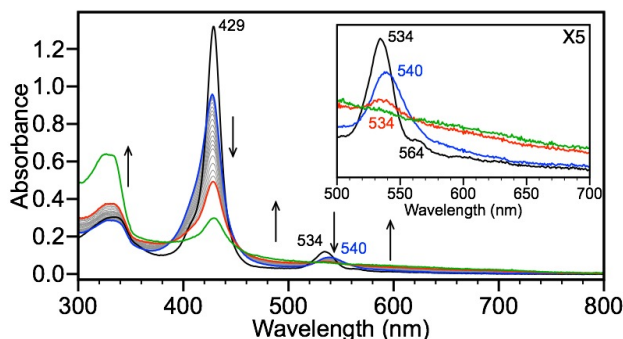


Figure V-5. Exposure of **3** to atmospheric oxygen leads to conversion to **7**. Titration of **7** (blue) with 0.25 equiv. increments of NBu₄SH leads to irreversible oxidation (red, 20 equiv. and green, 220 equiv.). Conditions: MePh solution of 5.6 μM **3** and 192 μM *N*-methylimidazole, exposed to atmosphere for 5 minutes, followed by purging headspace for 10 minutes with N₂, and titrated with NBu₄SH in a 1:39 acetonitrile-MePh solution.

[‡] This mass increase also suggests against the formation of verdoheme derivatives, which are another form of oxidized porphyrins in which the meso position of the porphyrin ring is oxidized. (Y. Du, G. Liu, Y. Yan, D. Huang, W. Luo, M. Martinkova, P. Man and T. Shimizu, *BioMetals*, **2013**, 26, 839-852. F. Yan, V. Fojtikova, P. Man, M. Stranova, M. Martinkova, Y. Du, D. Huang and T. Shimizu, *BioMetals*, **2015**, 28, 637-652.)

NMR Reactivity of Picket-fence Complexes with sulfide.

To complement the UV-Vis spectroscopic studies, and to determine any changes in the iron spin state upon HS^- binding, we used ^1H NMR spectroscopy to probe the reaction of **3** with NBu_4SH . The ^1H NMR spectrum of **3** in toluene- d_8 exhibits sharp features consistent with an Fe^{II} complex and allow for its reactivity to be monitored by NMR spectroscopy.¹⁸⁵⁻¹⁸⁶ Treatment of **3** in toluene- d_8 with 5 equiv. of NBu_4SH in CD_3CN results in a clean downfield shift of the pyrrole protons to 63 ppm, consistent with formation of a five-coordinate high-spin Fe^{II} complex ligated by a sulfur (Figure V-6).¹⁸⁷ The loss of the resonance at -14 ppm is consistent with dissociation of *N*-methylimidazole from the complex (Figures D-26 and D-33).¹⁸⁷⁻¹⁸⁸ These spectral changes, as well as the upfield shift of the phenyl protons to the 7-12 ppm region are all consistent with formation of **7**. Similarly, ^1H NMR spectroscopy of **1** with NBu_4SH also confirmed the reduction to **2**, followed by binding of HS^- to form **7**. The 80 ppm pyrrole resonance, indicative of a high spin Fe^{III} complex,¹⁸⁸ shifts upon treatment of **1** with 5 equiv. of NBu_4SH , consistent with reduction to Fe^{II} followed by formation of **7**.¹⁸⁷

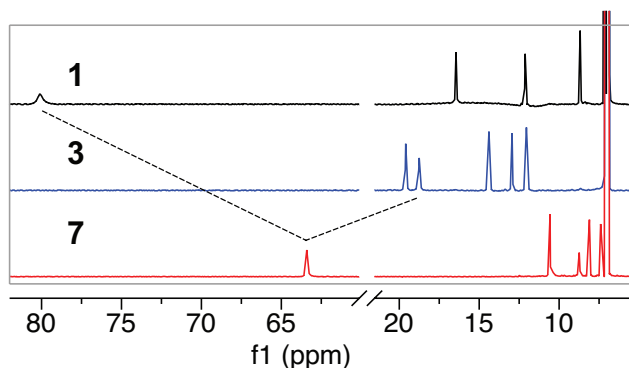


Figure V-6. ^1H NMR (600 MHz, toluene- d_8) spectra of **1** (4 mM, black), **3** (4 mM, blue) and **7** (red) in CD_3CN . The spectrum of **7** was recorded after addition of 5 equiv. of NBu_4SH to either **1** or **3**.

To confirm the spin and charge change from **1** to **7**, we measured the magnetic susceptibility of both complexes using the Evan's method.¹⁸⁹⁻¹⁹⁰ The magnetic susceptibility of **1** was measured to be $\mu_{\text{eff}} = 5.6 \mu_{\text{B}}$, supporting a high-spin ($S = 5/2$) Fe^{III} complex, which is consistent with solid state measurements.¹⁷⁶ Upon treatment of **1** with NBu_4SH , the magnetic susceptibility changes to $\mu_{\text{eff}} = 5.0 \mu_{\text{B}}$, supporting the formation of a high-spin ($S = 2$) Fe^{II} complex, matching previously reported Fe-SH bound structures.^{155,187,191} Taken together, the NMR data supports the reaction sequence in which HS^- initially reduces Fe^{III} to Fe^{II} , after which an additional equivalent of HS^- can bind to the metal center forming a ferrous hydrosulfide product.

Reaction of Fe(TPP) with sulfide.

Based on the identical reactivity of **1** and **3** in toluene and DMF, we reasoned that the protected axial binding pocket of the PFP compounds does not provide additional thermodynamic stability or protection from solvent over the un-protected systems. To provide a direct comparison for the experimental sulfide reactivity reactions of the picket-fence heme analogues, we performed analogous experiments with the parent tetraphenylporphyrin ($\text{Fe}^{\text{II}}(\text{TPP})(\text{N-MeIm})_2$, **6**). Upon treatment of **6** with NBu_4SH (Figure V-7a), similar spectral changes to those observed with **3** were observed, which are consistent with formation of $[\text{Fe}^{\text{II}}(\text{TPP})(\text{SH})]^-$ (**8**). The Soret band decreases in intensity and shifts to 418 nm with concomitant formation of a prominent shoulder at 463 nm with a well-anchored isosbestic point at 444 nm. The Q-band shows characteristic change from a prominent peak at 532 nm to three peaks at 532, 573, and 622 nm. Similarly, Treatment of $\text{Fe}^{\text{III}}(\text{TPP})\text{Cl}$ (**4**) with NBu_4SH (Figure V-7b) in DMF shows an initial change in the spectrum consistent with the formation of **6** with features at 432 and

563 nm. Further addition of NBu_4SH results in clean conversion to **8** with an associated Soret band shift from 432 nm to 418 nm and shoulder at 463 nm. The Q-bands adopt characteristic peaks at 532, 573, and 622 nm, decreasing in intensity with lower energy (Figure V-7b, inset). Similar to **1**, **2**, and **3**, treatment of **4**, **5**, or **6** in either DMF or toluene, in the presence or absence of *N*-methylimidazole, with S_8 or H_2S fails to perturb the UV-vis spectrum of the iron complexes.

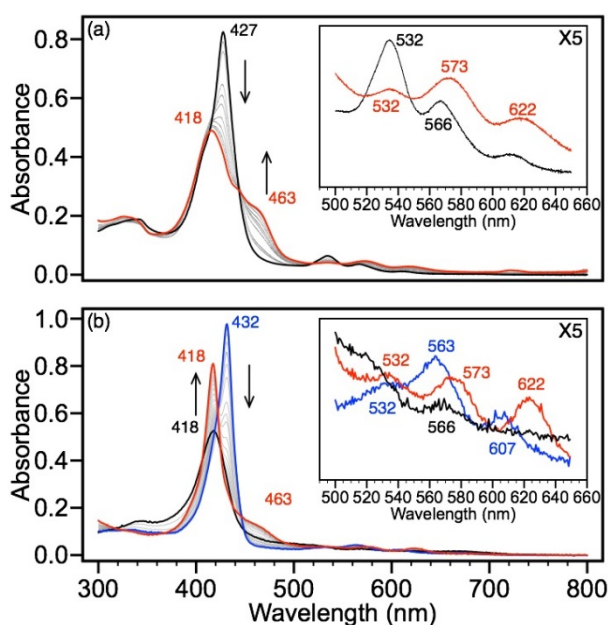


Figure V-7. (a) Titration of **6** (black) with 0.25 equivalent increments of NBu_4SH to form **8** (red). Conditions: MePh solution of 3.8 μM **6** with 35 μM *N*-methylimidazole titrated with 10 equivalents of NBu_4SH . (b) Titration of **4** (black) with 0.25 increments of NBu_4SH leads to reduction of Fe^{III} to Fe^{II} (**6**) (blue trace shows 0.75 equiv. NBu_4SH) followed by binding of HS^- to form **8** (red). Conditions: DMF solution of 4.5 μM **4** with 30 μM *N*-methylimidazole titrated with 10 equivalents NBu_4SH .

Sulfide Binding Affinities.

To confirm a 1:1 $\text{Fe}:\text{SH}$ binding stoichiometry, we constructed a competitive continuous variation (CCV) plot of **3** and NBu_4SH by varying the molar ratios of **3** and HS^- while keeping the *N*-methylimidazole concentration constant. These experiments

resulted in a plot with a clean break centered at 0.5, which is consistent with a 1:1 binding stoichiometry (Figure V-8).¹⁹²⁻¹⁹⁴ Based on this binding stoichiometry, we titrated solutions of **2** and **3** with NBu_4SH to determine the apparent association constants of sulfide and fit all titration data to a 1:1 Fe:SH model using the Thordarson method.^{139,153} The magnitude of these measurements matches binding constants associated with *Lucina Pectinata* HbI, and several synthetic porphyrin compounds including a cyclodextrin pyridine coordinated porphyrin, Fe(OEP), Fe(p-MeOPP), and Fe(TMP) (

Table V-1).^{75,94,178} Furthermore, the observed K_a values show that the binding affinity of HS^- for the porphyrin complexes are similar in DMF and toluene, and that the presence or absence of *N*-methylimidazole does not appreciably impact the observed sulfide binding affinity. Comparison of the picket-fence **3** with the parent **6** reveals that the presence of the protected binding pocket does not provide a significant thermodynamic stabilization of sulfide binding.

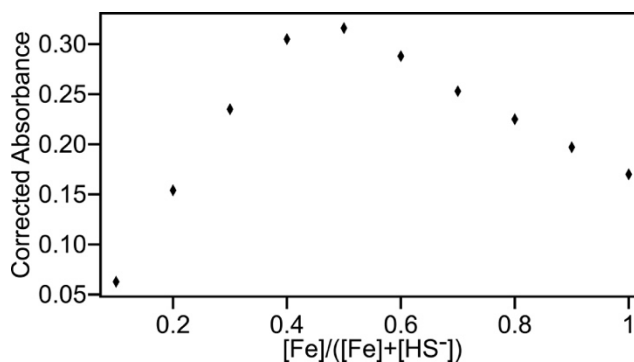


Figure V-8. A competitive continuous variation plot of **3** and NBu_4SH supports 1:1 binding. Conditions: Total concentration: $11.1 \mu\text{M}$ in 1:9 MePh:MeCN solution with 0.33 mM *N*-methylimidazole. The molar ratio of Fe was varied from 0.1 to 1 and the absorbance was corrected for the concentration of *N*-methylimidazole.

Table V-1. Comparison of HS⁻ binding constants for Fe-porphyrin systems.

Species	Solvent	log(K _a)	Source
Fe(TPivPP)(N-MeIm) ₂	MePh	4.5 ± 0.1	This work
Fe(TPivPP)(N-MeIm) ₂	DMF	5.0 ± 0.1	This work
Fe(TPivPP)	MePh	4.2 ± 0.1	This work
Fe(TPP)(N-MeIm) ₂	MePh	4.8 ± 0.2	This work
L. Pectinata HbI	Water	4.7	^{94,178}
Fe(OEP)	PhCl	5.0 ± 0.2	⁷⁵
Fe(p-MeOPP)	PhCl	4.7 ± 0.4	⁷⁵
Fe(TMP)	PhCl	4.6 ± 0.7	⁷⁵
Met-hemoCD3	Buffer	4.9	⁹⁴

Mass Spectrometry.

To gain further insight into sulfide binding, and to determine whether the picket-fence system provides a kinetic barrier to sulfide dissociation, we used HRMS to investigate HS⁻ binding and dissociation in the gas phase. Based on the 1:1 Fe:SH stoichiometry determined from the CCV plot, we expected to only observe ligation of one HS⁻ ligated to the metal center. Mass spectrometric analysis of ferrous **3** treated with 15 equiv. of NBu₄SH confirmed this expectation with the appearance of a parent ion peak at 1097.4294 m/z, which matches the expected mass (1097.4122 m/z) and isotope pattern of anionic **7** (Figure V-9a). We also observed a mass peak at 1063.4426 m/z corresponding to [2 - H⁺]⁻ (calculated 1063.4402 m/z), which we attribute to the loss of HS⁻ as well as H⁺ (likely from the amide NH in the PFP scaffold) from **7**. No peaks corresponding to ligation of two HS⁻ ligands were observed (Figure D-34). Consistent with the results obtained from **3**, treatment of ferric **1** with 15 equiv. of NBu₄SH in THF produces an identical mass spectrum as experiments with the ferrous species, which supports initial reduction followed by HS⁻ ligation (Figure V-9b). Taken with the CCV plot, this is consistent with a 1:1 binding ratio of Fe:SH.

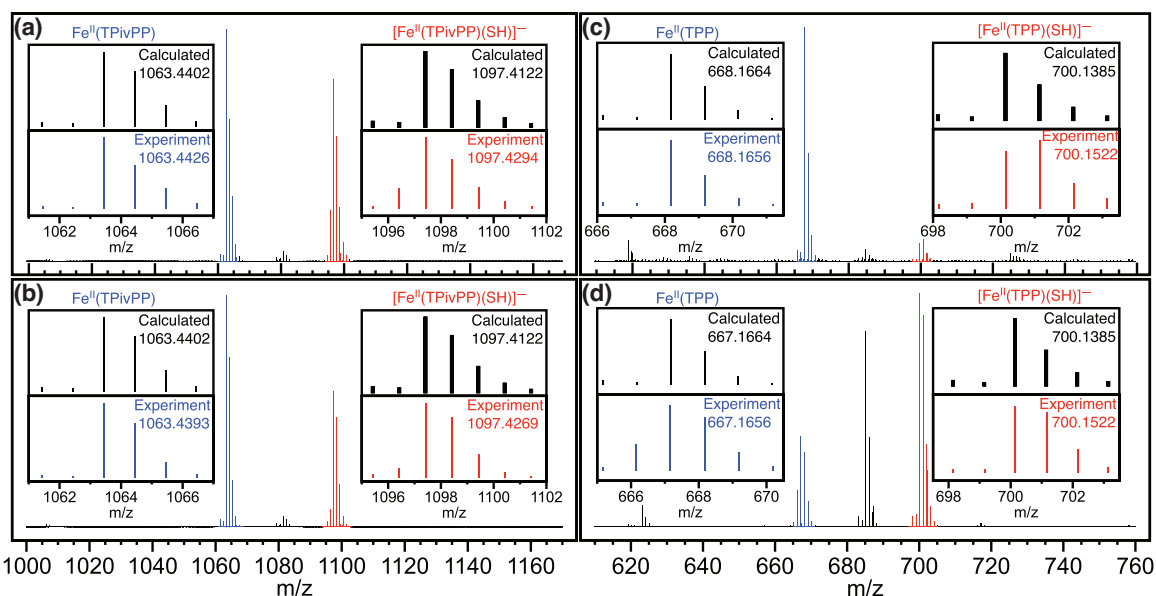


Figure V-9. (a) Mass spectrum of **3** with 15 equiv. of NBu_4SH added in THF results in formation of **2** (blue) and **7** (red), $[\text{Fe}^{\text{II}}(\text{TPivPP}) - \text{H}^+]^-$ and $[\text{Fe}(\text{TPivPP})(\text{SH})]^-$ respectively. (b) Mass spectrum of **1** with 15 equiv. of NBu_4SH added in THF results in the formation of **2** (blue) and **7** (red), $[\text{Fe}^{\text{II}}(\text{TPivPP}) - \text{H}^+]^-$ and $[\text{Fe}(\text{TPivPP})(\text{SH})]^-$ respectively. (c) Mass spectrum of **6** with 15 equiv. of NBu_4SH added in THF results in formation of **5** (blue) and **8** (red), which ionize as $[\text{Fe}^{\text{II}}(\text{TPP}) - \text{H}^+]^-$ and $[\text{Fe}^{\text{II}}(\text{TPP})(\text{SH}) - \text{H}^+]^-$ respectively. (d) Mass spectrum of **4** with 15 equiv. of NBu_4SH added in THF results in formation of **5** (blue) and **8** (red), which ionize as $[\text{Fe}^{\text{II}}(\text{TPP}) - \text{H}^+]^-$ and $[\text{Fe}^{\text{II}}(\text{TPP})(\text{SH}) - \text{H}^+]^-$ respectively. Conditions: electrospray in negative ion mode with $[\text{Fe}] = 1 \text{ mM}$ in THF with 15 equiv. NBu_4SH added in 1:1 THF-acetonitrile.

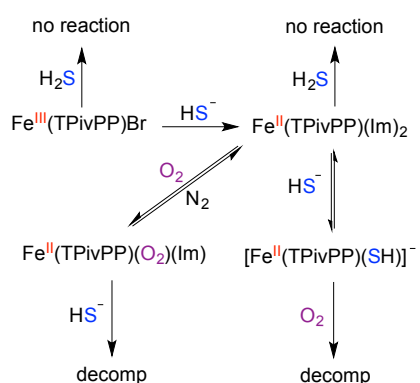
Similar to **1** and **3**, treatment of ferrous **6** in THF with 15 equiv. of NBu_4SH resulted in formation of mono-sulfur ligated **8** at 700.1522 m/z (ionized as $[\mathbf{8} - \text{H}^+]^-$, calculated 700.1385 m/z) (Figure V-9c). As observed in the PFP system, the second major peak at 668.1656 m/z corresponds with unligated **5** (calculated m/z 668.1664). Treatment of ferric **4** under identical conditions affords an identical spectrum as the reaction of the ferrous TPP **6** with NBu_4SH (Figure V-9d). Interestingly, the $[\text{M} - \text{H}_2\text{S}]^-$ peak observed in the PFP system was not observed in the TPP system ($[\text{M} - \text{SH}^*]^-$ was observed), suggesting that the proximity of the acidic N-H groups on the PFP ligand were involved in the H_2S ionization. A second notable difference between the PFP and parent

TPP system is the relative intensity of the HS⁻ ligated and unligated species. With both mass spectrometric experiments measured under identical instrumental conditions, these relative stabilities suggest that the protective pocket in the PFP system provides additional stability to the bound hydrosulfide ligand. Based on the similar binding thermodynamics measured in solution, this increased stability is likely due to an increased kinetic barrier for sulfide dissociation from the protected pocket in the PFP system rather than a thermodynamic ground state stabilization of bound sulfide. Variation of the collisional energy and comparison to the Fe(TPP) scaffold showed kinetic stabilization of the bound sulfide, suggesting it is bound inside the porphyrin pocket (See Appendix D).¹⁹⁵⁻¹⁹⁶

Conclusion

Motivated to extend the utility of synthetic heme structures we used the picket-fence porphyrin, which contains a protected axial binding pocket, as a model to investigate sulfide binding. Our spectroscopic investigations revealed that the Fe^{III} or Fe^{II} PFP scaffolds do not react with H₂S, but rather with HS⁻. Upon treatment with HS⁻, Fe^{III}(TPivPP)Br is reduced to its Fe^{II} form (Scheme V-1), after which a single HS⁻ ligand binds to the heme iron. This binding stoichiometry was confirmed by UV-Vis and NMR spectroscopic studies as well as mass spectrometric investigations. Comparison of the sulfide binding affinity to Fe^{II} in the PFP system to that observed in the less hindered TPP system revealed similar sulfide association constants, suggesting that the protected axial pocket of the PFP system did not provide significant thermodynamic stabilization of the bound sulfide. Mass spectrometric studies using variable collisional energy experiments established that sulfide dissociation from the PFP system had a larger kinetic barrier than

ionization of sulfide from the TPP system, which is consistent with a kinetic, rather than thermodynamic, stabilization of bound sulfide within sterically constrained PFP scaffold. Taken together, these results suggest that the sterically-constraining low-polarity environment alone is not the primary contributor for stabilization of ferric H₂S/HS⁻ species in model systems, but that other interactions, such as hydrogen bonding or the interplay between hydrogen-bonding and a low-polarity binding pocket must play a critical role. We are currently investigating other systems that probe these different interactions, which will be reported in due course.



Scheme V-1. Overall reactivity of the Fe^{III/II}(TPivPP) scaffold with H₂S, HS⁻, and O₂.

Bridge

Having established the sterically constrained, low-polarity pocket of Hb1 in *L. Pectinata* alone does not stabilize the binding of H₂S/HS⁻, we next turned our attention to understanding how other factors may contribute to the thermodynamic stability of sulfide transport. The binding pocket of Hb1 contains a proximal glutamate residue that acts as a hydrogen bond accepting moiety that contributes to the stabilization of H₂S. This structure is similar to the binding of O₂ in *H. Sapiens*, where a proximal histidine acts as a hydrogen bond donor to stabilize the binding of O₂. To explore the role of hydrogen

bond accepting moieties in the secondary coordination sphere, we collaborated with the Gilbertson group at Western Washington University. The Gilbertson group developed a zinc pyridinediimine ligand with an H-bond accepting amine in the secondary coordination sphere, which we used to bind and stabilized HS^- in Chapter VI.

Experimental

Materials and Methods.

All manipulations were performed under an inert atmosphere using standard Schlenk techniques or an Innovative Atmospheres N_2 -filled glove box unless otherwise noted. All chemicals were used as received unless otherwise noted. Pyrrole, 2-nitrobenzaldehyde, and *N*-methylimidazole were purchased from TCI Chemicals. Pivaloyl chloride, 1,2-dimethoxyethane, tetrabutylammonium chloride, and 1,3,5-trimethoxybenzene were purchased from Sigma-Aldrich. $\text{SnCl}_2 \cdot 2\text{H}_2\text{O}$ was purchased from Strem chemicals. FeBr_2 (anhydrous) and NaSH (anhydrous) were purchased from Strem chemicals and handled under nitrogen. Hydrogen sulfide gas was purchased from Sigma Aldrich and transferred through a custom-built stainless steel transfer line into a glass storage bulb prior to use. Tetrabutylammonium hydrosulfide (NBu_4SH) was synthesized as previously reported.⁴⁴ *Note:* Hydrogen sulfide and its salts are highly toxic and should be handled carefully to avoid exposure. Spectroscopic grade toluene, acetonitrile, and tetrahydrofuran were degassed by sparging with argon followed by passage through a Pure Process Technologies solvent purification system to remove water and stored over 4Å molecular sieves in an inert atmosphere glove box. Heptane was passed through an alumina column, dried and distilled over calcium hydride then deoxygenated by three freeze-pump-thaw cycles and stored in an inert atmosphere glove

box over 4Å molecular sieves. Spectroscopic grade *N,N*-dimethylformamide was dried and distilled over calcium hydride, deoxygenated by three freeze-pump-thaw cycles, and stored in an inert atmosphere glove box over 4Å molecular sieves. Toluene-*d*₈ and acetonitrile-*d*₃ were purchased from Cambridge Isotope laboratories and distilled from calcium hydride, deoxygenated by three freeze-pump-thaw cycles, and stored in an inert atmosphere glove box. Porphyrin stock solutions were prepared in dry toluene or DMF and stored in an inert atmosphere glove box until immediately prior to use.

Spectroscopic Methods.

UV-Vis measurements were acquired on an Agilent Cary 100 UV-Vis spectrophotometer equipped with a QNW dual cuvette temperature controller at 25.00 ± 0.05 °C. All spectroscopic samples were prepared under an inert atmosphere in septum-sealed cuvettes obtained from Starna Scientific. NMR spectra were acquired on a Bruker Avance-III-HD 600 spectrometer with a Prodigy multinuclear broadband cryoProbe at 25.0 °C. Chemical shifts are reported in parts per million (δ) and are referenced to residual solvent resonances. IR spectra were acquired on a Thermo Scientific Nicolet 6700 spectrometer equipped with a diamond crystal Smart ATR Attachment. Mass spectra were acquired on a Synapt G2-Si from Waters Corporation and introduced by nanoelectrospray using a platinum wire at 0.4 kV potential. All data were acquired with an ESI voltage of 500 V using “resolution” mode.

General procedure for UV-Vis spectroscopic studies.

In a glove box, the porphyrin stock solutions were diluted to the desired concentration by addition to 3.0 mL of solvent in a septum-sealed cuvette and removed from the glove box. Non-porphyrin reagents were prepared approximately 10⁵ times more

concentrate than the porphyrin to provide minimal dilution during addition. NBu₄SH, H₂S, and other reagents were added to the septum-sealed cuvettes by gas-tight syringe. Titration studies were performed using 0.25 equiv. increments unless otherwise noted. Binding constants (K_{assoc}) were determined from UV-Vis titration data and fit to a 1:1 model.^{139,153}

General procedure for NMR studies.

In a glove box, 1.6 μmol of the different Fe(TPivPP) species were added to ~ 0.4 mL of toluene-*d*₈ in a septum-capped NMR tube. Stock solution of NBu₄SH (0.688 M in acetonitrile-*d*₃) was prepared, and ~ 5 equiv. was added to the NMR tube using a gas-tight syringe.

General procedure for mass spectrometry studies.

Solutions of Fe species (1 mM) containing 1.5 mM *N*-methylimidazole were prepared in THF. To this solution, 15 equiv. of NBu₄SH in 1:1 THF-acetonitrile were added, and negative ion mode nano-electrospray mass spectra were acquired with a Synapt G2-Si quadrupole time-of-flight mass spectrometer (under identical conditions for each species).

General procedure for Evans' Method magnetic susceptibility measurements.

A stock solution containing 1,3,5-trimethoxybenzene (20.2 mg, 120 μmol) in 500 μL of toluene-*d*₈ and 100 μL of CD₃CN was prepared. Fe(TPivPP)Br (2.7 mg, 2.3 μmol) was added to 450 μL of the 1,3,5-trimethoxybenzene stock solution. NBu₄SH (36.5 mg, 132 μmol) was added to 100 μL of the stock solution and an additional 100 μL of CD₃CN was added to ensure complete solubility. The remaining 50 μL of 1,3,5-trimethoxybenzene stock solution was added to a capillary tube. A septum-sealed NMR

tube was charged with 400 μL of the $\text{Fe}(\text{TPivPP})\text{Br}$ stock solution and the capillary tube containing the 1,3,5-trimethoxybenzene standard. The ^1H NMR spectrum was recorded, after which 16 μL (5 equiv.) of the NBu_4SH stock solution was added. The NMR tube was sonication for 20 minutes to ensure complete mixing, after which another ^1H NMR spectrum was recorded. The chemical shift difference between the 1,3,5-trimethoxybenzene resonances in the capillary tube and the $\text{Fe}(\text{TPivPP})\text{Br}$ solution were measured and corrected using standard diamagnetic corrections.¹⁸⁹

Synthesis of $\text{Cr}(\text{OAc})_2$ and $\text{Cr}(\text{acac})_2$.

A 20 mL scintillation vial equipped with a stir bar was charged with $\text{K}_2\text{Cr}_2\text{O}_7$ (2.0 g, 6.8 mmol), powdered zinc (5 g, 76 mmol), and 5 mL of water under nitrogen. Concentrated hydrochloric acid (20 mL) was then added drop wise to the stirred reaction mixture for approximately 20 minutes, and the solution was stirred until the color of the reaction mixture changed from yellow to green and finally to blue. The supernatant was transferred by filter cannula to a 100 mL flask containing 20 mL of a saturated NaOAc solution, which resulted in formation of a red precipitate. The solid product was filtered, washed with EtOH and Et_2O , and then dried under vacuum overnight to yield the desired product (1.06 g, 41%). $\text{Cr}(\text{acac})_2$ was prepared from the crude $\text{Cr}(\text{OAc})_2$ product in a glove box as described in the literature.¹⁹⁷ *Note:* $\text{Cr}(\text{acac})_2$ is a pyrophoric powder and should be handled carefully under an inert atmosphere.

Synthesis of iron porphyrin complexes.

The synthesis of the iron porphyrin complexes was conducted according to published procedures using the modifications noted below.^{158,176-177} Spectroscopic

properties of the isolated product are provided to aid future preparations of these complexes.

5,10,15,20-tetrakis(2-nitrophenyl)porphyrin (H₂TNPP).

2-Nitrobenzaldehyde (25.0 g, 165 mmol) was dissolved in 500 mL of glacial acetic acid in a 3-neck 1-L round bottom flask fitted with a reflux condenser and a syringe pump inlet. The solution was then heated to reflux and stirred vigorously. Pyrrole (12 mL, 170 mmol) was added drop-wise via the syringe pump over 30 minutes. (*Note:* This is a highly exothermic reaction and care is needed to keep the reaction under control. We have found that uniform addition of pyrrole using a syringe pump facilitates maintaining a vigorous, but controllable, reaction and increases the reproducibility). After the addition of pyrrole was completed, the solution had turned black and was refluxed for 30 minutes. The oil bath was then allowed to cool to 35 °C and CHCl₃ (65 mL) was added to prevent tar formation. (*Note:* Fast cooling or cooling below 35 °C can lead to intractable tar formation, as noted previously.)¹⁷⁶ After stirring for 1 h, the reaction mixture was filtered through an extra course frit, and the collected solid was washed with 5 x 100 mL of CHCl₃. Additional product can be obtained by pouring the filtrate through a medium porosity frit and washing the collected solid with 5 x 50 mL of CHCl₃. The purple solids obtained by filtration were combined and dried overnight at 100 °C under vacuum to yield the desired product (2.89 g, 8.7%). FTIR (ATR, neat) cm⁻¹: 3316 (w, C-H), 1518 (s, NO₂), 1341 (s, NO₂); ¹H NMR (300 MHz, DMSO-*d*₆) δ: 8.98-7.95 (m, 24H), -2.80 (s, 2H); λ_{max} (DMF): 420, 516, 550, 593, 650 nm.

5,10,15,20-tetrakis(2-aminophenyl)porphyrin (H₂TAPP).

A 1-L round bottom flask was charged with H₂TNPP (2.5 g, 3.14 mmol) and 125 mL of concentrated HCl. Reagent grade SnCl₂•2H₂O (10.6 g, 47.0 mmol, 15 equiv.) dissolved in 10 mL of HCl was added to the H₂TNPP solution and stirred for 1 h at room temperature, after which the flask was transferred to an oil bath that had been preheated to 65 °C. (*Note:* The activity of the SnCl₂ can be tested by mixing 1 g of SnCl₂•2H₂O in 1.5 mL of HCl with 0.25 g of 3-nitrobenzaldehyde. The mixture should become warm and turn red-orange within 10 minutes.)¹⁷⁶ After heating with vigorous stirring for 25 min, the flask was removed from the oil bath and cooled to room temperature in an ice bath. The reaction mixture was then neutralized carefully with 250 mL concentrated NH₄OH over 25 minutes. After the pH was adjusted to > 10 with NH₄OH, 200 mL of CHCl₃ was added and the biphasic solution was stirred for at least 12 hours, after which the organic layer was separated. The aqueous layer was transferred to a 1-L separatory funnel, diluted with water, and extracted with CHCl₃ (3 x 150 mL). The combined organic layers were washed with 400 mL of 10% NH₄OH and concentrated to ~50 mL and filtered through celite to remove any remaining tin compounds. The celite was washed with CHCl₃ until the filtrate had faded in color, and the combined filtrates were concentrated to ~50 mL. EtOH (34 mL) and NH₄OH (2 mL) were added, and the solution was further concentrated to ~40 mL, after which an additional 20 mL of EtOH was added and the solution was concentrated to ~16 mL. The resultant solution was filtered through a medium porosity frit and the purple-black crystals were rinsed with small amounts of ethanol and dried in a 140 °C oven for 1 h to afford 1.65 g (78%) of the desired product. FTIR (ATR, neat) cm⁻¹: 3350 (w, N-H), 3312 (w, N-H), 3023 (w); ¹H NMR (600 MHz,

CDCl₃) δ 8.91 (s, 8H), 7.91-7.81 (m, 4H), 7.59 (t, $J = 7.9$ Hz, 4H), 7.16 (q, $J = 6.4$ Hz, 4H), 7.09 (d, $J = 8.0$ Hz, 4H), 3.51 (d, $J = 17.3$ Hz, 8H), -2.67 (s, 2H); ¹³C{¹H} NMR (151 MHz, CDCl₃) δ : 146.9, 134.9, 131.4, 129.8, 127.0, 117.7, 116.0, 115.4; λ_{max} (CHCl₃): 420, 515, 550, 590, 650 nm.

Separation of all-cis-H₂TAPP.

The separation was carried out in a one-column procedure that enriches the desired all-*cis* isomer as described in the literature.¹⁷⁷ To separate the mixture, 45 g of silica, 100 mL of benzene, and a stir bar were added to a 250 mL 3-neck round bottom flask equipped with a reflux condenser and a benzene-saturated nitrogen stream. After heating at 75 °C for 2 h, 1.25 g of H₂TAPP in 6 mL of benzene was added via syringe and the resultant mixture was stirred at 75 °C for 20 h. The resultant dark slurry was cooled to room temperature and poured into a 50 mm OD column. The undesired isomers were eluted with 1:1 C₆H₆:Et₂O until the eluent became a pale red color (~400 mL). The solvent was then switched to 1:1 Et₂O:acetone and the desired isomer was eluted. The collected fractions were checked for purity by TLC (SiO₂, 4:1 CHCl₃:Et₂O, R_f = 0.57) and stored at 4 °C for no longer than 12 hours prior to use. Isolated fractions were not reduced in volume in order to minimize isomerization.

(all-cis)-5,10,15,20-tetrakis[2-(2,2-dimethylpropionamido)phenyl]porphyrin
(H₂TPivPP).

All of the pure collected fractions of the all-*cis* isomer were placed in a 1-L round bottom flask under N₂. Pyridine (3 mL) and pivaloyl chloride (3 mL) were added and the reaction mixture was stirred for 2.5 h, after which 5 mL of MeOH was added to quench any residual acid chloride. The reaction mixture was evaporated to dryness, dissolved in

125 mL CHCl₃, and washed with 80 mL of 10% NH₄OH and 2 x 80 mL of water. The combined aqueous washes were combined and extracted with 2 x 30 mL of CHCl₃. The combined organic layers were dried with Na₂SO₄, filtered, and evaporated to dryness under reduced pressure. The crude residue was purified by column chromatograph (SiO₂, 4:1 CHCl₃:Et₂O). Further purification was achieved by dissolving the product in CHCl₃, adding EtOH and heptane, reducing the volume under reduced pressure, and filtering the purple crystalline product. The crystals were dried overnight under vacuum to yield 0.72 g (39%) of the desired isomerically-pure product. FTIR (ATR, neat) cm⁻¹: 3430 (m, N-H), 3315 (m, N-H), 3060 (w, C-H), 2956 (m, C-H), 2867 (m, C-H), 1686 (s, C=O); ¹H NMR (600 MHz, CDCl₃) δ: 8.83 (s, 8H), 8.73 (d, *J* = 8.45 Hz, 4H), 7.90 (d, *J* = 6.43 Hz, 4H), 7.85 (t, *J* = 8.59 Hz, 4H), 7.50 (t, *J* = 7.84, 4H), 7.21 (s, 4H), 0.07 (s, 36H), -2.59 (s, 2H); ¹³C{¹H} NMR (151 MHz, CDCl₃) δ: 175.6, 138.6, 134.4, 131.0, 130.3, 123.2, 121.0, 115.0, 39.1, 26.6; λ_{max} (CHCl₃): 418, 512, 545, 588, 641 nm.

Bromo{(all-cis)-5,10,15,20-tetrakis-[2-(2,2-dimethylpropionamido)phenyl]porphyrinato(2-)}-iron(III), (Fe(TPivPP)Br)

In an inert atmosphere glove box, H₂TPivPP (0.54 g, 0.53 mmol), anhydrous FeBr₂ (0.54 g, 2.5 mmol) 1,2-dimethoxyethane (35 mL), pyridine (0.25 mL) and a stir bar were added to a 250 mL round bottom flask equipped with a reflux condenser. The apparatus was then removed from the glove box, placed under positive pressure of N₂, and refluxed at a bath temperature of 100 °C for 1 h. The progress of the reaction was monitored by UV-Vis spectroscopy by removing small aliquots, exposing them to the atmosphere and acidifying the solution with a few drops of concentrated HBr. Any remaining free base porphyrin is readily detected by its characteristic absorption at 450

nm (Figure D-19). When no remaining free porphyrin was detected, the reaction mixture was cooled to room temperature, exposed to the atmosphere, and brought to dryness under reduced pressure. The crude residue was dissolved in 16 mL of CHCl₃ and purified by column chromatograph (basic Al₂O₃, CHCl₃). The black residue obtained after removing the solvent from the combined fractions was suspended in 10 mL of MeOH and 0.1 mL of HBr. The resultant reaction mixture was heated to 70 °C for 5 minutes and cooled to room temperature. CH₂Cl₂ (5 mL) was added to dissolve any remaining solid while warm, and the flask was placed in a 20 °C refrigerator overnight to afford a crystalline product. The crystals were filtered, washed with MeOH, and dried at 70 °C under vacuum overnight. A second crop of crystals was obtained from the filtrate, total: 0.15 g (24%). FTIR (ATR, neat) cm⁻¹: 3430 (m, N-H), 3315 (m, N-H), 3060 (w, C-H), 2956 (m, C-H), 2867 (m, C-H), 1686 (s, C=O); ¹H NMR (600 MHz, toluene-*d*₈) δ: 8.09, 16.45, 12.13, 8.68, 1.35, 0.93, 0.28, -0.16; λ_{max} (CHCl₃): 359(sh), 391(sh), 419, 509, 584, 655, 685 nm.

Bis(N-methylimidazole)[all-cis]-5,10,15,20-tetrakis-[2-(2,2-dimethylpropionamido)phenyl]porphyrinato(2-)]-iron(II) (Fe(TPivPP)(N-MeIm)₂).

In a glove box, a 20 mL scintillation vial was charged with Fe(TPivPP)Br (30 mg, 26 μmol), Cr(acac)₂ (19.7 mg, 110 μmol), THF (10 mL), *N*-methylimidazole (21 μL, 260 μmol), and a stir bar. The stirred reaction mixture was heated to boiling for 5 minutes, filtered hot, then cooled to room temperature, while layering with heptane, and cooled to -25 °C overnight. The resultant microcrystalline solution was filtered through a glass wool filter, washed with heptane, extracted from the filter with THF, and evaporated to dryness under vacuum to yield the desired product (7.1 mg, 54%). FTIR (ATR, neat) cm⁻¹

1 : 3425 (m, N-H), 2658 (m, C-H), 2868 (m, C-H), 1686 (s, C=O); 1 H NMR (600 MHz, toluene- d_8) δ : 19.60, 18.75, 14.40, 12.94, 12.04, 3.35, 1.35, 0.29, -14.01; λ_{max} (toluene): 333, 429, 535, 564, 606 nm.

CHAPTER VI

STABILIZATION OF A ZINC(II) HYDROSULFIDO COMPLEX UTILIZING A HYDROGEN-BOND ACCEPTING LIGAND

Published as Hartle, M. D.; Delgado, M.; Gilbertson, J. D.; Pluth, M. D. “Stabilization of a Zn(ii) hydrosulfido complex utilizing a hydrogen-bond accepting ligand” *Chemical Communications* **2016**, 52(49) 7680-7682. Experimental work was completed by me. Ligand synthesis was performed by M. Delgado. Editorial assistance was provided by J. D. Gilbertson and M. D. Pluth. Associated content can be found in Appendix E.

Preface

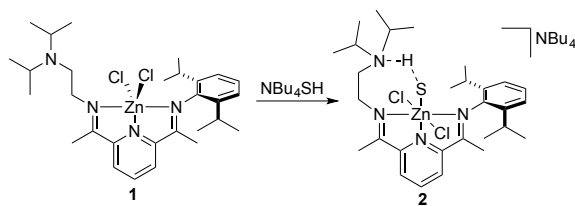
Hydrogen sulfide (H₂S) has gained recent attention as an important biological analyte that interacts with bioinorganic targets. Despite this importance, stable H₂S or HS⁻ adducts of bioinorganic metal complexes remain rare due to the redox activity of sulfide and its propensity to form insoluble metal sulfides. We report here reversible coordination of HS⁻ to Zn(didpa)Cl₂, which is enabled by an intramolecular hydrogen bond between the zinc hydrosulfido product and the pendant tertiary amine of the didpa ligand.

Introduction

Although historically known for its malodor and toxicity, hydrogen sulfide (H₂S) has joined nitric oxide (NO) and carbon monoxide (CO) as a physiologically important gasotransmitter.¹ Complicating its reactivity with different bioinorganic targets, H₂S has multiple protonation states, participates in complex redox chemistry, and is highly metallophilic.^{62,163} For example, the high affinity between zinc and sulfide ($\Delta G_f^\circ = -48.11$

kcal/mol, sphalerite)¹⁹⁸ limits generation of stable sulfide-ligated products, but has also been leveraged as a sulfide sequestration strategy in quantification and detection methods.¹⁹⁹⁻²⁰⁰ Consequently, stable zinc hydrosulfido complexes remain rare,²⁰¹⁻²⁰⁵ with reported examples including (tris)pyrazolylborate zinc hydrosulfide (TpZnSH) complexes, supported by the steric protection from the Tp ligand.²⁰¹⁻²⁰² Complementing the use of steric protection, secondary-coordination sphere interactions have also been used to stabilize metal-sulfide species with other metals, such as iron.⁷¹ Additionally, these stabilizing forces are hypothesized to be important in the mechanism of carbonyl sulfide fixation by carbonic anhydrase.²⁰⁶⁻²⁰⁷

Toward increasing our understanding of the solution state stabilization of metal hydrosulfido complexes, we viewed that a ligand scaffold with a pendant hydrogen-bond (H-bond) acceptor would provide a viable scaffold for Zn-SH stabilization. We noted that the pyridinediimine (PDI) ligand scaffold didpa ($[(2,6\text{-}i\text{PrC}_6\text{H}_3)\text{N}=\text{CMe})(\text{N}(i\text{Pr})_2\text{C}_2\text{H}_4)\text{N}=\text{CMe})\text{C}_5\text{H}_3\text{N}]$) has been demonstrated to function as an H-bond donor when the pendant diisopropylamine is protonated and used to stabilize metal halogen hydrogen bonds (MHHBs), with calculated MHHB strengths of ~6 kcal/mol for $[\text{Zn}(\text{Hdidpa})\text{Cl}_2][\text{PF}_6]$.²⁰⁸ Additionally, the protonated form of the ligand can also function as an H-bond donor to stabilize rare Fe-OH species.²⁰⁹ Although ligands displaying hydrogen-bond donors in the secondary coordination sphere are now frequently used in bioinorganic model complexes,²¹⁰⁻²¹¹ hydrogen-bond accepting ligands are rare.²¹²⁻²¹⁶ On the basis of these properties, we reasoned that the didpa ligand could function as an H-bond acceptor in its neutral form to provide a suitable ligation environment for metal hydrosulfido stabilization.



Scheme VI-1. Reaction of $\text{Zn}(\text{didpa})\text{Cl}_2$ (**1**) with NBu_4SH to generate hydrosulfide adduct **2**.

Results and Discussion

Treatment of $\text{Zn}(\text{didpa})\text{Cl}_2$ (**1**) with H_2S gas failed to produce any reaction, however treatment of **1** with NBu_4SH ⁴⁴ in either CH_2Cl_2 (Figure VI-1) or MeCN (Figure E-1) resulted in a significant change in the UV-Vis spectrum. In CH_2Cl_2 the shoulder at 313 nm decreased in intensity with a concomitant increase in absorbance at 280 nm and a well-anchored isosbestic point at 296 nm upon addition of HS^- . A Job plot was consistent with 1:1 binding of HS^- to **1** (Figure VI-1, inset). In addition, titration with HO^- resulted in 1:1 binding (Figure E-13). Based on these results, and because chloride abstraction was not required for HS^- binding, we propose that HS^- binds to **1** to generate six-coordinate $[\text{Zn}(\text{didpa})\text{Cl}_2\text{SH}]^-$ (**2**, Scheme VI-1). All attempts to grow single crystals suitable for X-ray structural determination of **2** resulted in precipitation of a white amorphous powder after prolonged standing. Supporting the associative formation of a six-coordinate product, titration of **1** with excess Cl^- showed similar spectral changes by UV-Vis spectroscopy (Figures E-3 and E-4), and the Job plot was consistent with 1:1 Cl^- binding (Figure E-12). Attempts to isolate and crystallize the six-coordinate 1:1 adduct of Cl^- and **1** with a range of different Cl^- sources (Bu_4NCl , Ph_4PCl , PPNCl) resulted in simple recrystallization of the starting chloride salt and **1**, presumably due to the reversibility of the process.

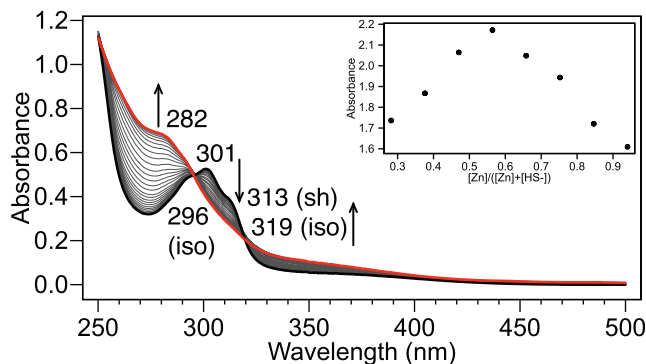


Figure VI-1. Titration of $\text{Zn}(\text{didpa})\text{Cl}_2$ ($87.3 \mu\text{M}$, CH_2Cl_2 , black) with NBu_4SH (0.1 equiv. increments up to 6 equiv., red). The inset shows the Job plot of **1** with NBu_4SH in MeCN at a total concentration of $420 \mu\text{M}$. The observed break is consistent with 1:1 binding.

To gain further insights into the HS^- binding, we used ^1H NMR spectroscopy to investigate the stability of **2** and the role of hydrogen-bonding in the complex. Treatment of **1** with 1.5 equiv. of NBu_4SH in CD_3CN resulted in significant changes in the ^1H NMR spectrum. The resultant spectrum did not match that of the free ligand,²⁰⁸ suggesting that addition of HS^- does not remove Zn from the didpa ligand (Figure VI-2). Upon HS^- addition, the pyridine and other aryl resonances of **1** shifted significantly in a pattern consistent with loss of free rotation of the 2,6-diisopropylphenyl group of the ligand. Similarly, the isopropyl resonance at 1.00 ppm, corresponding to the isopropyl methyl groups of the pendant amine, shifts downfield and bifurcates. Each of these spectral changes indicated a significant change in the primary coordination sphere of the zinc and are consistent with formation of a six-coordinate complex in which the Zn-SH moiety is hydrogen bonded to the pendant diisopropylamine (Scheme VI-1).

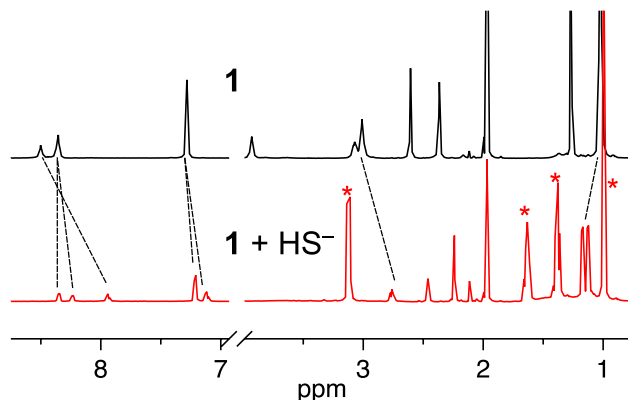


Figure VI-2. ^1H NMR spectra of **1** (11.8 mM in CD_3CN) before (top, black) and after (bottom, red) addition of 1.5 equiv. of NBu_4SH . Peaks denoted with a (*) correspond to the NBu_4^+ counterion.

Low temperature ^1H NMR investigations provided additional information about the structural flexibility of the scaffold and the presence of the coordinated hydrosulfide. Although we were unable to observe an appreciable signal corresponding to the coordinated HS^- at room temperature, we expected that lowering the temperature would not only enable HS^- observation, but also lock the conformation of the ethylene backbone of the ligand. Consistent with these expectations, cooling to $-35\text{ }^\circ\text{C}$ in CD_3CN resulted in the appearance of a new resonance at 11.05 ppm, matching the general chemical shift expected for partial protonation of the nitrogen as an H-bond acceptor (Figure VI-3).²¹⁷ For comparison, the ^1H NMR spectrum of the previously reported $[\text{Zn}(\text{Hdidpa})\text{Cl}_2][\text{PF}_6]$ displays an N-H resonance at 8.50 ppm in CD_2Cl_2 due to the protonated diisopropylamine of the didpa ligand acting as an H-bond donor and forming an intramolecular MHHB with a chloride ligand.²⁰⁸ The downfield shift observed for **2** is consistent with the diisopropylamine acting as an H-bond acceptor, likely accepting a hydrogen bond from the Zn-ligated SH moiety.²¹⁸

Additionally, we observed that the broad peak centered at 3.6 ppm corresponding to the ethylene bridge decoalesced upon cooling. The presence of the internal hydrogen bond between the sulfhydryl group and the tertiary amine significantly limits the flexibility of the secondary coordination sphere, resulting in a sharpening in the signal produced by the ethylene linker, methine protons, and methyl groups (Figure E-8). Supporting the presence of an intramolecular SH hydrogen bond, a ^1H NOESY experiment at $-35\text{ }^\circ\text{C}$ revealed cross peaks between the SH and the ethylene, methine, and methyl signals of the tertiary amine linker (Figure E-5).

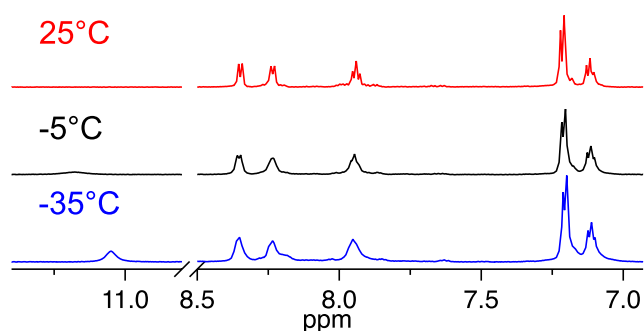


Figure VI-3. Variable temperature ^1H NMR spectra of 11.4 mM $\text{Zn}(\text{didpa})\text{Cl}_2$, and 1.5 equiv. NBu_4SH in CD_3CN . Cooling to $-35\text{ }^\circ\text{C}$ results in sharpening and an upfield shift of the broad SH peak to 11.05 ppm. See Figure E-9 for an expanded spectrum of the SH peak.

Although the N---HS interaction was not observed by solution state FTIR, we note that the N-H stretch involved in hydrogen bonding in the $[\text{Zn}(\text{Hdidpa})\text{Cl}_2][\text{PF}_6]$ system is also absent in solution FTIR spectra.²⁰⁸ The N-H stretch in the N---HS moiety is likely severely broadened or obscured, which is common in many hydrogen bonding systems.²¹⁷

To demonstrate the reversibility of **2**, and to provide evidence for the formation of a six-coordinate complex, we performed a displacement experiment by ^1H NMR

spectroscopy. Treatment of **1** with 1.5 equiv. of NBu_4SH resulted in the formation of **2** with characteristic shifts in the aryl peaks, and broad resonance at 3.6 ppm (Figure VI-4). Upon addition of 20 equiv. of NBu_4Cl , the aryl protons maintained the same configuration; however, the broad resonance at 3.6 ppm resolved, characteristic of the Cl^- adduct of **1** (Figure E-6).*

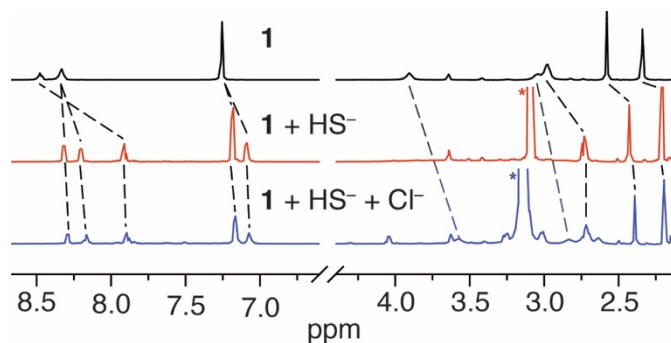
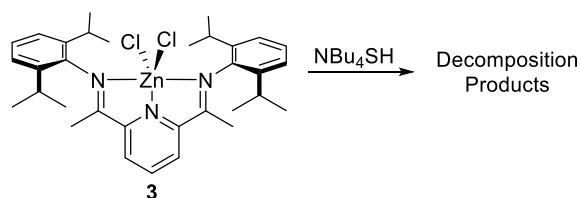


Figure VI-4. ^1H NMR spectrum of 10.3 mM **1** (black), upon addition of 1.5 equiv. of NBu_4SH (red) is characteristic for **2**. Addition of 20 equiv. of NBu_4Cl produces the spectrum characteristic of the Cl^- adduct.

To further determine whether the internal hydrogen-bond was necessary for stabilization of the zinc-sulfido product, we also titrated a Zn-pyridinediimine compound which does not possess the pendant amine hydrogen-bond acceptor (Scheme VI-2). Upon addition of 0.5 equiv. of HS^- to a solution of $\text{Zn}(\text{}^i\text{PrPDI})\text{Cl}_2$ (**3**) (${}^i\text{PrPDI}$ = 2,6-(2,6- ${}^i\text{Pr}_2\text{C}_6\text{H}_3\text{N}=\text{CMe})_2\text{C}_5\text{H}_3\text{N}$) a white precipitate (ZnS) was immediately observed, along with a significant change in the NMR spectrum. The shifts in the NMR spectrum and formation of precipitate continued until 1 equiv. of HS^- was added, after which no more changes were observed (Figure E-11). The resultant solid was isolated, washed with acetonitrile to remove any excess free sulfide, then acidified and subjected to the

* Given the number of equivalents required for the displacement of hydrosulfide by chloride, we estimate the binding constant of hydrosulfide to be of a similar magnitude, and no larger than 10 times greater than that of chloride. See Figure E-3.

methylene blue assay, which provided a positive response for acid-labile sulfur and was consistent with ZnS formation.²¹⁹ These data illustrate the importance of the hydrogen-bond acceptor in the stabilization of the zinc-sulfido complex, as the pendant amine in **1** is vital in this system.



Scheme VI-2. Reaction of **3** with NBU₄SH shows decomposition, demonstrating the importance of the H-bond acceptor in **2**.

Conclusion

In conclusion, we have shown the stabilization of a rare synthetic zinc hydrosulfide complex stabilized by a hydrogen bond accepting ligand. Removal of the hydrogen bonding ability of the ligand resulted in decomposition and ZnS precipitation, highlighting the importance of the second coordination sphere in stabilizing the zinc hydrosulfido adduct.

Bridge

In this chapter, we established the necessity of hydrogen bonding in the stabilization of metal-sulfido complexes. Given the high importance of hydrogen bonds in metal complexes, we began to think of how other systems in which the stabilization of H₂S or HS⁻ via hydrogen bonding would be beneficial. This investigation led to supramolecular anion binding, or the non-covalent interaction of anions with synthetic scaffolds in solution. Supramolecular scaffolds help researchers understand anion-binding environments in biology, while also providing new real-time detection methods

that do not consume the target analyte. To explore the supramolecular chemistry of H₂S and HS⁻, we describe a collaboration with the Johnson and Haley groups at the University of Oregon using their bis(ethynylaniline) anion-binding receptors in Chapter VII.

Experimental

General considerations.

All manipulations were performed under an inert atmosphere using standard Schlenk techniques or an Innovative Atmospheres N₂-filled glove box unless otherwise noted. Tetrabutylammonium chloride and butane thiol were purchased from TCI Chemicals and used without purification. 1,3,5-Trimethoxybenzene was purchased from Sigma Aldrich and used without further purification. Sodium hydride was purchased from TCI chemicals, taken into a dry glove box and washed several times with hexanes before use. Tetrabutylammonium hydrosulfide (NBu₄SH) was prepared as described in the literature.⁴⁴ *Note:* Hydrogen sulfide and its salts are highly toxic and should be handled carefully to avoid exposure. Zn(didpa)Cl₂ and Zn(ⁱPrPDI)Cl₂ were prepared according to reported methods.^{208,220} Spectroscopic grade acetonitrile and dichloromethane were degassed by sparging with argon followed by passage through a Pure Process Technologies solvent purification system to remove water and stored over 4 Å molecular sieves in an inert atmosphere glove box. Acetonitrile-*d*₃ and dichloromethane-*d*₂ were purchased from Cambridge Isotope laboratories and distilled from calcium hydride, deoxygenated by three freeze-pump-thaw cycles, and stored in an inert atmosphere glove box. Zn(didpa)Cl₂ and NBu₄SH stock solutions were prepared in dry acetonitrile and stored in an inert atmosphere glove box until immediately prior to

use. Concentrations of $\text{Zn}(\text{didpa})\text{Cl}_2$ were corrected to account for uncoordinated $\text{Zn}(\text{II})$ as determined by titration with N,N,N',N' -tetrakis(2-pyridylmethyl)ethylenediamine (TPEN), *vide infra*. Dichloromethane stock solutions of NBu_4SH were always prepared immediately prior to use.

Spectroscopic Methods.

UV-Vis measurements were acquired on an Agilent Cary 100 UV-Vis spectrophotometer equipped with a QNW dual cuvette temperature controller at $25.00 \pm 0.05^\circ\text{C}$. All spectroscopic samples were prepared under an inert atmosphere in septum-sealed cuvettes obtained from Starna Scientific. NMR spectra were acquired on a Bruker Avance-III-HD 600 spectrometer with a Prodigy multinuclear broadband cryoProbe or Varian INOVA 500 MHz spectrometer at 25.0°C unless otherwise indicated. Chemical shifts are reported in parts per million (δ) and are referenced to the residual solvent resonances.

UV-Vis Titrations.

In a glove box, $\text{Zn}(\text{didpa})\text{Cl}_2$ stock solutions were diluted to the desired concentration by addition to a 3.0 mL of solvent in a septum-sealed cuvette and removed from the glove box. NBu_4SH stock solutions were prepared approximately 10^5 times more concentrated than the Zn solution to provide minimal dilution during addition, and were added to the septum-sealed cuvettes by gas-tight syringe. Sodium butane thiolate solutions were prepared immediately prior to use by injecting butane thiol into a suspension of sodium hydride in acetonitrile. After shaking and a cessation of bubbling, the suspension was allowed to settle before aliquots were removed from the supernatant.

Control experiments of sodium hydride suspensions and butane thiol solutions were conducted as well, and showed no reactivity.

NMR experiments.

In a glove box, a 10 mM Zn(didpa)Cl₂ solution was prepared in either acetonitrile-*d*₃ or dichloromethane-*d*₂ and added to a septum-capped NMR tube. Stock solutions of NBu₄SH (~0.5 M in acetonitrile-*d*₃) were prepared. Aliquots of the NBu₄SH stock solutions were added to the NMR tube by gas-tight syringe.

Determination of excess Zinc in Zn(didpa)Cl₂.

Stock solutions of *N,N,N',N'*-tetrakis(2-pyridylmethyl)ethylenediamine (TPEN) and Zn(didpa)Cl₂ were prepared in CD₃CN, with each stock solution containing 50.5 mM 1,3,5-trimethoxybenzene as an internal standard. Two equivalents of TPEN from the stock solution were added to the Zn(didpa)Cl₂ solution, and the spectrum was measured. Integration of the signals corresponding to free TPEN and Zn(TPEN) against the internal standard established that 6.0% free zinc was present, which is due to small excess of zinc being present regardless of purification method.

CHAPTER VII

A SYNTHETIC SUPRAMOLECULAR RECEPTOR FOR HYDROSULFIDE ANION

Published as Hartle, M. D; Hansen R. J; Tresca, B. W; Prakel, S. S; Zakharov, L. N; Haley, M. M; Pluth, M. D; Johnson, D. W. “A Synthetic Supramolecular Receptor for Hydrosulfide Anion” *Angewandte Chemie International Edition* **2016** 55(38) 11480-11484. Experimental work completed by either me, S. S. Prakel under my direction, or R. J. Hansen. Computational work completed by B. W. Tresca. Crystallographic data provided by L. N. Zakharov. Written primarily by me and R. J. Hansen with editorial assistance from B. W. Tresca, M. M. Haley, M. D. Pluth, and D. W. Johnson. Associated content can be found in Appendix F.

Preface

Hydrogen sulfide (H₂S) has emerged as a crucial biomolecule in physiology and cellular signaling. Key challenges associated with developing new chemical tools for understanding the biological roles of H₂S include developing platforms that enable reversible binding of this important biomolecule. Here we report the first synthetic small molecule receptor for hydrosulfide anion, HS⁻, solely utilizing reversible, hydrogen-bonding interactions in a series of bis(ethynylaniline) derivatives. Binding constants up to 90,300 ± 8700 M⁻¹ were obtained. The fundamental science of reversible sulfide binding—in this case featuring a key CH···S hydrogen bond—will expand the possibility for discovery of sulfide protein targets and molecular recognition agents.

Introduction

Supramolecular hosts have been developed to selectively bind a variety of anionic species in solution, ranging from inorganic phosphates and phosphorylated biomolecules,

to halides, to other anions of environmental and/or biological relevance.²²¹⁻²²⁶ These synthetic supramolecular receptors use reversible, mostly non-covalent interactions to select anions based on factors such as their basicity, shape/charge, softness/hardness, position on the Hofmeister series, hydrophobic/solvophobic effects, among others. Notably lacking in the anion binding literature are efforts to target hydrosulfide (HS^-), the smallest monoanionic sulfur species, which has recently gained interest as an important biomolecule. We report here the first examples of synthetic receptors that reversibly bind HS^- using solely hydrogen bonding interactions. Importantly, a critical $\text{CH}\cdots\text{S}$ hydrogen bond is key to the strong binding of hydrosulfide, lending support to the hypothesis that appropriately polarized CH hydrogen bond donors^{106,226-231} can target softer anions.^{225,232}

Hydrogen sulfide (H_2S) plays diverse roles in the global sulfur cycle and has recently been implicated as an important biologically-relevant signaling molecule.¹ In the last decade, H_2S (and its more prevalent HS^- conjugate base form under biological conditions) has emerged as the third endogenously produced gasotransmitter, along with CO and NO. H_2S is now implicated in diverse (patho)physiological functions in the cardiovascular, immune, gastrointestinal, as well as other systems, making its absence in the supramolecular chemistry of anions even more surprising.^{3,17,233-235} In parallel to the biological advances in H_2S research, chemical tools for detecting and imaging H_2S are rapidly emerging and form a cornerstone of the investigative approaches used to study this critical biomolecule.^{3,236} Despite this importance, current detection methods are plagued by irreversibility, which presents a significant problem in developing chemical tools that provide real-time information on biological processes, suggesting a

supramolecular (i.e., reversible) approach to HS^- binding would represent an important contribution.

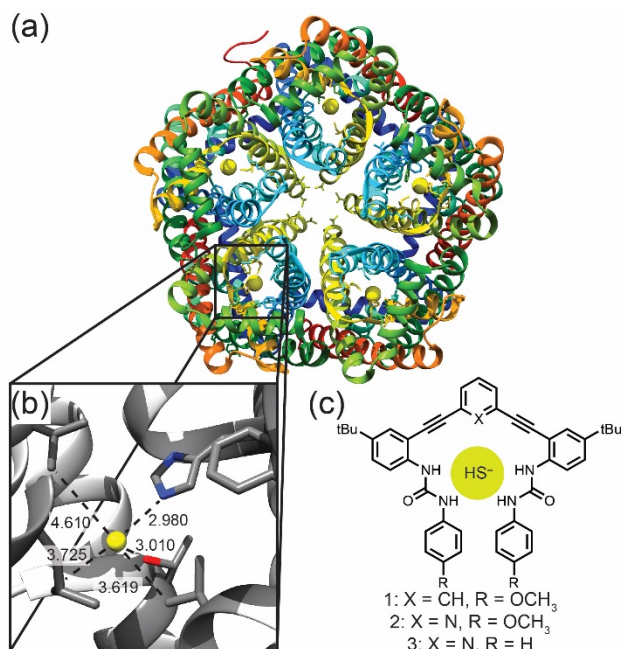


Figure VII-1. (a) Protein structure of HSC (PDB:3TDX) showing five individual channels with the bound anion represented as a yellow sphere. (b) Enlargement of the binding pocket showing short contacts to His (2.980 Å), Thr (3.010 Å), Leu (3.725 Å) and Val (3.619 and 4.610 Å). Non-interacting helices are excluded for clarity. (c) Synthetic receptors **1-3**.

Complicating biological H_2S investigations, the $\text{p}K_a$ of H_2S (7.0) ensures that both the neutral (H_2S) and monoanionic (HS^-) forms are present under physiological conditions, leading to significant and unresolved questions on the specific chemistry and recognition events associated with the individual protonation states. Heightening this dichotomy, HS^- was recently identified to be a viable substrate for $\text{Cl}^-/\text{HCO}_3^-$ anion exchange proteins,²³⁷ and a bacterial ion channel for HS^- transport was recently identified (Figure VII-1a-b).⁶⁴ Importantly, the recognition events in sulfide transport in these systems rely on non-covalent, reversible interactions with HS^- rather than metal

coordination or interaction with the sulfane-sulfur pool. Taken together, these examples suggest that HS^- , which has until now been almost entirely overlooked, needs to be included in the complex landscape of biologically-relevant anions, such as Cl^- , HCO_3^- , I^- , and NO_2^- . Despite the emerging importance of sulfide, HS^- has only appeared in anion screening sporadically, and we are unaware of any synthetic receptors able to bind H_2S or HS^- reversibly through well-defined non-covalent interactions.^{103,222,238-240} Systems that could bind H_2S or HS^- selectively through reversible interactions would not only provide significant insights into potential HS^- binding environments in biological contexts, but also provide new strategies for developing reversible and real-time H_2S detection methods.

To approach this challenge, we reasoned that synthetic anion receptors could provide a viable platform to develop reversible HS^- binding systems. To optimize selective binding for hydrosulfide, we initially assumed the ideal receptor should feature hydrogen bond donors to target the anionic portion of hydrosulfide and a hydrogen bond acceptor (or suitable pocket of electron density) to accommodate the slightly acidic hydrogen atom. Aligned with these requirements, sulfide has a similar ionic radius to Cl^- ($\text{S}^{2-} = 1.84 \text{ \AA}$, $\text{Cl}^- = 1.81 \text{ \AA}$) and biological examples reveal that HS^- can fill similar roles as Cl^- .²⁴¹ This similarity has not yet been exploited in the synthetic supramolecular community to target HS^- , perhaps because of a prevailing assumption that Cl^- and HS^- should have quite different binding properties based on their different protonation states, nucleophilicities, hardness/softness, shape, pK_b (-8 vs 7, respectively) and resulting hydrogen bond accepting ability.

In this light we reinvestigated the bis(ethynylaniline) anion-binding receptors we have developed for Cl^- as a viable platform for non-covalent HS^- binding.²⁴²⁻²⁴³ These modular scaffolds bind anions through tunable urea NH hydrogen bonds, and the central core can be easily modified to incorporate an additional hydrogen bond donating arene (**1**) or a hydrogen bond accepting pyridine group (**2-3**).²³² The semi-preorganized binding pocket significantly reduces the entropic penalty for anion encapsulation, while maintaining flexibility to accommodate different anions. The ability to tune the urea hydrogen bond donors as well as the central core binding motif has resulted in a family of receptors that can selectively target a diverse range of analytes.^{233,244} In addition, recent work has suggested that CH hydrogen bond donors polarized by inductive electron withdrawing groups (e.g., the electronegative *sp*-hybridized alkyne carbon atoms in **1**) should exhibit selectivity for softer anions.²³² Although the place of HS^- on the Hofmeister series and HSAB theory tables is not clear, intuition suggests that hydrosulfide should be a softer anion than chloride. Motivated by these challenges, we report here the first examples of synthetic receptors that reversibly bind HS^- using solely supramolecular interactions (Figure VII-1c).

Results and Discussion

To investigate whether HS^- is a suitable guest for hosts **1-3**, we titrated $\text{NBu}_4\text{SH}^{44}$ into 0.5-1.0 mM solution of each host in 10% $\text{DMSO-}d_6/\text{CD}_3\text{CN}$ and monitored the titrations by ^1H NMR spectroscopy (Figure F-1). In each case, we observed that the urea NH resonances shifted significantly downfield upon HS^- addition, consistent with anion binding (Figure VII-2). For example, upon addition of HS^- to a solution of **1**, the aryl CH_a shifted from 7.99 to 9.24 ppm, and the NH_b and NH_c urea protons shifted downfield

from 7.94 and 8.92 to 8.63 and 11.18 ppm, respectively. Highlighting the preference of each receptor **1-3** for HS⁻ rather than H₂S, addition of H₂S gas to any of the receptors failed to change the UV-Vis or NMR spectra of the hosts. We also confirmed that the observed changes in the NMR spectra upon HS⁻ addition were not due to deprotonation of the urea NH groups. Addition of the strong base 1,8-diazabicyclo[5.4.0]undec-7-ene (DBU) produced significantly different UV-Vis and NMR spectra than those observed upon HS⁻ addition (Figure F-14). On the basis of the high nucleophilicity of HS⁻, we also confirmed that the anion did not irreversibly modify the alkyne moieties of the host scaffolds by monitoring the ¹³C{¹H} NMR spectrum of **1** before and after addition of 10 equivalents of HS⁻ (Figure F-13). Additionally, titration data of HS⁻ with the host fit to simple 1:1 binding isotherm models. Taken together, these results support the hypothesis that HS⁻ binds within the host pocket and does not covalently modify the host scaffold.

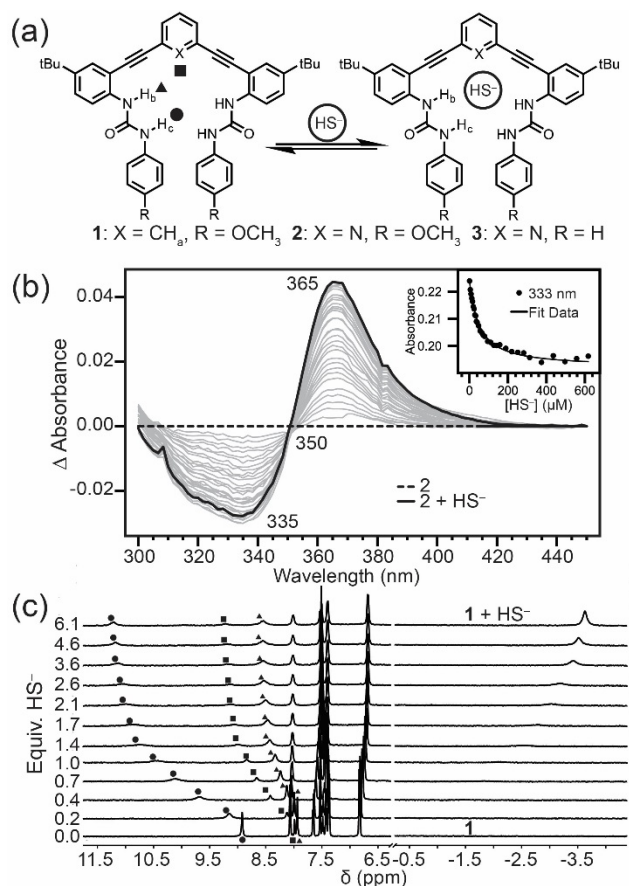


Figure VII-2. (a) Scheme showing HS^- host-guest equilibrium. (b) Representative UV-Vis difference titration of NBu_4SH with $10 \mu\text{M}$ **2** in CH_3CN and fit to a 1:1 binding isotherm (inset). (c) ^1H NMR spectra of a titration of 0.988 mM **1** with NBu_4SH in 10% $\text{DMSO-}d_6/\text{CD}_3\text{CN}$.

To determine whether receptors **1-3** exhibited selectivity for HS^- over similar anions, we performed comparison titrations with NBu_4Cl under identical conditions. We initially expected that pyridine-based hosts **2** and **3** would exhibit higher binding affinities for HS^- because of the hydrogen bond accepting pyridine core; however, titration data established hosts **2** and **3** had significantly lower binding constants for both anions than did phenyl core host **1**. This difference suggests that the extra CH hydrogen bond donated from the phenyl core is a key component in establishing the binding magnitude and selectivity. This result was contrary to our initial hypothesis that HS^-

should also act as a weak hydrogen bond donor to an acceptor on the host receptor (e.g., the pyridine nitrogen of **2** and **3**).²⁴⁵ Despite the lower binding affinities, the pyridine-based hosts **2** and **3** exhibited 6-fold selectivity for HS⁻ over Cl⁻, whereas host **1** exhibited 2.8-fold selectivity. The higher selectivity could be due to the putative N[⋯]HS⁻ hydrogen bond from the pyridine lone pair acting as a hydrogen bond acceptor, which provides an additional stabilizing interaction for HS⁻ and a destabilizing interaction for Cl⁻. The phenyl core of host **1** donates a hydrogen bond to both anionic guests, resulting in decreased selectivity for hydrosulfide, even if this CH hydrogen bond is an important component to the higher overall binding energy.

To further investigate the difference in anion selectivity, binding constants were also measured by UV-Vis spectroscopy in CH₃CN (Table VII-1). We expected that removal of the DMSO co-solvent would increase the observed binding affinities since acetonitrile is a slightly less competitive solvent (especially as a hydrogen bond acceptor). Addition of NBu₄SH to 10 μM solutions of **1**, **2**, or **3** resulted in attenuation of the 330 nm absorbance with concomitant increase at 360 nm, while proceeding through a well-anchored isosbestic point near 350 nm. As expected, removal of DMSO produced significantly higher binding affinities, with host **1** having a binding constant of 90,300 M⁻¹ and hosts **2** and **3** providing binding constants of ~25,000 M⁻¹. For **1**, the selectivity for HS⁻ over Cl⁻ remained similar to the 10% DMSO-*d*₆/CD₃CN system, whereas in the case of the pyridine core, a significant increase in selectivity is observed (~18.5:1 HS⁻:Cl⁻). The difference between the binding energy of HS⁻ with **1** and **2** is the same in both solvents ($\Delta\Delta G = 0.90$ kcal mol⁻¹), whereas the Cl⁻ binding energy exhibits a larger solvent dependence ($\Delta\Delta G = 1.24$ (DMSO/CH₃CN) vs. 1.83 (CH₃CN) kcal mol⁻¹). For

HS⁻, the $\Delta\Delta G$ is the difference between two stabilizing hydrogen bond motifs and leads to an estimate that a C–H \cdots S hydrogen bond is up to 0.90 kcal mol⁻¹ stronger than an S–H \cdots N hydrogen bond. The $\Delta\Delta G$ of Cl⁻ binding is larger because this represents the difference between a small repulsive N: \cdots Cl contact and an attractive C–H \cdots Cl hydrogen bond.

Table VII-1. HS⁻ and Cl⁻ Binding Parameters in Hosts **1-3**.

Host	Solvent	HS ⁻ (log(K_a)) ΔG (kcal mol ⁻¹)	Cl ⁻ (log(K_a)) ΔG (kcal mol ⁻¹)
1	10% DMSO- <i>d</i> ₆ /CD ₃ CN	3.70 ± 0.07 ^[a]	3.25 ± 0.03 ^[a]
		-5.05	-4.43
	CH ₃ CN	4.96 ± 0.04 ^[b]	4.53 ± 0.07 ^[b]
2	10% DMSO- <i>d</i> ₆ /CD ₃ CN	3.04 ± 0.06 ^[a]	2.34 ± 0.07 ^[a]
		-4.15	-3.19
	CH ₃ CN	4.30 ± 0.07 ^[b]	3.19 ± 0.07 ^[b]
3	10% DMSO- <i>d</i> ₆ /CD ₃ CN	3.12 ± 0.07 ^[a]	2.34 ± 0.02 ^[a]
		-4.25	-3.19
	CH ₃ CN	4.45 ± 0.07 ^[b]	3.08 ± 0.06 ^[b]
		-6.07	-4.20

^[a] Fitting NMR spectroscopic data. ^[b] Fitting UV-Vis spectroscopic data.

To further establish the reversibility of HS⁻ binding, we treated a solution of **1** in 10% DMSO-*d*₆/CD₃CN (Figure VII-3a) with two equivalents of NBu₄SH to form the HS⁻ bound adduct (Figure VII-3b), after which four equivalents of Zn(OAc)₂ were added. Addition of Zn(OAc)₂ rapidly resulted in precipitation of ZnS and regenerated the NMR spectrum corresponding to free **1** (Figure VII-3c). Further addition of five equivalents of NBu₄SH regenerated the HS⁻ host-guest complex, confirming reversible binding. Importantly, the ¹³C{¹H} resonances of the alkyne carbons did not shift significantly (Figure VII-3b, d), confirming that there was no covalent modification of the receptor scaffold.

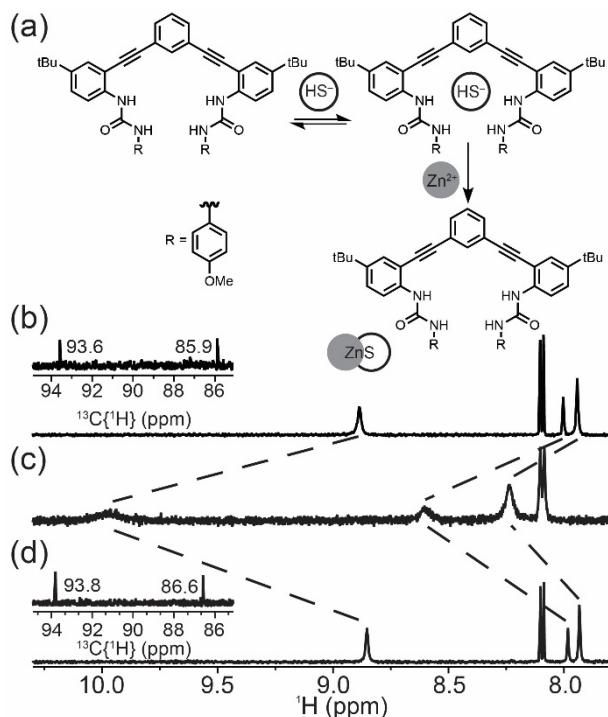


Figure VII-3. (a) Reversibility reaction scheme. (b) ^1H NMR spectrum of a 1.0 mM solution of **1** in 10% $\text{DMSO-}d_6/\text{CD}_3\text{CN}$. (c) Treatment with 2 equiv. of NBu_4SH . (d) Addition of 4 equiv. $\text{Zn}(\text{OAc})_2$. Each inset shows the $^{13}\text{C}\{^1\text{H}\}$ resonances corresponding to the alkyne region of **1**.

Single crystals of $[\mathbf{1}\cdot\text{HS}^-][\text{NBu}_4^+]$ were grown by layering *n*-hexanes onto an equimolar solution of **1** and NBu_4SH in THF in a glovebox. $[\mathbf{1}\cdot\text{HS}^-][\text{NBu}_4^+]$ crystallizes in the space group $Pna2_1$ with one molecule of THF per unit cell. Consistent with the solution NMR data, the HS^- occupies the binding pocket created by an aryl proton and four urea protons with the NBu_4^+ cation sitting just above the sulfide – phenyl core plane (Figure F-15). The structure shows five hydrogen bonds from the host to the bound sulfide guest. The $\text{C-H}\cdots\text{S}$ hydrogen bond (3.711 Å) is longer than those formed between the distal bis(urea) protons (3.277, 3.281 Å) (Figure VII-4a). The average of all five hydrogen bond distances from the host to the guest is 3.56 Å, and all fall within previously defined criteria for hydrogen bonds.^{228,246-248} The host conformation in $[\mathbf{1}\cdot\text{HS}^-]$ is remarkably similar to the previously published chloride-bound structure, with an

RMS distance between the two structures of only 0.184 Å (Figure F-16).²⁴⁵ These data demonstrate the similar recognition geometries required for Cl⁻ and HS⁻ binding, again highlighting the potential for HS⁻ to be a substrate for classical Cl⁻ binding domains in both native and synthetic systems.

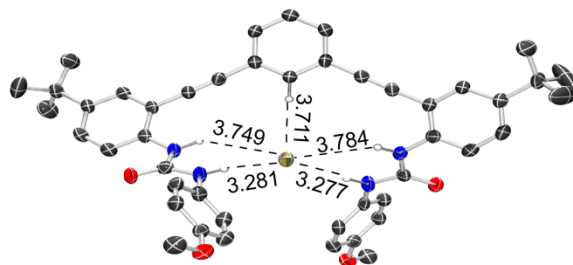


Figure VII-4. ORTEP representation showing selected hydrogen bond distances. Atoms are drawn at the 50% probability level. Hydrogens not interacting with the bound HS⁻ are removed for clarity.

Conclusion

In conclusion, we report a series of bis(ethynylaniline) derivatives capable of binding hydrosulfide anion with association constants as high as $90,300 \pm 8700 \text{ M}^{-1}$, representing the first reversible binding of the hydrosulfide anion in a synthetic receptor. ¹H NMR and UV-Vis spectroscopy both indicate stronger binding of hydrosulfide by the phenyl core receptor **1**; however, a greater selectivity for HS⁻ is observed in the pyridine cores (**2** and **3**). The preference for the phenyl core highlights the unexpected conclusion that a C–H···S contact is favored over an N···H–S contact by up to 0.9 kcal mol⁻¹. This difference may be related to the mechanisms that underlie anion binding selectivities beyond shape, size, and charge. Importantly, these results indicate that hydrogen bond polarizability and other aspects of hard/soft acid base theory are relevant to the characterization of anion selective host-guest systems. Additionally, these data suggest

that CH hydrogen bond donors are important components in targeting hydrosulfide reversibly. Taken in total, these experiments establish the reversible binding of HS⁻ to synthetic host molecules, and highlight that HS⁻ is an important, and thus far overlooked, biologically-important anion that can be targeted by synthetic molecular architectures. These studies also begin to establish the design rules for targeting hydrosulfide anion using such synthetic receptors. Moreover, we anticipate that the basic science of non-covalent sulfide binding to synthetic targets will help to identify new target proteins for sulfide binding, while also informing on new potential sulfide detection strategies that do not rely on the irreversible covalent modification of sensing platforms.

Summary

This final chapter culminates the entire work of the dissertation. After an overview of the currently available tools to study H₂S at the interface of chemistry and biology, chapter II began with an identification of the differential reactivity of HS⁻ and H₂S with metal centers. This led to chapter III, which reported a simple method to prepare tetrabutylammonium hydrosulfide (NBu₄SH) as an organic soluble salt for studies in organic aprotic solutions. With NBu₄SH in hand, chapter IV expanded the reaction of H₂S with metal centers in the protoporphyrin scaffold, showing three reaction pathways: no reaction, reduction, or binding. Chapter V expanded upon this by investigating the protected pocket stabilization hypothesis for sulfide transport in *L. Pectinata* by using the picket fence porphyrin. The picket fence identified that a protected binding pocket alone is insufficient for stabilizing binding. Chapter VI built upon the conclusion of chapter V by exploring the thermodynamic stabilization provided by hydrogen bond accepting motifs in the secondary coordination sphere of a zinc complex.

Chapter VII removed the metal center, and showed stabilization of HS⁻ by a completely synthetic organic receptor, modeling the hydrogen bonding interactions of a bacterial hydrosulfide transport protein.

Experimental

Materials and Methods.

All manipulations were performed under an inert atmosphere using standard Schlenk techniques or an Innovative Atmospheres N₂-filled glove box unless otherwise noted. Tetrabutylammonium chloride (NBu₄Cl) was purchased from Sigma-Aldrich, and tetrabutylammonium hydrosulfide (NBu₄SH) was prepared as described in the literature.⁴⁴ Spectroscopic grade MeCN was degassed by sparging with argon followed by passage through a Pure Process Technologies solvent purification system to remove water and stored over 4Å molecular sieves in an inert atmosphere glove box. CD₃CN and DMSO-*d*₆ were purchased from Cambridge Isotope laboratories, distilled from CaH₂, deoxygenated by three freeze-pump-thaw cycles, and stored in an inert atmosphere glove box.

Spectroscopic Methods.

UV-Vis measurements were acquired on an Agilent Cary 100 UV-Vis spectrophotometer equipped with a QNW dual cuvette temperature controller at 25.00 ± 0.05 °C. All spectroscopic samples were prepared under an inert atmosphere in septum-sealed cuvettes obtained from Starna Scientific. NMR spectra were acquired on a Bruker Avance-III-HD 600 spectrometer with a Prodigy multinuclear broadband cryoProbe at 25.0 °C or on a Varian 500 MHz spectrometer. Chemical shifts are reported in parts per

million (δ) and are referenced to residual solvent resonances (CD_3CN ^1H 1.94 ppm, $^{13}\text{C}\{^1\text{H}\}$ 118.26 ppm and $\text{DMSO-}d_6$ ^1H 2.50 ppm, $^{13}\text{C}\{^1\text{H}\}$ 39.52 ppm).

General procedure for UV-Vis titrations.

A septum-sealed cuvette was charged with a 10 μM solution of the desired host in MeCN. A second reference cuvette was also prepared with the same volume of MeCN, and a stock solution of NBu_4SH was prepared in a septum-sealed vial. NBu_4SH was added to both the reference and sample cuvette via gas-tight syringe, and the spectrum was recorded after each addition. All spectra were corrected for dilution and fit to a 1:1 model using the Thordarson method.^{139,153}

General procedure for NMR titrations.

In an N_2 -filled glove box, a stock solution of 1-3 in 10% $\text{DMSO-}d_6/\text{CD}_3\text{CN}$ (3 ml) was prepared and used to prepare an NBu_4SH stock solution (2.4 ml). The remaining host stock solution (0.6 ml) was added to a septum-sealed NMR tube using a Hamilton gas-tight syringe. Spectra were recorded after each addition of NBu_4SH , and the $\Delta\delta$ of urea proton Hc was used to follow the progress of the titration. Association constants were determined using a 1:1 model with the Thordarson method.^{139,153}

X-ray crystallography.

Diffraction intensities for 1 were collected at 173 K on a Bruker Apex2 CCD diffractometer using $\text{CuK}\alpha$ radiation ($\lambda = 1.54178 \text{ \AA}$). The space group was determined based on systematic absences and the absorption correction was applied by SADABS.¹¹⁴ The structure was solved by direct methods and Fourier techniques and refined on F2 using full matrix least-squares procedures. All non-H atoms were refined with anisotropic thermal parameters. All H atoms were treated in calculated positions except five H atoms

at the C and N atoms involved in C–H···S and N–H···S hydrogen bonds, which were located from the residual density map and refined with isotropic thermal parameters. The hydrogen atom in the HS[−] anion was not located, but the residual density map contains a peak with orientation opposite to the C–H···S hydrogen bond, which appears to be the HS[−] hydrogen. Structural refinement without any restrictions on the S–H fragment did not provide a stable position for this hydrogen atom, suggesting that it may be disordered over several positions. The structure was determined in non-centrosymmetric space group symmetry, and the value of Flack parameter, 0.59(3), shows that the sample is a racemic twin. All calculations were performed by the Bruker SHELXL-2013 package.²⁴⁹

CCDC 1472308 contains the supplementary crystallographic data. These data can be obtained free of charge from The Cambridge Crystallographic Data Centre via www.ccdc.cam.ac.uk/data_request/cif.

APPENDIX A

SUPPORTING INFORMATION: CHEMICALLY REVERSIBLE REACTIONS OF HYDROGEN SULFIDE WITH METAL PHTHALOCYANINES

Contents

Titration of CoPc with [NBu ₄][BH ₄].....	121
Job Plots.....	121
¹ H NMR spectra for ZnPc.....	123
¹ H NMR spectra for CoPc.....	126

Titration of CoPc with $[\text{NBu}_4][\text{BH}_4]$.

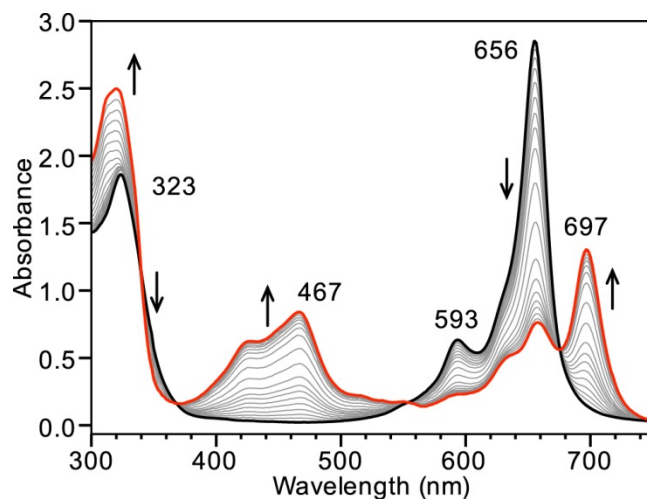


Figure A-1. UV-vis titration data of 3.0 mL of 10 μM CoPc with 2.8 mM $[\text{NBu}_4][\text{BH}_4]$ in 5.9 μL aliquots in THF showing reduction of CoPc to $[\text{CoPc}]^-$. The band at 320 nm observed in the $[\text{NBu}_4][\text{BH}_4]$ titration is consistent with formation of borane-THF complex.

Job Plots

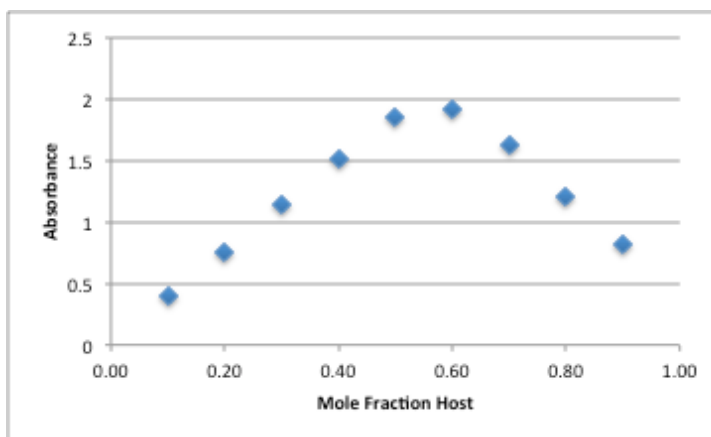
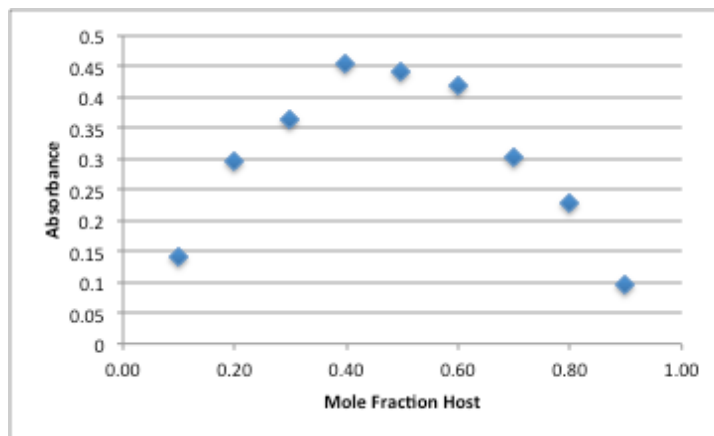


Figure A-2. Job plot of ZnPc and NaSH in 1:1 THF:DMSO following the absorbance at 426 nm.

Table A-1. Parameters for ZnPc Job Plot in 1:1 THF:DMSO.

Host (μL)	2700	2400	2100	1800	1500	1200	900	600	300
Host Concentration (M)	1.65E-04	1.47E-04	1.28E-04	1.10E-04	9.17E-05	7.34E-05	5.50E-05	3.67E-05	1.83E-05
Guest (μL)	300	600	900	1200	1500	1800	2100	2400	2700
Guest Concentration (M)	1.83E-05	3.66E-05	5.49E-05	7.32E-05	9.16E-05	1.10E-04	1.28E-04	1.46E-04	1.65E-04
Mol fraction of Host	0.90	0.80	0.70	0.60	0.50	0.40	0.30	0.20	0.10
Total Concentration	1.83E-04	1.83E-04	1.83E-04	1.83E-04	1.83E-04	1.83E-04	1.83E-04	1.83E-04	1.83E-04

**Figure A-3.** Job plot of CoPc and NaSH in 1:1 THF:DMSO following the absorbance at 467 nm.**Table A-2.** Parameters for CoPc Job Plot in 1:1 THF:DMSO.

Host (μL)	2700	2400	2100	1800	1500	1200	900	600	300
Host Concentration (M)	3.46E-05	3.08E-05	2.69E-05	2.31E-05	1.92E-05	1.54E-05	1.15E-05	7.70E-06	3.85E-06
Guest (μL)	300	600	900	1200	1500	1800	2100	2400	2700
Guest Concentration (M)	3.88E-06	7.76E-06	1.16E-05	1.55E-05	1.94E-05	2.33E-05	2.72E-05	3.10E-05	3.49E-05
Mol fraction of Host	0.90	0.80	0.70	0.60	0.50	0.40	0.30	0.20	0.10
Total Concentration	3.85E-05	3.86E-05	3.86E-05	3.86E-05	3.86E-05	3.87E-05	3.87E-05	3.87E-05	3.88E-05

^1H NMR spectra for ZnPc

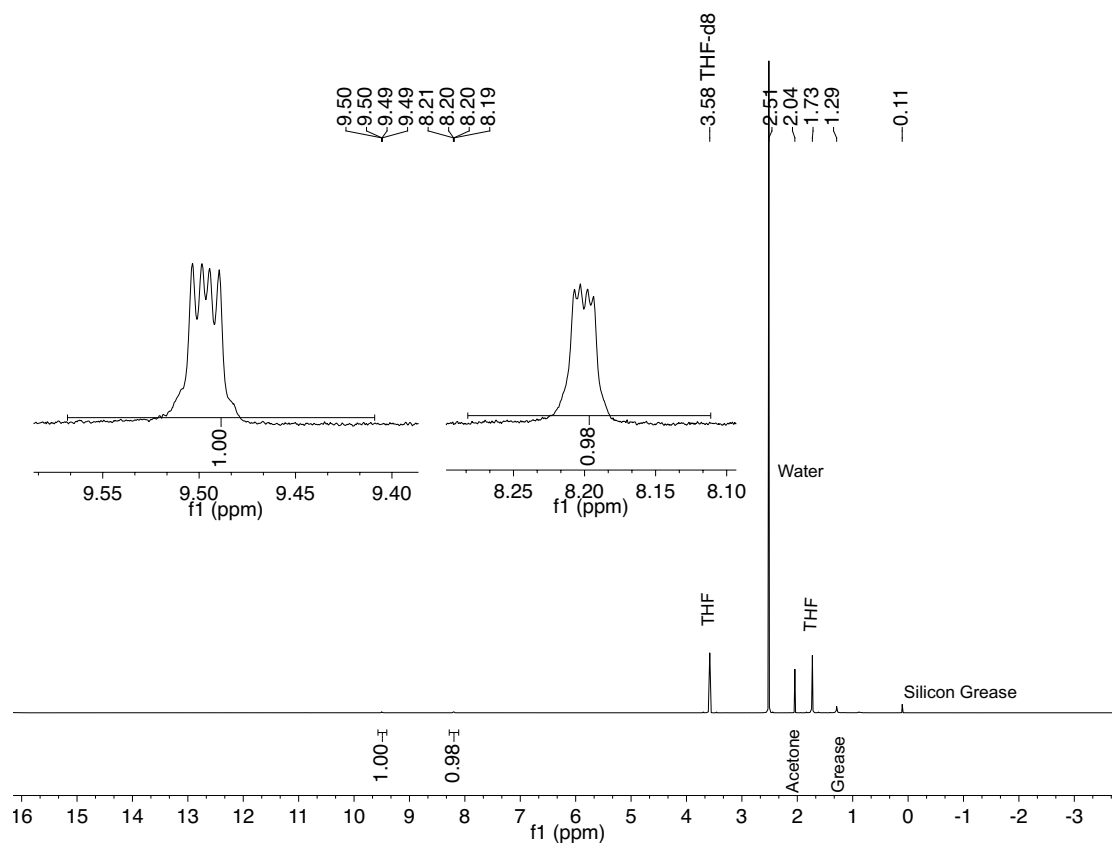


Figure A-4. ^1H NMR spectrum of ZnPc in $\text{THF-}d_8$.

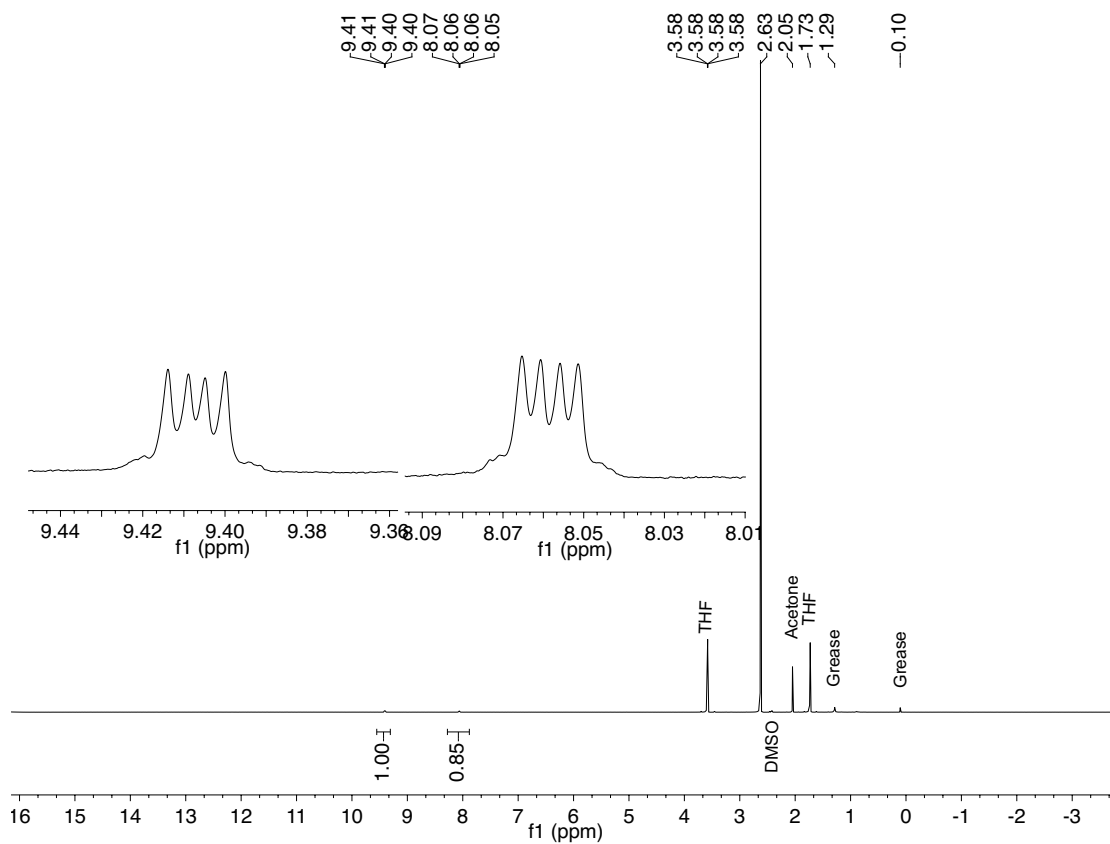


Figure A-5. ^1H NMR spectrum of ZnPc in THF- d_8 with 2 equiv. of NaSH in DMSO- d_6 .

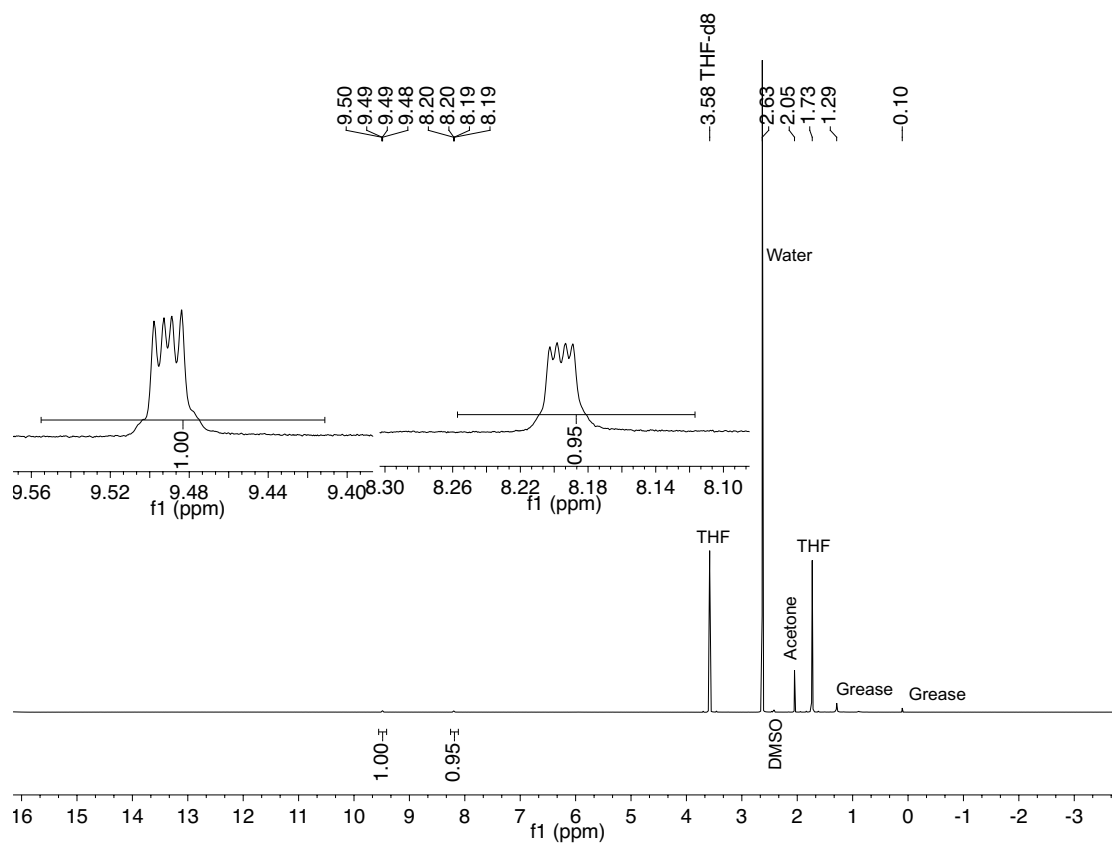


Figure A-6. ^1H NMR spectrum of ZnPc in THF- d_8 with 2 equiv. of KOH in DMSO- d_6 .

^1H NMR spectra for CoPc

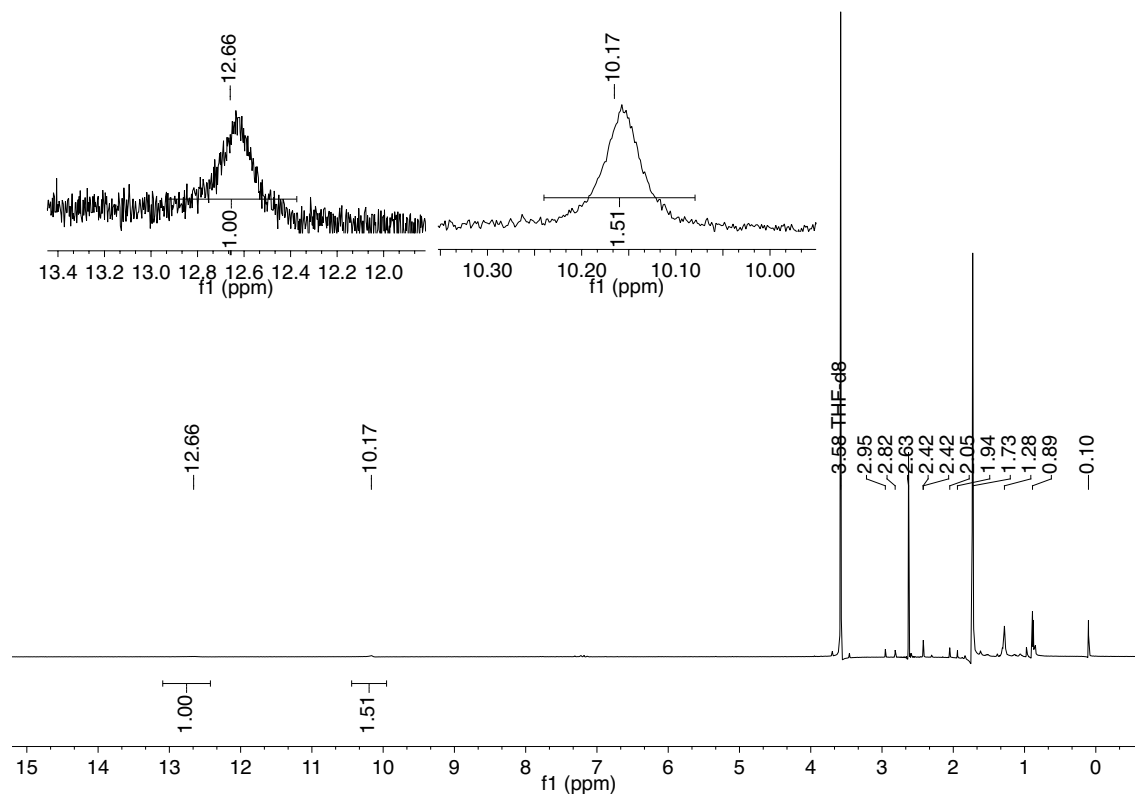


Figure A-7. ^1H NMR spectrum of 0.136 mM CoPc in 750 μL of $\text{THF-}d_8$ with 40 μL of added $\text{DMSO-}d_6$.

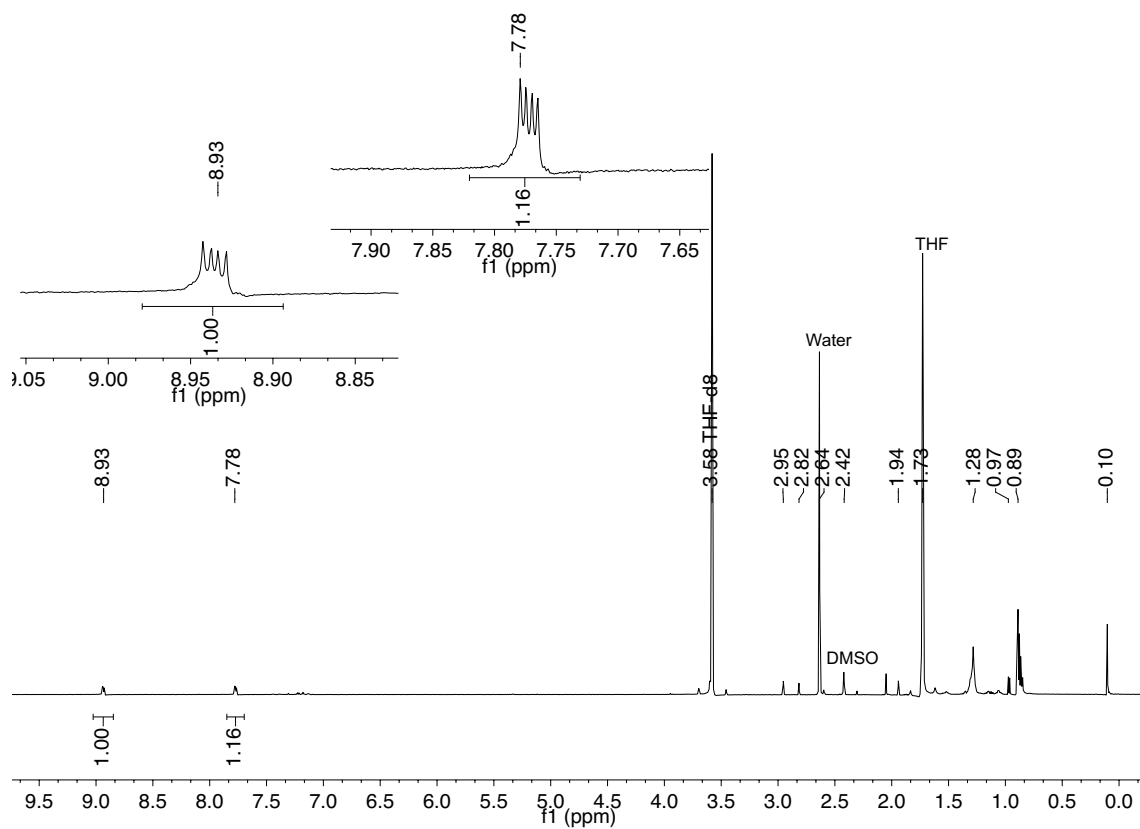


Figure A-8. ^1H NMR spectrum of 0.136 mM $[\text{Co}(\text{I})\text{Pc}]^-$ in 750 μL of $\text{THF-}d_8$ with 40 μL of 22.6 mM NaSH (8.8 equiv.) in $\text{DMSO-}d_6$ added. The change in the Pc resonances from a broad singlet to well defined peaks is consistent with a change from paramagnetic $\text{Co}(\text{II})$ to diamagnetic $\text{Co}(\text{I})$.

APPENDIX B

SUPPORTING INFORMATION: TETRABUTYLAMMONIUM HYDROSULFIDE PROVIDES A CONVENIENT SOURCE OF HS⁻ SOLUBLE IN ORGANIC SOLUTION FOR H₂S AND ANION-BINDING RESEARCH

Contents

NMR Spectroscopic Data	129
IR Spectroscopic Data.....	132
X-Ray crystallographic data	133

NMR Spectroscopic Data

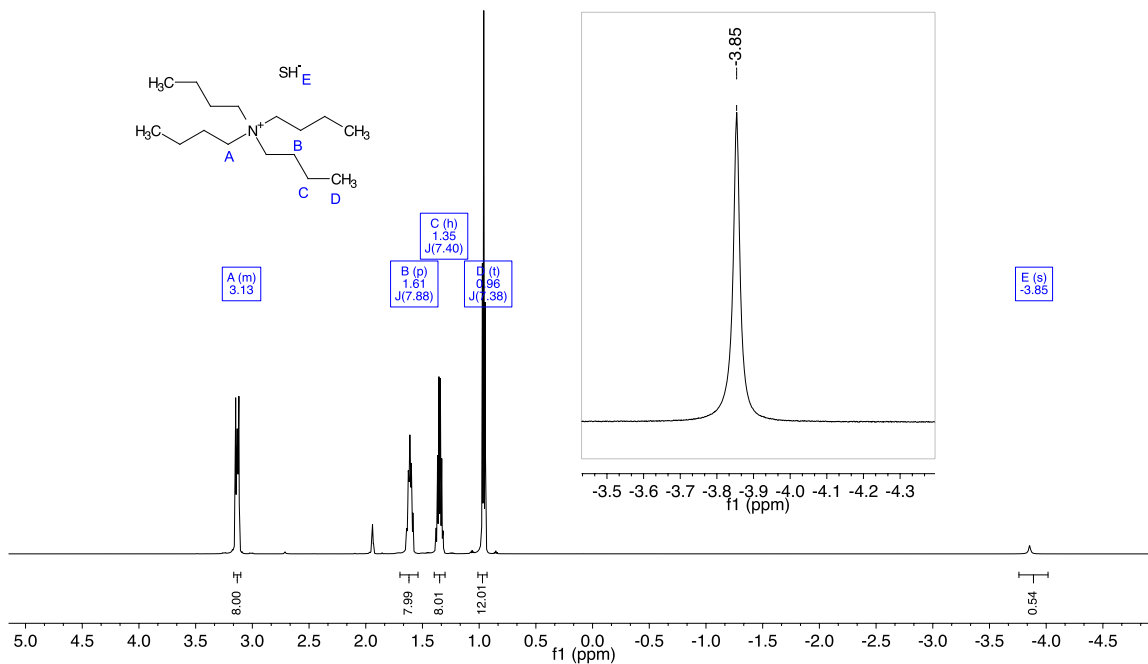


Figure B-1 ¹H (600 MHz, CD₃CN) NMR spectrum of NBu₄SH.

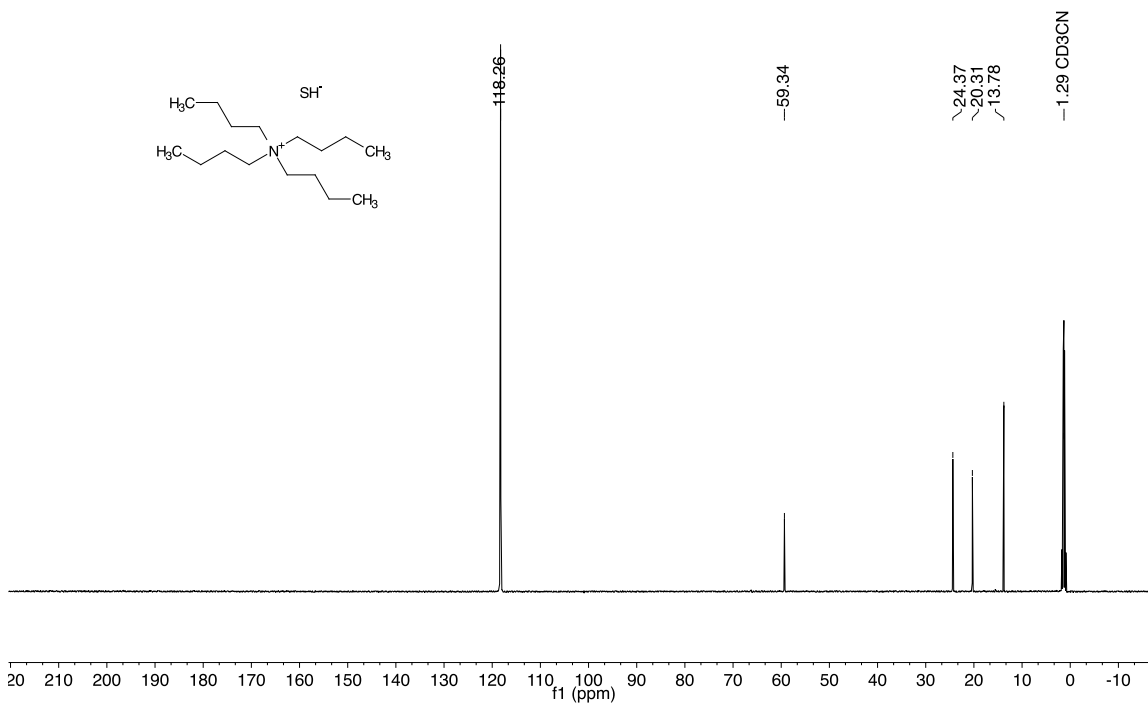


Figure B-2. ¹³C{¹H} (151 MHz, CD₃CN) NMR spectrum of NBu₄SH.

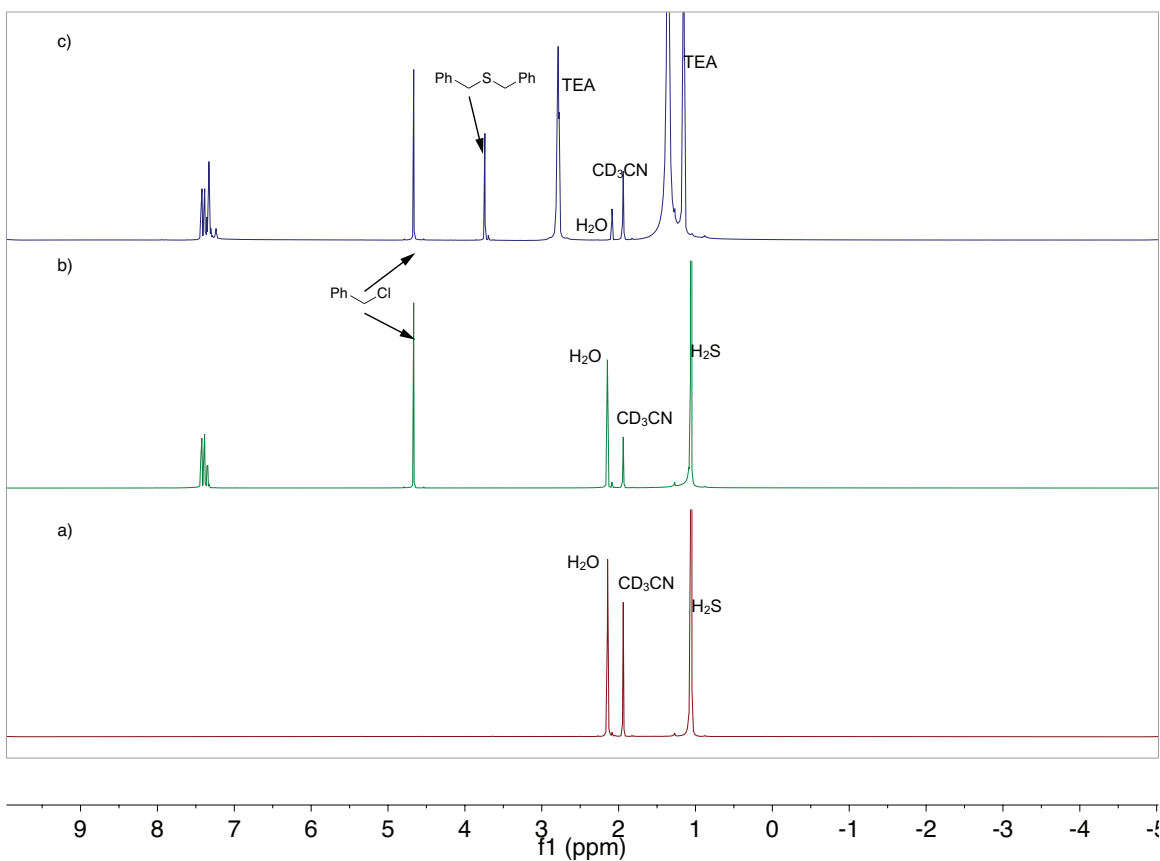


Figure B-3. ^1H NMR spectra demonstrating that H_2S is not sufficiently nucleophilic to react with BnCl . Only upon deprotonation to form HS^- does nucleophilic attack on BnCl occur. a) A saturated solution of H_2S gas in CD_3CN . b) Addition of BnCl does not result in any reaction. c) Addition of NET_3 (TEA) to deprotonated H_2S generates HS^- , which is quickly trapped by BnCl to form Bn_2S .

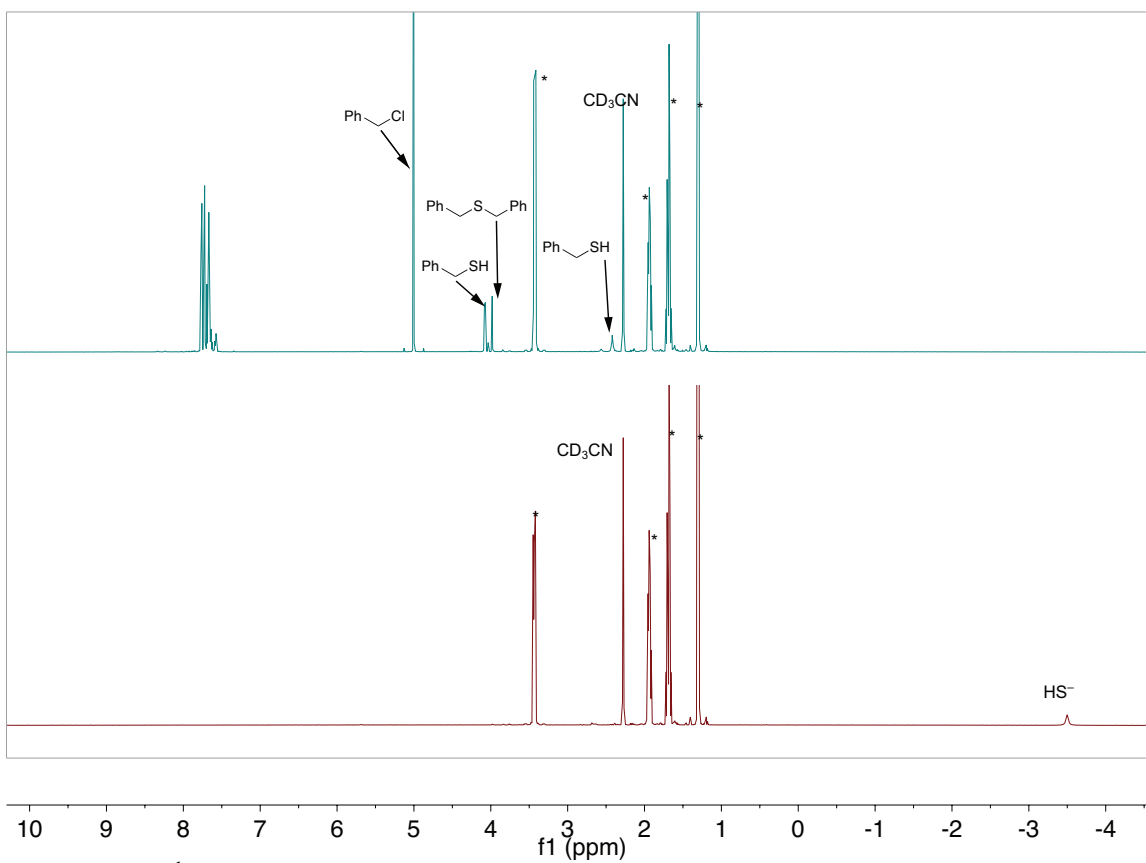


Figure B-4. ¹H NMR spectrum of the reaction of NBu₄SH with BnCl to form Bn₂S and BnSH. Unlike in Figure B-3, no added base is required for this reaction to occur. Bottom: NBu₄SH in CD₃CN. Top: Addition of 3 equiv. of BnCl.

IR Spectroscopic Data

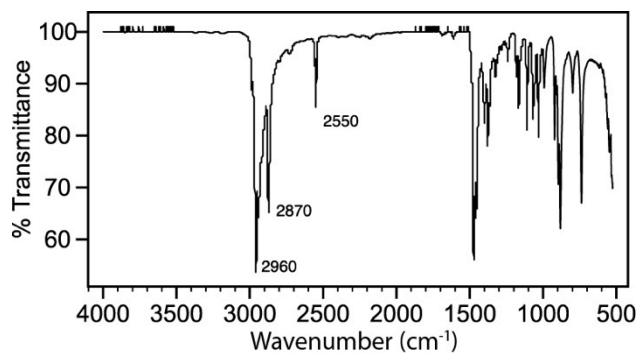


Figure B-5. FTIR (ATR, neat) spectrum of NBu₄SH.

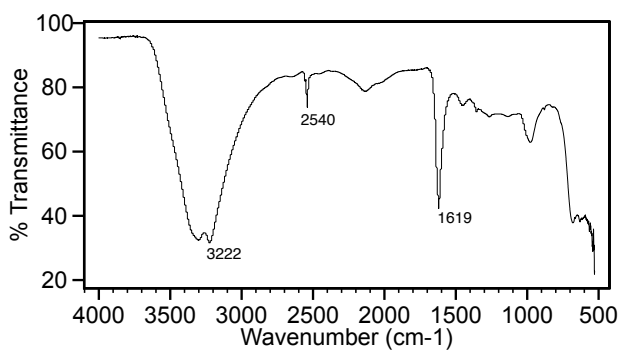


Figure B-6. FTIR (ATR, neat) spectrum of NaSH.

X-Ray crystallographic data

Table B-1. Crystal data and structure refinement for NBu₄SH.

	NBu ₄ SH
Empirical formula	C _{19.50} H ₄₁ NS [C ₁₆ H ₃₆ N] ⁺ [SH] ⁻ (C ₇ H ₈) _{0.5}
Formula weight	321.59
Wavelength (Å)	1.54178
Crystal size (mm)	0.14 x 0.13 x 0.04
Temperature (K)	173 K
Crystal system, space group	Monoclinic, C2/c
Unit cell dimensions (Å)	a = 22.043(10) b = 14.9292(7) c = 14.8080(6) β = 118.618(3)°
Volume (Å ³)	4277.7(3)
Z	8
Calculated density (Mg/m ³)	0.999
μ (mm ⁻¹)	1.295
F(000)	1448
2θ _{max}	135.36°
Reflections collected	14231
Independent reflections	3729
R _{int}	0.0489
[I > 2σ(I)]	
R1	0.0741
wR2	0.2044
GOF	1.053
	3729 reflections
	163 parameters
R1	0.934
wR2	0.2180
GOF	1.053
	All reflections
Residual electron density (e/Å ³) Max	Max = 0.565
	Min = -0.330

APPENDIX C

SUPPORTING INFORMATION: SPECTROSCOPIC INVESTIGATION OF THE REACTION OF METALLO-PROTOPORPHYRINS WITH HYDROGEN SULFIDE

Contents

Summary of Results	135
Additional UV-Vis spectroscopy experiments of Zn ^{II} PPIX	135
Additional UV-Vis spectroscopy experiments of Cr ^{III} (PPIX)Cl	138
Additional UV-Vis spectroscopy experiments of Sn ^{IV} PPIX	139
Additional UV-Vis spectroscopy experiments of Mn ^{II/III} PPIX	141
Additional EPR Spectra and simulation parameters	144
Cr ^{III} PPIX	144
Fitting parameters for Mn ^{III} PPIX	145
Fitting parameters for Mn ^{II} PPIX	145

Summary of Results

Table C-1. Summary of Results.

Metal	Sulfide			Reversibility			Control experiments						
	HS ⁻	Log(<i>K_a</i>)	HS ⁻ S ₈ H ₂ S	AcOH	O ₂	Dilute	AcOH	AcO ⁻	O ₂	Dilute	DBU ^a	DCHA ^b	Cp ₂ Co
Zn	Bind	4.24 ± 0.02	None None	Yes	Yes	Yes	None	Bind	None	None	Bind	Bind	None
Cr	Bind	3.92 ± 0.02	None None	Yes	Yes	No	None	None	None	None	None	None	None
Sn	Bind	— ^c	None None	Yes ^d	No	No	None	Bind	None	None	Bind	Bind	None
Mn ^{II}	Bind	4.36 ± 0.04	None Bind	Yes	Mn ^{III}	No	None	Bind	Mn ^{III}	None	Bind	Bind	None

^a1,8-Diazabicyclo[5.4.0]undec-7-ene ^bdicyclohexylamine ^cUnable to obtain. ^dReverts to the Sn-SH₂spectrum.

Additional UV-Vis spectroscopy experiments of Zn^{II}PPIX

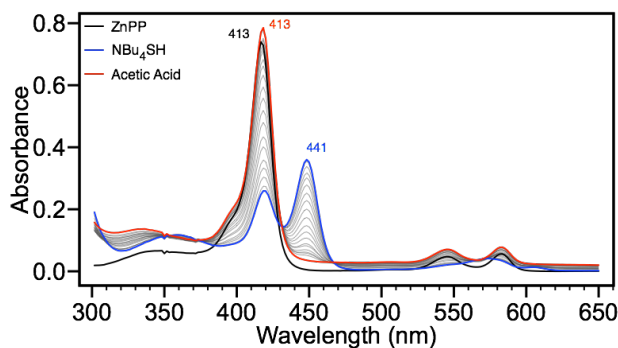


Figure C-1. Titration of ZnPPIX (1.8 μM) with NBu₄SH (30 equiv.) followed by titration with AcOH (30 equiv.) in THF.

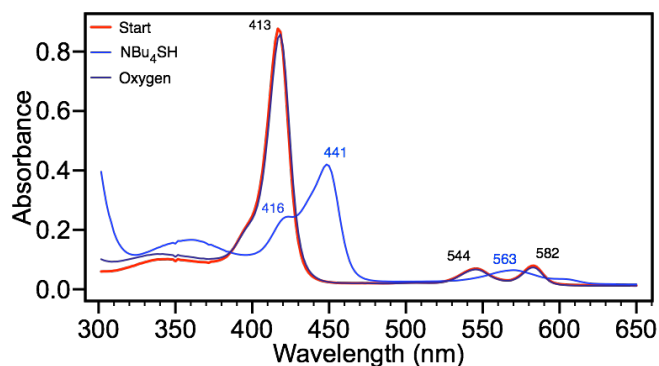


Figure C-2. Treatment of ZnPPIX (2.4 μM, black) with NBu₄SH (80 equiv., blue) followed by exposure to the atmosphere for 15 minutes (purple) in THF.

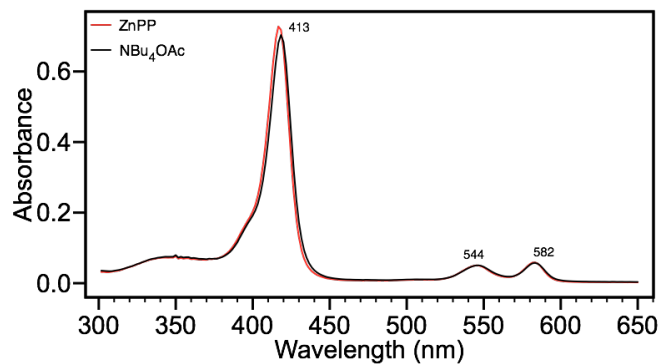


Figure C-3. Treatment of ZnPPIX (2.3 μM) with NBu₄OAc (20 equiv.) in THF.

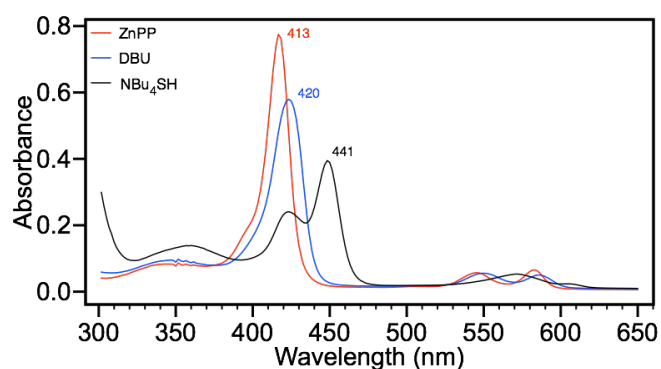


Figure C-4. Treatment of ZnPPIX (2.5 μM) with DBU (890 equiv.) followed by NBu₄SH (30 equiv.) in THF.

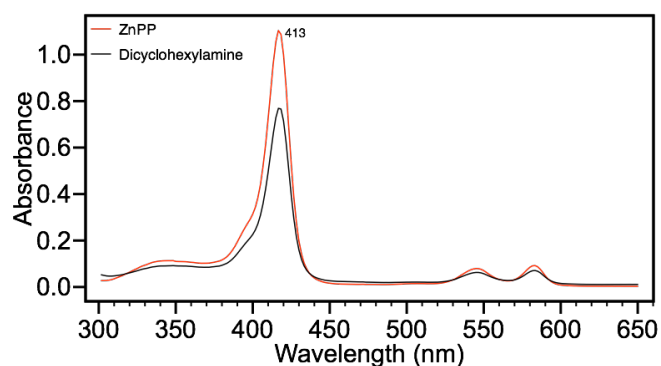


Figure C-5. Treatment of ZnPPIX (2.6 μM) with dicyclohexylamine (4.5 equiv.) in THF.

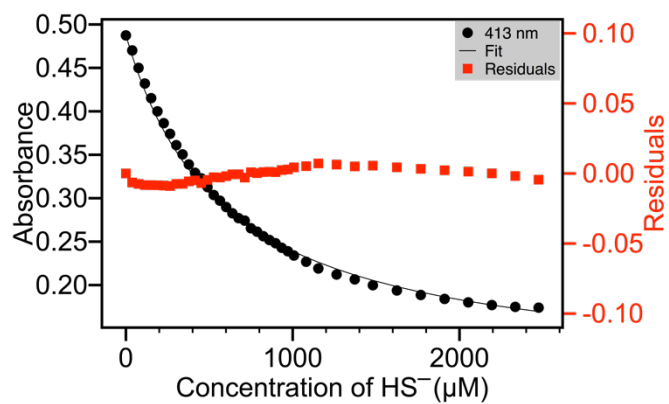


Figure C-6. ZnPPiX binding isotherm and associated fit for titration data shown in Figure 2b. Data points related to the deprotonation of carboxylic acid moieties removed (first equivalent), as they did not show significant spectral change.

Additional UV-Vis spectroscopy experiments of Cr^{III}(PPIX)Cl

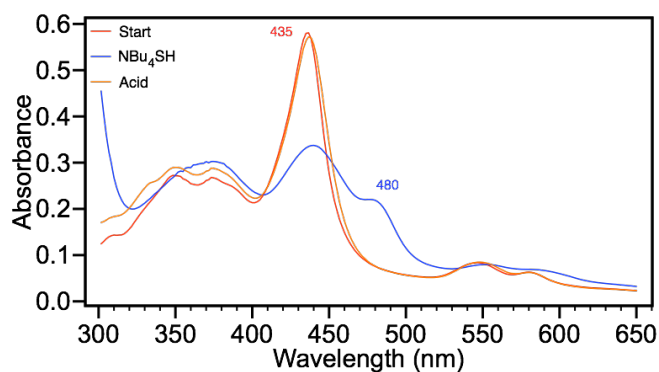


Figure C-7. Treatment of Cr^{III}(PPIX)Cl (2.4 μM, red) with NBu₄SH (26 equiv., blue) in THF, followed by AcOH (50 equiv., orange). Note: The reverse reaction was kinetically slow.

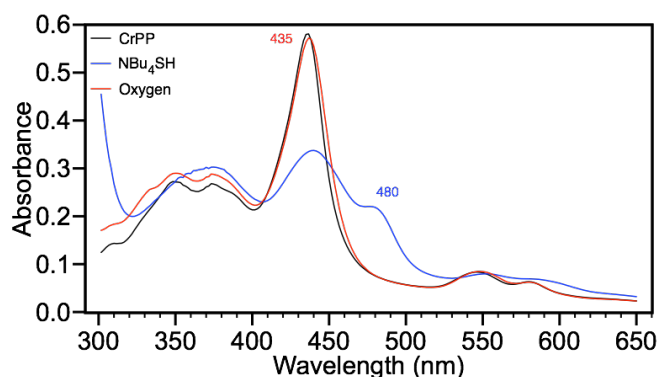


Figure C-8. Treatment of Cr^{III}(PPIX)Cl (2.4 μM, black) with NBu₄SH (25 equiv., blue) in THF followed by exposure to the atmosphere for 30 minutes (red).

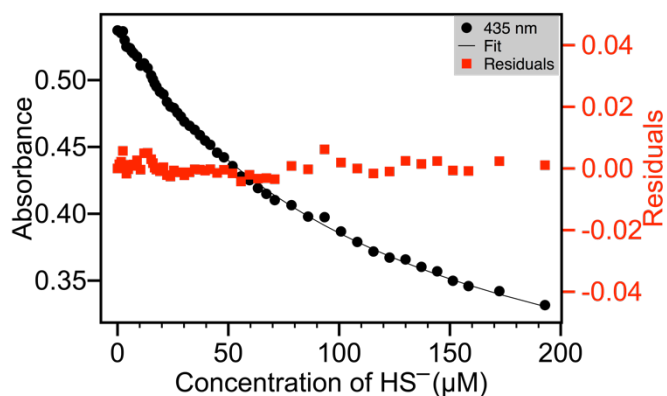


Figure C-9. Cr^{III}(PPIX)Cl binding isotherm and associated fit for titration data shown in Figure 4b. Data points corresponding to deprotonation (1st equiv.) showed no spectral change and were removed before fitting.

Additional UV-Vis spectroscopy experiments of Sn^{IV}PPIX

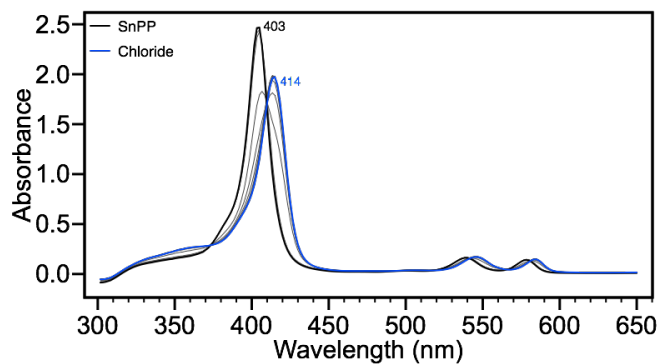


Figure C-10. Treatment of Sn^{IV}PPIX (6 μM) with Cl⁻ (25 equiv.) in THF.

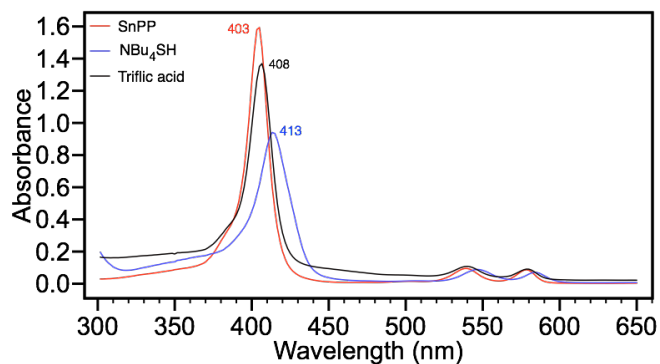


Figure C-11. Treatment of Sn^{IV}PPIX (3.9 μM, red) with NBu₄SH (20 equiv., blue) followed by addition of triflic acid (1 μL, black) in THF.

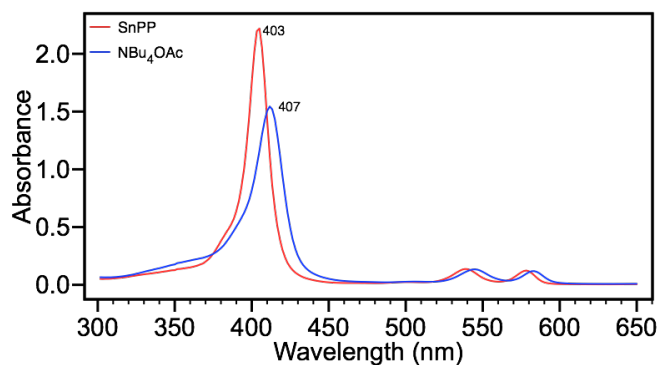


Figure C-12. Treatment of Sn^{IV}PPIX (5.5 μM, red) with NBu₄OAc (20 equiv., blue) in THF.

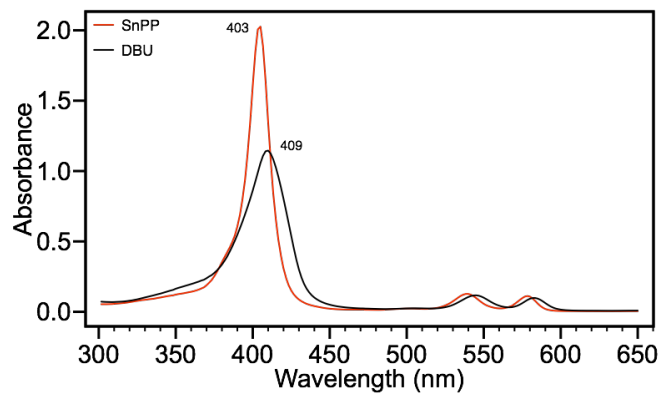


Figure C-13. Treatment of Sn^{IV}PPIX (5.4 μM, red) with DBU (200 equiv., black) in THF.

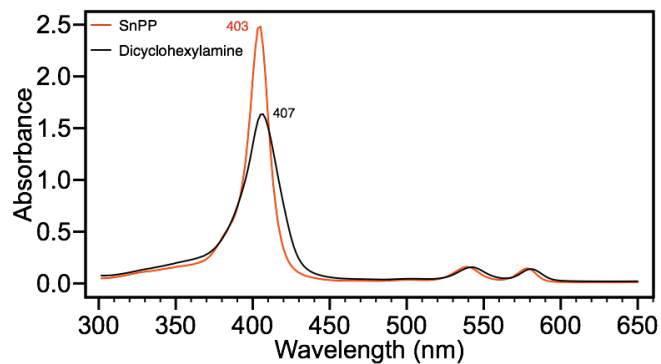


Figure C-14. Treatment of Sn^{IV}PPIX (6 μM, red) with dicyclohexylamine (11 equiv., black) in THF.

Additional UV-Vis spectroscopy experiments of Mn^{II/III}PPIX

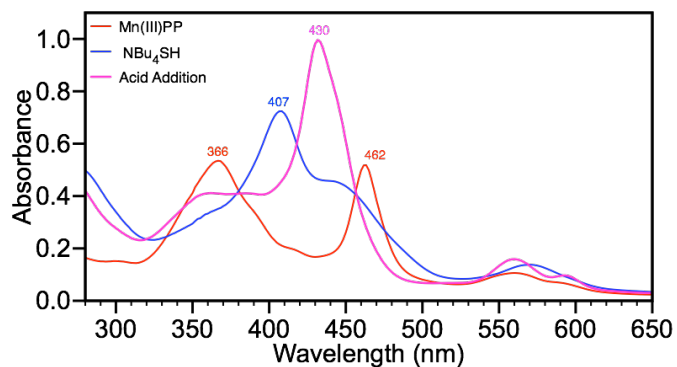


Figure C-15. Treatment of Mn^{III}PPIX (9.6 μ M, red) with NBu₄SH (15 equiv., blue) followed by AcOH (40 equiv., purple) in THF

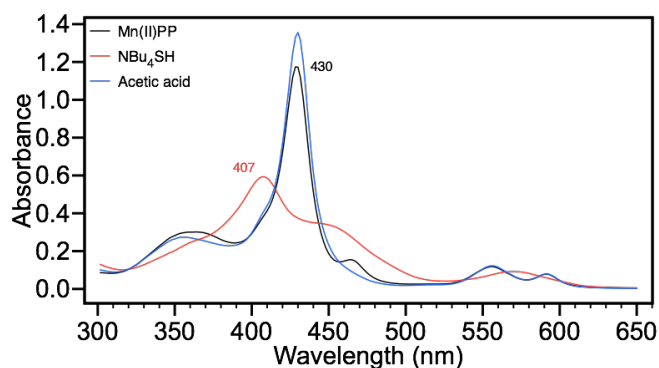


Figure C-16. Treatment of Mn^{II}PPIX (7.7 μ M, black) with NBu₄SH (4 equiv., red) followed by AcOH (40 equiv., blue) in THF.

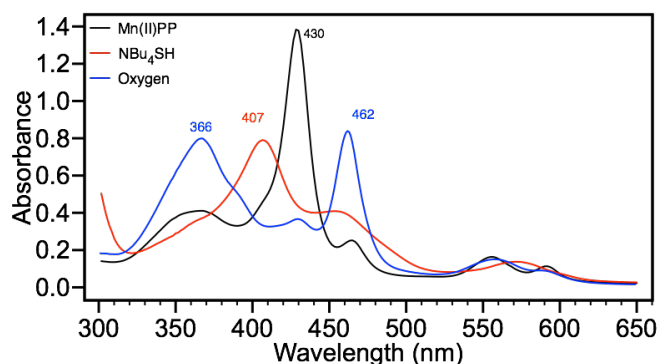


Figure C-17. Treatment of Mn^{II}PPIX (7.7 μ M, black) with NBu₄SH (4 equiv., red) followed by exposure to the atmosphere for 60 minutes (blue) in THF.

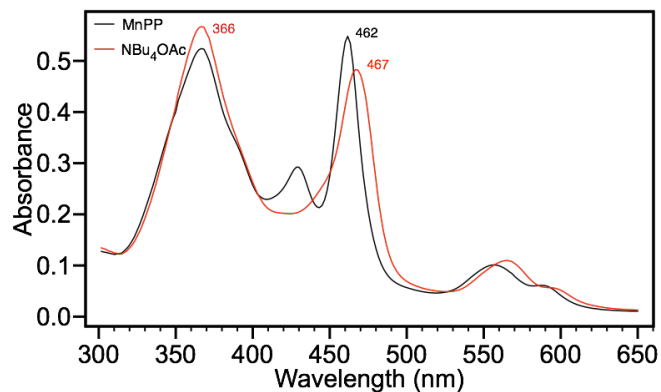


Figure C-18. Treatment of Mn^{III}PPIX (10 μ M, black) with NBU₄OAc (20 equiv., red) in THF.

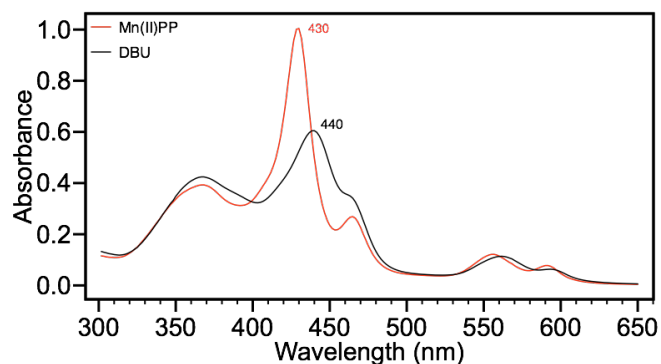


Figure C-19. Treatment of Mn^{II}PPIX (6.4 μ M, red) with DBU (1 μ L, black) in THF.

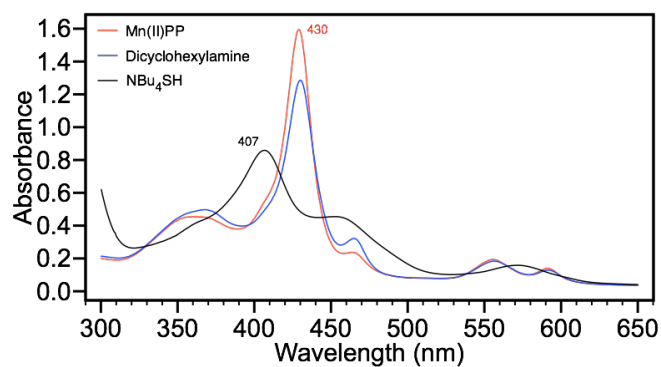


Figure C-20. Treatment of Mn^{II}PPIX (10 μ M, red) with dicyclohexylamine (50 equiv., blue), followed by addition of NBU₄SH (30 equiv., black) in THF.

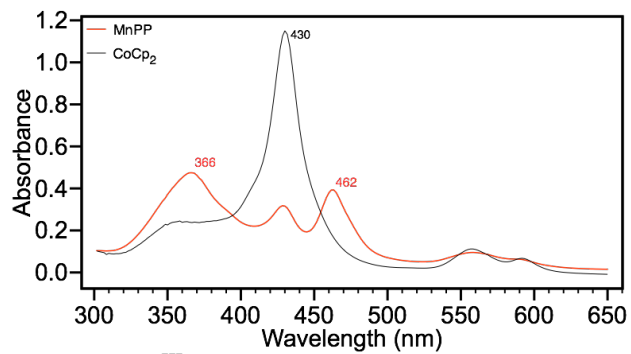


Figure C-21. Treatment of Mn^{III}PPIX (7.5 μ M, red) with CoCp₂ (1.5 equiv., black) in THF.

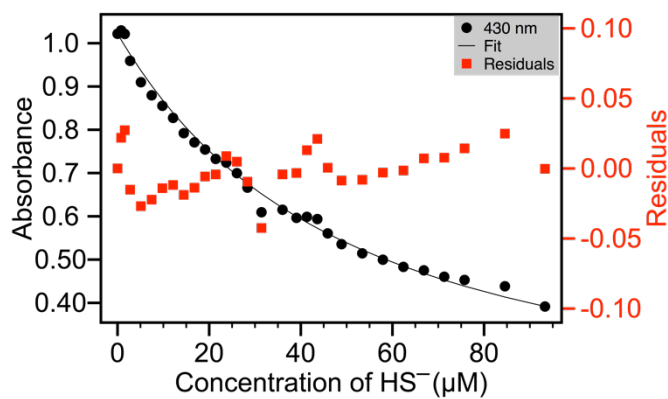


Figure C-22. Mn^{II}PPIX binding isotherm and associated fit for titration data shown in Figure 6b after complete conversion to Mn^{II}(PPIX).

Additional EPR Spectra and simulation parameters

$Cr^{III}PPIX$

In addition to UV-vis spectroscopy, we also used EPR spectroscopy to explore the electronic effects of binding HS^- with $Cr^{III}(PPIX)Cl$. A frozen solution (1:2 DMSO:DCM, 7 K) of $Cr^{III}(PPIX)Cl$ provided the spectrum of a typical axial high-spin chromium porphyrin (Figure C-24a).²⁵⁰ Chromium porphyrins are notably difficult to simulate,²⁵¹ and we were unable to produce a reasonable simulation of the porphyrin; however, visual comparison of this spectrum with those of known ZFS values indicate a D value of 0.23 cm^{-1} and isotropic g value of 1.98.²⁵² Upon addition of excess NBu_4SH , an axial EPR spectrum in which the axial components are reversed was produced (Figure C-24b). The exchange of axial g-values is unusual, but consistent with displacement of the Cl^- ligand for HS^- , which has a higher field-strength¹⁵⁴ and the resultant spectrum is similar to other axial-ligated chalcogenide Cr^{III} species, though not of other porphyrin species.^{154,252}

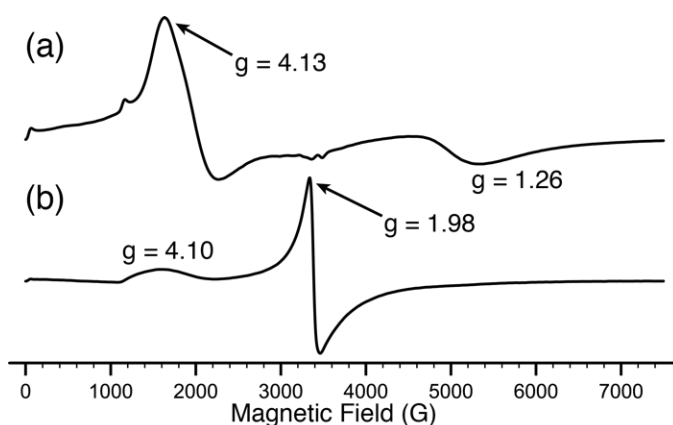


Figure C-23. Continuous wave EPR spectra (DMSO/ CH_2Cl_2 , 7 K) of (a) $Cr^{III}(PPIX)$ (2 mM), (b) $Cr^{III}(PPIX)SH$ upon addition of 20.4 equiv. of NBu_4SH .

Fitting parameters for Mn^{III}PPIX

Mn^{III}(PPIX)Cl+NBu₄SH General Spectrum: S = 5/2, NucS = Mn, g_x = 6.154, g_y = 5.724, g_z = 1.975, A_x = 672.05 MHz, A_y = 628.74 MHz, A_z = 279.89 MHz D = 4.69 MHz, E = 44.25 MHz, lwpp_{Gaussian} = 0.70 MHz, lwpp_{Lorenzian} = 1.96 MHz

Fitting parameters for Mn^{II}PPIX

Mn^{II}(PPIX): S = 5/2, NucS = Mn, g_x = 6.203, g_y = 5.706, g_z = 1.968 A_x = 650.22 MHz, A_y = 619.40 MHz, g_z = 263.00 MHz, D = 12.971 MHz, E = 13.62 MHz, lwpp_{Gaussian} = 3.29 MHz, lwpp_{Lorenzian} = 2.34 MHz.

Mn^{II}(PPIX)+NBu₄SH: S = 5/2, NucS = Mn, g_x = 6.154, g_y = 5.735, g_z = 1.974 A_x = 674.79 MHz, A_y = 629.05 MHz, A_z = 277.65 MHz, D = 4.86 MHz, E = 44.60 MHz, lwpp_{Gaussian} = 0.73 MHz, lwpp_{Lorenzian} = 2.37 MHz.

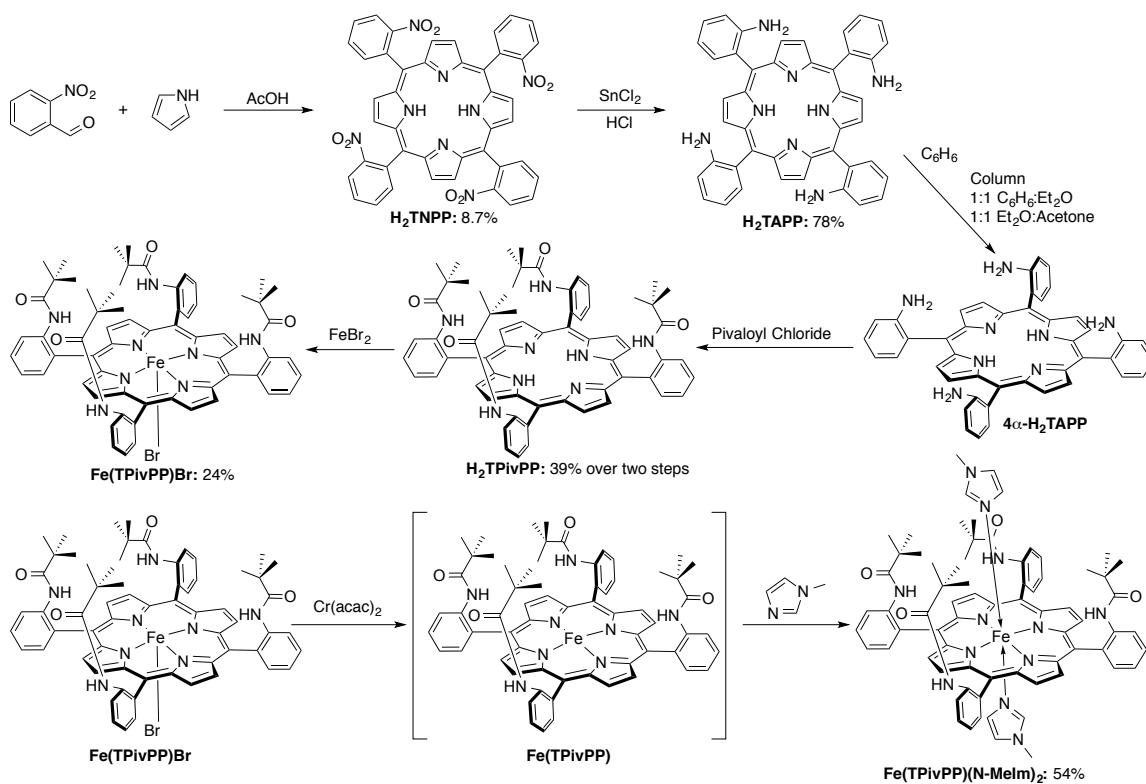
APPENDIX D

SUPPORTING INFORMATION: SPECTROSCOPIC INVESTIGATIONS INTO THE BINDING OF HYDROGEN SULFIDE TO SYNTHETIC PICKET-FENCE PORPHYRINS

CONTENTS

Synthetic scheme for porphyrin materials	147
Spectroscopic characterization data	148
5,10,15,20-tetrakis(2-nitrophenyl)porphyrin, (H2TNPP).....	148
5,10,15,20-tetrakis(2-aminophenyl)porphyrin, (H2TAPP)	149
(all-cis)-5,10,15,20-tetrakis[2-(2,2-dimethylpropionamido)phenyl]porphyrin, (H2TPivPP).....	151
Bromo{(all-cis)-5,10,15,20-tetrakis-[2-(2,2- dimethylpropionamido)phenyl]porphyrinato(2-)}-iron(III), (Fe(TPivPP)Br).....	156
Bis(N-methylimidazole)[(all-cis)-5,10,15,20-tetrakis-[2-(2,2- dimethylpropionamido)phenyl]porphyrinato(2-)]-iron(II), (Fe(TPivPP)(Im) ₂) ..	159
Interactions of O ₂ with FeII(TPivPP).....	161
Full ¹ H-NMR spectra of NBu ₄ SH addition	161
Binding characterization	163
Negative ion mode mass spectra.....	163
Absorption data for different Fe complexes	166

Synthetic scheme for porphyrin materials



Scheme D-1. Synthesis of Fe(TPivPP)(Im)₂.

Spectroscopic characterization data

5,10,15,20-tetrakis(2-nitrophenyl)porphyrin, (H_2TNPP)

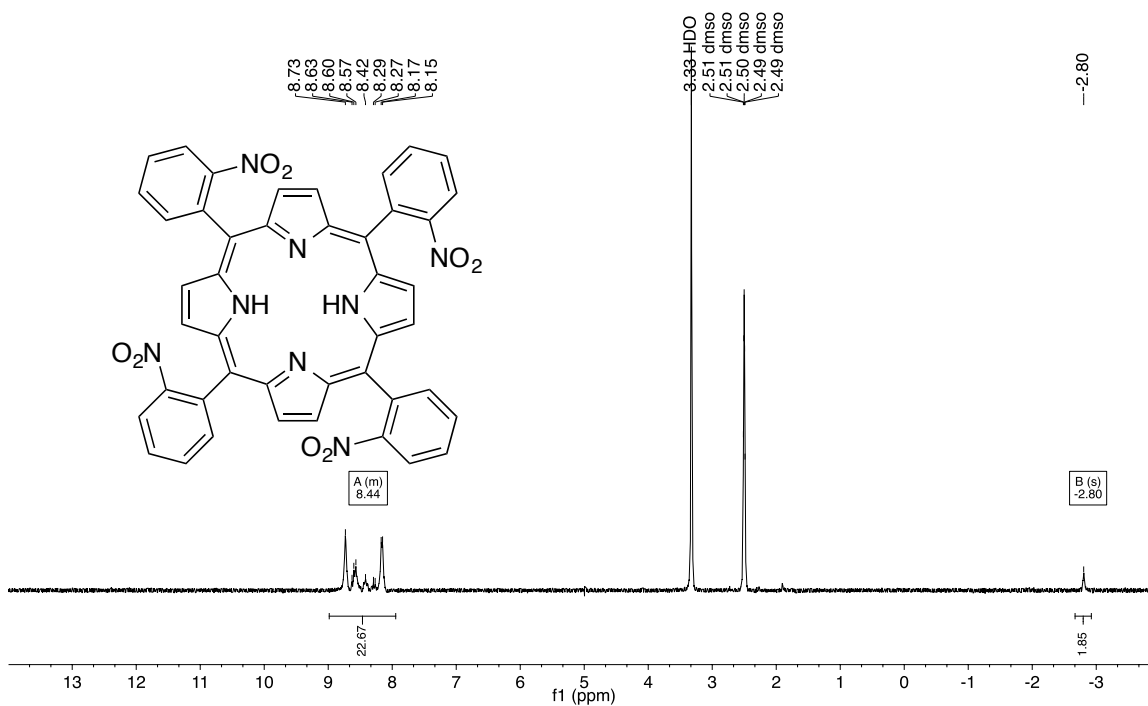


Figure D-1. 1H (600 MHz, $DMSO-d_6$) NMR spectrum of H_2TNPP .

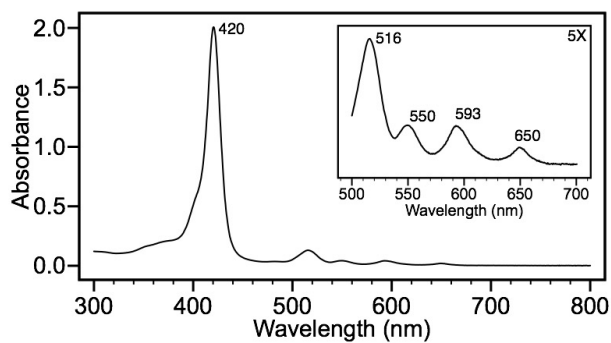


Figure D-2. UV-Vis spectrum of H_2TNPP in DMF.

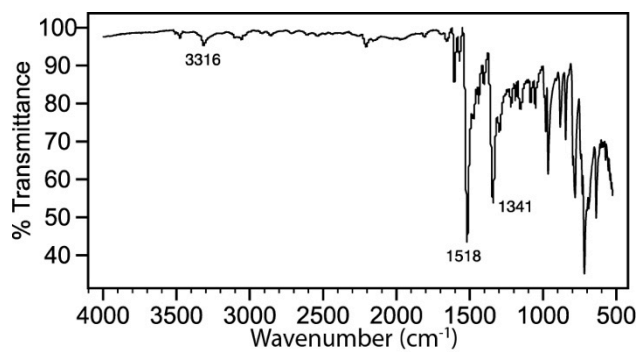


Figure D-3. FTIR (ATR, neat) spectrum of H_2TNPP .

5,10,15,20-tetrakis(2-aminophenyl)porphyrin, (H_2TAPP)

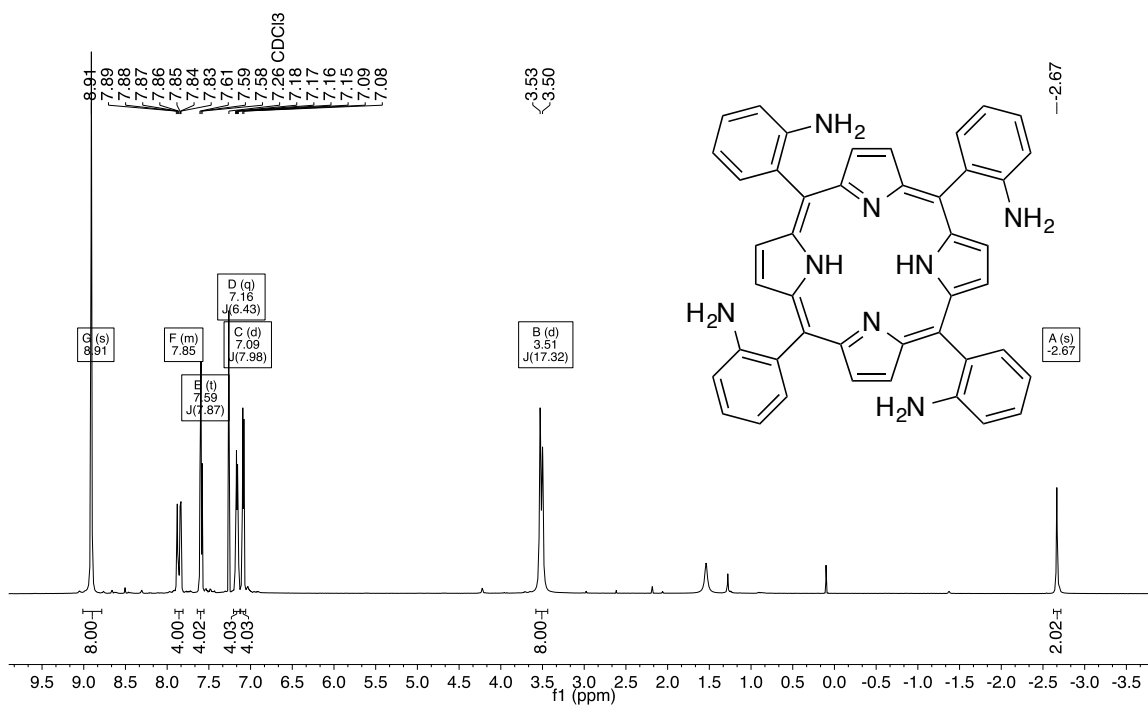


Figure D-4. 1H (600 MHz, $CDCl_3$) NMR spectrum of H_2TAPP .

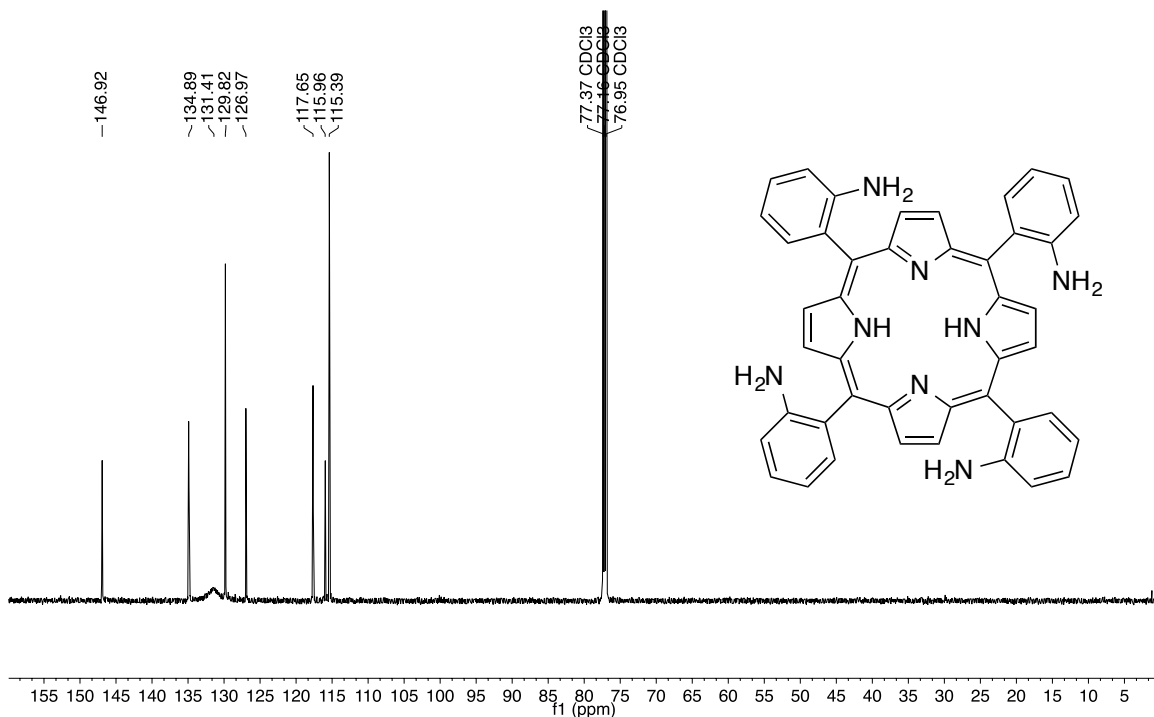


Figure D-5. $^{13}\text{C}\{^1\text{H}\}$ (151 MHz, CDCl_3) NMR spectrum of H₂TAPP.

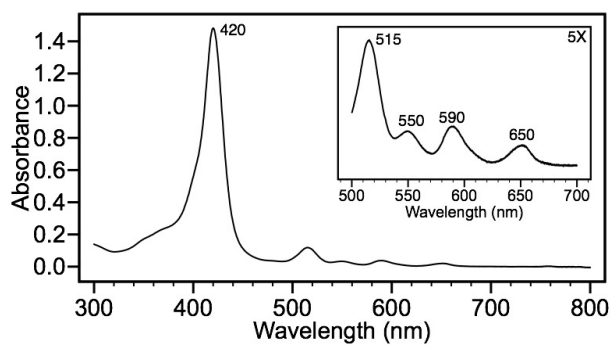


Figure D-6. UV-Vis spectrum of H₂TAPP in CHCl_3 .

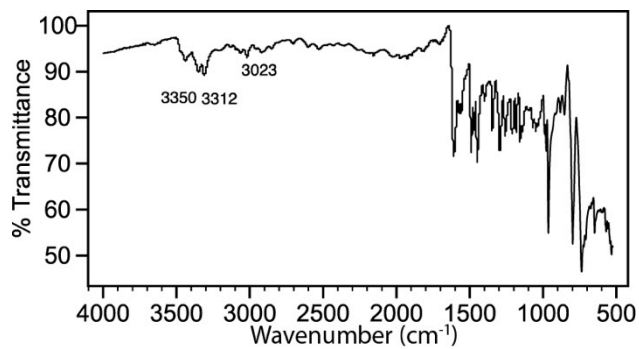


Figure D-7. FTIR (ATR, neat) spectrum of H₂TAPP.

(all-cis)-5,10,15,20-tetrakis[2-(2,2-dimethylpropionamido)phenyl]porphyrin,
(H₂TPivPP)

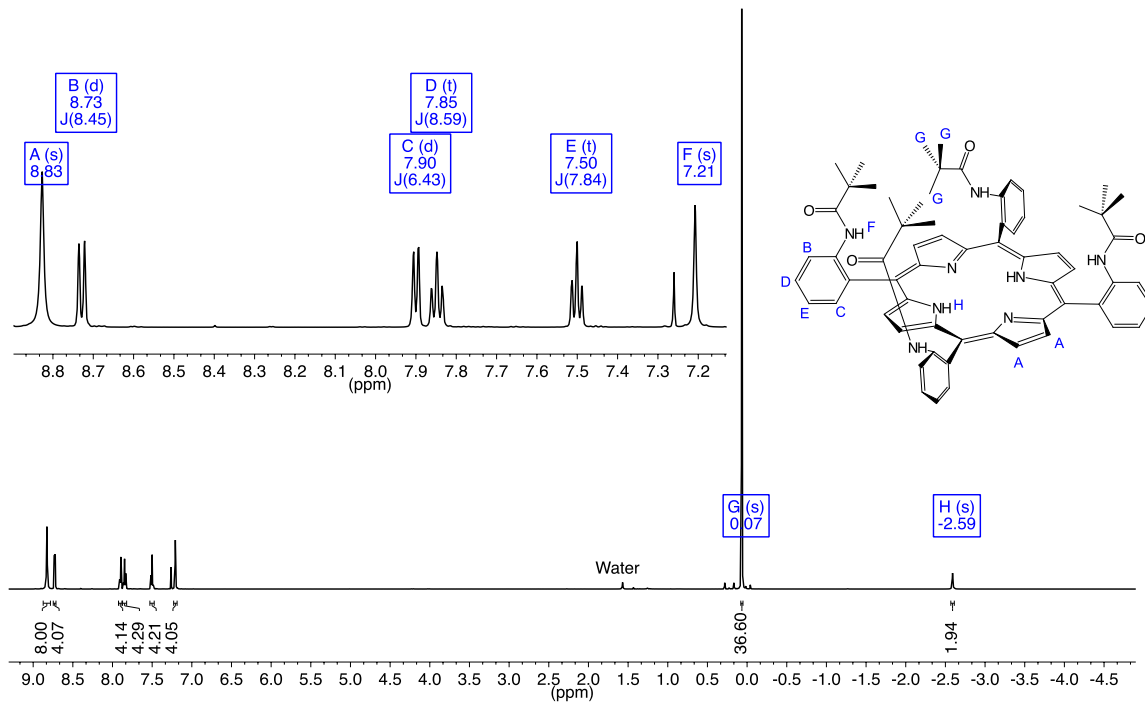


Figure D-8. ¹H (600 MHz, CDCl₃) NMR spectrum of H₂TPivPP.

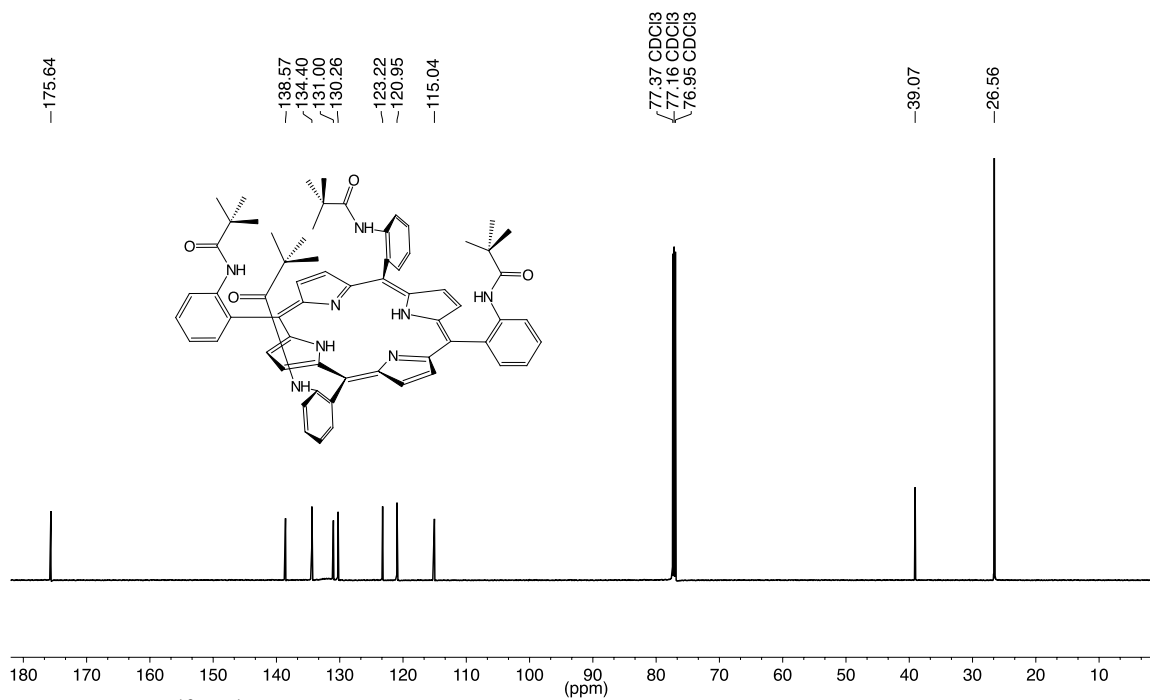


Figure D-9. $^{13}\text{C}\{^1\text{H}\}$ (151 MHz, CDCl_3) NMR spectrum of H_2TPivPP .

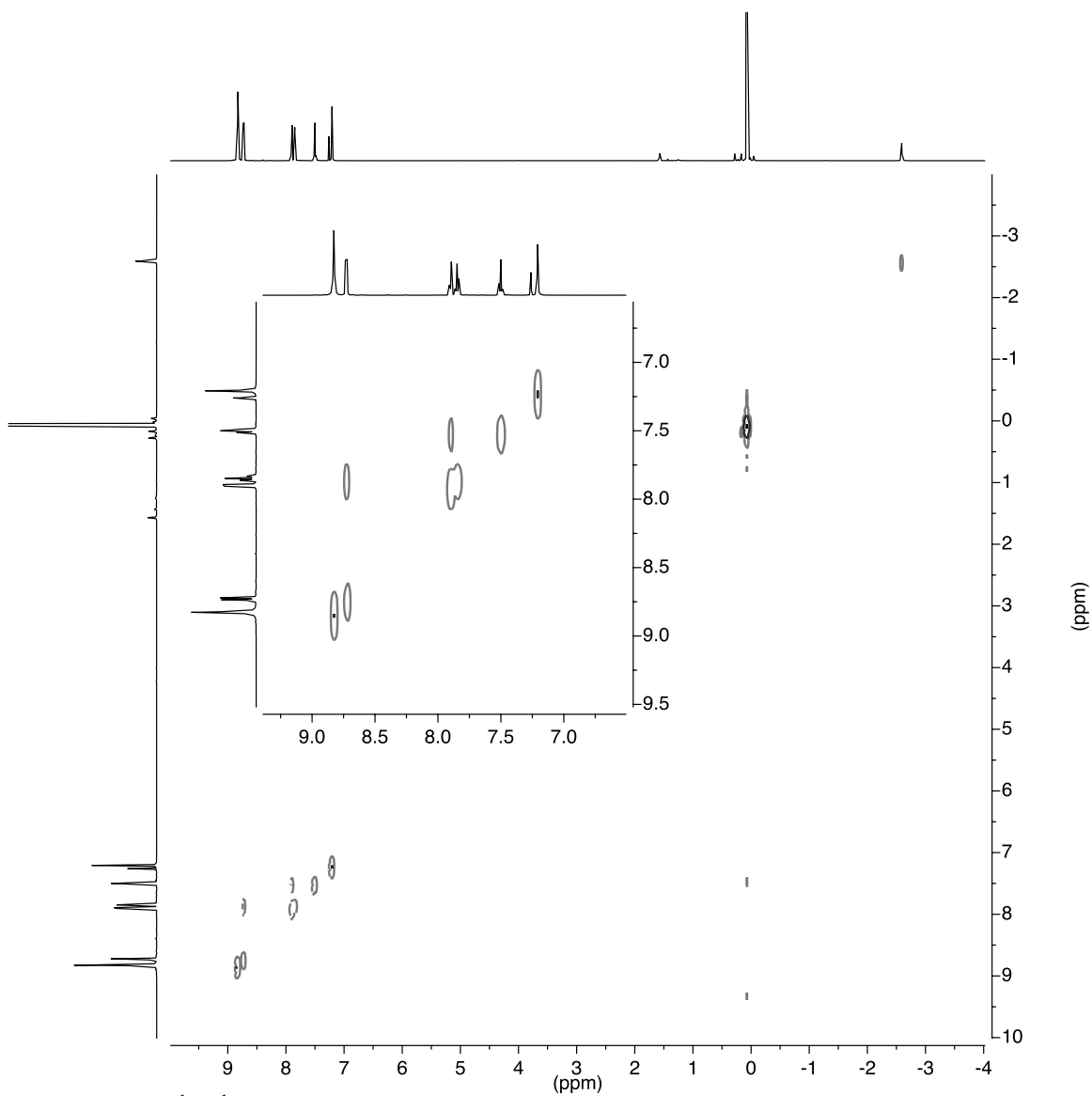


Figure D-10. ¹H-¹H COSY NMR spectrum of H₂TPivPP.

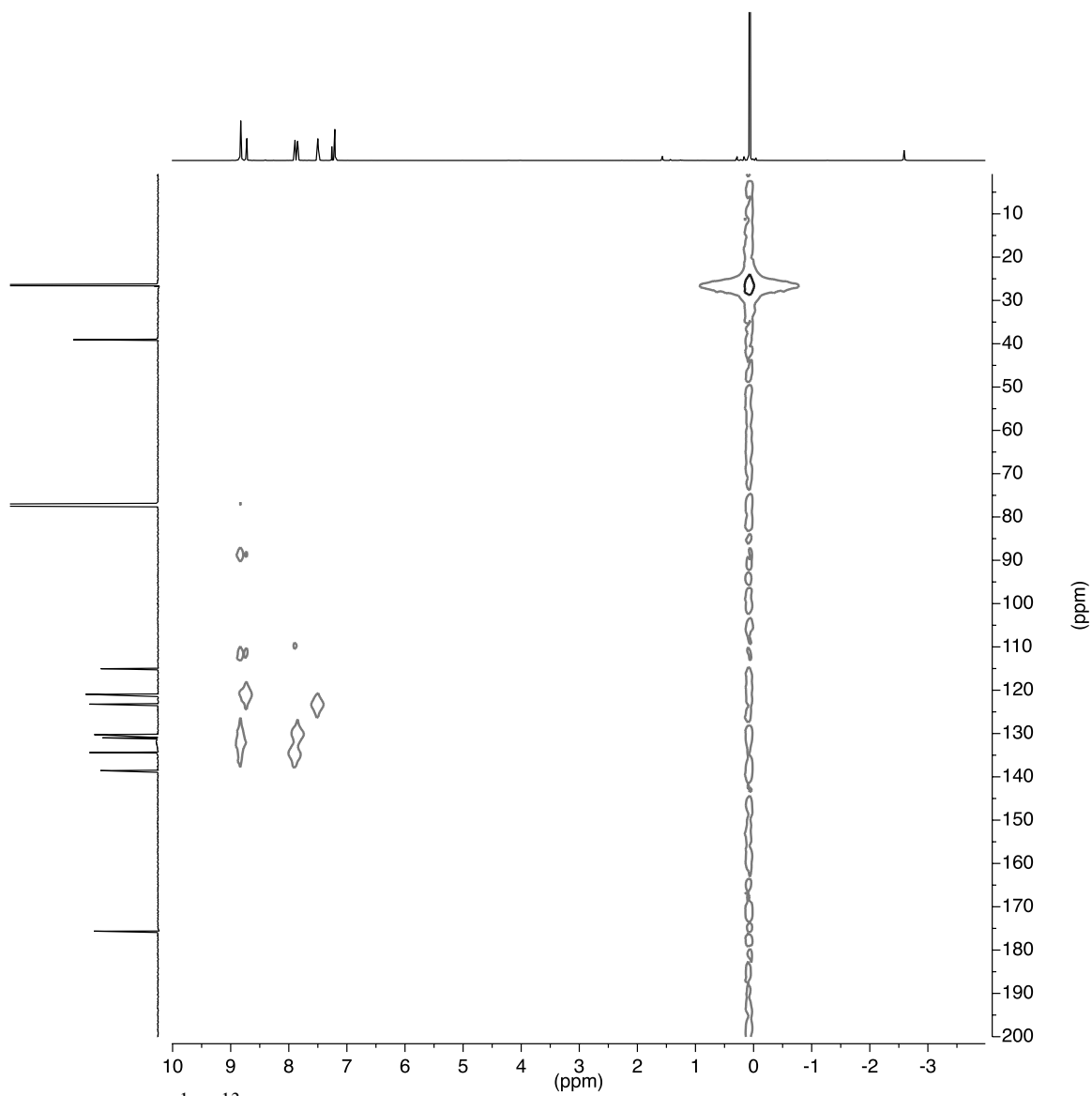


Figure D-11. ^1H - ^{13}C HMQC NMR spectrum of H_2TPivPP .

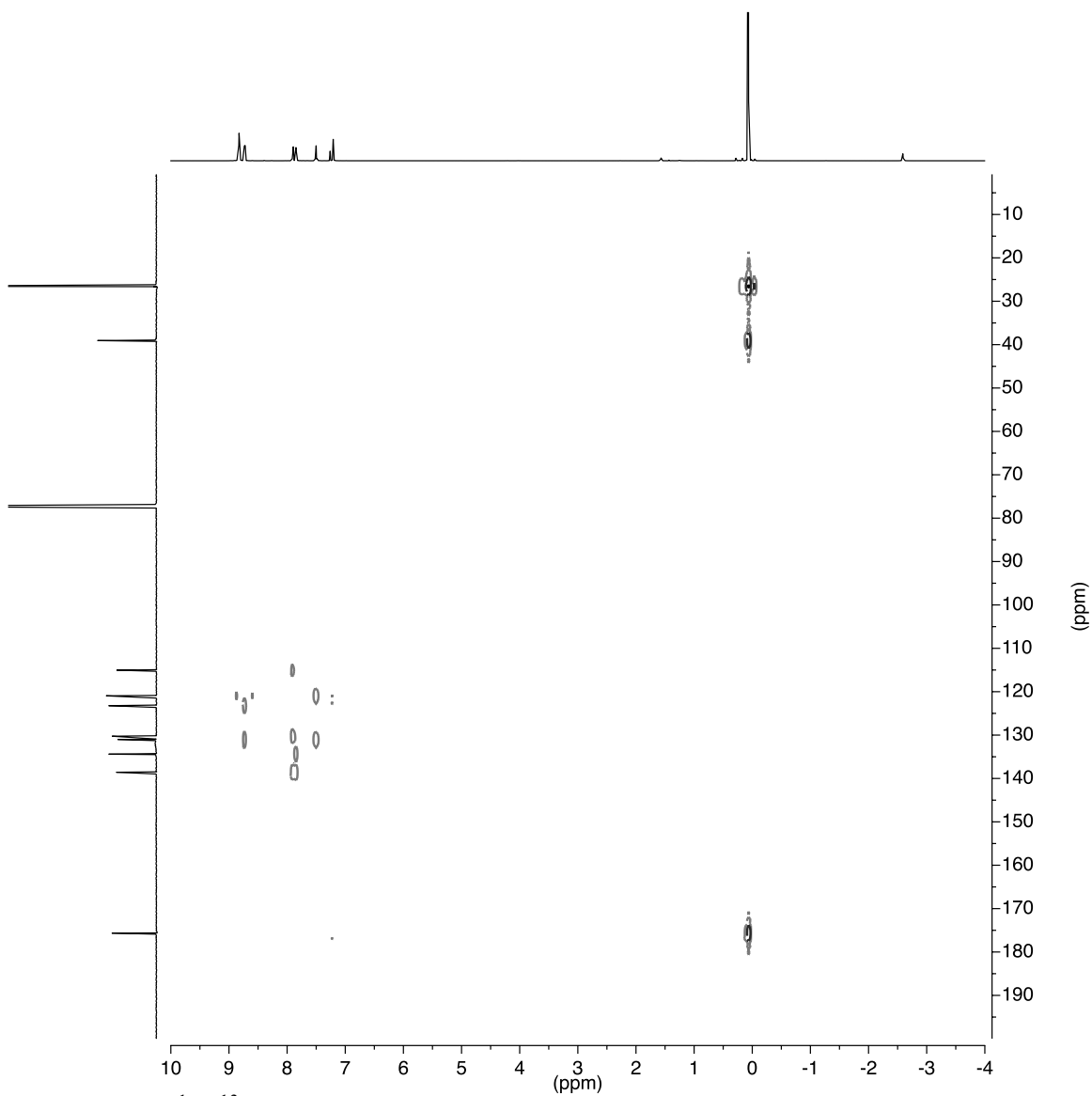


Figure D-12. ^1H - ^{13}C HMBC NMR spectrum of H_2TPivPP .

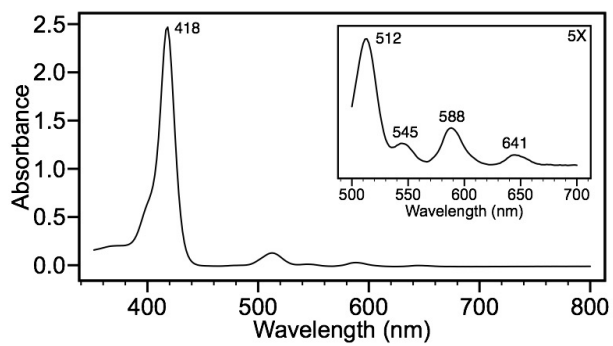


Figure D-13. UV-Vis spectrum of H_2TPivPP in CHCl_3 .

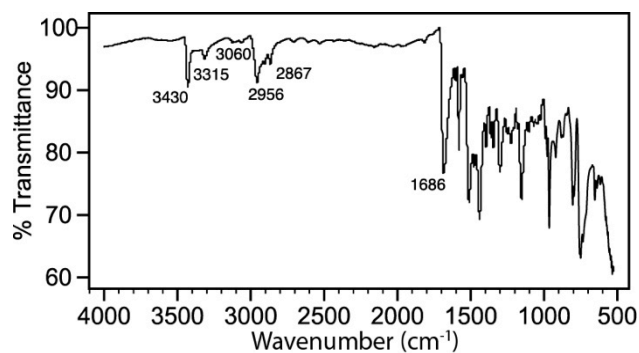


Figure D-14. FTIR (ATR, neat) spectrum of H₂TPivPP.

Bromo{(all-cis)-5,10,15,20-tetrakis-[2-(2,2-dimethylpropionamido)phenyl]porphyrinato(2-)}-iron(III), (Fe(TPivPP)Br)

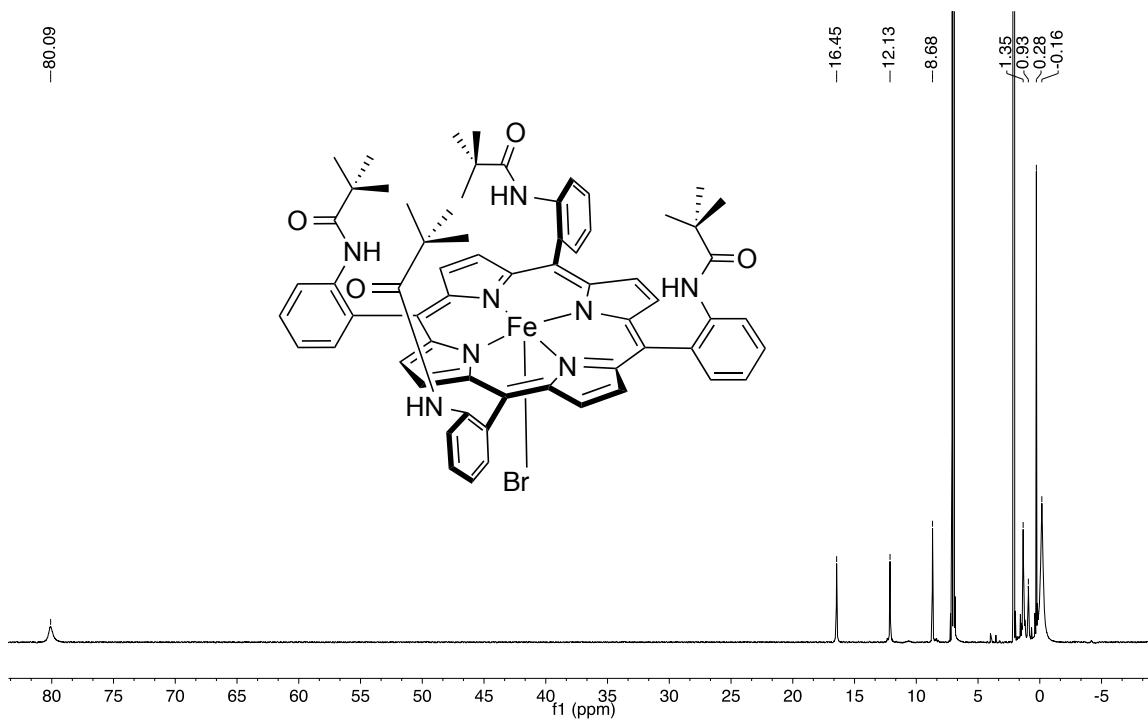


Figure D-15. ¹H (600 MHz, toluene-*d*₈) NMR spectrum of Fe(TPivPP)Br.

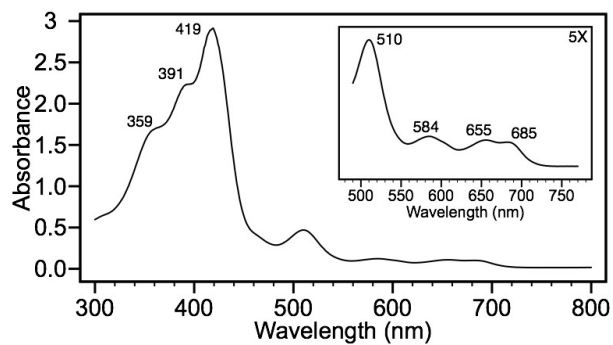


Figure D-16. UV-Vis spectrum of Fe(TPivPP)Br in CHCl₃.

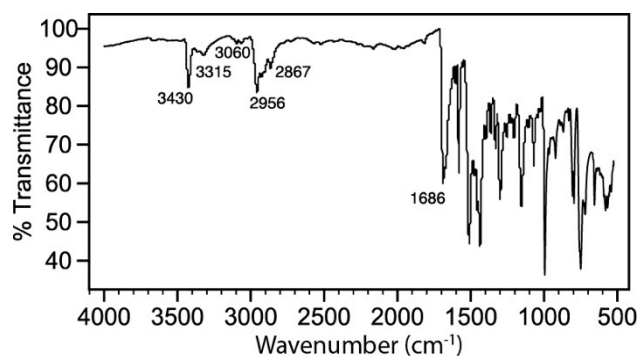


Figure D-17. FTIR (ATR, neat) spectrum of Fe(TPivPP)Br.

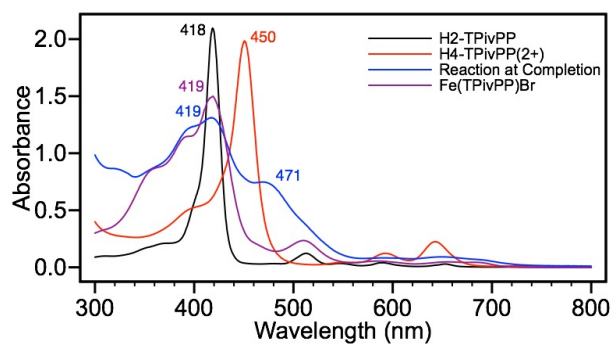


Figure D-18. Comparison of the UV-Vis spectra of different species in the metalation reaction for Fe(TPivPP)Br in CHCl₃.

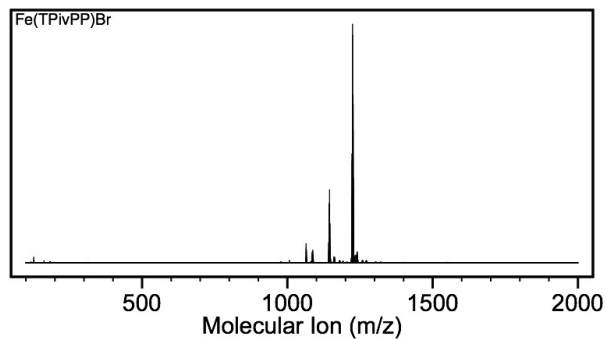


Figure D-19. Full electrospray negative ion mode mass spectrum of Fe(TPivPP)Br.

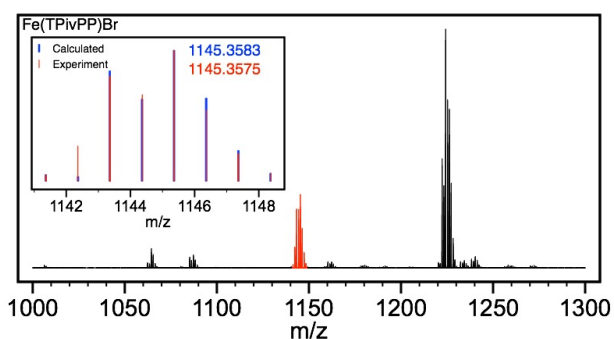


Figure D-20. Area of interest for negative ion mode mass spectrum of Fe(TPivPP)Br including the isotopic distribution of the observed and calculated peaks.

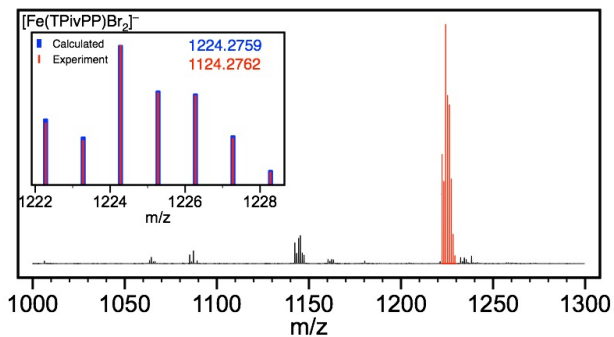


Figure D-21. Area of interest for negative ion mode mass spectrum of Fe(TPivPP)Br₂⁻ including the isotopic distribution of the observed and calculated peaks.

Bis(N-methylimidazole)[(all-cis)-5,10,15,20-tetrakis-[2-(2,2-dimethylpropionamido)phenyl]porphyrinato(2-)]-iron(II), (Fe(TPivPP)(Im)₂)

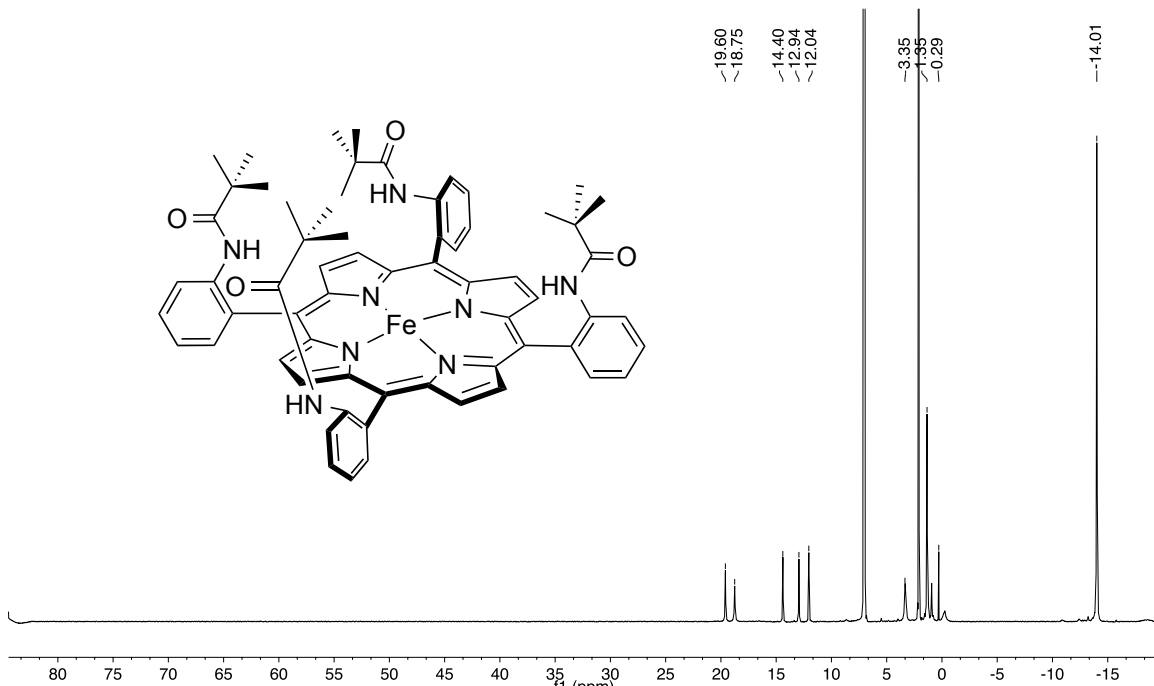


Figure D-22. ¹H (600 MHz, toluene-*d*₈) NMR spectrum of Fe(TPivPP).

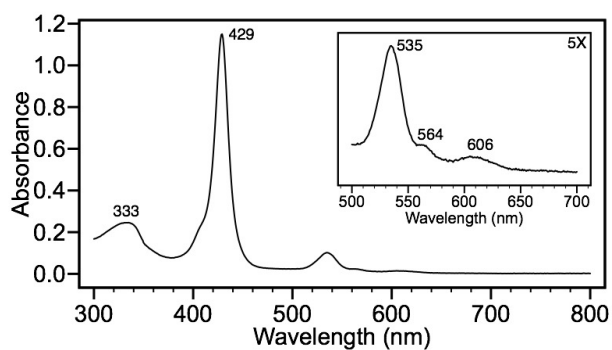


Figure D-23. UV-Vis spectrum of Fe(TPivPP)(Im)₂ (10.8 μM) in toluene with 33-fold excess of *N*-methyl imidazole.

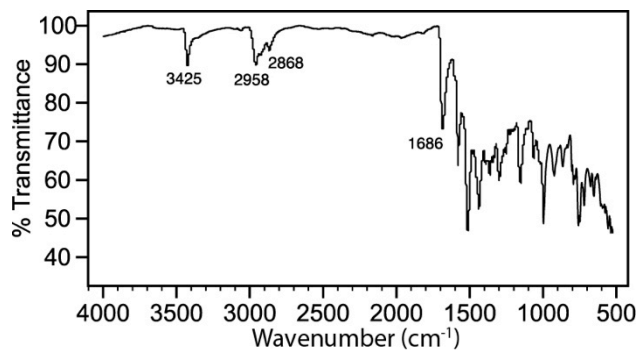


Figure D-24. FTIR (ATR, neat) spectrum of Fe(TPivPP).

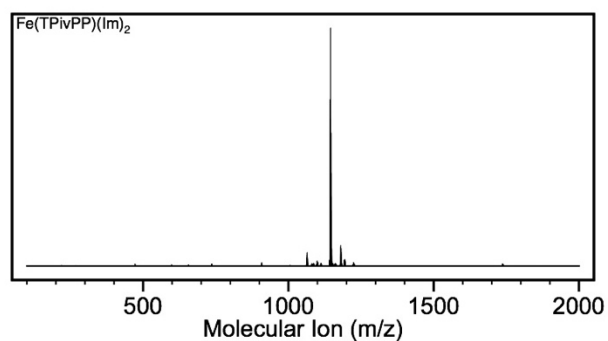


Figure D-25. Full negative ion mode mass spectrum of Fe(TPivPP)(Im)

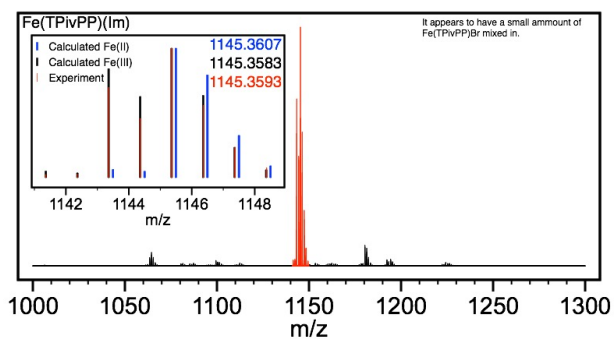


Figure D-26. Area of interest for negative ion mode mass spectrum of Fe(TPivPP)(Im) including the isotopic distribution of the observed and calculated peaks.

Interactions of O₂ with Fe^{II}(TPivPP)

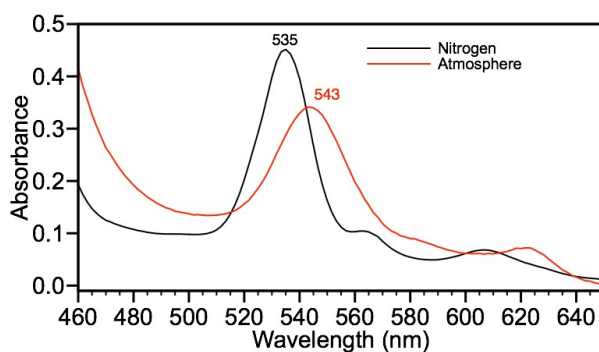


Figure D-27. UV-Vis spectrum of representative oxygen binding of Fe(TPivPP)(Im)₂ (23 μM) in toluene.

Full ¹H-NMR spectra of NBu₄SH addition

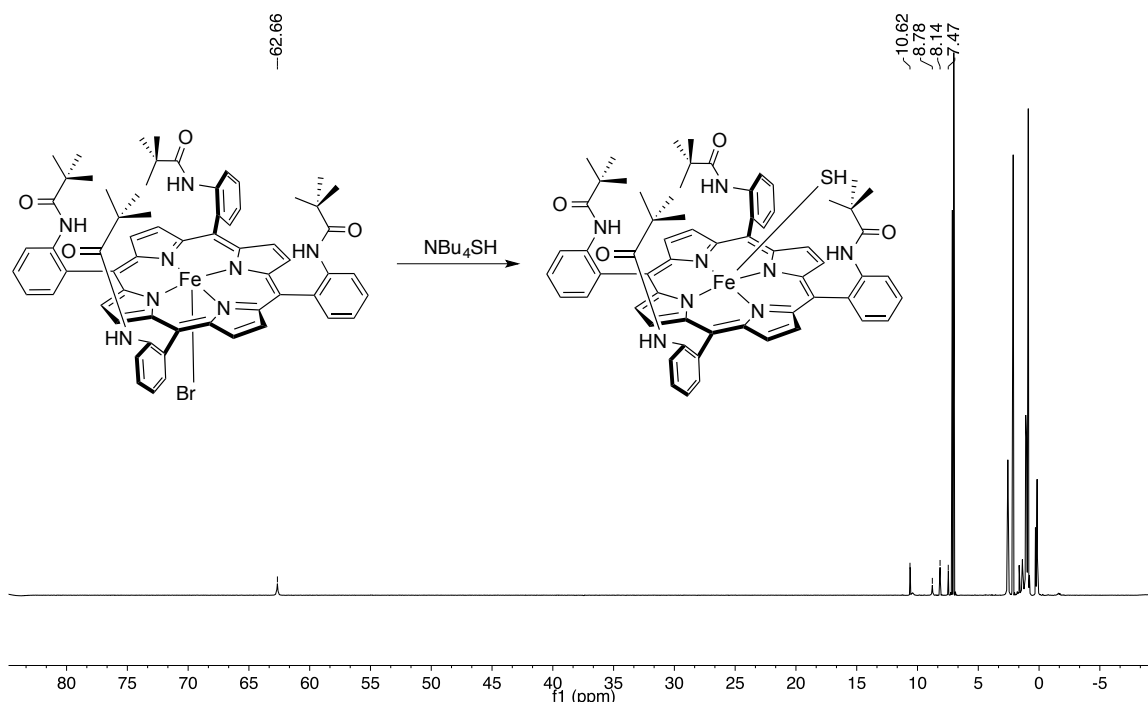


Figure D-28. ¹H (600 MHz, toluene-*d*₈) NMR Spectrum of Fe(TPivPP)(SH) after reaction with Fe(TPivPP)Br.

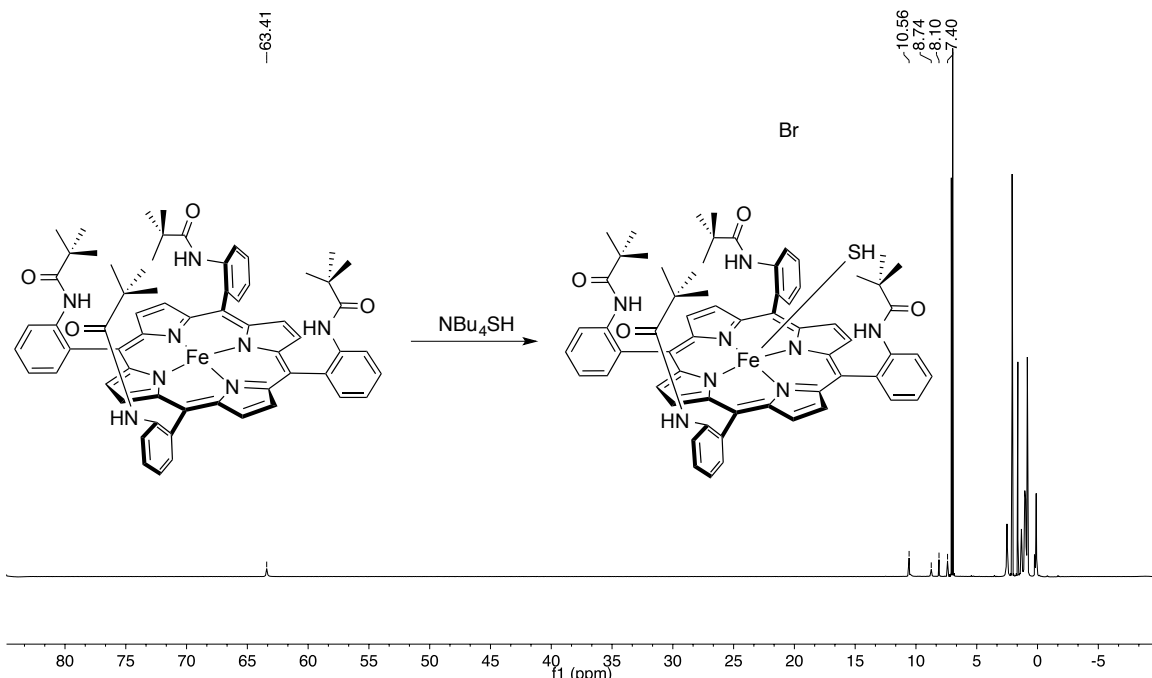


Figure D-29. ¹H (600 MHz, toluene-*d*₈) NMR spectrum of Fe(TPivPP)(SH) after reaction with Fe(TPivPP).

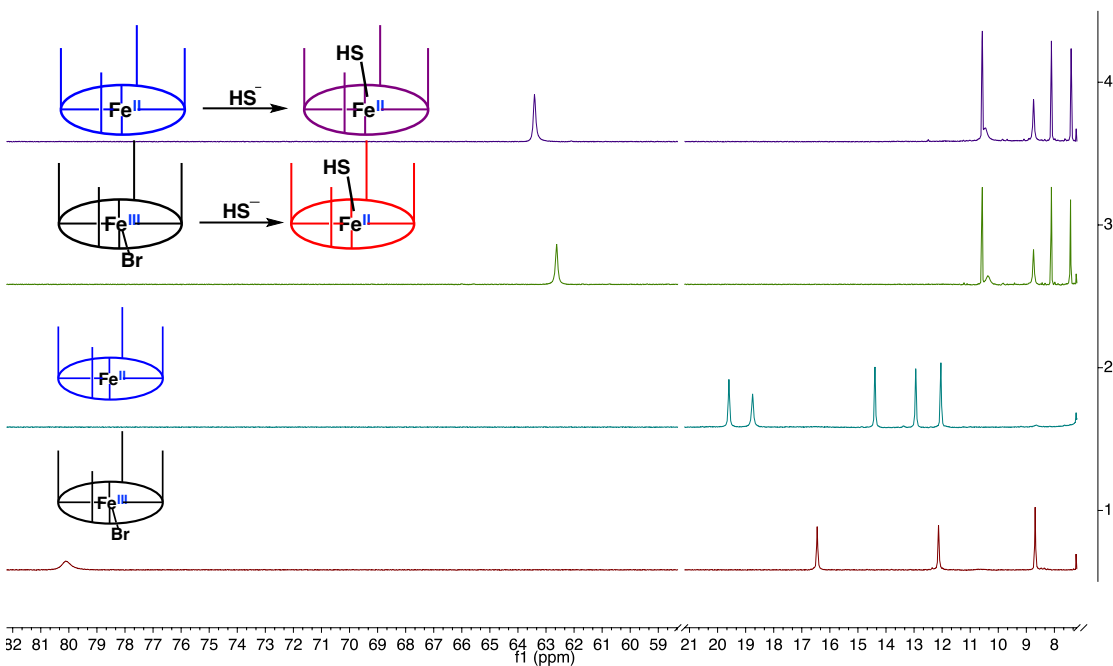


Figure D-30. ¹H (600 MHz, toluene-*d*₈) NMR spectra of different Fe species and the reaction results with NBU₄SH.

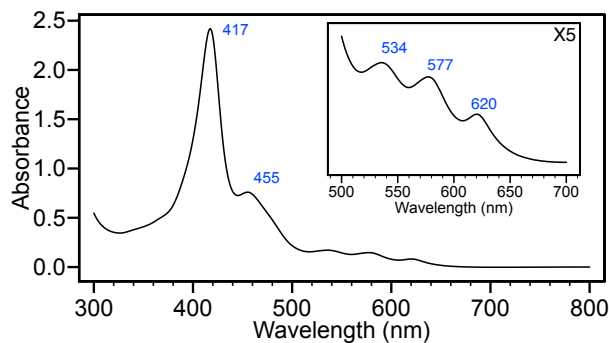


Figure D-31. UV-Vis of the starting and final product for NMR titrations.

Binding characterization

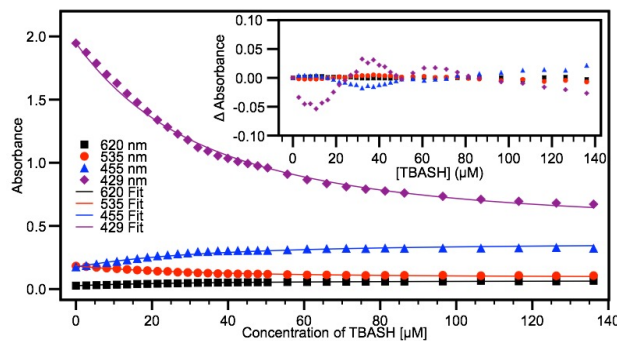


Figure D-32. Representative UV-Vis titration data (in toluene) and residual (inset).

Negative ion mode mass spectra

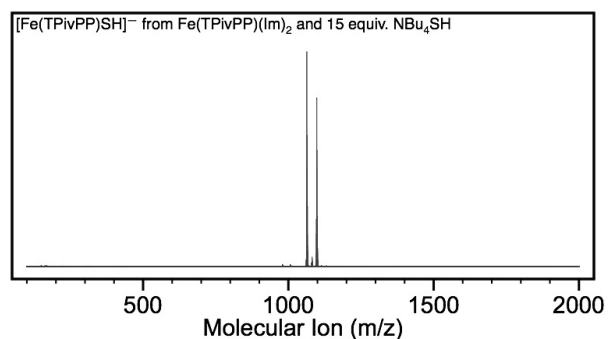


Figure D-33. Negative ion mode mass spectrum of $\text{Fe}(\text{TPivPP})(\text{Im})_2$ with 15 equiv. of NBu_4SH in THF.

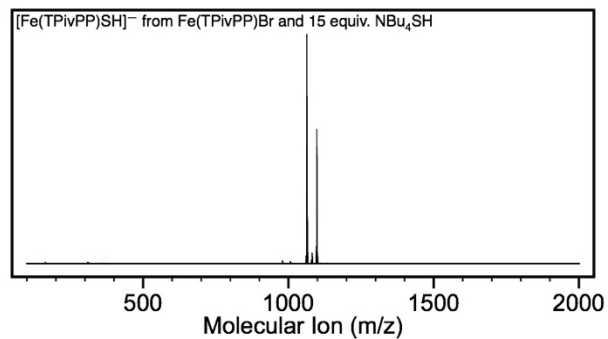


Figure D-34. Negative ion mode mass spectrum of Fe(TPivPP)Br with 15 equiv. of NBu₄SH.

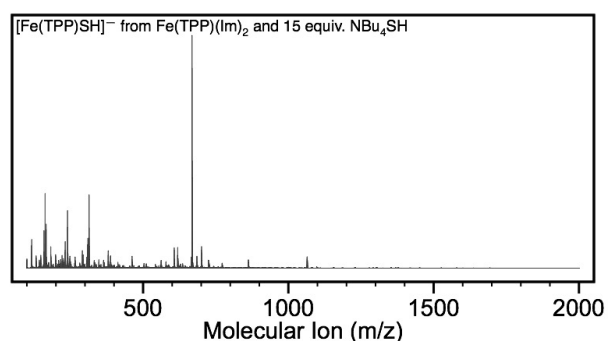


Figure D-35. Negative ion mode mass spectrum of Fe(TPP)(Im)₂ with 15 equiv. of NBu₄SH.

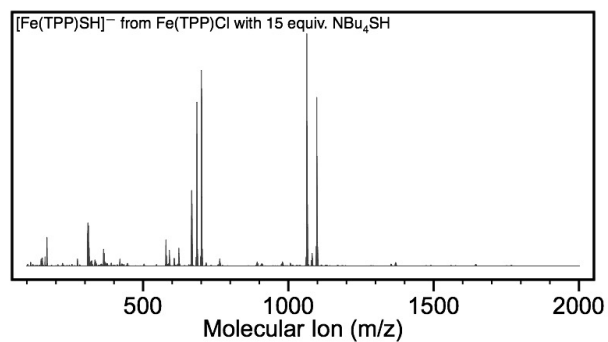


Figure D-36. Negative ion mode mass spectrum of Fe(TPP)Cl with 15 equiv. of NBu₄SH.

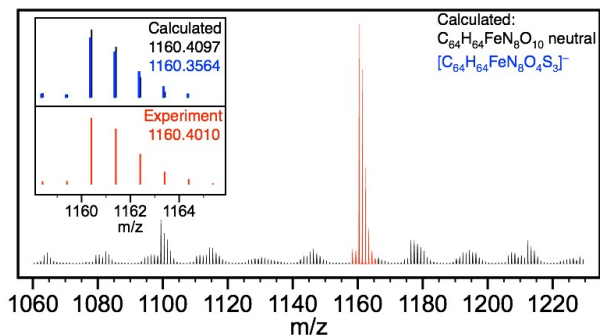


Figure D-37. Negative ion mode mass spectrum of the degradation product of Fe(TPivPP)(Im)₂ treated with 15 equiv. of NBu₄SH and exposed to the atmosphere.

To test the hypothesis that the binding of HS⁻ is kinetically stabilized by the PFP scaffold, solutions of ferrous **3** and **6** were treated with 15 equiv. of NBu₄SH and their mass spectra were recorded at different collisional energies. Our expectation was that the kinetic stability of the bound sulfide in the PFP scaffold would require a higher collisional energy to dissociate sulfide than in the TPP system. To test this hypothesis, we isolated the sulfur-containing precursor ions (m/z 1097.4294 and 700.1522, respectively) and monitored the ratio of sulfur-ligated to unligated porphyrin species as a function of collisional energy using samples of **3** and **6** prepared under identical conditions (Figure S46). At the lowest collision energy (0.00 kV), the PFP exhibited a 33:1 sulfide-ligated:unligated ratio, which was significantly larger than the 1.59:1 ratio observed in the TPP system. Increasing the collisional energy to 0.20 kV resulted in ratios of 1.25:1 and 1.08:1 for the PFP and TPP systems, respectively. When taken together with the previous mass spectrometry studies, these data are consistent with an increased kinetic barrier for sulfide release from the PFP pocket by comparison to the TPP system.¹⁹⁵⁻¹⁹⁶

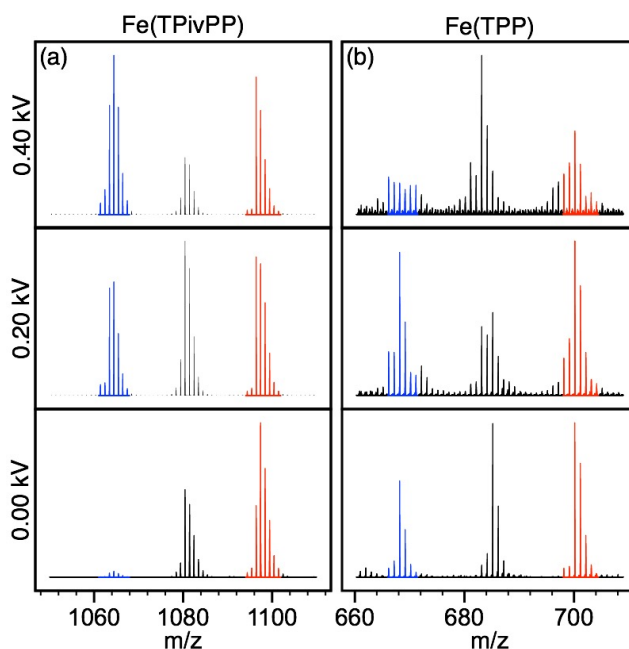


Figure D-38. (a) Mass spectrum of **3** after addition of 15 equiv. of NBu_4SH in THF shows the formation of **2** (blue) and **7** (red). (b) Mass spectrum of **6** after addition 15 equiv. of NBu_4SH in THF shows the formation of **5** (blue) and **8** (red). In both cases, increasing the collisional energy results in a decrease in the peak intensity corresponding to the SH-ligated iron complex with respect to the unligated porphyrin. The decrease in (b) is greater than that of (a), consistent with sulfur bound inside the pocket of the porphyrin.

Absorption data for different Fe complexes

Table D-1. Table of porphyrin compounds and absorbances.

Species	Compound #	λ_{max} (toluene)	λ_{max} (DMF)
$\text{Fe}^{\text{III}}(\text{TPivPP})\text{Br}$	1	419, 510, 582, 655, 684	425, 570, 668
$\text{Fe}^{\text{II}}(\text{TPivPP})$	2	414, 571, 661	Not measured
$\text{Fe}^{\text{II}}(\text{TPivPP})(\text{Im})_2$	3	429, 534, 564 (sh), 610	419, 455, 538, 575, 621
$\text{Fe}^{\text{III}}(\text{TPP})\text{Cl}$	4	Not measured	418, 566
$\text{Fe}^{\text{II}}(\text{TPP})$	5	Not measured	Not measured
$\text{Fe}^{\text{II}}(\text{TPP})(\text{Im})_2$	6	427, 532, 566	Not measured
$[\text{Fe}^{\text{II}}(\text{TPivPP})(\text{SH})]^-$	7	419, 455 (sh), 534, 578, 620	419, 455 (sh), 534, 578, 620
$[\text{Fe}^{\text{II}}(\text{TPP})(\text{SH})]^-$	8	418, 463 (sh), 532, 573, 622	418, 463 (sh), 532, 573, 622
$\text{Fe}^{\text{II}}(\text{TPivPP})(\text{O}_2)(\text{Im})$	9	429, 540	Not measured

APPENDIX E

SUPPORTING INFORMATION: STABILIZATION OF A ZINC(II) HYDROSULFIDO

COMPLEX UTILIZING A HYDROGEN-BOND ACCEPTING LIGAND

CONTENTS

Additional UV-Vis experiments	168
Additional NMR experiments.....	170
Job Plot	176

Additional UV-Vis experiments

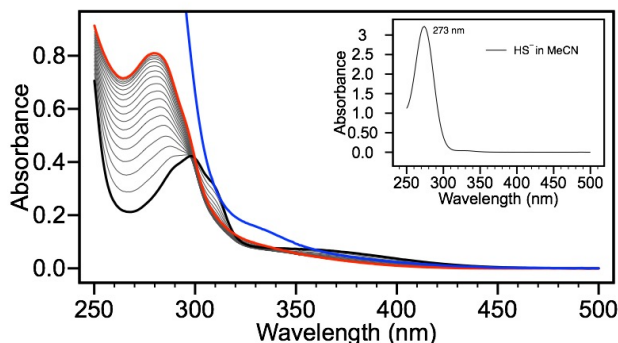


Figure E-1. Titration of a $88 \mu\text{M}$ solution of $\text{Zn}(\text{didpa})\text{Cl}_2$ in MeCN (black) with NBu_4SH added in 0.1 equiv. increments up to 1.5 equiv. (red). The titration was continued up to 5 equiv. (blue) of NBu_4SH , which results in a spectrum primarily dominated by the absorption of free HS^- , which has an absorbance at 273 nm (inset) in MeCN. Attempts to fit this data to a 1:1 or 1:2 binding model were unsuccessful due to overlapping peaks.

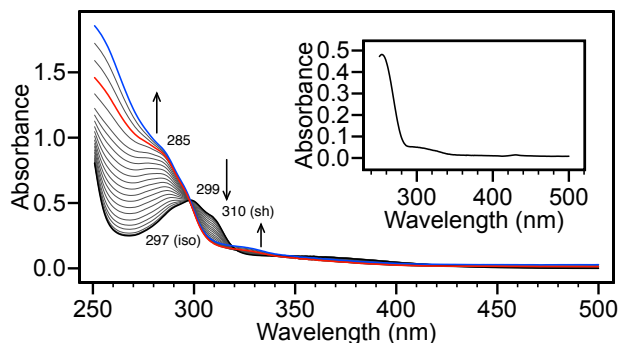


Figure E-2. Titration of a $87 \mu\text{M}$ solution of $\text{Zn}(\text{didpa})\text{Cl}_2$ in MeCN (black) with sodium butylthiolate added in 0.3 equiv. increments up to 6 equivalents (red). Further increase in the spectrum at 250 nm is due to sodium butane thiolate (blue). The spectrum of sodium butylthiolate is shown in the inset for comparison. Attempts to fit this data to a 1:1 or 1:2 binding model were unsuccessful.

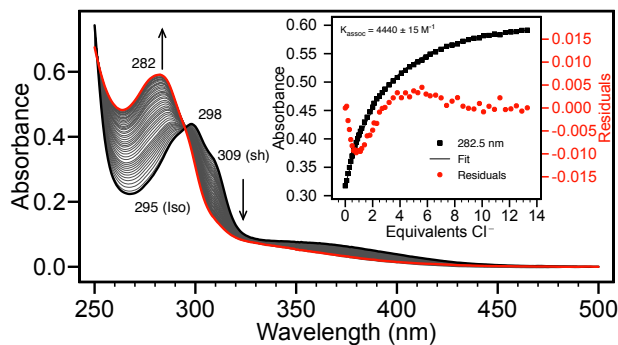


Figure E-3. Titration of a 88 μM solution of $\text{Zn}(\text{didpa})\text{Cl}_2$ in MeCN with NBu_4Cl added in 0.1 equiv. increments of NBu_4Cl up to 13.6 equivalents (red). Inset shows the binding isotherm at 282 nm with fit of $4,440 \pm 15 \text{ M}^{-1}$. Residuals are assigned to the right y-axis.

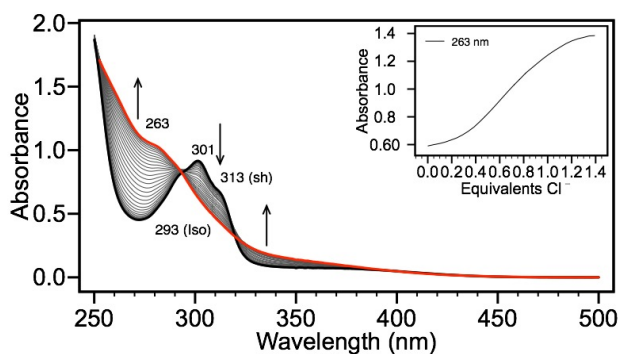


Figure E-4. Titration of 175 μM solution of $\text{Zn}(\text{didpa})\text{Cl}_2$ in DCM with NBu_4Cl added in 0.1 equiv. increments of NBu_4Cl up to 4.0 equivalents (red). Inset shows the binding isotherm at 263 nm and was unable to be fit due to its sinusoidal nature. The apparent induction behavior could be due to chloride binding free zinc (see methods); however, removal of these initial points does not provide reasonable fits to a 1:1 or 1:2 model.

Additional NMR experiments

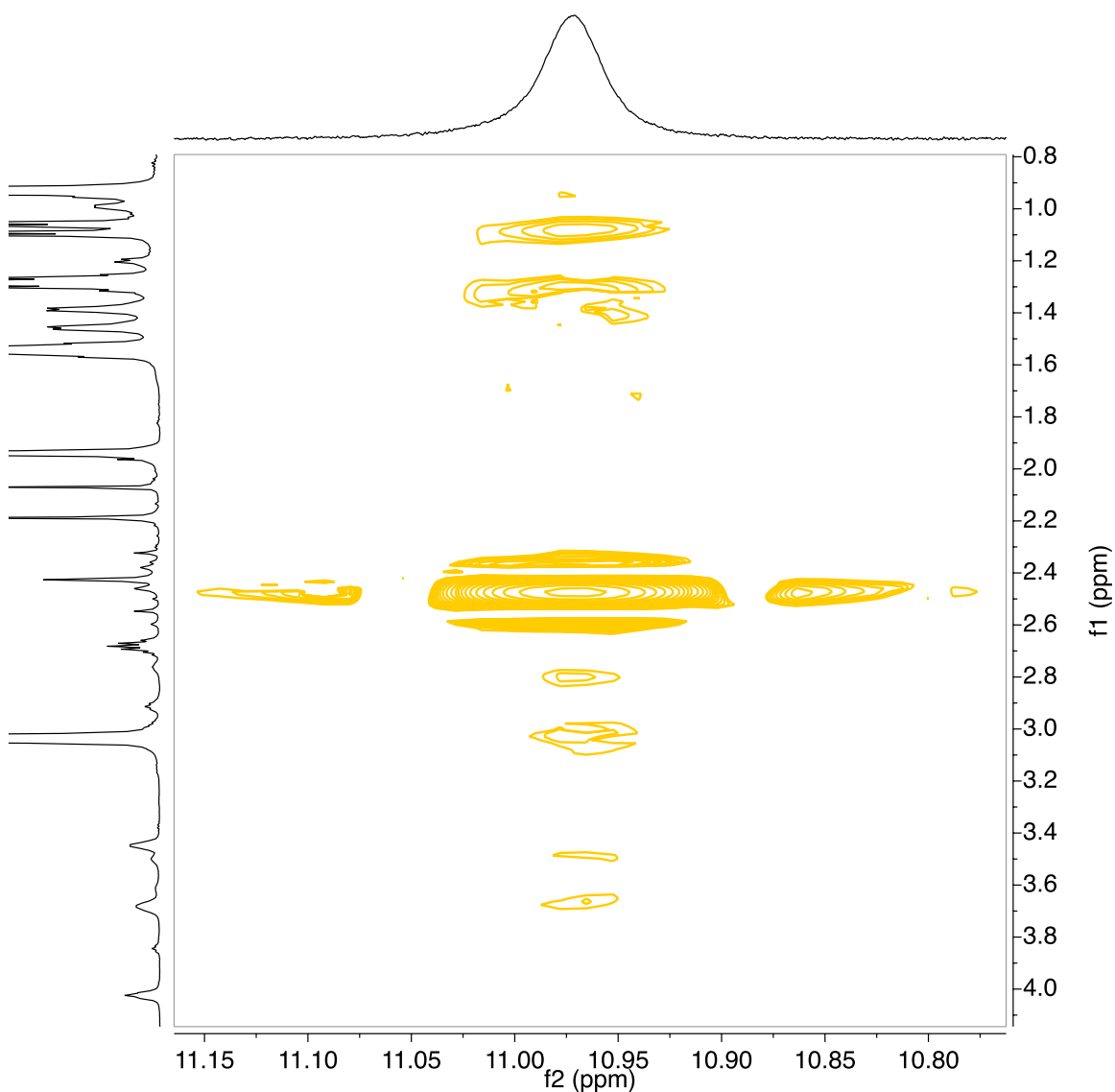


Figure E-5. NOESY spectrum of 11.6 mM Zn(didpa)Cl₂, and 18.9 mM NBu₄SH (1.6 equiv.) in CD₃CN recorded at -35 °C. The spectra were recorded with a 2.0 s relaxation delay and a 0.4 s mixing time. The largest observed peak is an exchange peak with residual water.

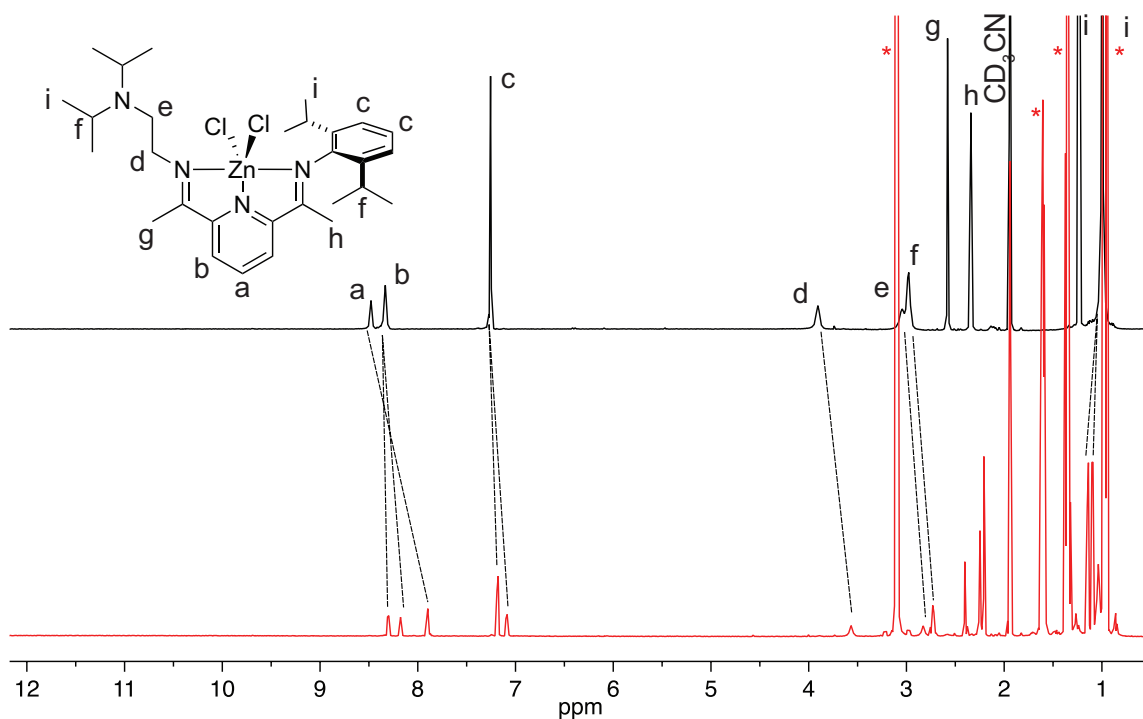


Figure E-6. ¹H NMR spectra of Zn(didpa)Cl₂ (5.8 mM in CD₃CN) before (top, black spectrum) and after (bottom, red spectrum) addition of 5.7 equiv. of NBu₄Cl. The (*) correspond to NBu₄⁺.

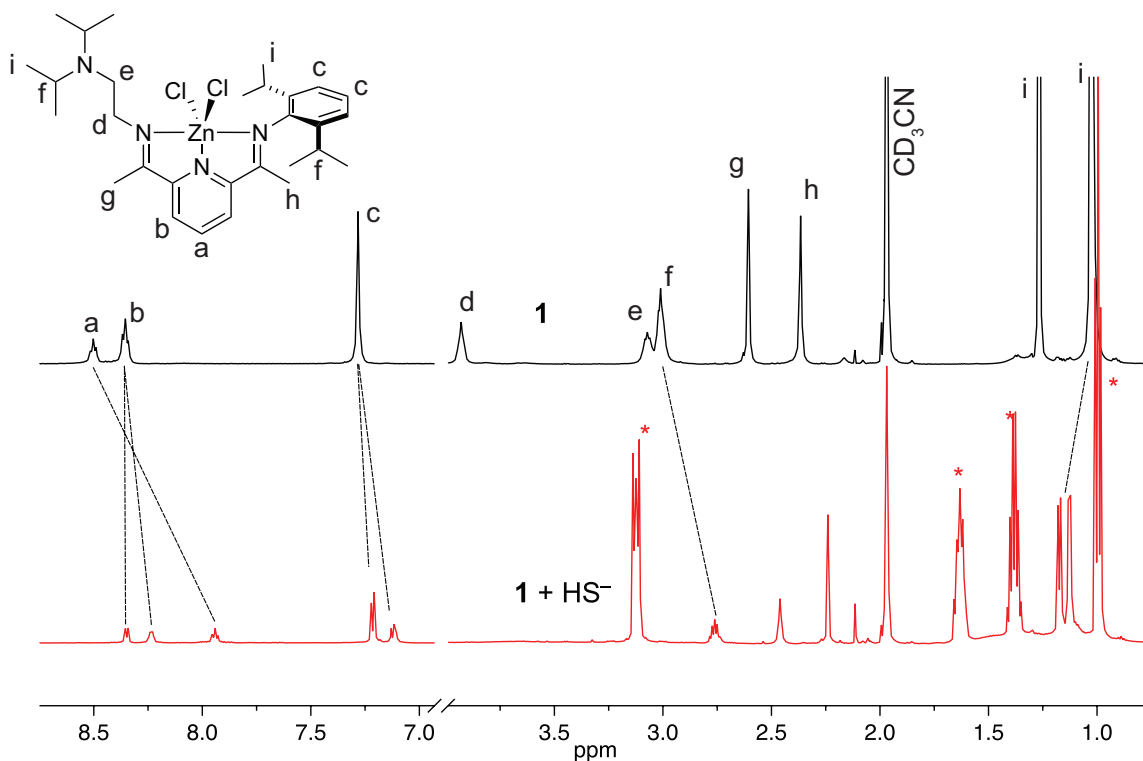


Figure E-7. ^1H NMR spectra of **1** (11.8 mM in CD_3CN before (top, black) and after (bottom, red) addition of 1.5 equiv. of NBU_4SH . Peaks denoted with (*) correspond to the NBU_4^+ counterion. (reprint of figure 2)

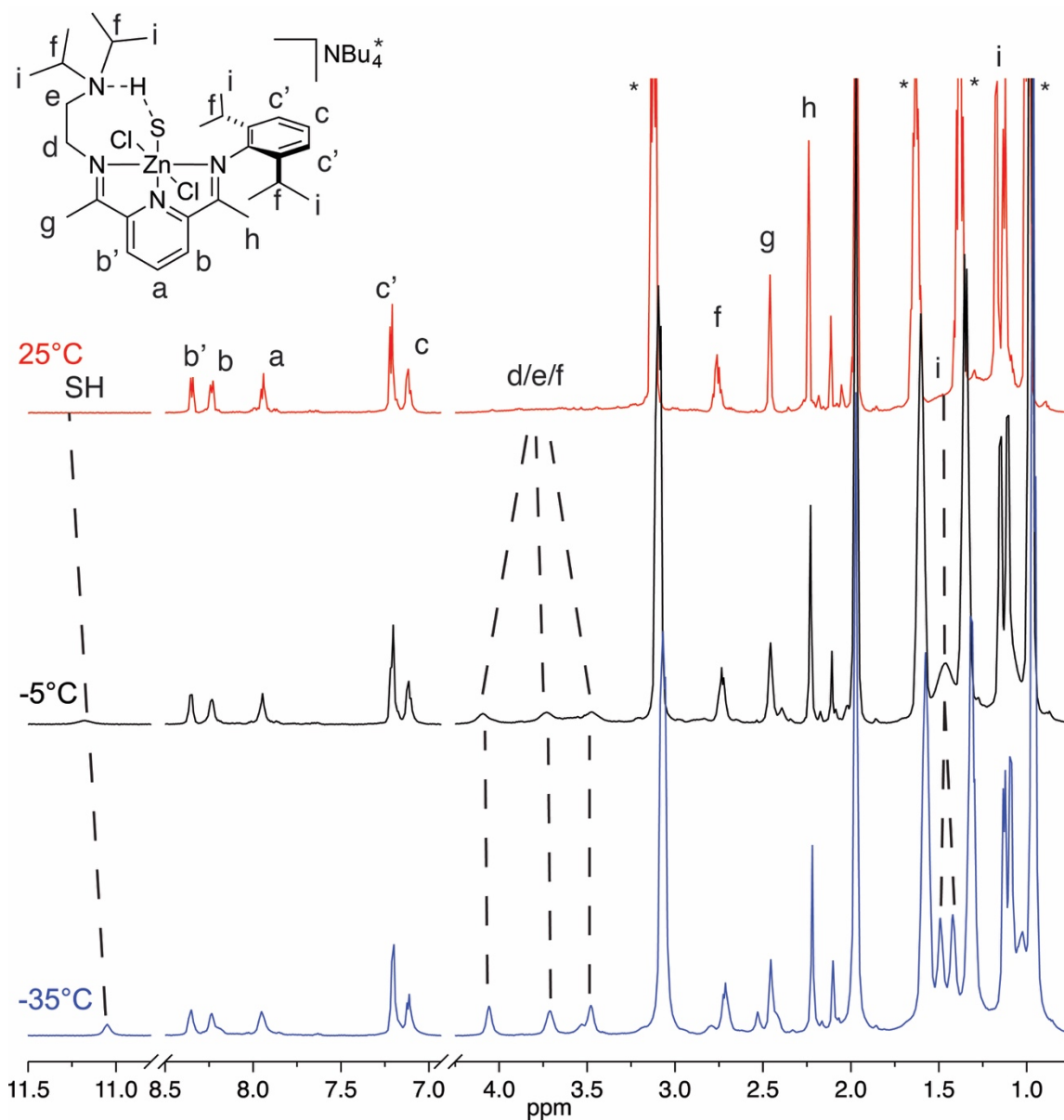


Figure E-8. Variable temperature ^1H NMR spectra of 11.4 mM Zn(didpa)Cl₂, and 1.5 equiv. NBU₄SH in CD₃CN. Cooling to -35 °C results in sharpening and an upfield shift of the broad SH peak to 11.05 ppm. See Figure S6 for an expanded view of the SH peak.

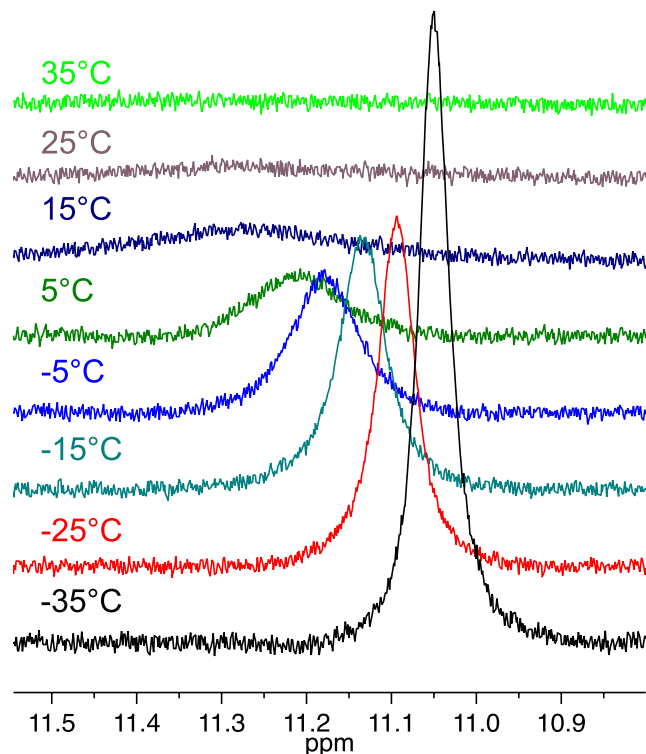


Figure E-9. ^1H NMR spectra of 11.4 mM $\text{Zn}(\text{didpa})\text{Cl}_2$, and 16.7 mM NBu_4SH (1.5 equiv.) in CD_3CN showing the SH resonance upon cooling. All spectra were measured with a 5 second relaxation delay.

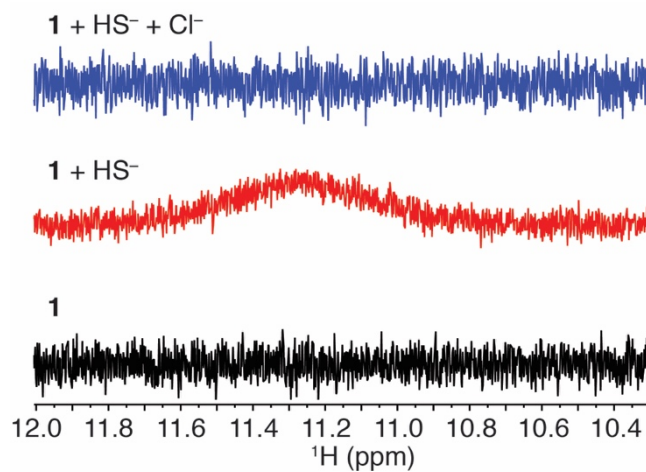


Figure E-10. ^1H NMR spectra of 10.3 mM **1** (black) at 25 °C. Addition of 1.5 equivalents NBu_4SH at 25 °C (red). Addition of 20 equiv. of NBu_4Cl at 25 °C (blue).

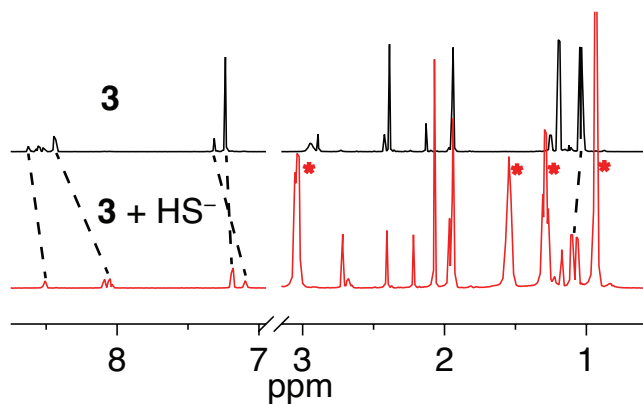


Figure E-11. ¹H NMR spectra of 2.63 mM Zn(*i*PrPDI)Cl₂ and 4.85 mM NBu₄SH in CD₃CN. Formation of a white precipitate was observed during addition of the first two equivalents of sulfide.

Job Plot

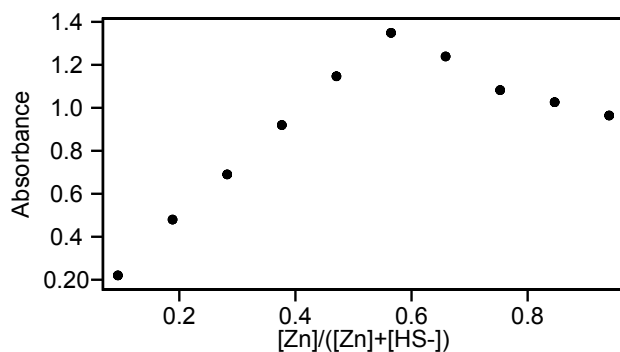


Figure E-12. Job plot of $\text{Zn}(\text{didpa})\text{Cl}_2$ with NBu_4Cl in MeCN at an overall concentration of $412 \mu\text{M}$. The break is consistent with a 1:1 binding event. The plot was corrected for 6.0% excess zinc as determined by addition of TPEN by subtraction of that percentage from the mol ratio of zinc as described in the experimental details above.

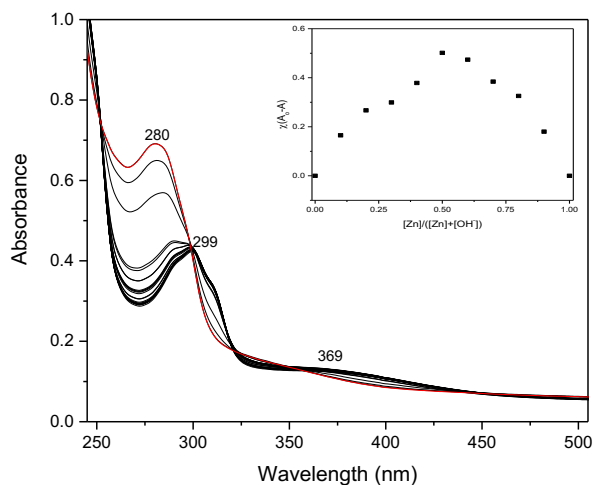


Figure E-13. Titration of $\text{Zn}(\text{didpa})\text{Cl}_2$ ($85.5 \mu\text{M}$, CH_2Cl_2 , black) with tetramethylammonium hydroxide pentahydrate (0.1 equiv. increments up to 3 equivalents, red). The inset shows the Job plot of **1** with tetramethylammonium hydroxide pentahydrate in MeCN at a total concentration of $413 \mu\text{M}$. The break is consistent with 1:1 binding.

APPENDIX F

SUPPORTING INFORMATION: A SYNTHETIC SUPRAMOLECULAR RECEPTOR FOR HYDROSULFIDE ANION

CONTENTS

NMR Titration Experiments	178
UV-Vis Titrations	184
$^{13}\text{C}\{^1\text{H}\}$ NMR Spectra of Non-covalent Host-Guest Complex	196
Deprotonation Control Experiment.....	197
X-Ray Crystallographic Data.....	198

NMR Titration Experiments

Table F-1. Titration of 1 with HS⁻. (Stock [HS⁻] = 19.99 mM)

Entry	Guest (μL)	[1] (M)	[HS ⁻] (M)	Equiv.	δ (ppm)
0	0	9.88E-04	0.00E+00	0.00	8.922
1	5	9.88E-04	1.49E-04	0.15	9.148
2	10	9.88E-04	2.95E-04	0.30	9.429
3	15	9.88E-04	4.39E-04	0.44	9.678
4	20	9.88E-04	5.80E-04	0.59	9.913
5	25	9.88E-04	7.20E-04	0.73	10.113
6	30	9.88E-04	8.57E-04	0.87	10.318
7	35	9.88E-04	9.91E-04	1.00	10.455
8	40	9.88E-04	1.12E-03	1.14	10.550
9	50	9.88E-04	1.38E-03	1.40	10.769
10	60	9.88E-04	1.64E-03	1.66	10.872
11	80	9.88E-04	2.12E-03	2.14	10.983
12	100	9.88E-04	2.57E-03	2.60	11.074
13	150	9.88E-04	3.60E-03	3.64	11.129
14	200	9.88E-04	4.50E-03	4.55	11.171
15	300	9.88E-04	6.00E-03	6.07	11.215
16	500	9.88E-04	8.18E-03	8.28	11.237
17	800	9.88E-04	1.03E-02	10.41	11.244
18	1200	9.88E-04	1.20E-02	12.14	11.184
19	1500	9.88E-04	1.28E-02	13.01	11.176

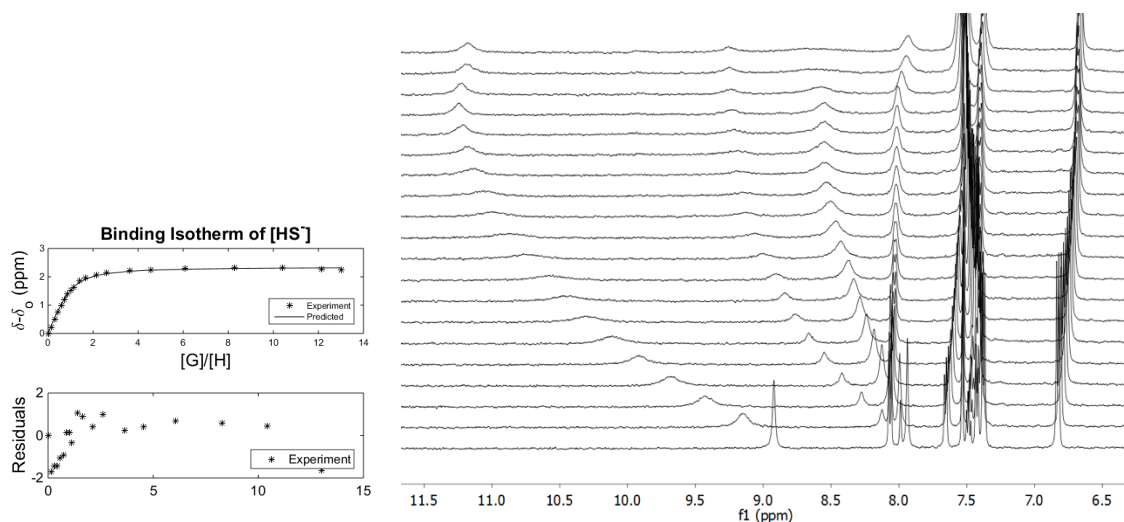


Figure F-1. Binding isotherm for HS⁻ titration of 1 in 10% DMSO-*d*₆/CD₃CN determined by ¹H NMR spectroscopy. ¹H NMR stacked plot of 1 (0.988 mM) titrated with NBU₄SH (0-13 equiv., bottom to top) in 10% DMSO-*d*₆/CD₃CN.

Table F-2. Titration of 1 with Cl⁻. (Stock [Cl⁻] = 44.59 mM)

Entry	Guest (μL)	[1] (M)	[Cl ⁻] (M)	Equiv.	δ (ppm)
0	0	6.49E-04	0.00E+00	0.00	8.921
1	5	6.49E-04	3.68E-04	0.57	9.306
2	10	6.49E-04	7.31E-04	1.13	9.583
3	15	6.49E-04	1.09E-03	1.68	9.771
4	20	6.49E-04	1.44E-03	2.22	9.898
5	25	6.49E-04	1.78E-03	2.75	9.986
6	30	6.49E-04	2.12E-03	3.27	10.050
7	35	6.49E-04	2.46E-03	3.79	10.102
8	40	6.49E-04	2.79E-03	4.29	10.143
9	50	6.49E-04	3.43E-03	5.28	10.197
10	60	6.49E-04	4.05E-03	6.24	10.237
11	80	6.49E-04	5.25E-03	8.08	10.285
12	100	6.49E-04	6.37E-03	9.81	10.316
13	150	6.49E-04	8.92E-03	13.74	10.364
14	200	6.49E-04	1.11E-02	17.17	10.391
15	300	6.49E-04	1.49E-02	22.89	10.423
16	500	6.49E-04	2.03E-02	31.22	10.454
17	800	6.49E-04	2.55E-02	39.25	10.470
18	1200	6.49E-04	2.97E-02	45.79	10.472
19	1500	6.49E-04	3.18E-02	49.06	10.472

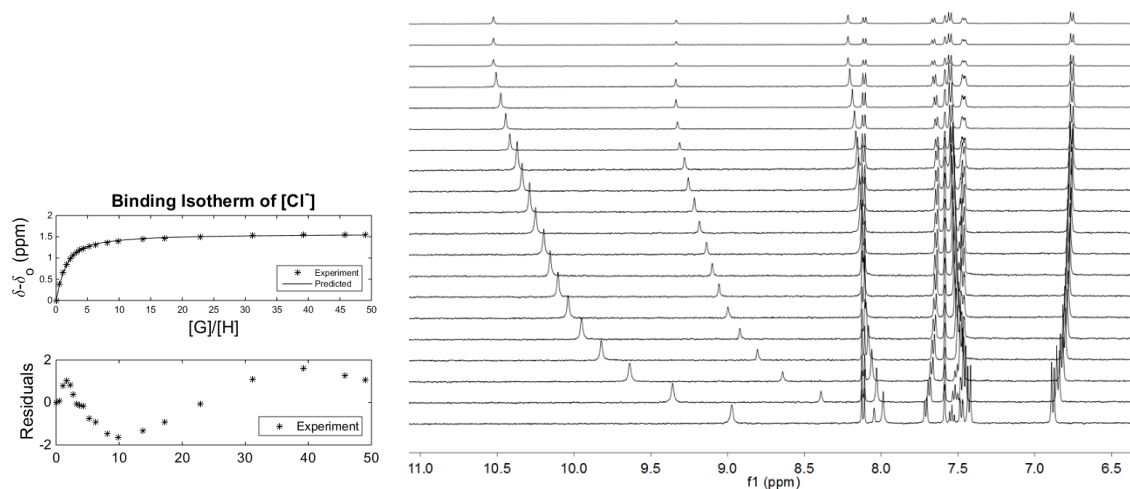
**Figure F-2.** Binding isotherm for Cl⁻ titration of 1 in 10% DMSO-*d*₆/CD₃CN determined by ¹H NMR spectroscopy. ¹H NMR stacked plot of 1 (0.649mM) titrated with NBu₄Cl (0-49 equiv., bottom to top) in 10% DMSO-*d*₆/CD₃CN.

Table F-3. Titration of 2 with HS⁻. (Stock [HS⁻] = 25.40 mM)

Entry	Guest (μL)	[2] (M)	[HS ⁻] (M)	Equiv.	δ (ppm)
0	0	6.81E-04	0.00E+00	0.00	8.920
1	5	6.81E-04	2.10E-04	0.31	9.146
2	10	6.81E-04	4.16E-04	0.61	9.409
3	15	6.81E-04	6.20E-04	0.91	9.673
4	20	6.81E-04	8.20E-04	1.20	9.901
5	25	6.81E-04	1.02E-03	1.49	10.079
6	30	6.81E-04	1.21E-03	1.78	10.222
7	35	6.81E-04	1.40E-03	2.06	10.333
8	40	6.81E-04	1.59E-03	2.33	10.442
9	50	6.81E-04	1.95E-03	2.87	10.579
10	60	6.81E-04	2.31E-03	3.39	10.674
11	80	6.81E-04	2.99E-03	4.39	10.804
12	100	6.81E-04	3.63E-03	5.33	10.883
13	150	6.81E-04	5.08E-03	7.46	11.008
14	200	6.81E-04	6.35E-03	9.33	11.088
15	300	6.81E-04	8.47E-03	12.44	11.179
16	500	6.81E-04	1.15E-02	16.96	11.283
17	800	6.81E-04	1.45E-02	21.33	11.292
18	1200	6.81E-04	1.69E-02	24.88	11.293
19	1600	6.81E-04	1.85E-02	27.14	11.314

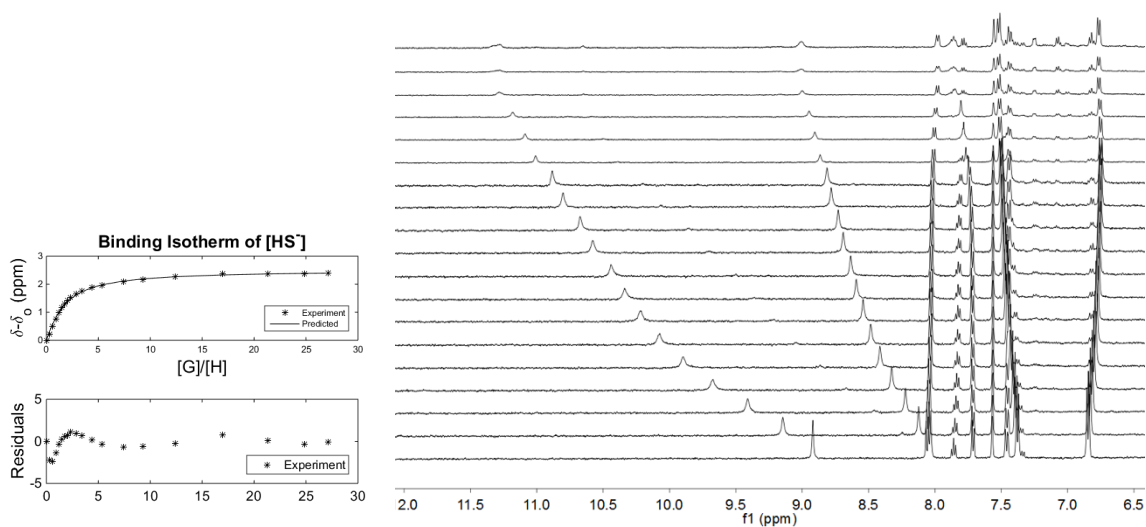
**Figure F-3.** Binding isotherm for HS⁻ titration of 2 in 10% DMSO-*d*₆/CD₃CN determined by ¹H NMR spectroscopy. ¹H NMR stacked plot of 2 (0.681 mM) titrated with NBU₄SH (0-27 equiv., bottom to top) in 10% DMSO-*d*₆/CD₃CN.

Table F-4. Titration of 2 with Cl^- . (Stock $[\text{Cl}^-] = 35.04 \text{ mM}$)

Entry	Guest (μL)	[2] (M)	$[\text{Cl}^-]$ (M)	Equiv.	δ (ppm)
0	0	1.04E-03	0.00E+00	0.00	8.900
1	5	1.04E-03	2.90E-04	0.28	8.994
2	10	1.04E-03	5.74E-04	0.55	9.075
3	15	1.04E-03	8.55E-04	0.82	9.147
4	20	1.04E-03	1.13E-03	1.09	9.214
5	25	1.04E-03	1.40E-03	1.35	9.275
6	30	1.04E-03	1.67E-03	1.60	9.325
7	35	1.04E-03	1.93E-03	1.85	9.370
8	40	1.04E-03	2.19E-03	2.10	9.412
9	50	1.04E-03	2.70E-03	2.59	9.482
10	60	1.04E-03	3.19E-03	3.06	9.544
11	80	1.04E-03	4.12E-03	3.96	9.638
12	100	1.04E-03	5.01E-03	4.81	9.716
13	150	1.04E-03	7.01E-03	6.73	9.854
14	200	1.04E-03	8.76E-03	8.41	9.953
15	300	1.04E-03	1.17E-02	11.21	10.091
16	500	1.04E-03	1.59E-02	15.29	10.193
17	800	1.04E-03	2.00E-02	19.22	10.197
18	1200	1.04E-03	2.34E-02	22.42	10.233
19	1500	1.04E-03	2.50E-02	24.03	10.236

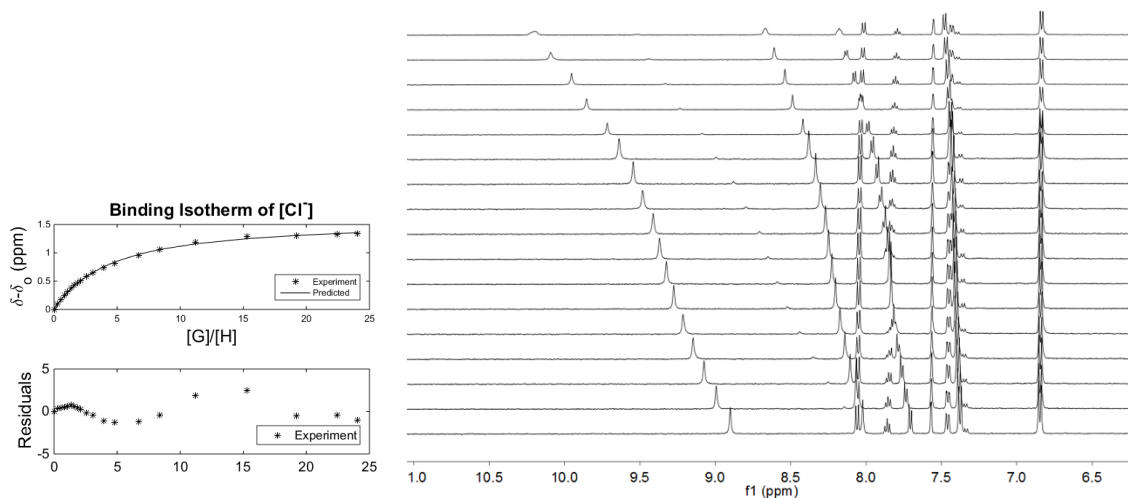
**Figure F-4.** Binding isotherm for Cl^- titration of 2 in 10% $\text{DMSO-}d_6/\text{CD}_3\text{CN}$ determined by ^1H NMR spectroscopy. ^1H NMR stacked plot of 2 (1.04 mM) titrated with NBu_4Cl (0-24 equiv., bottom to top) in 10% $\text{DMSO-}d_6/\text{CD}_3\text{CN}$.

Table F-5. Titration of 3 with HS⁻. (Stock [HS⁻] = 23.7 mM)

Entry	Guest (μL)	[3] (M)	[HS ⁻] (M)	Equiv.	δ (ppm)
0	0	8.64E-04	0.00E+00	0.00	9.165
1	5	8.64E-04	1.96E-04	0.23	9.365
2	10	8.64E-04	3.88E-04	0.45	9.590
3	15	8.64E-04	5.77E-04	0.67	9.785
4	20	8.64E-04	7.64E-04	0.88	9.959
5	25	8.64E-04	9.47E-04	1.10	10.106
6	30	8.64E-04	1.13E-03	1.30	10.234
7	35	8.64E-04	1.30E-03	1.51	10.339
8	40	8.64E-04	1.48E-03	1.71	10.432
9	50	8.64E-04	1.82E-03	2.11	10.572
10	60	8.64E-04	2.15E-03	2.49	10.681
11	80	8.64E-04	2.78E-03	3.22	10.832
12	100	8.64E-04	3.38E-03	3.91	10.937
13	150	8.64E-04	4.73E-03	5.48	11.092
14	200	8.64E-04	5.92E-03	6.85	11.183
15	300	8.64E-04	7.89E-03	9.13	11.295
16	500	8.64E-04	1.08E-02	12.45	11.385
17	800	8.64E-04	1.35E-02	15.66	11.441
18	1200	8.64E-04	1.58E-02	18.27	11.440
19	1600	8.64E-04	1.72E-02	19.93	11.452

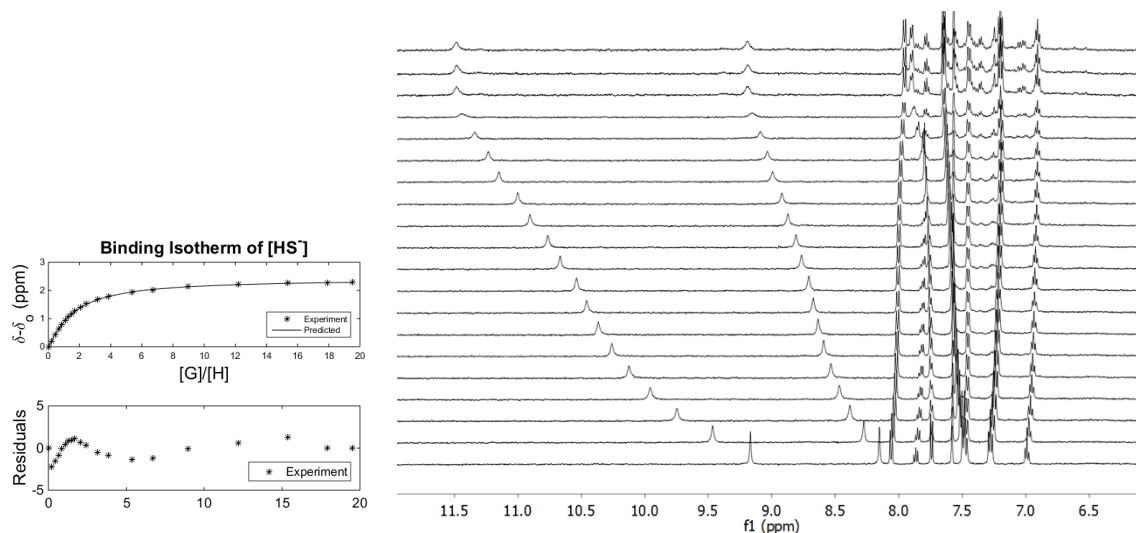
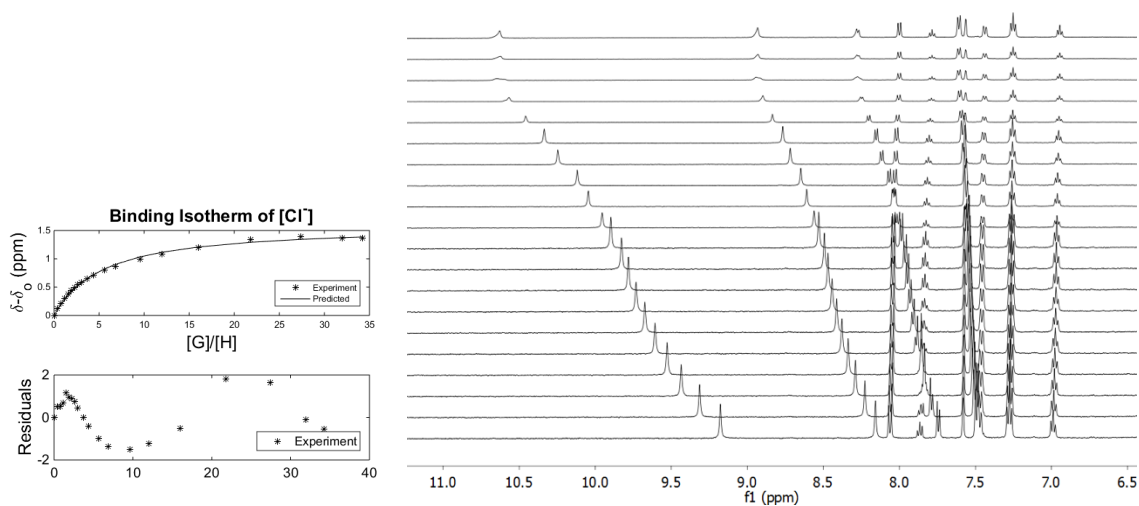
**Figure F-5.** Binding isotherm for HS⁻ titration of 3 in 10% DMSO-*d*₆/CD₃CN determined by ¹H NMR spectroscopy. ¹H NMR stacked plot of 3 (0.864 mM) titrated with NBU₄SH (0-20 equiv., bottom to top) in 10% DMSO-*d*₆/CD₃CN.

Table F-6. Titration of 3 with Cl⁻. (Stock [Cl⁻] = 43.35 mM)

Entry	Guest (μL)	[3] (M)	[Cl ⁻] (M)	Equiv.	δ (ppm)
0	0	9.04E-04	0.00E+00	0.00	9.173
1	5	9.04E-04	3.58E-04	0.40	9.291
2	10	9.04E-04	7.11E-04	0.79	9.383
3	15	9.04E-04	1.06E-03	1.17	9.468
4	20	9.04E-04	1.40E-03	1.55	9.553
5	25	9.04E-04	1.73E-03	1.92	9.612
6	30	9.04E-04	2.06E-03	2.28	9.667
7	35	9.04E-04	2.39E-03	2.64	9.715
8	40	9.04E-04	2.71E-03	3.00	9.754
9	50	9.04E-04	3.33E-03	3.69	9.822
10	60	9.04E-04	3.94E-03	4.36	9.879
11	80	9.04E-04	5.10E-03	5.64	9.970
12	100	9.04E-04	6.19E-03	6.85	10.039
13	150	9.04E-04	8.67E-03	9.59	10.167
14	200	9.04E-04	1.08E-02	11.98	10.255
15	300	9.04E-04	1.44E-02	15.98	10.367
16	500	9.04E-04	1.97E-02	21.79	10.515
17	800	9.04E-04	2.48E-02	27.39	10.562
18	1200	9.04E-04	2.89E-02	31.96	10.544
19	1500	9.04E-04	3.10E-02	34.24	10.544

**Figure F-6.** Binding isotherm for Cl⁻ titration of 3 in 10% DMSO-*d*₆/CD₃CN determined by ¹H NMR spectroscopy. ¹H NMR stacked plot of 3 (0.904 mM) titrated with NBu₄Cl (0-34 equiv., bottom to top) in 10% DMSO-*d*₆/CD₃CN.

UV-Vis Titrations

Table F-7. Titration of 1 with HS⁻.

Entry	[1] (M)	[SH ⁻] (M)	Equiv.	Absorbance (310 nm)	Absorbance (322 nm)	Absorbance (330 nm)	Absorbance (347 nm)
0	1.03E-05	0.00E+00	0.00	0.189	0.215	0.203	0.095
1	1.03E-05	3.30E-06	0.32	0.187	0.212	0.205	0.105
2	1.03E-05	6.59E-06	0.64	0.183	0.211	0.206	0.110
3	1.03E-05	9.89E-06	0.96	0.181	0.208	0.206	0.113
4	1.03E-05	1.32E-05	1.28	0.180	0.208	0.206	0.117
5	1.03E-05	1.65E-05	1.60	0.179	0.207	0.207	0.120
6	1.03E-05	1.98E-05	1.92	0.176	0.205	0.207	0.122
7	1.03E-05	2.30E-05	2.24	0.175	0.204	0.207	0.122
8	1.03E-05	2.63E-05	2.56	0.175	0.204	0.208	0.125
9	1.03E-05	2.96E-05	2.87	0.174	0.204	0.208	0.126
10	1.03E-05	3.29E-05	3.19	0.175	0.205	0.209	0.128
11	1.03E-05	3.94E-05	3.83	0.175	0.204	0.210	0.130
12	1.03E-05	4.60E-05	4.46	0.174	0.203	0.210	0.131
13	1.03E-05	5.25E-05	5.10	0.174	0.204	0.210	0.133
14	1.03E-05	5.90E-05	5.73	0.172	0.203	0.209	0.134
15	1.03E-05	6.56E-05	6.37	0.173	0.204	0.211	0.136
16	1.03E-05	7.86E-05	7.63	0.174	0.205	0.213	0.137
17	1.03E-05	9.15E-05	8.89	0.170	0.201	0.209	0.135
18	1.03E-05	1.04E-04	10.14	0.173	0.204	0.214	0.140
19	1.03E-05	1.17E-04	11.40	0.174	0.204	0.213	0.141
20	1.03E-05	1.30E-04	12.65	0.173	0.204	0.213	0.140
21	1.03E-05	1.56E-04	15.14	0.173	0.203	0.213	0.140
22	1.03E-05	1.81E-04	17.62	0.174	0.205	0.213	0.141
23	1.03E-05	2.07E-04	20.08	0.176	0.206	0.216	0.143
24	1.03E-05	2.32E-04	22.54	0.173	0.204	0.213	0.141
25	1.03E-05	2.57E-04	24.98	0.174	0.204	0.213	0.141

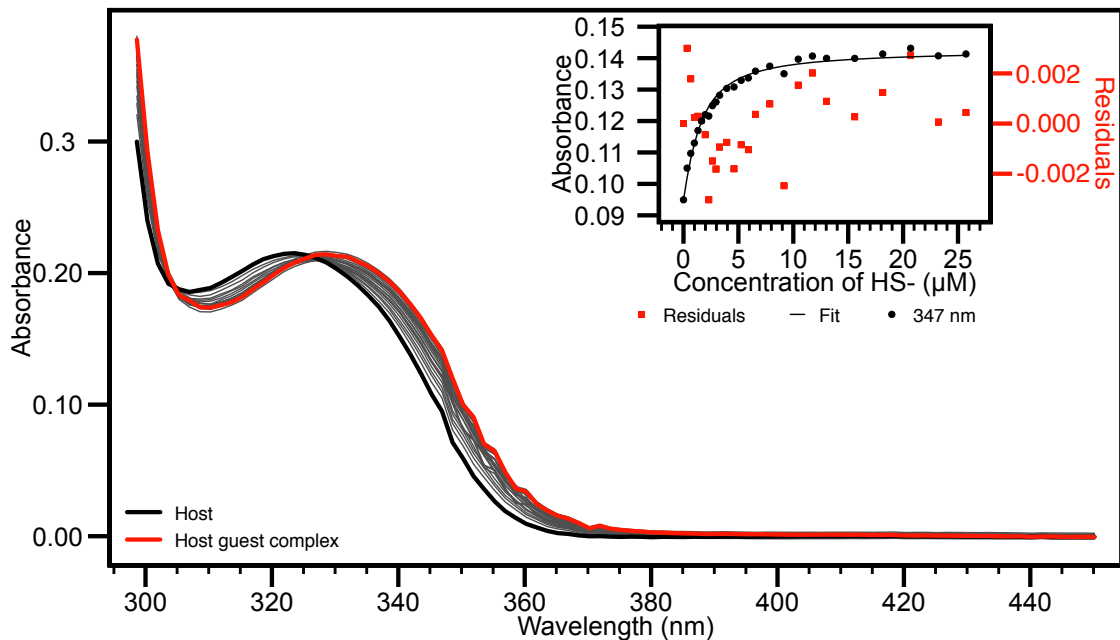


Figure F-7. UV-Vis titration of 1 with HS⁻ in MeCN. HS⁻ was incrementally added to a 10.3 μM solution of 1. Inset: Representative curve at 333 nm: black dots are data collected, line is experimental fit, and red dots are residuals, corresponding to the right (red) axis.

Table F-8. Titration of 1 with Cl⁻.

Entry	[1] (M)	[Cl ⁻] (M)	Equiv.	Absorbance (335 nm)	Absorbance (338 nm)	Absorbance (340 nm)	Absorbance (343 nm)
0	1.03E-05	0.00E+00	0.00	0.192	0.172	0.160	0.132
1	1.03E-05	1.56E-06	0.15	0.193	0.174	0.161	0.133
2	1.03E-05	3.12E-06	0.30	0.194	0.175	0.163	0.134
3	1.03E-05	4.67E-06	0.45	0.195	0.176	0.164	0.136
4	1.03E-05	6.23E-06	0.60	0.197	0.177	0.166	0.137
5	1.03E-05	7.79E-06	0.75	0.196	0.177	0.165	0.137
6	1.03E-05	1.09E-05	1.05	0.197	0.178	0.166	0.138
7	1.03E-05	1.40E-05	1.35	0.200	0.181	0.169	0.141
8	1.03E-05	1.71E-05	1.65	0.202	0.183	0.172	0.143
9	1.03E-05	2.02E-05	1.95	0.204	0.185	0.174	0.146
10	1.03E-05	2.33E-05	2.25	0.204	0.186	0.174	0.146
11	1.03E-05	2.64E-05	2.55	0.206	0.187	0.176	0.149
12	1.03E-05	3.25E-05	3.15	0.208	0.190	0.179	0.151
13	1.03E-05	3.87E-05	3.74	0.210	0.192	0.181	0.154
14	1.03E-05	4.48E-05	4.34	0.211	0.194	0.182	0.155
15	1.03E-05	5.09E-05	4.93	0.213	0.196	0.185	0.158
16	1.03E-05	5.70E-05	5.52	0.214	0.197	0.186	0.158
17	1.03E-05	6.31E-05	6.11	0.214	0.198	0.187	0.160
18	1.03E-05	6.92E-05	6.69	0.216	0.200	0.188	0.161
19	1.03E-05	7.52E-05	7.28	0.216	0.200	0.189	0.162
20	1.03E-05	8.73E-05	8.45	0.218	0.202	0.191	0.164
21	1.03E-05	9.93E-05	9.61	0.219	0.203	0.192	0.166
22	1.03E-05	1.11E-04	10.76	0.219	0.203	0.192	0.165
23	1.03E-05	1.23E-04	11.91	0.221	0.205	0.195	0.168
24	1.03E-05	1.35E-04	13.06	0.221	0.206	0.195	0.169
25	1.03E-05	1.47E-04	14.19	0.221	0.205	0.195	0.168
26	1.03E-05	1.58E-04	15.33	0.222	0.206	0.196	0.169
27	1.03E-05	1.70E-04	16.45	0.221	0.206	0.195	0.168
28	1.03E-05	1.82E-04	17.57	0.222	0.206	0.196	0.170
29	1.03E-05	1.93E-04	18.69	0.222	0.207	0.196	0.170
30	1.03E-05	2.05E-04	19.80	0.222	0.207	0.196	0.170

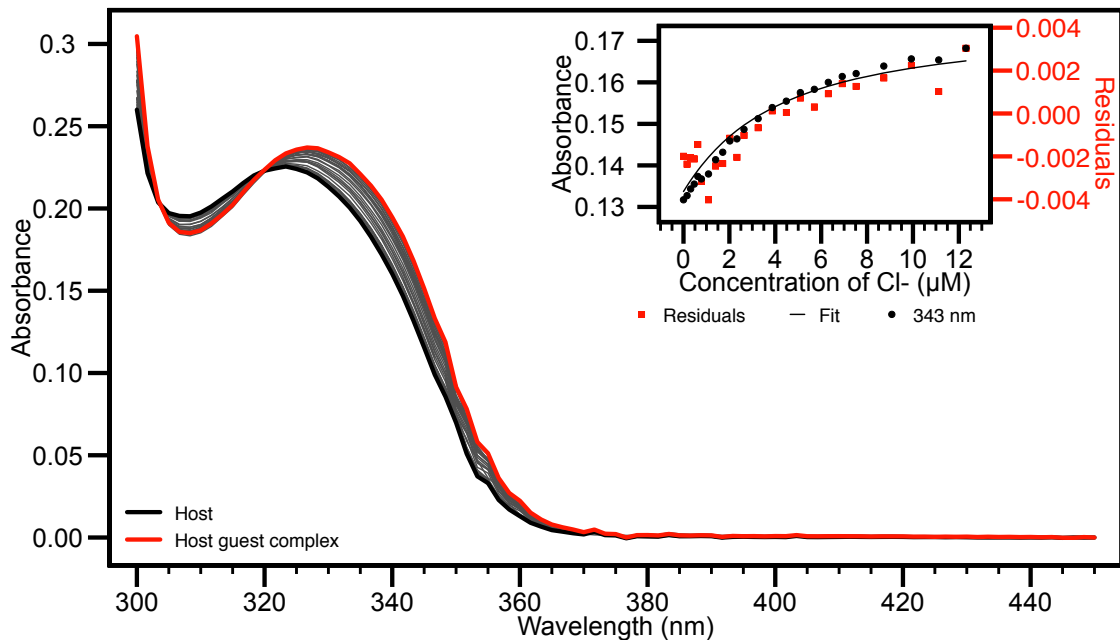


Figure F-8. UV-Vis titration of 1 with Cl⁻ in MeCN. Cl⁻ was incrementally added to a 10.3 μM solution of 1. Inset: Representative curve at 343 nm: black dots are data collected, line is experimental fit, and red dots are residuals, corresponding to the right (red) axis.

Table F-9. Titration of 2 with HS⁻.

Entry	[2] (M)	[SH ⁻] (M)	Equiv.	Absorbance (327 nm)	Absorbance (333 nm)	Absorbance (360 nm)	Absorbance (375 nm)
0	1.06E-05	0.00E+00	0.00	0.220	0.224	0.095	0.012
1	1.06E-05	3.24E-06	0.31	0.219	0.223	0.097	0.013
2	1.06E-05	6.47E-06	0.61	0.218	0.222	0.098	0.014
3	1.06E-05	9.70E-06	0.92	0.218	0.221	0.099	0.015
4	1.06E-05	1.29E-05	1.22	0.216	0.219	0.101	0.016
5	1.06E-05	1.62E-05	1.53	0.215	0.219	0.102	0.016
6	1.06E-05	1.94E-05	1.83	0.214	0.217	0.103	0.018
7	1.06E-05	2.26E-05	2.14	0.214	0.217	0.105	0.020
8	1.06E-05	2.59E-05	2.44	0.213	0.216	0.106	0.021
9	1.06E-05	2.91E-05	2.75	0.212	0.215	0.107	0.021
10	1.06E-05	3.23E-05	3.05	0.212	0.214	0.108	0.023
11	1.06E-05	3.55E-05	3.36	0.211	0.213	0.109	0.023
12	1.06E-05	3.88E-05	3.66	0.210	0.213	0.110	0.024
13	1.06E-05	4.52E-05	4.27	0.208	0.210	0.111	0.026
14	1.06E-05	5.16E-05	4.88	0.207	0.210	0.113	0.027
15	1.06E-05	5.81E-05	5.48	0.207	0.210	0.115	0.029
16	1.06E-05	6.45E-05	6.09	0.206	0.208	0.115	0.029
17	1.06E-05	7.09E-05	6.70	0.205	0.207	0.116	0.030
18	1.06E-05	7.74E-05	7.31	0.206	0.208	0.118	0.033
19	1.06E-05	8.38E-05	7.91	0.204	0.206	0.117	0.031
20	1.06E-05	9.02E-05	8.52	0.203	0.205	0.118	0.032
21	1.06E-05	1.03E-04	9.73	0.200	0.203	0.120	0.035
22	1.06E-05	1.16E-04	10.94	0.200	0.202	0.122	0.036
23	1.06E-05	1.29E-04	12.15	0.200	0.203	0.123	0.036
24	1.06E-05	1.41E-04	13.35	0.199	0.201	0.123	0.038
25	1.06E-05	1.54E-04	14.56	0.198	0.201	0.123	0.037
26	1.06E-05	1.80E-04	16.96	0.198	0.200	0.125	0.039
27	1.06E-05	2.05E-04	19.36	0.197	0.200	0.125	0.040
28	1.06E-05	2.30E-04	21.75	0.198	0.200	0.127	0.040
29	1.06E-05	2.56E-04	24.14	0.197	0.199	0.127	0.041
30	1.06E-05	2.81E-04	26.52	0.197	0.200	0.128	0.042
31	1.06E-05	3.31E-04	31.26	0.197	0.200	0.130	0.042
32	1.06E-05	3.81E-04	35.98	0.196	0.198	0.131	0.043
33	1.06E-05	4.31E-04	40.68	0.196	0.198	0.131	0.044
34	1.06E-05	4.80E-04	45.35	0.195	0.198	0.131	0.044
35	1.06E-05	5.30E-04	50.00	0.195	0.197	0.132	0.044
36	1.06E-05	5.79E-04	54.62	0.194	0.196	0.133	0.044
37	1.06E-05	6.27E-04	59.23	0.194	0.197	0.133	0.044

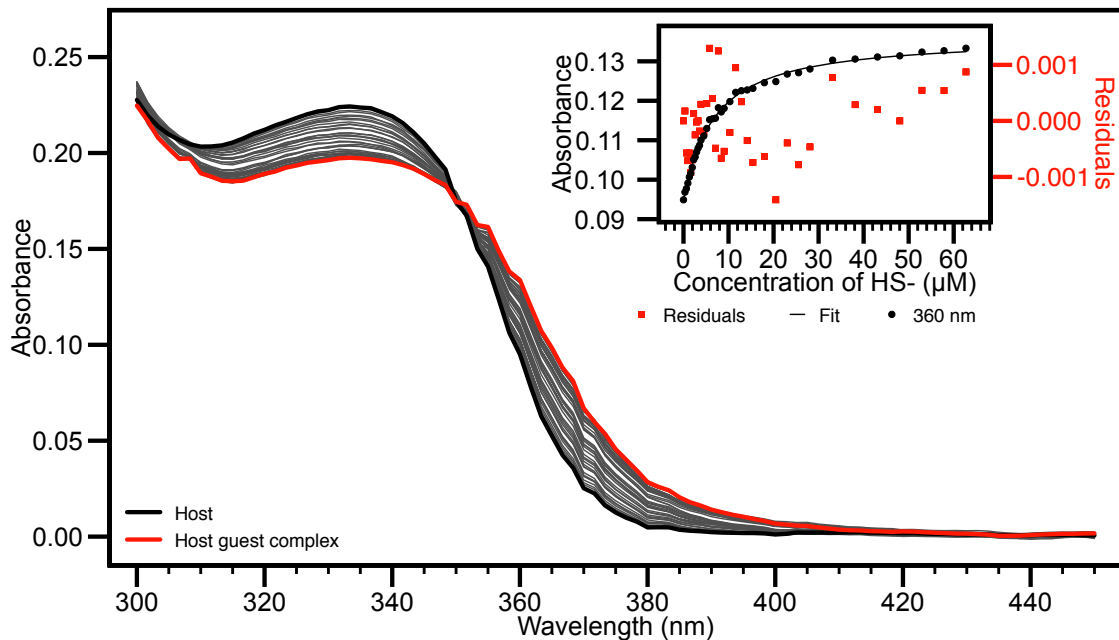


Figure F-9. UV-Vis titration of 2 with HS⁻ in MeCN. HS⁻ was incrementally added to a 10.6 μM solution of 2. Inset: Representative curve at 360 nm: black dots are data collected, line is experimental fit, and red dots are residuals, corresponding to the right (red) axis.

Table F-10. Titration of 2 with Cl⁻.

Entry	[2] (M)	[Cl ⁻] (M)	Equiv.	Absorbance (352 nm)	Absorbance (355 nm)	Absorbance (357 nm)	Absorbance (360 nm)
0	1.06E-05	0.00E+00	0.00	0.169	0.150	0.137	0.115
1	1.06E-05	3.59E-06	0.34	0.170	0.150	0.137	0.115
2	1.06E-05	7.18E-06	0.68	0.170	0.150	0.137	0.116
3	1.06E-05	1.43E-05	1.35	0.171	0.151	0.138	0.116
4	1.06E-05	2.15E-05	2.03	0.170	0.151	0.138	0.116
5	1.06E-05	2.87E-05	2.71	0.173	0.154	0.140	0.118
6	1.06E-05	3.58E-05	3.38	0.172	0.152	0.139	0.117
7	1.06E-05	4.29E-05	4.05	0.171	0.152	0.139	0.117
8	1.06E-05	5.00E-05	4.73	0.173	0.153	0.140	0.118
9	1.06E-05	5.72E-05	5.40	0.172	0.153	0.140	0.118
10	1.06E-05	6.43E-05	6.07	0.173	0.154	0.141	0.119
11	1.06E-05	7.14E-05	6.74	0.174	0.155	0.142	0.120
12	1.06E-05	7.84E-05	7.41	0.174	0.154	0.141	0.119
13	1.06E-05	9.26E-05	8.74	0.175	0.155	0.142	0.120
14	1.06E-05	1.07E-04	10.07	0.175	0.156	0.143	0.121
15	1.06E-05	1.21E-04	11.40	0.176	0.157	0.143	0.121
16	1.06E-05	1.35E-04	12.73	0.176	0.157	0.144	0.121
17	1.06E-05	1.49E-04	14.05	0.177	0.158	0.145	0.122
18	1.06E-05	1.63E-04	15.37	0.178	0.159	0.146	0.123
19	1.06E-05	1.77E-04	16.69	0.178	0.159	0.146	0.124
20	1.06E-05	1.91E-04	18.00	0.178	0.159	0.146	0.124
21	1.06E-05	2.18E-04	20.61	0.179	0.160	0.147	0.125
22	1.06E-05	2.46E-04	23.21	0.180	0.162	0.149	0.126
23	1.06E-05	2.73E-04	25.80	0.181	0.162	0.149	0.126
24	1.06E-05	3.01E-04	28.38	0.182	0.163	0.150	0.127
25	1.06E-05	3.28E-04	30.94	0.184	0.165	0.151	0.129
26	1.06E-05	3.55E-04	33.49	0.183	0.165	0.152	0.129
27	1.06E-05	3.82E-04	36.03	0.185	0.166	0.153	0.131
28	1.06E-05	4.08E-04	38.56	0.185	0.166	0.153	0.130
29	1.06E-05	4.35E-04	41.07	0.186	0.168	0.155	0.132
30	1.06E-05	4.61E-04	43.57	0.186	0.168	0.155	0.132
31	1.06E-05	4.88E-04	46.06	0.186	0.168	0.155	0.132
32	1.06E-05	5.14E-04	48.53	0.186	0.168	0.155	0.132
33	1.06E-05	5.40E-04	51.00	0.188	0.169	0.156	0.133
34	1.06E-05	5.66E-04	53.45	0.188	0.169	0.156	0.133

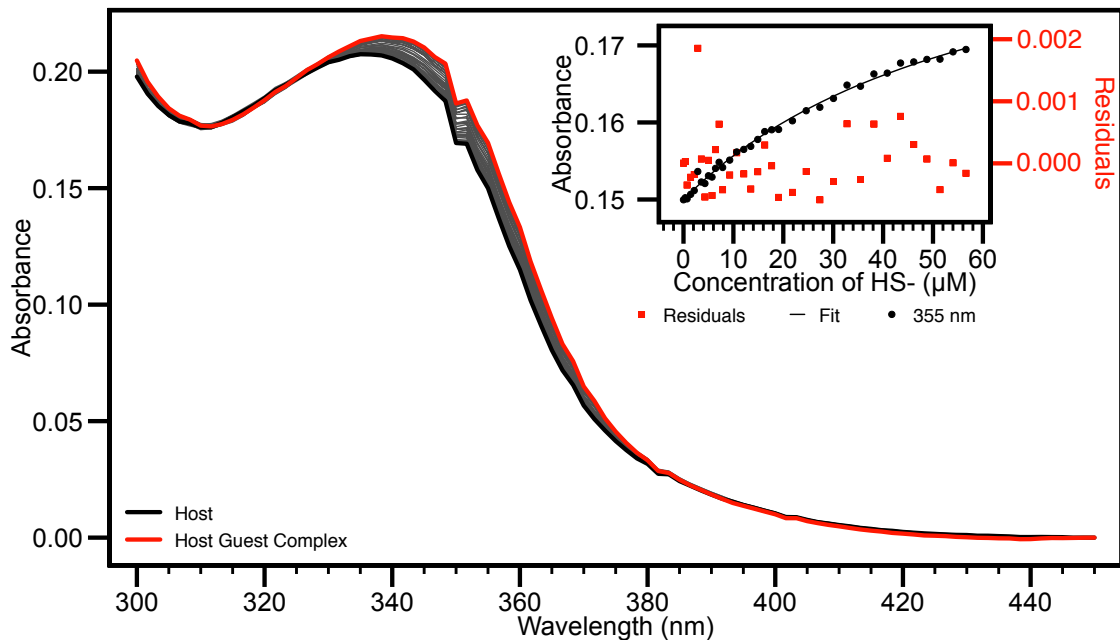


Figure F-10. UV-Vis titration of 2 with Cl⁻ in MeCN. Cl⁻ was incrementally added to a 10.6 μM solution of 2. Inset: Representative curve at 355 nm: black dots are data collected, line is experimental fit, and red dots are residuals, corresponding to the right (red) axis.

Table F-11. Titration of 3 with HS⁻.

Entry	[3] (M)	[HS ⁻] (M)	Equiv.	Absorbance (324 nm)	Absorbance (333 nm)
0	1.07E-05	0.00E+00	0.00	0.2286	0.2370
1	1.07E-05	1.44E-06	0.13	0.2285	0.2347
2	1.07E-05	2.87E-06	0.27	0.2283	0.2350
3	1.07E-05	4.31E-06	0.40	0.2279	0.2351
4	1.07E-05	5.74E-06	0.54	0.2267	0.2337
5	1.07E-05	7.17E-06	0.67	0.2254	0.2321
6	1.07E-05	8.60E-06	0.80	0.2263	0.2326
7	1.07E-05	1.00E-05	0.93	0.2260	0.2329
8	1.07E-05	1.15E-05	1.07	0.2253	0.2312
9	1.07E-05	1.29E-05	1.21	0.2255	0.2315
10	1.07E-05	1.43E-05	1.34	0.2243	0.2301
11	1.07E-05	1.57E-05	1.47	0.2238	0.2285
12	1.07E-05	1.72E-05	1.61	0.2243	0.2294
13	1.07E-05	1.86E-05	1.74	0.2243	0.2290
14	1.07E-05	2.00E-05	1.87	0.2229	0.2277
15	1.07E-05	2.14E-05	2.00	0.2232	0.2271
16	1.07E-05	2.43E-05	2.27	0.2221	0.2259
17	1.07E-05	2.71E-05	2.53	0.2212	0.2248
18	1.07E-05	3.00E-05	2.80	0.2200	0.2237
19	1.07E-05	3.28E-05	3.07	0.2188	0.2225
20	1.07E-05	3.56E-05	3.33	0.2189	0.2219
21	1.07E-05	3.85E-05	3.60	0.2200	0.2228
22	1.07E-05	4.13E-05	3.86	0.2194	0.2222
23	1.07E-05	4.69E-05	4.38	0.2190	0.2211
24	1.07E-05	5.25E-05	4.91	0.2159	0.2171
25	1.07E-05	5.82E-05	5.44	0.2191	0.2208
26	1.07E-05	6.37E-05	5.95	0.2183	0.2194
27	1.07E-05	6.93E-05	6.48	0.2179	0.2196
28	1.07E-05	8.05E-05	7.52	0.2150	0.2167
29	1.07E-05	9.15E-05	8.55	0.2159	0.2173
30	1.07E-05	1.03E-04	9.58	0.2145	0.2149
31	1.07E-05	1.13E-04	10.61	0.2127	0.2132
32	1.07E-05	1.24E-04	11.63	0.2142	0.2150
33	1.07E-05	1.35E-04	12.64	0.2113	0.2104
34	1.07E-05	1.46E-04	13.65	0.2138	0.2143
35	1.07E-05	1.57E-04	14.65	0.2130	0.2133
36	1.07E-05	1.67E-04	15.65	0.2125	0.2126
37	1.07E-05	1.78E-04	16.65	0.2142	0.2151
38	1.07E-05	1.89E-04	17.64	0.2130	0.2135
39	1.07E-05	1.99E-04	18.62	0.2116	0.2116
40	1.07E-05	2.10E-04	19.60	0.2120	0.2122

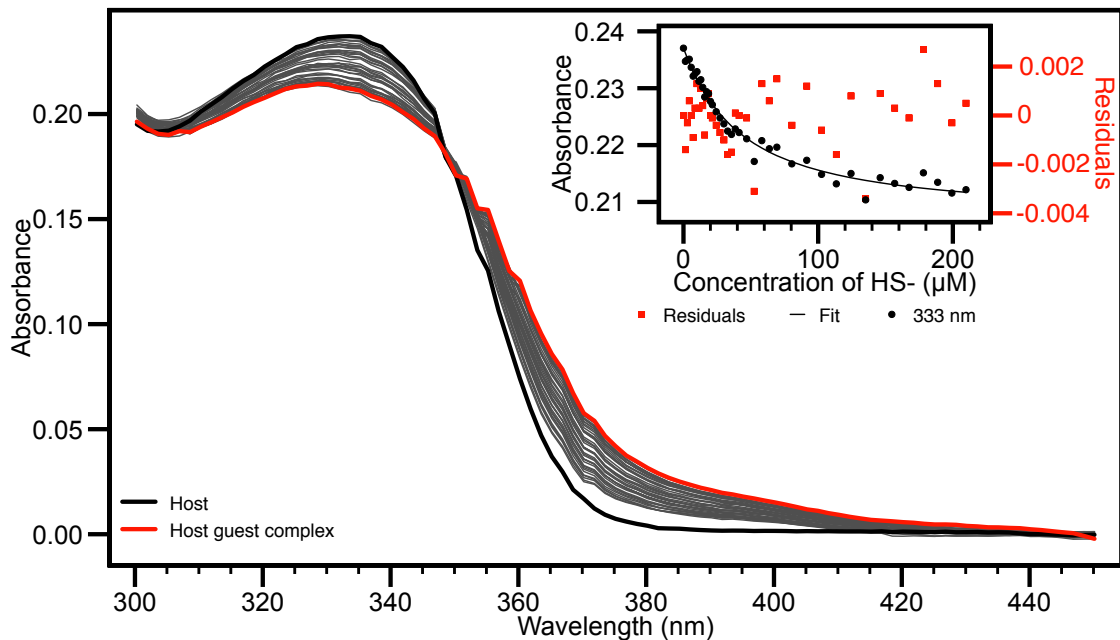


Figure F-11. UV-Vis titration of 3 with HS⁻ in MeCN. HS⁻ was incrementally added to a 10.7 μM solution of 3. Inset: Representative curve at 333 nm: black dots are data collected, line is experimental fit, and red dots are residuals, corresponding to the right (red) axis.

Table F-12. Titration of 3 with Cl⁻.

Entry	[3] (M)	[Cl ⁻] (M)	Equiv.	Absorbance (350 nm)	Absorbance (353 nm)	Absorbance (355 nm)	Absorbance (360 nm)
0	1.08E-05	0.00E+00	0.00	0.180	0.145	0.128	0.081
1	1.08E-05	2.03E-05	1.88	0.182	0.148	0.130	0.082
2	1.08E-05	4.07E-05	3.77	0.178	0.149	0.133	0.083
3	1.08E-05	6.10E-05	5.65	0.185	0.151	0.133	0.084
4	1.08E-05	8.12E-05	7.52	0.181	0.152	0.136	0.087
5	1.08E-05	1.01E-04	9.40	0.181	0.153	0.136	0.087
6	1.08E-05	1.42E-04	13.14	0.184	0.155	0.139	0.089
7	1.08E-05	1.82E-04	16.87	0.186	0.157	0.140	0.091
8	1.08E-05	2.22E-04	20.60	0.193	0.159	0.141	0.091
9	1.08E-05	2.63E-04	24.31	0.187	0.159	0.143	0.092
10	1.08E-05	3.03E-04	28.02	0.189	0.161	0.145	0.094
11	1.08E-05	3.82E-04	35.40	0.198	0.163	0.145	0.094
12	1.08E-05	4.62E-04	42.75	0.195	0.166	0.150	0.098
13	1.08E-05	5.41E-04	50.06	0.196	0.168	0.152	0.100
14	1.08E-05	6.19E-04	57.33	0.200	0.172	0.155	0.102
15	1.08E-05	6.97E-04	64.57	0.200	0.172	0.155	0.103
16	1.08E-05	7.75E-04	71.78	0.201	0.173	0.157	0.103
17	1.08E-05	8.52E-04	78.95	0.202	0.173	0.157	0.104
18	1.08E-05	9.30E-04	86.08	0.207	0.174	0.156	0.103
19	1.08E-05	1.01E-03	93.18	0.205	0.176	0.160	0.106
20	1.08E-05	1.10E-03	102.01	0.205	0.178	0.161	0.107
21	1.08E-05	1.20E-03	110.78	0.209	0.180	0.164	0.109
22	1.08E-05	1.29E-03	119.50	0.207	0.180	0.163	0.109
23	1.08E-05	1.38E-03	128.17	0.208	0.181	0.165	0.110
24	1.08E-05	1.48E-03	136.79	0.209	0.182	0.165	0.110
25	1.08E-05	1.57E-03	145.35	0.214	0.186	0.170	0.115
26	1.08E-05	1.66E-03	153.87	0.212	0.185	0.168	0.114
27	1.08E-05	1.75E-03	162.33	0.212	0.184	0.168	0.113
28	1.08E-05	1.84E-03	170.75	0.214	0.187	0.170	0.115
29	1.08E-05	1.93E-03	179.11	0.214	0.188	0.171	0.116
30	1.08E-05	2.02E-03	187.43	0.216	0.189	0.171	0.116

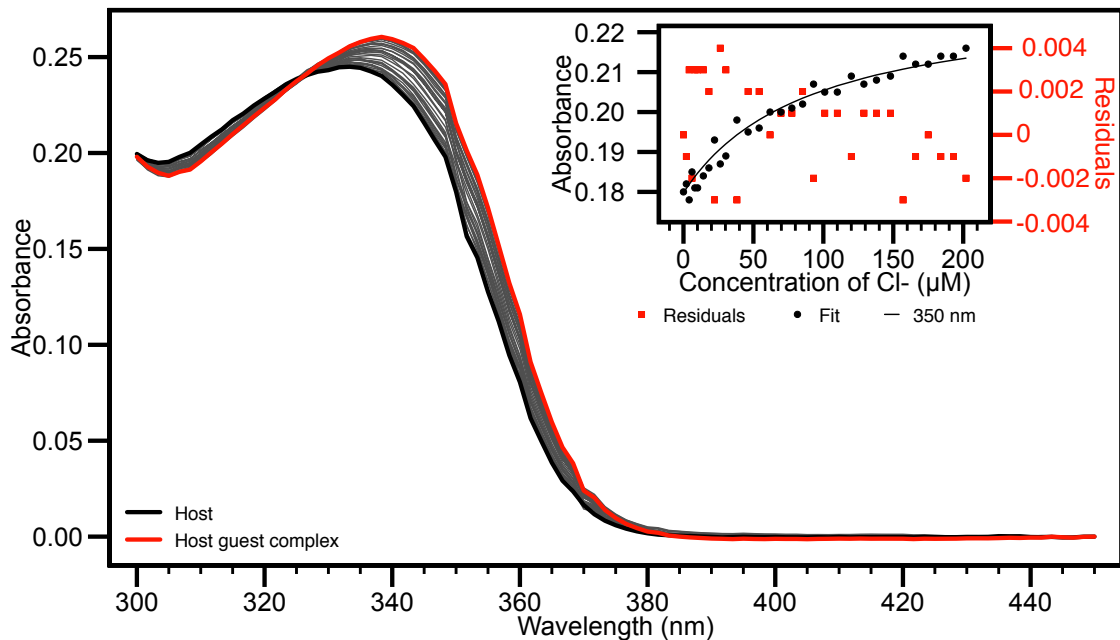


Figure F-12. UV-Vis titration of 3 with Cl⁻ in MeCN. Cl⁻ was incrementally added to a 10.8 μM solution of 3. Inset: Representative curve at 350 nm: black dots are data collected, line is experimental fit, and red dots are residuals, corresponding to the right (red) axis.

$^{13}\text{C}\{^1\text{H}\}$ NMR Spectra of Non-covalent Host-Guest Complex

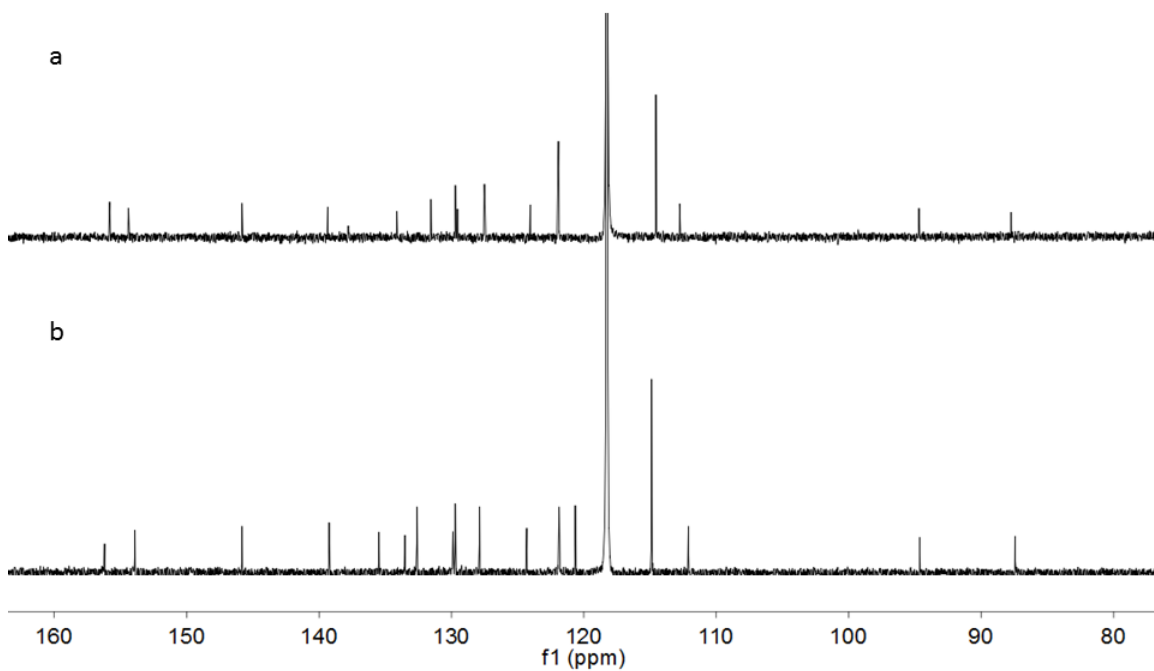


Figure F-13. a, $^{13}\text{C}\{^1\text{H}\}$ NMR spectrum of a 2.318 mM solution of **1** with addition of 10 equivalents of NBu_4SH . ^{13}C NMR (151 MHz, CD_3CN) δ 154.97, 153.56, 144.98, 138.51, 136.94, 133.28, 130.71, 128.86, 128.70, 126.68, 123.21, 121.14, 121.08, 113.72, 111.92, 93.85, 86.89. b, $^{13}\text{C}\{^1\text{H}\}$ NMR spectrum of a 2.318 mM solution of **1**. ^{13}C NMR (151 MHz, CD_3CN) δ 155.36, 153.07, 144.98, 138.39, 134.64, 132.68, 131.76, 129.06, 128.87, 127.03, 123.48, 121.03, 119.81, 114.05, 111.26, 93.80, 86.60.

Deprotonation Control Experiment

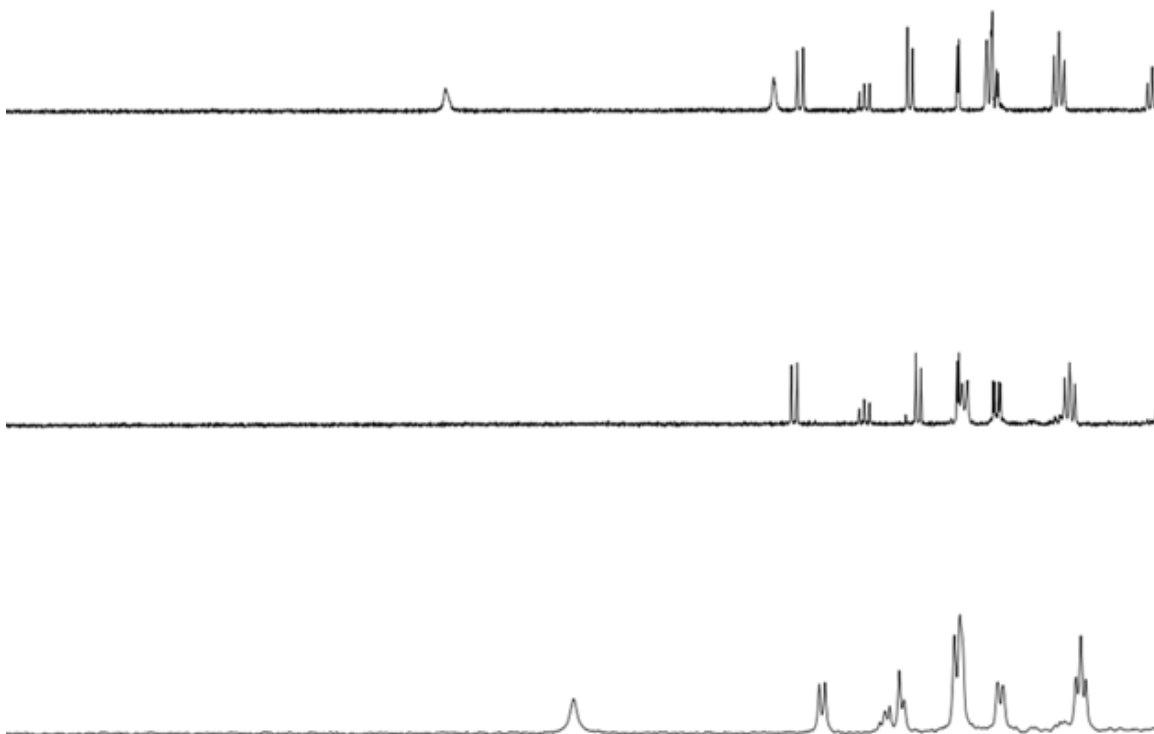


Figure F-14. a ^1H NMR spectrum of a 1.5 mM solution of 3. b ^1H NMR spectrum of a 1.5 mM solution of 3 with 150 mM solution of 1,8-diazabicyclo[5.4.0]undec-7-ene (DBU). This results in the disappearance of urea protons NH_b and NH_c , as well as upfield shifting of remaining aryl protons. c 1.5 mM of 3 with 3.74 mM of NBu_4SH . Spectrum of the host-guest complex bears a marked difference to the deprotonated host.

X-Ray Crystallographic Data

Table F-13. Crystal data and structure refinement for 1 + HS⁻.

1 + NBu ₄ SH + THF	
Empirical formula	C ₆₆ H ₉₁ N ₅ O ₅ S [C ₄₆ H ₄₆ N ₄ O ₄][C ₁₆ H ₃₆ N][C ₄ H ₈ O][S]
Formula weight	1066.49
Wavelength (Å)	1.54178
Temperature (K)	173(2)
Crystal System	Orthorhombic
Crystal system, space group	P n a 2 ₁
Hall group	P 2c -2n
Unit cell dimensions (Å)	a = 24.5943(5) b = 9.7176(2) c = 25.6717(4) α = β = γ = 90°
Volume (Å ³)	6135.5(2)
Z	4
ρ (mm ⁻¹)	1.155
μ(Cu) (mm ⁻¹)	0.870
F(000)	2312.0
Crystal Size (mm x mm x mm)	0.18 x 0.16 x 0.03
Limiting indices	-29 ≤ h ≤ 29; -11 ≤ k ≤ 11; -30 ≤ l ≤ 30
θ range (°)	3.44 – 66.55
2θ _{max} (°)	
Completeness to ϕ	99.7
Total reflections	63889
Independent reflections	10802
R _{int}	0.0557
data/restraints/param	10802/1/715
max, min transmission	0.7528, 0.6436
R1 (wR2) [I > 2σ(I)]	0.0451 (0.1125)
R1 (wR2)	0.0562 (0.1209)
GOF (F ²)	1.018
Max, min peaks (e Å ⁻³)	0.275, -0.294

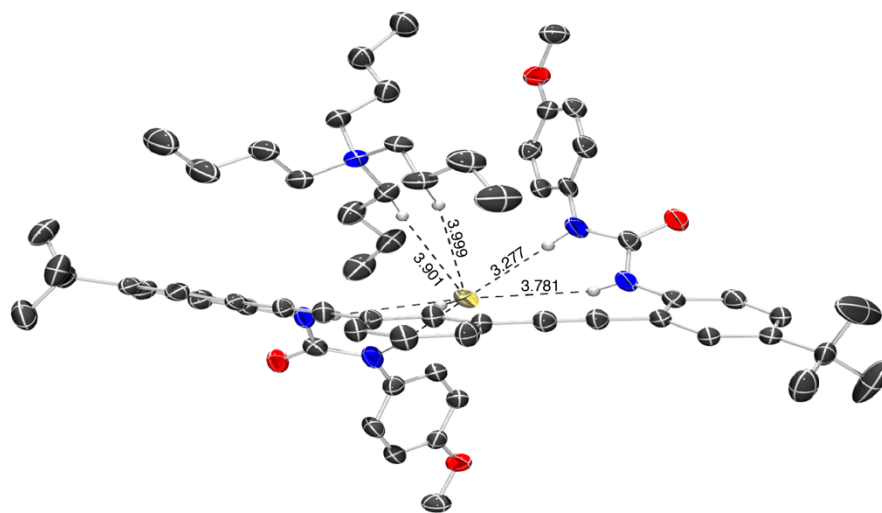


Figure F-15. ORTEP representation of the crystal structure of 1 and NBu₄SH, showing short contacts to the NBu₄ counterion. Non-coordinating hydrogen atoms omitted for clarity.

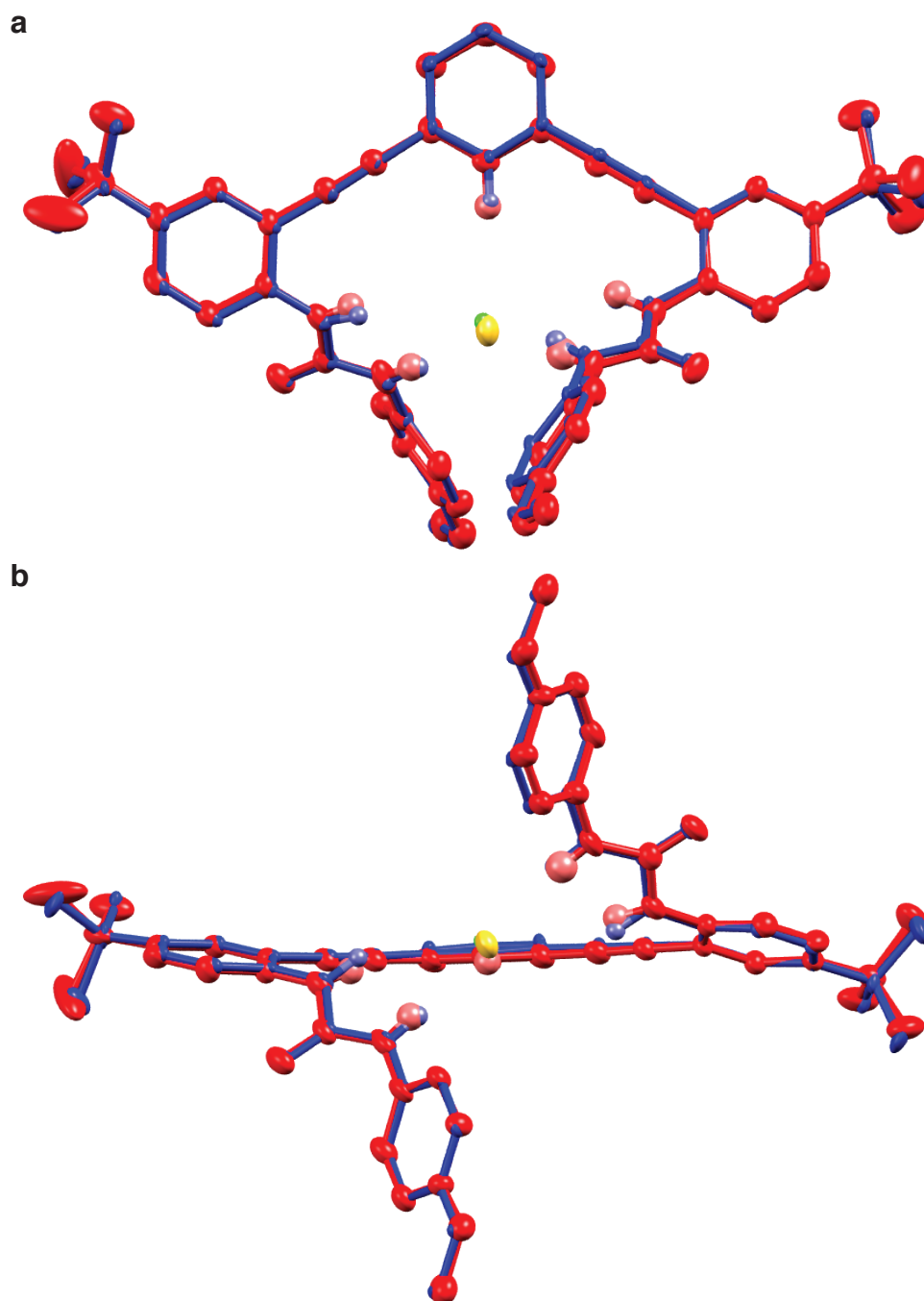


Figure F-16. Overlay of the X-ray crystal structures of 1 bound to Cl^- and HS^- . Non-coordinating hydrogen atoms omitted for clarity. In the images, the hydrosulfide structure is represented in red with a yellow anion, while the chloride structure is represented in blue with a green anion. The RMS distance between the two structures is 0.184 Å. A, top view of the two structures overlaid. B, side view looking toward the phenyl core through the anions.

REFERENCES CITED

1. Wang, R. "Physiological implications of hydrogen sulfide: a whiff exploration that blossomed" *Physiological Reviews* **2012**, 92(2), 791-896.
2. Wallace, J. L.; Wang, R. "Hydrogen sulfide-based therapeutics: exploiting a unique but ubiquitous gasotransmitter" *Nature Reviews. Drug Discovery* **2015**, 14(5), 329-345.
3. Yetik-Anacak, G.; Sorrentino, R.; Linder, A. E.; Murat, N. "Gas what: NO is not the only answer to sexual function" *British Journal of Pharmacology* **2015**, 172(6), 1434-1454.
4. Feng, S.; Zhao, Y.; Xian, M.; Wang, Q. "Biological thiols-triggered hydrogen sulfide releasing microfibers for tissue engineering applications" *Acta Biomaterialia* **2015**, 27205-213.
5. Nagy, P.; Palinkas, Z.; Nagy, A.; Budai, B.; Toth, I.; Vasas, A. "Chemical aspects of hydrogen sulfide measurements in physiological samples" *Biochimica et Biophysica Acta* **2014**, 1840(2), 876-891.
6. Cortese-Krott, M. M.; Kuhnle, G. G.; Dyson, A.; Fernandez, B. O.; Grman, M.; DuMond, J. F.; Barrow, M. P.; McLeod, G.; Nakagawa, H.; Ondrias, K.; Nagy, P.; King, S. B.; Saavedra, J. E.; Keefer, L. K.; Singer, M.; Kelm, M.; Butler, A. R.; Feelisch, M. "Key bioactive reaction products of the NO/H₂S interaction are S/N-hybrid species, polysulfides, and nitroxyl" *Proceedings of the National Academy of Sciences of the United States of America* **2015**, 112(34), E4651-4660.
7. Mishanina, T. V.; Libiad, M.; Banerjee, R. "Biogenesis of reactive sulfur species for signaling by hydrogen sulfide oxidation pathways" *Nature Chemical Biology* **2015**, 11(7), 457-464.
8. Hughes, M. N.; Centelles, M. N.; Moore, K. P. "Making and working with hydrogen sulfide: The chemistry and generation of hydrogen sulfide in vitro and its measurement in vivo: a review" *Free Radical Biology & Medicine* **2009**, 47(10), 1346-1353.
9. Pandey, S. K.; Kim, K.-H.; Tang, K.-T. "A review of sensor-based methods for monitoring hydrogen sulfide" *Trends in Analytical Chemistry* **2012**, 3287-99.
10. Kimura, Y.; Toyofuku, Y.; Koike, S.; Shibuya, N.; Nagahara, N.; Lefer, D.; Ogasawara, Y.; Kimura, H. "Identification of H₂S₃ and H₂S produced by 3-mercaptopyruvate sulfurtransferase in the brain" *Scientific Reports* **2015**, 514774.

11. Greiner, R.; Palinkas, Z.; Basell, K.; Becher, D.; Antelmann, H.; Nagy, P.; Dick, T. P. "Polysulfides link H₂S to protein thiol oxidation" *Antioxidants & Redox Signaling* **2013**, *19*(15), 1749-1765.
12. Toohey, J. I. "Sulphane sulphur in biological systems: a possible regulatory role" *Biochem J* **1989**, *264*(3), 625-632.
13. Bailey, T. S.; Pluth, M. D. "Reactions of isolated persulfides provide insights into the interplay between H₂S and persulfide reactivity" *Free Radical Biology & Medicine* **2015**, 89662-667.
14. Zhao, Y.; Biggs, T. D.; Xian, M. "Hydrogen sulfide (H₂S) releasing agents: chemistry and biological applications" *Chemical Communications* **2014**, *50*(80), 11788-11805.
15. Wood, J. L. In *Methods in Enzymology* 1987; Vol. 143, p 25-29.
16. Zhang, D.; Macinkovic, I.; Devarie-Baez, N. O.; Pan, J.; Park, C. M.; Carroll, K. S.; Filipovic, M. R.; Xian, M. "Detection of protein S-sulfhydration by a tag-switch technique" *Angewandte Chemie International Edition* **2014**, *53*(2), 575-581.
17. Papapetropoulos, A.; Whiteman, M.; Cirino, G. "Pharmacological tools for hydrogen sulphide research: a brief, introductory guide for beginners" *British Journal of Pharmacology* **2015**, *172*(6), 1633-1637.
18. Watanabe, M.; Osada, J.; Aratani, Y.; Kluckman, K.; Reddick, R.; Malinow, M. R.; Maeda, N. "Mice deficient in cystathionine beta-synthase: animal models for mild and severe homocyst(e)inemia" *Proceedings of the National Academy of Sciences of the United States of America* **1995**, *92*(5), 1585-1589.
19. Yang, G.; Wu, L.; Jiang, B.; Yang, W.; Qi, J.; Cao, K.; Meng, Q.; Mustafa, A. K.; Mu, W.; Zhang, S.; Snyder, S. H.; Wang, R. "H₂S as a physiologic vasorelaxant: hypertension in mice with deletion of cystathionine gamma-lyase" *Science* **2008**, *322*(5901), 587-590.
20. Ishii, I.; Akahoshi, N.; Yamada, H.; Nakano, S.; Izumi, T.; Suematsu, M. "Cystathionine gamma-Lyase-deficient mice require dietary cysteine to protect against acute lethal myopathy and oxidative injury" *The Journal of Biological Chemistry* **2010**, *285*(34), 26358-26368.
21. Nagahara, N.; Nagano, M.; Ito, T.; Shimamura, K.; Akimoto, T.; Suzuki, H. "Antioxidant enzyme, 3-mercaptopyruvate sulfurtransferase-knockout mice exhibit increased anxiety-like behaviors: a model for human mercaptolactate-cysteine disulfiduria" *Scientific Reports* **2013**, 31986.

22. Nishida, M.; Sawa, T.; Kitajima, N.; Ono, K.; Inoue, H.; Ihara, H.; Motohashi, H.; Yamamoto, M.; Suematsu, M.; Kurose, H.; van der Vliet, A.; Freeman, B. A.; Shibata, T.; Uchida, K.; Kumagai, Y.; Akaike, T. "Hydrogen sulfide anion regulates redox signaling via electrophile sulphydration" *Nature Chemical Biology* **2012**, 8(8), 714-724.
23. Modis, K.; Coletta, C.; Erdelyi, K.; Papapetropoulos, A.; Szabo, C. "Intramitochondrial hydrogen sulfide production by 3-mercaptopyruvate sulfurtransferase maintains mitochondrial electron flow and supports cellular bioenergetics" *FASEB J* **2013**, 27(2), 601-611.
24. Asimakopoulou, A.; Panopoulos, P.; Chasapis, C. T.; Coletta, C.; Zhou, Z.; Cirino, G.; Giannis, A.; Szabo, C.; Spyroulias, G. A.; Papapetropoulos, A. "Selectivity of commonly used pharmacological inhibitors for cystathionine beta synthase (CBS) and cystathionine gamma lyase (CSE)" *British Journal of Pharmacology* **2013**, 169(4), 922-932.
25. Finkelstein, J. D.; Kyle, W. E.; Martin, J. L.; Pick, A. M. "Activation of cystathionine synthase by adenosylmethionine and adenosylethionine" *Biochem Biophys Res Commun* **1975**, 66(1), 81-87.
26. Abe, K.; Kimura, H. "The possible role of hydrogen sulfide as an endogenous neuromodulator" *Journal of Neuroscience* **1996**, 16(3), 1066-1071.
27. Modis, K.; Coletta, C.; Asimakopoulou, A.; Szczesny, B.; Chao, C.; Papapetropoulos, A.; Hellmich, M. R.; Szabo, C. "Effect of S-adenosyl-L-methionine (SAM), an allosteric activator of cystathionine-beta-synthase (CBS) on colorectal cancer cell proliferation and bioenergetics in vitro" *Nitric Oxide* **2014**, 41/146-156.
28. Sen, N.; Paul, B. D.; Gadalla, M. M.; Mustafa, A. K.; Sen, T.; Xu, R.; Kim, S.; Snyder, S. H. "Hydrogen sulfide-linked sulphydration of NF-kappaB mediates its antiapoptotic actions" *Molecular Cell* **2012**, 45(1), 13-24.
29. Zhu, X. Y.; Liu, S. J.; Liu, Y. J.; Wang, S.; Ni, X. "Glucocorticoids suppress cystathionine gamma-lyase expression and H₂S production in lipopolysaccharide-treated macrophages" *Cellular and Molecular Life Sciences : CMLS* **2010**, 67(7), 1119-1132.
30. Whiteman, M.; Winyard, P. G. "Hydrogen sulfide and inflammation: the good, the bad, the ugly and the promising" *Expert Review of Clinical Pharmacology* **2011**, 4(1), 13-32.
31. Kashfi, K.; Olson, K. R. "Biology and therapeutic potential of hydrogen sulfide and hydrogen sulfide-releasing chimeras" *Biochem Pharmacol* **2013**, 85(5), 689-703.

32. Song, Z. J.; Ng, M. Y.; Lee, Z.-W.; Dai, W.; Hagen, T.; Moore, P. K.; Huang, D.; Deng, L.-W.; Tan, C.-H. "Hydrogen sulfide donors in research and drug development" *MedChemComm* **2014**, 5(5), 557.
33. Pluth, M.; Bailey, T.; Hammers, M.; Hartle, M.; Henthorn, H.; Steiger, A. "Natural Products Containing Hydrogen Sulfide Releasing Moieties" *Synlett* **2015**, 26(19), 2633-2643.
34. Benavides, G. A.; Squadrito, G. L.; Mills, R. W.; Patel, H. D.; Isbell, T. S.; Patel, R. P.; Darley-Usmar, V. M.; Doeller, J. E.; Kraus, D. W. "Hydrogen sulfide mediates the vasoactivity of garlic" *Proceedings of the National Academy of Sciences of the United States of America* **2007**, 104(46), 17977-17982.
35. Zhao, Y.; Bhushan, S.; Yang, C.; Otsuka, H.; Stein, J. D.; Pacheco, A.; Peng, B.; Devarie-Baez, N. O.; Aguilar, H. C.; Lefer, D. J.; Xian, M. "Controllable hydrogen sulfide donors and their activity against myocardial ischemia-reperfusion injury" *ACS Chemical Biology* **2013**, 8(6), 1283-1290.
36. Zhao, Y.; Yang, C.; Organ, C.; Li, Z.; Bhushan, S.; Otsuka, H.; Pacheco, A.; Kang, J.; Aguilar, H. C.; Lefer, D. J.; Xian, M. "Design, Synthesis, and Cardioprotective Effects of N-Mercapto-Based Hydrogen Sulfide Donors" *Journal of Medicinal Chemistry* **2015**, 58(18), 7501-7511.
37. Zhao, Y.; Wang, H.; Xian, M. "Cysteine-activated hydrogen sulfide (H₂S) donors" *Journal of the American Chemical Society* **2011**, 133(1), 15-17.
38. Carter, J. M.; Qian, Y.; Foster, J. C.; Matson, J. B. "Peptide-based hydrogen sulphide-releasing gels" *Chemical Communications* **2015**, 51(66), 13131-13134.
39. Li, L.; Whiteman, M.; Guan, Y. Y.; Neo, K. L.; Cheng, Y.; Lee, S. W.; Zhao, Y.; Baskar, R.; Tan, C. H.; Moore, P. K. "Characterization of a novel, water-soluble hydrogen sulfide-releasing molecule (GYY4137): new insights into the biology of hydrogen sulfide" *Circulation* **2008**, 117(18), 2351-2360.
40. Alexander, B. E.; Coles, S. J.; Fox, B. C.; Khan, T. F.; Maliszewski, J.; Perry, A.; Pitak, M. B.; Whiteman, M.; Wood, M. E. "Investigating the generation of hydrogen sulfide from the phosphoramidodithioate slow-release donor GYY4137" *MedChemComm* **2015**, 6(9), 1649-1655.
41. Yang, G.; Sun, X.; Wang, R. "Hydrogen sulfide-induced apoptosis of human aorta smooth muscle cells via the activation of mitogen-activated protein kinases and caspase-3" *FASEB J* **2004**, 18(14), 1782-1784.
42. Beltowski, J. "Hydrogen sulfide in pharmacology and medicine--An update" *Pharmacological Reports* **2015**, 67(3), 647-658.

43. Hammers, M. D.; Singh, L.; Montoya, L. A.; Moghaddam, A. D.; Pluth, M. D. "Synthesis of Amino-ADT Provides Access to Hydrolytically Stable Amide-Coupled Hydrogen Sulfide Releasing Drug Targets" *Synlett* **2016**, 27(9), 1349-1353.
44. Hartle, M. D.; Meininger, D. J.; Zakharov, L. N.; Tonzetich, Z. J.; Pluth, M. D. "NBu₄SH provides a convenient source of HS(-) soluble in organic solution for H₂S and anion-binding research" *Dalton Transactions* **2015**, 44(46), 19782-19785.
45. Xu, T.; Scafa, N.; Xu, L. P.; Zhou, S.; Abdullah Al-Ghanem, K.; Mahboob, S.; Fugetsu, B.; Zhang, X. "Electrochemical hydrogen sulfide biosensors" *The Analyst* **2016**, 141(4), 1185-1195.
46. Lin, V. S.; Chen, W.; Xian, M.; Chang, C. J. "Chemical probes for molecular imaging and detection of hydrogen sulfide and reactive sulfur species in biological systems" *Chemical Society Reviews* **2015**, 44(14), 4596-4618.
47. Shen, X.; Peter, E. A.; Bir, S.; Wang, R.; Kevil, C. G. "Analytical measurement of discrete hydrogen sulfide pools in biological specimens" *Free Radical Biology & Medicine* **2012**, 52(11-12), 2276-2283.
48. Ida, T.; Sawa, T.; Ihara, H.; Tsuchiya, Y.; Watanabe, Y.; Kumagai, Y.; Suematsu, M.; Motohashi, H.; Fujii, S.; Matsunaga, T.; Yamamoto, M.; Ono, K.; Devarie-Baez, N. O.; Xian, M.; Fukuto, J. M.; Akaike, T. "Reactive cysteine persulfides and S-polythiolation regulate oxidative stress and redox signaling" *Proceedings of the National Academy of Sciences of the United States of America* **2014**, 111(21), 7606-7611.
49. Lippert, A. R.; New, E. J.; Chang, C. J. "Reaction-based fluorescent probes for selective imaging of hydrogen sulfide in living cells" *Journal of the American Chemical Society* **2011**, 133(26), 10078-10080.
50. Peng, H.; Cheng, Y.; Dai, C.; King, A. L.; Predmore, B. L.; Lefer, D. J.; Wang, B. "A fluorescent probe for fast and quantitative detection of hydrogen sulfide in blood" *Angewandte Chemie International Edition* **2011**, 50(41), 9672-9675.
51. Montoya, L. A.; Pluth, M. D. "Selective turn-on fluorescent probes for imaging hydrogen sulfide in living cells" *Chemical Communications* **2012**, 48(39), 4767-4769.
52. Henthorn, H. A.; Pluth, M. D. "Mechanistic Insights into the H(2)S-Mediated Reduction of Aryl Azides Commonly Used in H(2)S Detection" *Journal of the American Chemical Society* **2015**, 137(48), 15330-15336.

53. Qian, Y.; Karpus, J.; Kabil, O.; Zhang, S. Y.; Zhu, H. L.; Banerjee, R.; Zhao, J.; He, C. "Selective fluorescent probes for live-cell monitoring of sulphide" *Nature Communications* **2011**, 2495.
54. Liu, C.; Pan, J.; Li, S.; Zhao, Y.; Wu, L. Y.; Berkman, C. E.; Whorton, A. R.; Xian, M. "Capture and visualization of hydrogen sulfide by a fluorescent probe" *Angewandte Chemie International Edition* **2011**, 50(44), 10327-10329.
55. Peng, B.; Chen, W.; Liu, C.; Rosser, E. W.; Pacheco, A.; Zhao, Y.; Aguilar, H. C.; Xian, M. "Fluorescent probes based on nucleophilic substitution-cyclization for hydrogen sulfide detection and bioimaging" *Chemistry - A European Journal* **2014**, 20(4), 1010-1016.
56. Qian, Y.; Zhang, L.; Ding, S.; Deng, X.; He, C.; Zheng, X. E.; Zhu, H.-L.; Zhao, J. "A fluorescent probe for rapid detection of hydrogen sulfide in blood plasma and brain tissues in mice" *Chemical Science* **2012**, 3(10), 2920.
57. Sasakura, K.; Hanaoka, K.; Shibuya, N.; Mikami, Y.; Kimura, Y.; Komatsu, T.; Ueno, T.; Terai, T.; Kimura, H.; Nagano, T. "Development of a highly selective fluorescence probe for hydrogen sulfide" *Journal of the American Chemical Society* **2011**, 133(45), 18003-18005.
58. Chen, W.; Liu, C.; Peng, B.; Zhao, Y.; Pacheco, A.; Xian, M. "New fluorescent probes for sulfane sulfurs and the application in bioimaging" *Chemical Science* **2013**, 4(7), 2892-2896.
59. Liu, C.; Chen, W.; Shi, W.; Peng, B.; Zhao, Y.; Ma, H.; Xian, M. "Rational design and bioimaging applications of highly selective fluorescence probes for hydrogen polysulfides" *Journal of the American Chemical Society* **2014**, 136(20), 7257-7260.
60. Chen, W.; Rosser, E. W.; Matsunaga, T.; Pacheco, A.; Akaike, T.; Xian, M. "The Development of Fluorescent Probes for Visualizing Intracellular Hydrogen Polysulfides" *Angewandte Chemie International Edition* **2015**, 54(47), 13961-13965.
61. Mustafa, A. K.; Gadalla, M. M.; Snyder, S. H. "Signaling by gasotransmitters" *Science Signaling* **2009**, 2(68), re2.
62. Hartle, M. D.; Sommer, S. K.; Dietrich, S. R.; Pluth, M. D. "Chemically reversible reactions of hydrogen sulfide with metal phthalocyanines" *Inorganic Chemistry* **2014**, 53(15), 7800-7802.
63. Blackstone, E.; Morrison, M.; Roth, M. B. "H₂S induces a suspended animation-like state in mice" *Science* **2005**, 308(5721), 518.

64. Czyzewski, B. K.; Wang, D. N. "Identification and characterization of a bacterial hydrosulphide ion channel" *Nature* **2012**, 483(7390), 494-497.
65. Kabil, O.; Banerjee, R. "Redox biochemistry of hydrogen sulfide" *The Journal of Biological Chemistry* **2010**, 285(29), 21903-21907.
66. Qu, K.; Lee, S. W.; Bian, J. S.; Low, C. M.; Wong, P. T. "Hydrogen sulfide: neurochemistry and neurobiology" *Neurochem Int* **2008**, 52(1-2), 155-165.
67. Shatalin, K.; Shatalina, E.; Mironov, A.; Nudler, E. "H₂S: a universal defense against antibiotics in bacteria" *Science* **2011**, 334(6058), 986-990.
68. Chen, C. Q.; Xin, H.; Zhu, Y. Z. "Hydrogen sulfide: third gaseous transmitter, but with great pharmacological potential" *Acta Pharmacologica Sinica* **2007**, 28(11), 1709-1716.
69. James, B. R. "Coordination chemistry, and catalytic conversions, of H₂S" *Pure and Applied Chemistry* **1997**, 69(10), 2213-2220.
70. English, D. R.; Hendrickson, D. N.; Suslick, K. S.; Eigenbrot, C. W.; Scheidt, W. R. "Low-spin five-coordinate ferric porphyrin complex: [5, 10, 15, 20-tetrakis(4-methoxyphenyl)porphyrinato](hydrosulfido)iron(III)" *Journal of the American Chemical Society* **1984**, 106(23), 7258-7259.
71. Galardon, E.; Roger, T.; Deschamps, P.; Roussel, P.; Tomas, A.; Artaud, I. "Synthesis of a Fe(II)SH complex stabilized by an intramolecular N-H...S hydrogen bond, which acts as a H₂S donor" *Inorganic Chemistry* **2012**, 51(19), 10068-10070.
72. Ma, E. S.; Rettig, S. J.; Patrick, B. O.; James, B. R. "Ruthenium(II) thiol and H₂S complexes: synthesis, characterization, and thermodynamic properties" *Inorganic Chemistry* **2012**, 51(9), 5427-5434.
73. Ma, E. S. F.; Rettig, S. J.; James, B. R. "Extension of the Karplus relationship to vicinal coupling within the P–Ru–S–H moiety of the H₂S complexes cis-RuX₂(P–N)(PPh₃)(SH₂) {X = Cl, Br; P–N = [o-(N,N-dimethylamino)phenyl]diphenylphosphine}" *Chemical Communications* **1999**(24), 2463-2464.
74. Reboucas, J. S.; James, B. R. "Molecular recognition using ruthenium(II) porphyrin thiol complexes as probes" *Inorganic Chemistry* **2013**, 52(2), 1084-1098.
75. Pavlik, J. W.; Noll, B. C.; Oliver, A. G.; Schulz, C. E.; Scheidt, W. R. "Hydrosulfide (HS⁻) coordination in iron porphyrinates" *Inorganic Chemistry* **2010**, 49(3), 1017-1026.

76. Reboucas, J. S.; Patrick, B. O.; James, B. R. "Thiol, disulfide, and trisulfide complexes of Ru porphyrins: potential models for iron-sulfur bonds in heme proteins" *Journal of the American Chemical Society* **2012**, *134*(7), 3555-3570.
77. Meininger, D. J.; Caranto, J. D.; Arman, H. D.; Tonzetich, Z. J. "Studies of iron(III) porphyrinates containing silanethiolate ligands" *Inorganic Chemistry* **2013**, *52*(21), 12468-12476.
78. Collman, J. P.; Ghosh, S.; Dey, A.; Decreau, R. A. "Using a functional enzyme model to understand the chemistry behind hydrogen sulfide induced hibernation" *Proceedings of the National Academy of Sciences of the United States of America* **2009**, *106*(52), 22090-22095.
79. Collamati, I.; Ercolani, C.; Rossi, G. "Reversible addition of O₂, NO, and CO to phthalocyanineiron(II) in concentrated sulphuric acid" *Inorganic and Nuclear Chemistry Letters* **1976**, *12*(10), 799-802.
80. Lieber, C. M.; Lewis, N. S. "Catalytic reduction of carbon dioxide at carbon electrodes modified with cobalt phthalocyanine" *Journal of the American Chemical Society* **1984**, *106*(17), 5033-5034.
81. Ghani, F.; Kristen, J.; Riegler, H. "Solubility Properties of Unsubstituted Metal Phthalocyanines in Different Types of Solvents" *Journal of Chemical and Engineering Data* **2012**, *57*(2), 439-449.
82. Leznoff, C. C.; Lever, A. B. P. *Phthalocyanines: Properties and Applications*; Wiley-VCH: New York, 1996; Vol. 1-4.
83. Harris, D. C. *Quantitative Chemical Analysis*; 8th ed.; W. H. Freeman and Company: New York, 2010.
84. Day, P.; Hill, H. A. O.; Price, M. G. "Some Reactions of Cobalt Phthalocyanines" *Journal of the Chemical Society a -Inorganic Physical Theoretical* **1968**(1), 90-&.
85. Clack, D. W.; Yandle, J. R. "Electronic spectra of the negative ions of some metal phthalocyanines" *Inorganic Chemistry* **1972**, *11*(8), 1738-1742.
86. Fischer, H.; Schulz-Ekloff, G.; Wohrle, D. "Oxidation of aqueous sulfide solutions by dioxygen - Part II: Catalysis by soluble and immobilized cobalt(II) phthalocyanines" *Chemical Engineering & Technology* **1997**, *20*(9), 624-632.
87. Pereira-Rodrigues, N.; Cofre, R.; Zagal, J. H.; Bedioui, F. "Electrocatalytic activity of cobalt phthalocyanine CoPc adsorbed on a graphite electrode for the oxidation of reduced L-glutathione (GSH) and the reduction of its disulfide (GSSG) at physiological pH" *Bioelectrochemistry* **2007**, *70*(1), 147-154.

88. Qi, X. "Selective Oxidation of Thiols to Disulfides at Polymeric Cobalt Phthalocyanine Chemically Modified Electrodes" *Journal of the Electrochemical Society* **1996**, *143*(4), 1283.
89. Rao, T. V.; Rao, K. N.; Jain, S. L.; Sain, B. "Cobalt Phthalocyanine Mediated Aerobic Oxidation of Thiols: A Simple and Convenient Preparation of Disulphides" *Synthetic Communications* **2002**, *32*(8), 1151-1157.
90. Faddeenkova, G. A.; Kundo, N. N. "Use of cobalt(II) phthalocyanine sulfonates in gas purification to remove hydrogen sulfide" *Russian Journal of Applied Chemistry* **2003**, *76*(12), 1946-1950.
91. Olson, K. R. "The therapeutic potential of hydrogen sulfide: separating hype from hope" *Am J Physiol Regul Integr Comp Physiol* **2011**, *301*(2), R297-312.
92. Tsou, C. C.; Chiu, W. C.; Ke, C. H.; Tsai, J. C.; Wang, Y. M.; Chiang, M. H.; Liaw, W. F. "Iron(III) Bound by Hydrosulfide Anion Ligands: NO-Promoted Stabilization of the Fe-III-SH Motif" *Journal of the American Chemical Society* **2014**, *136*(26), 9424-9433.
93. Tran, C. T.; Williard, P. G.; Kim, E. "Nitric oxide reactivity of [2Fe-2S] clusters leading to H₂S generation" *Journal of the American Chemical Society* **2014**, *136*(34), 11874-11877.
94. Watanabe, K.; Suzuki, T.; Kitagishi, H.; Kano, K. "Reaction between a haemoglobin model compound and hydrosulphide in aqueous solution" *Chemical Communications* **2015**, *51*(19), 4059-4061.
95. Wedmann, R.; Zahl, A.; Shubina, T. E.; Durr, M.; Heinemann, F. W.; Bugenhagen, B. E.; Burger, P.; Ivanovic-Burmazovic, I.; Filipovic, M. R. "Does perthionitrite (SSNO(-)) account for sustained bioactivity of NO? A (bio)chemical characterization" *Inorganic Chemistry* **2015**, *54*(19), 9367-9380.
96. Bailey, T. S.; Zakharov, L. N.; Pluth, M. D. "Understanding hydrogen sulfide storage: probing conditions for sulfide release from hydrodisulfides" *Journal of the American Chemical Society* **2014**, *136*(30), 10573-10576.
97. Filipovic, M. R.; Miljkovic, J.; Nauser, T.; Royzen, M.; Klos, K.; Shubina, T.; Koppenol, W. H.; Lippard, S. J.; Ivanovic-Burmazovic, I. "Chemical characterization of the smallest S-nitrosothiol, HSNO; cellular cross-talk of H₂S and S-nitrosothiols" *Journal of the American Chemical Society* **2012**, *134*(29), 12016-12027.
98. Cortese-Krott, M. M.; Fernandez, B. O.; Santos, J. L.; Mergia, E.; Grman, M.; Nagy, P.; Kelm, M.; Butler, A.; Feelisch, M. "Nitrosopersulfide (SSNO(-))

- accounts for sustained NO bioactivity of S-nitrosothiols following reaction with sulfide" *Redox Biol* **2014**, 2234-244.
99. Galardon, E.; Padovani, D. "Reactivity of persulfides toward strained bicyclo[6.1.0]nonyne derivatives: relevance to chemical tagging of proteins" *Bioconjug Chem* **2015**, 26(6), 1013-1016.
 100. Cotton, J. D.; Waddington, T. C. "Liquid hydrogen sulphide as an ionising solvent. Part I. Base analogues and their neutralisation with hydrogen halides" *Journal of the Chemical Society A: Inorganic, Physical, Theoretical* **1966**, 785-789.
 101. Schaumann, E.; Wriede, U.; Ehlers, J. "Tetraethylammonium Hydrogen Sulfide: A Convenient Reagent for Thiolation of 1,1-Dichloroalkenes" *Synthesis* **1980**, 1980(11), 907-908.
 102. Heller, G.; Eysenbach, W. "Studies of the interactions between boron trihalides and tris(ethylthio)borane with hydrogen sulfide and their reactions with tetraalkylammonium hydrosulfides" *Inorganic Chemistry* **1979**, 18(2), 380-383.
 103. Gale, P. A.; Busschaert, N.; Haynes, C. J. E.; Karagiannidis, L. E.; Kirby, I. L. "Anion receptor chemistry: highlights from 2011 and 2012" *Chemical Society Reviews* **2014**, 43(1), 205-241.
 104. Montoya, L. A.; Pearce, T. F.; Hansen, R. J.; Zakharov, L. N.; Pluth, M. D. "Development of selective colorimetric probes for hydrogen sulfide based on nucleophilic aromatic substitution" *The Journal of Organic Chemistry* **2013**, 78(13), 6550-6557.
 105. Bryantsev, V. S.; Hay, B. P. "Are C-H groups significant hydrogen bonding sites in anion receptors? Benzene complexes with Cl⁻, NO₃⁻, and ClO₄⁻" *Journal of the American Chemical Society* **2005**, 127(23), 8282-8283.
 106. Lee, S.; Chen, C.-H.; Flood, A. H. "A pentagonal cyanostar macrocycle with cyanostilbene CH donors binds anions and forms dialkylphosphate 3 rotaxanes" *Nature Chemistry* **2013**, 5(8), 704-710.
 107. Tresca, B. W.; Zakharov, L. N.; Carroll, C. N.; Johnson, D. W.; Haley, M. M. "Aryl C-H center dot center dot center dot Cl⁻ hydrogen bonding in a fluorescent anion sensor" *Chemical Communications* **2013**, 49(65), 7240-7242.
 108. Schneider, H. J. "Binding mechanisms in supramolecular complexes" *Angewandte Chemie International Edition* **2009**, 48(22), 3924-3977.

109. Li, Y.; Flood, A. H. "Pure C-H hydrogen bonding to chloride ions: a preorganized and rigid macrocyclic receptor" *Angewandte Chemie International Edition* **2008**, *47*(14), 2649-2652.
110. Briceno, A.; Chander, S. "Oxidation of hydrosulphide ions on gold Part I: A cyclic voltammetry study" *Journal of Applied Electrochemistry* **1990**, *20*(3), 506-511.
111. Kelsall, G. H.; Thompson, I. "Redox chemistry of H₂S oxidation by the British Gas Stretford Process Part. II: Electrochemical behaviour of aqueous hydrosulphide (HS⁻) solutions" *Journal of Applied Electrochemistry* **1993**, *23*(4), 287-295.
112. Hartle, M. D.; Prell, J. S.; Pluth, M. D. "Spectroscopic investigations into the binding of hydrogen sulfide to synthetic picket-fence porphyrins" *Dalton Transactions* **2016**, *45*(11), 4843-4853.
113. Pavlik, J. W.; Noll, B. C.; Oliver, A. G.; Schulz, C. E.; Scheidt, W. R. "Hydrosulfide (HS⁻) coordination in iron porphyrinates" *Inorganic Chemistry* **2010**, *49*(3), 1017-1026.
114. Sheldrick, G. M.; Bruker AXS: Madison, WI, 1998.
115. van der Sluis, P.; Spek, A. L. "BYPASS: an effective method for the refinement of crystal structures containing disordered solvent regions" *Acta Crystallographica Section A Foundations of Crystallography* **1990**, *46*(3), 194-201.
116. Hartle, M. D.; Pluth, M. D. "A practical guide to working with H₂S at the interface of chemistry and biology" *Chemical Society Reviews* **2016**, *45*(22), 6108-6117.
117. Miyamoto, R.; Otsuguro, K.; Yamaguchi, S.; Ito, S. "Contribution of cysteine aminotransferase and mercaptopyruvate sulfurtransferase to hydrogen sulfide production in peripheral neurons" *J Neurochem* **2014**, *130*(1), 29-40.
118. Ellison, M. K.; Schulz, C. E.; Scheidt, W. R. "Syntheses, characterization, and structural studies of several (Nitro)(nitrosyl)iron(III) porphyrinates: [Fe(Porph)(NO₂)(NO)]" *Inorganic Chemistry* **1999**, *38*(1), 100-108.
119. Ford, P. C.; Pereira, J. C. M.; Miranda, K. M. In *Nitrosyl Complexes in Inorganic Chemistry, Biochemistry and Medicine II* 2014; Vol. 154, p 99-135.
120. Hoshino, M.; Laverman, L.; Ford, P. C. "Nitric oxide complexes of metalloporphyrins: an overview of some mechanistic studies" *Coordination Chemistry Reviews* **1999**, *187*(1), 75-102.

121. Pietri, R.; Lewis, A.; Leon, R. G.; Casabona, G.; Kiger, L.; Yeh, S. R.; Fernandez-Alberti, S.; Marden, M. C.; Cadilla, C. L.; Lopez-Garriga, J. "Factors controlling the reactivity of hydrogen sulfide with heme proteins" *Biochemistry* **2009**, *48*(22), 4881-4894.
122. Spiro, T. G.; Wasbotten, I. H. "CO as a vibrational probe of heme protein active sites" *Journal of Inorganic Biochemistry* **2005**, *99*(1), 34-44.
123. Wolak, M.; van Eldik, R. "To be or not to be NO in coordination chemistry? A mechanistic approach" *Coordination Chemistry Reviews* **2002**, *230*(1-2), 263-282.
124. Franke, A.; van Eldik, R. "Factors That Determine the Mechanism of NO Activation by Metal Complexes of Biological and Environmental Relevance" *European Journal of Inorganic Chemistry* **2013**, *2013*(4), 460-480.
125. Tsai, M. L.; Tsou, C. C.; Liaw, W. F. "Dinitrosyl iron complexes (DNICs): from biomimetic synthesis and spectroscopic characterization toward unveiling the biological and catalytic roles of DNICs" *Accounts of Chemical Research* **2015**, *48*(4), 1184-1193.
126. Tran, C. T.; Skodje, K. M.; Kim, E. In *Progress in Inorganic Chemistry, Vol 59* 2014; Vol. 59, p 339-379.
127. Hartle, M. D.; Delgado, M.; Gilbertson, J. D.; Pluth, M. D. "Stabilization of a Zn(ii) hydrosulfido complex utilizing a hydrogen-bond accepting ligand" *Chemical Communications* **2016**, *52*(49), 7680-7682.
128. Rios-Gonzalez, B. B.; Roman-Morales, E. M.; Pietri, R.; Lopez-Garriga, J. "Hydrogen sulfide activation in heme proteins: the sulfheme scenario" *Journal of Inorganic Biochemistry* **2014**, 13378-86.
129. Meininger, D. J.; Arman, H. D.; Tonzetich, Z. J. "Synthesis, characterization, and binding affinity of hydrosulfide complexes of synthetic iron(II) porphyrinates" *Journal of Inorganic Biochemistry* **2016**.
130. Guillard, R.; Ratti, C.; Barbe, J. M.; Dubois, D.; Kadish, K. M. "Synthesis and characterization of tin(IV) porphyrins with sulfide and selenide axial ligands" *Inorganic Chemistry* **1991**, *30*(7), 1537-1542.
131. Lelj, F. "Formation, crystal structure and co-ordination chemistry of the [MnIII(oespz)(SH)] [oespz²⁻ = 2,3,7,8,12,13,17,18-octakis(ethylsulfanyl)-5,10,15,20-tetraazaporphyrinate dianion] complex" *Journal of the Chemical Society, Dalton Transactions* **1998**(12), 1985-1992.

132. Meininger, D. J.; Chee-Garza, M.; Arman, H. D.; Tonzetich, Z. J. "Gallium(III) Tetraphenylporphyrinates Containing Hydrosulfide and Thiolate Ligands: Structural Models for Sulfur-Bound Iron(III) Hemes" *Inorganic Chemistry* **2016**, 55(5), 2421-2426.
133. Ramos-Alvarez, C.; Yoo, B. K.; Pietri, R.; Lamarre, I.; Martin, J. L.; Lopez-Garriga, J.; Negrerie, M. "Reactivity and dynamics of H₂S, NO, and O₂ interacting with hemoglobins from *Lucina pectinata*" *Biochemistry* **2013**, 52(40), 7007-7021.
134. Pietri, R.; Roman-Morales, E.; Lopez-Garriga, J. "Hydrogen sulfide and heme proteins: knowledge and mysteries" *Antioxidants & Redox Signaling* **2011**, 15(2), 393-404.
135. Bieza, S. A.; Boubeta, F.; Feis, A.; Smulevich, G.; Estrin, D. A.; Boechi, L.; Bari, S. E. "Reactivity of inorganic sulfide species toward a heme protein model" *Inorganic Chemistry* **2015**, 54(2), 527-533.
136. Shen, J.; Kortlever, R.; Kas, R.; Birdja, Y. Y.; Diaz-Morales, O.; Kwon, Y.; Ledezma-Yanez, I.; Schouten, K. J.; Mul, G.; Koper, M. T. "Electrocatalytic reduction of carbon dioxide to carbon monoxide and methane at an immobilized cobalt protoporphyrin" *Nature Communications* **2015**, 68177.
137. Li, C. Z.; Alwarappan, S.; Zhang, W.; Scafa, N.; Zhang, X. "Metallo Protoporphyrin Functionalized Microelectrodes for Electrocatalytic Sensing of Nitric Oxide" *Am J Biomed Sci* **2009**, 1(3), 274-282.
138. Guldi, D. M.; Hambright, P.; Lexa, D.; Neta, P.; Saveant, J. M. "One-Electron Reduction of Chromium(III) Porphyrins - Formation of Chromium(I) Porphyrins or Chromium(III) Porphyrin Pi-Radical Anions" *Journal of Physical Chemistry* **1992**, 96(11), 4459-4466.
139. Thordarson, P. "Determining association constants from titration experiments in supramolecular chemistry" *Chemical Society Reviews* **2011**, 40(3), 1305-1323.
140. Tong, A. J.; Tong, C. Y.; Yang, Q. Y. "Study on the binding mode of zinc(II) protoporphyrin and ctDNA in water" *Spectrochim Acta A Mol Biomol Spectrosc* **2003**, 59(13), 2967-2970.
141. Ballester, P.; Costa, A.; Castilla, A. M.; Deya, P. M.; Frontera, A.; Gomila, R. M.; Hunter, C. A. "DABCO-directed self-assembly of bisporphyrins (DABCO=1,4-diazabicyclo[2.2.2]octane)" *Chemistry - A European Journal* **2005**, 11(7), 2196-2206.

142. Etxebarria, J.; Vidal-Ferran, A.; Ballester, P. "The effect of complex stoichiometry in supramolecular chirality transfer to zinc bisporphyrin systems" *Chemical Communications* **2008**, 2008(45), 5939-5941.
143. Pintre, I. C.; Pierrefixe, S.; Hamilton, A.; Valderrey, V.; Bo, C.; Ballester, P. "Influence of the solvent and metal center on supramolecular chirality induction with bisporphyrin tweezer receptors. Strong metal modulation of effective molarity values" *Inorganic Chemistry* **2012**, 51(8), 4620-4635.
144. Yamamoto, Y.; Nanai, N.; Inoue, Y.; Chûijô, R. "Quantitative Mapping of Metal-Centered Dipolar Field in Hemin Dicyano Complex by Solution NMR" *Bulletin of the Chemical Society of Japan* **1989**, 62(6), 1771-1776.
145. Sakurai, H.; Tamura, J.; Yoshimura, T. "An unusual hyperporphyrin spectrum for a bithiolato-chromium(III) tetraphenylporphyrin complex" *Inorganic Chemistry* **1985**, 24(25), 4227-4229.
146. We attempted to obtain ¹H NMR spectra of the Cr(PPIX)Cl and Cr(PPIX)SH compounds; however, the complexes remained paramagnetic, even in the presence of 30 equivalents of NBu₄SH.
147. Lipiner, G.; Willner, I.; Aizenshtat, Z. "Transmetallation of a manganese(II)-porphyrin by Zn²⁺ ions in the presence of thiols" *Journal of the Chemical Society, Chemical Communications* **1985**, 1985(5), 305.
148. Mu, L.; Huang, J.; Zhou, Y.; Shen, P. "Synthesis and spectroscopic studies of manganese porphyrin-thiolate complexes" *Polyhedron* **1997**, 16(16), 2885-2888.
149. Hoffman, B. M.; Weschler, C. J.; Basolo, F. "The dioxygen adduct of meso-tetraphenylporphyrinmanganese(II), a synthetic oxygen carrier" *Journal of the American Chemical Society* **1976**, 98(18), 5473-5482.
150. Yu, Q.; Liu, Y.; Liu, D.; Li, J. "Geometric and electronic structures of five-coordinate manganese(ii) "picket fence" porphyrin complexes" *Dalton Transactions* **2015**, 44(20), 9382-9390.
151. Yonetani, T.; Drott, H. R.; Leigh, J. S., Jr.; Reed, G. H.; Waterman, M. R.; Asakura, T. "Electromagnetic Properties of Hemoproteins. III. Electron Paramagnetic Resonance Characteristics of Iron (III) and Manganese (II) Protoporphyrins IX and Their Apohemoprotein Complexes in High Spin States" *Journal of Biological Chemistry* **1970**, 245(11), 2998-3003.
152. Stoll, S.; Schweiger, A. "EasySpin, a comprehensive software package for spectral simulation and analysis in EPR" *J Magn Reson* **2006**, 178(1), 42-55.

153. In *MATLAB and Statistics Toolbox Release 2014b*; version 8.4.0.150421 ed.; The MathWorks Inc.: Natick, Massachusetts, United States, The MathWorks Inc.; Natick, Massachusetts, United States, 2014.
154. Karlin, K. D. "Progress in Inorganic Chemistry, Volume 49" *Progress in Inorganic Chemistry, Volume 49* **2009**.
155. Dhifet, M.; Belkhiria, M. S.; Daran, J. C.; Nasri, H. "(Cryptand-222)potassium(+) (hydrogensulfido)[5,10,15,20-tetra-kis(2-pival-amido-phenyl)porphyrinato]ferrate (II)" *Acta Crystallographica. Section E, Structure Reports Online* **2009**, 65(Pt 8), m967-968.
156. Berg, J. M.; Tymoczko, J. L.; Lubert, S. *Biochemistry*; 6th ed.; W. H. Freeman and Company: 41 Madison Avenue, New York, NY 10010, 2007.
157. Collman, J. P.; Gagne, R. R.; Halbert, T. R.; Marchon, J. C.; Reed, C. A. "Reversible Oxygen Adduct Formation in Ferrous Complexes Derived from a Picket Fence Porphyrin - Model for Oxymyoglobin" *Journal of the American Chemical Society* **1973**, 95(23), 7868-7870.
158. Collman, J. P.; Gagne, R. R.; Reed, C. A.; Halbert, T. R.; Lang, G.; Robinson, W. T. "'Picket fence porphyrins." Synthetic models for oxygen binding hemoproteins" *Journal of the American Chemical Society* **1975**, 97(6), 1427-1439.
159. Heinecke, J.; Ford, P. C. "Mechanistic studies of nitrite reactions with metalloproteins and models relevant to mammalian physiology" *Coordination Chemistry Reviews* **2010**, 254(3-4), 235-247.
160. Lim, M. D.; Lorkovic, I. M.; Ford, P. C. "NO and NOx interactions with group 8 metalloporphyrins" *Journal of Inorganic Biochemistry* **2005**, 99(1), 151-165.
161. Lehnert, N.; Scheidt, W. R.; Wolf, M. W. "Structure and Bonding in Heme-Nitrosyl Complexes and Implications for Biology" **2013**, 154155-223.
162. Cheng, L.; Powell, D. R.; Khan, M. A.; Richter-Addo, G. B. "The first unambiguous determination of a nitrosyl-to-nitrite conversion in an iron nitrosyl porphyrin" *Chemical Communications* **2000**(23), 2301-2302.
163. Tsou, C. C.; Chiu, W. C.; Ke, C. H.; Tsai, J. C.; Wang, Y. M.; Chiang, M. H.; Liaw, W. F. "Iron(III) bound by hydrosulfide anion ligands: NO-promoted stabilization of the [Fe(III)-SH] motif" *Journal of the American Chemical Society* **2014**, 136(26), 9424-9433.

164. Berzofsky, J. A.; Peisach, J.; Alben, J. O. "Sulfheme Proteins. III. Carboxysulfmyoglobin: The Relation Between Electron Withdrawal From Iron and Ligand Binding" *Journal of Biological Chemistry* **1972**, *247*(12), 3774-3782.
165. Berzofsky, J. A.; Peisach, J.; Blumberg, W. E. "Sulfheme proteins. I. Optical and magnetic properties of sulfmyoglobin and its derivatives" *The Journal of Biological Chemistry* **1971**, *246*(10), 3367-3377.
166. Berzofsky, J. A.; Peisach, J.; Blumberg, W. E. "Sulfheme proteins. II. The reversible oxygenation of ferrous sulfmyoglobin" *The Journal of Biological Chemistry* **1971**, *246*(23), 7366-7372.
167. Beauchamp, R. O., Jr.; Bus, J. S.; Popp, J. A.; Boreiko, C. J.; Andjelkovich, D. A. "A critical review of the literature on hydrogen sulfide toxicity" *Critical Reviews in Toxicology* **1984**, *13*(1), 25-97.
168. Walsh, T. J.; Beehler, C. "Fundus in sulfhemoglobinemia" *Archives of Internal Medicine* **1969**, *124*(3), 377-378.
169. Rizzi, M.; Wittenberg, J. B.; Coda, A.; Fasano, M.; Ascenzi, P.; Bolognesi, M. "Structure of the sulfide-reactive hemoglobin from the clam *Lucina pectinata*. Crystallographic analysis at 1.5 Å resolution" *Journal of Molecular Biology* **1994**, *244*(1), 86-99.
170. Rizzi, M.; Wittenberg, J. B.; Coda, A.; Ascenzi, P.; Bolognesi, M. "Structural bases for sulfide recognition in *Lucina pectinata* hemoglobin I" *Journal of Molecular Biology* **1996**, *258*(1), 1-5.
171. Collman, J. P.; Fu, L.; Zingg, A.; Diederich, F. "Dioxygen and carbon monoxide binding in dendritic iron(II)porphyrins" *Chemical Communications* **1997**(2), 193-194.
172. Kerr, E. A.; Mackin, H. C.; Yu, N. T. "Resonance Raman studies of carbon monoxide binding to iron "picket fence" porphyrin with unhindered and hindered axial bases. An inverse relationship between binding affinity and the strength of iron-carbon bond" *Biochemistry* **1983**, *22*(19), 4373-4379.
173. Nasri, H.; Haller, K. J.; Wang, Y.; Huynh Boi, H.; Scheidt, W. R. "Reactions of bis(nitro)[α , α , α , α -meso-tetrakis(o-pivalamidophenyl)porphinato]iron(III) with 2,3,5,6-tetrafluorothiophenol and 2,3,5,6-tetrafluorothiophenolate. EPR and Moessbauer spectra and molecular structures" *Inorganic Chemistry* **1992**, *31*(16), 3459-3467.
174. Heinecke, J. L.; Khin, C.; Pereira, J. C.; Suarez, S. A.; Iretskii, A. V.; Doctorovich, F.; Ford, P. C. "Nitrite reduction mediated by heme models. Routes

- to NO and HNO?" *Journal of the American Chemical Society* **2013**, *135*(10), 4007-4017.
175. Conradie, J.; Ghosh, A. "Iron(III)-nitro porphyrins: theoretical exploration of a unique class of reactive molecules" *Inorganic Chemistry* **2006**, *45*(13), 4902-4909.
 176. Sorrell, T. N.; Bump, C. M.; Jordan, J. "(Dioxygen)(N-Methylimidazole) (All-Cis)-5,10,15,20-Tetrakis 2-(2,2-Dimethylpropionamido)-Phenyl Porphyrinato(2-) Iron(II)" *Inorganic Syntheses* **1980**, *20* 161-169.
 177. Lindsey, J. "Increased yield of a desired isomer by equilibriums displacement on binding to silica gel, applied to meso-tetrakis(o-aminophenyl)porphyrin" *The Journal of Organic Chemistry* **1980**, *45*(25), 5215-5215.
 178. Kraus, D. W.; Wittenberg, J. B. "Hemoglobins of the *Lucina pectinata*/bacteria symbiosis. I. Molecular properties, kinetics and equilibria of reactions with ligands" *The Journal of Biological Chemistry* **1990**, *265*(27), 16043-16053.
 179. Brittain, T.; Yosaatmadja, Y.; Henty, K. "The interaction of human neuroglobin with hydrogen sulphide" *IUBMB Life* **2008**, *60*(2), 135-138.
 180. Collman, J. P.; Basolo, F.; Bunnenberg, E.; Collins, T. J.; Dawson, J. H.; Ellis, P. E.; Marrocco, M. L.; Moscovitz, A.; Sessler, J. L.; Szymanski, T. "Use of Magnetic Circular-Dichroism to Determine Axial Ligation for Some Sterically Encumbered Iron(II) Porphyrin Complexes" *Journal of the American Chemical Society* **1981**, *103*(19), 5636-5648.
 181. Chen, K. Y.; Gupta, S. K. "Formation of polysulfides in aqueous solution" *Environ Lett* **1973**, *4*(3), 187-200.
 182. O'Brien, D. J.; Birkner, F. B. "Kinetics of oxygenation of reduced sulfur species in aqueous solution" *Environmental Science & Technology* **1977**, *11*(12), 1114-1120.
 183. Schwarzenbach, G.; Fischer, A. "Die Acidität der Sulfane und die Zusammensetzung wässriger Polysulfidlösungen" *Helvetica Chimica Acta* **1960**, *43*(5), 1365-1390.
 184. Seel, F.; Guttler, H. J.; Simon, G.; Wieckowski, A. "Colored sulfur species in EPD-solvents" *Pure and Applied Chemistry* **1977**, *49*(1), 45-54.
 185. Latos-Grazynski, L.; Cheng, R. J.; La Mar, G. N.; Balch, A. L. "Oxygenation patterns for substituted meso-tetraphenylporphyrin complexes of iron(II). Spectroscopic detection of dioxygen complexes in the absence of amines" *Journal of the American Chemical Society* **1982**, *104*(22), 5992-6000.

186. Sinyakov, G. N.; Shulga, A. M. "1H NMR spectra and electronic structure of reduced iron porphyrins: Fe(II), Fe(I) and Fe(0) porphyrins" *Journal of Molecular Structure* **1993**, 2951-14.
187. Parmely, R. C.; Goff, H. M. "Proton nmr spectroscopy of high-spin ferrous cytochrome P-450 models" *Journal of Inorganic Biochemistry* **1980**, 12(3), 269-280.
188. Walker, F. A.; Buchler, J.; West, J. T.; Hinds, J. L. "Models of the cytochromes b. 4. Effects of axial ligand plane orientation on the proton NMR spectra of symmetrically substituted low-spin iron(III) porphyrins" *Journal of the American Chemical Society* **1983**, 105(23), 6923-6929.
189. Bain, G. A.; Berry, J. F. "Diamagnetic corrections and Pascal's constants" *Journal of Chemical Education* **2008**, 85(4), 532-536.
190. Evans, D. F. "400. The determination of the paramagnetic susceptibility of substances in solution by nuclear magnetic resonance" *Journal of the Chemical Society (Resumed)* **1959**2003.
191. Schappacher, M.; Ricard, L.; Fischer, J.; Weiss, R.; Montiel-Montoya, R.; Bill, E.; Trautwein, A. X. "Synthesis, structure, and spectroscopic properties of five-coordinate mercaptoiron(II) porphyrins. Models for the reduced state of cytochrome P450" *Inorganic Chemistry* **1989**, 28(26), 4639-4645.
192. Brault, D.; Rougee, M. "Ferrous porphyrins in organic solvents. I. Preparation and coordinating properties" *Biochemistry* **1974**, 13(22), 4591-4597.
193. Landy, D.; Tetart, F.; Truant, E.; Blach, P.; Fourmentin, S.; Surpateanu, G. "Development of a competitive continuous variation plot for the determination of inclusion compounds stoichiometry" *Journal of Inclusion Phenomena and Macrocyclic Chemistry* **2007**, 57(1-4), 409-413.
194. Martin, C. J.; Marini, M. A. "Spectral detection of the reaction of formaldehyde with the histidine residues of alpha-chymotrypsin" *The Journal of Biological Chemistry* **1967**, 242(24), 5736-5743.
195. Schäfer, R.; Schmidt, P. C. *Methods in Physical Chemistry (2nd Edition)*; John Wiley & Sons: Somerset, NJ, USA, 2012.
196. Schroder, D.; Wiley-VCH Verlag GmbH & Co. KGaA: 2012; Vol. 1, p 63-84.
197. Ocone, L. R.; Block, B. P.; Collman, J. P.; Buckingham, D. A. "Anhydrous Chromium (II) Acetate, Chromium (II) Acetate 1-Hydrate, and Bis(2,4-Pentanedionato) Chromium (II)" *Inorganic Syntheses* **1966**, 8125-132.

198. Patnaik, P. *Handbook of Inorganic Chemicals*; McGraw-Hill: New York, 2002.
199. Fogo, J. K.; Popowsky, M. "Spectrophotometric Determination of Hydrogen Sulfide" *Analytical Chemistry* **1949**, 21(6), 732-734.
200. Galardon, E.; Tomas, A.; Roussel, P.; Artaud, I. "New fluorescent zinc complexes: towards specific sensors for hydrogen sulfide in solution" *Dalton Transactions* **2009**(42), 9126-9130.
201. Rombach, M.; Vahrenkamp, H. "Pyrazolylborate-zinc-hydrosulfide complexes and their reactions" *Inorganic Chemistry* **2001**, 40(24), 6144-6150.
202. Ruf, M.; Vahrenkamp, H. "Small Molecule Chemistry of the Pyrazolylborate-Zinc Unit TpCum₂MeZn" *Inorganic Chemistry* **1996**, 35(22), 6571-6578.
203. Morlok, M. M.; Janak, K. E.; Zhu, G.; Quarless, D. A.; Parkin, G. "Intramolecular N-H...S hydrogen bonding in the zinc thiolate complex [Tm(Ph)]ZnSCH₂C(O)NHPh: a mechanistic investigation of thiolate alkylation as probed by kinetics studies and by kinetic isotope effects" *Journal of the American Chemical Society* **2005**, 127(40), 14039-14050.
204. Spiropoulos, N. G.; Standley, E. A.; Shaw, I. R.; Ingalls, B. L.; Diebels, B.; Krawczyk, S. V.; Gherman, B. F.; Arif, A. M.; Brown, E. C. "Synthesis of zinc and cadmium O-alkyl thiocarbonate and dithiocarbonate complexes and a cationic zinc hydrosulfide complex" *Inorganica Chimica Acta* **2012**, 38683-92.
205. Kuwata, S.; Hidai, M. "Hydrosulfido complexes of transition metals" *Coordination Chemistry Reviews* **2001**, 213(1), 211-305.
206. Notni, J.; Schenk, S.; Protoschill-Krebs, G.; Kesselmeier, J.; Anders, E. "The missing link in COS metabolism: a model study on the reactivation of carbonic anhydrase from its hydrosulfide analogue" *Chembiochem : A European Journal of Chemical Biology* **2007**, 8(5), 530-536.
207. Namuswe, F.; Berg, J. M. "Secondary interactions involving zinc-bound ligands: roles in structural stabilization and macromolecular interactions" *Journal of Inorganic Biochemistry* **2012**, 111146-149.
208. Delgado, M.; Sommer, S. K.; Swanson, S. P.; Berger, R. F.; Seda, T.; Zakharov, L. N.; Gilbertson, J. D. "Probing the Protonation State and the Redox-Active Sites of Pendant Base Iron(II) and Zinc(II) Pyridinediimine Complexes" *Inorganic Chemistry* **2015**, 54(15), 7239-7248.

209. Kendall, A. J.; Zakharov, L. N.; Gilbertson, J. D. "Synthesis and stabilization of a monomeric iron(II) hydroxo complex via intramolecular hydrogen bonding in the secondary coordination sphere" *Inorganic Chemistry* **2010**, *49*(19), 8656-8658.
210. Borovik, A. S. "Bioinspired hydrogen bond motifs in ligand design: the role of noncovalent interactions in metal ion mediated activation of dioxygen" *Accounts of Chemical Research* **2005**, *38*(1), 54-61.
211. Cook, S. A.; Borovik, A. S. "Molecular designs for controlling the local environments around metal ions" *Accounts of Chemical Research* **2015**, *48*(8), 2407-2414.
212. Park, Y. J.; Sickerman, N. S.; Ziller, J. W.; Borovik, A. S. "Utilizing tautomerization of 2-amino-oxazoline in hydrogen bonding tripodal ligands" *Chemical Communications* **2010**, *46*(15), 2584-2586.
213. Sickerman, N. S.; Park, Y. J.; Ng, G. K.; Bates, J. E.; Hilbert, M.; Ziller, J. W.; Furche, F.; Borovik, A. S. "Synthesis, structure, and physical properties for a series of trigonal bipyramidal M(II)-Cl complexes with intramolecular hydrogen bonds" *Dalton Transactions* **2012**, *41*(15), 4358-4364.
214. Shirin, Z.; Carrano, C. J. "New heteroscorpionate ligands with hydrogen bond donor and acceptor groups: synthesis, characterization and reactivity with divalent Co, Zn and Ni ions" *Polyhedron* **2004**, *23*(2-3), 239-244.
215. Moore, C. M.; Szymczak, N. K. "A tris(2-quinolylmethyl)amine scaffold that promotes hydrogen bonding within the secondary coordination sphere" *Dalton Transactions* **2012**, *41*(26), 7886-7889.
216. Matson, E. M.; Bertke, J. A.; Fout, A. R. "Isolation of iron(II) aqua and hydroxyl complexes featuring a tripodal H-bond donor and acceptor ligand" *Inorganic Chemistry* **2014**, *53*(9), 4450-4458.
217. Steiner, T. "The hydrogen bond in the solid state" *Angewandte Chemie International Edition* **2002**, *41*(1), 49-76.
218. Brzeninski, B.; Zundel, G. "An intramolecular sh \cdots N \rightleftharpoons S- \cdots H+N hydrogen bond with large proton polarizability" *Journal of Molecular Structure* **1982**, *84*(3-4), 205-211.
219. Shen, X.; Pattillo, C. B.; Pardue, S.; Bir, S. C.; Wang, R.; Kevill, C. G. "Measurement of plasma hydrogen sulfide in vivo and in vitro" *Free Radical Biology & Medicine* **2011**, *50*(9), 1021-1031.
220. Fan, R. Q.; Zhu, D. S.; Ding, H.; Mu, Y.; Su, Q.; Xia, H. "Blue luminescent zinc(II) complexes of 2,6-bis[1-(2,6-diisopropylphenylimino)ethyl]pyridine and

- 2,6-bis[1-(2,6-dimethylphenylimino)ethyl]pyridine" *Synthetic Metals* **2005**, *149*(2-3), 135-141.
221. Gale, P. A.; Caltagirone, C. "Anion sensing by small molecules and molecular ensembles" *Chemical Society Reviews* **2015**, *44*(13), 4212-4227.
222. Lee, M. H.; Kim, J. S.; Sessler, J. L. "Small molecule-based ratiometric fluorescence probes for cations, anions, and biomolecules" *Chemical Society Reviews* **2015**, *44*(13), 4185-4191.
223. Carnegie, R. S.; Gibb, C. L.; Gibb, B. C. "Anion complexation and the Hofmeister effect" *Angewandte Chemie International Edition* **2014**, *53*(43), 11498-11500.
224. Gibb, C. L.; Oertling, E. E.; Velaga, S.; Gibb, B. C. "Thermodynamic profiles of salt effects on a host-guest system: new insight into the Hofmeister effect" *The Journal of Physical Chemistry B* **2015**, *119*(17), 5624-5638.
225. Lisbjerg, M.; Valkenier, H.; Jessen, B. M.; Al-Kerdi, H.; Davis, A. P.; Pittelkow, M. "Biotin[6]juril Esters: Chloride-Selective Transmembrane Anion Carriers Employing C-H...Anion Interactions" *Journal of the American Chemical Society* **2015**, *137*(15), 4948-4951.
226. Hargrove, A. E.; Nieto, S.; Zhang, T.; Sessler, J. L.; Anslyn, E. V. "Artificial receptors for the recognition of phosphorylated molecules" *Chemical Reviews* **2011**, *111*(11), 6603-6782.
227. Cai, J.; Sessler, J. L. "Neutral CH and cationic CH donor groups as anion receptors" *Chemical Society Reviews* **2014**, *43*(17), 6198-6213.
228. Hay, B. P.; Bryantsev, V. S. "Anion-arene adducts: C-H hydrogen bonding, anion- π interaction, and carbon bonding motifs" *Chemical Communications* **2008**(21), 2417-2428.
229. Hua, Y.; Flood, A. H. "Click chemistry generates privileged CH hydrogen-bonding triazoles: the latest addition to anion supramolecular chemistry" *Chemical Society Reviews* **2010**, *39*(4), 1262-1271.
230. Bryantsev, V. S.; Hay, B. P. "Influence of substituents on the strength of aryl C-H...anion hydrogen bonds" *Org Lett* **2005**, *7*(22), 5031-5034.
231. Berryman, O. B.; Johnson, D. W. "Experimental evidence for interactions between anions and electron-deficient aromatic rings" *Chemical Communications* **2009**(22), 3143-3153.

232. Tresca, B. W.; Hansen, R. J.; Chau, C. V.; Hay, B. P.; Zakharov, L. N.; Haley, M. M.; Johnson, D. W. "Substituent Effects in CH Hydrogen Bond Interactions: Linear Free Energy Relationships and Influence of Anions" *Journal of the American Chemical Society* **2015**, *137*(47), 14959-14967.
233. Watt, M. M.; Zakharov, L. N.; Haley, M. M.; Johnson, D. W. "Selective nitrate binding in competitive hydrogen bonding solvents: do anion- π interactions facilitate nitrate selectivity?" *Angewandte Chemie International Edition* **2013**, *52*(39), 10275-10280.
234. Singh, S. B.; Lin, H. C. "Hydrogen Sulfide in Physiology and Diseases of the Digestive Tract" *Microorganisms* **2015**, *3*(4), 866-889.
235. Wu, D.; Si, W.; Wang, M.; Lv, S.; Ji, A.; Li, Y. "Hydrogen sulfide in cancer: Friend or foe?" *Nitric Oxide* **2015**, 5038-45.
236. Yu, F.; Han, X.; Chen, L. "Fluorescent probes for hydrogen sulfide detection and bioimaging" *Chemical Communications* **2014**, *50*(82), 12234-12249.
237. Jennings, M. L. "Transport of H₂S and HS(-) across the human red blood cell membrane: rapid H₂S diffusion and AE1-mediated Cl(-)/HS(-) exchange" *Am J Physiol Cell Physiol* **2013**, *305*(9), C941-950.
238. Sessler, J. L.; Gale, P.; Cho, W.-S.; Stoddart, J. F.; Rowan, S. J.; Aida, T.; Rowan, A. E. *Anion Receptor Chemistry*; The Royal Society of Chemistry, 2006.
239. Anzenbacher, P., Jr.; Liu, Y.; Palacios, M. A.; Minami, T.; Wang, Z.; Nishiyabu, R. "Leveraging material properties in fluorescence anion sensor arrays: a general approach" *Chemistry - A European Journal* **2013**, *19*(26), 8497-8506.
240. Palacios, M. A.; Nishiyabu, R.; Marquez, M.; Anzenbacher, P., Jr. "Supramolecular chemistry approach to the design of a high-resolution sensor array for multianion detection in water" *Journal of the American Chemical Society* **2007**, *129*(24), 7538-7544.
241. Marcus, Y. "Thermodynamics of solvation of ions. Part 5.—Gibbs free energy of hydration at 298.15 K" *J. Chem. Soc., Faraday Trans.* **1991**, *87*(18), 2995-2999.
242. Vonnegut, C. L.; Tresca, B. W.; Johnson, D. W.; Haley, M. M. "Ion and molecular recognition using aryl-ethynyl scaffolding" *Chemistry, an Asian journal* **2015**, *10*(3), 522-535.
243. Carroll, C. N.; Naleway, J. J.; Haley, M. M.; Johnson, D. W. "Arylethynyl receptors for neutral molecules and anions: emerging applications in cellular imaging" *Chemical Society Reviews* **2010**, *39*(10), 3875-3888.

244. Gavette, J. V.; Mills, N. S.; Zakharov, L. N.; Johnson, C. A., 2nd; Johnson, D. W.; Haley, M. M. "An anion-modulated three-way supramolecular switch that selectively binds dihydrogen phosphate, H₂PO₄" *Angewandte Chemie International Edition* **2013**, 52(39), 10270-10274.
245. Tresca, B. W.; Zakharov, L. N.; Carroll, C. N.; Johnson, D. W.; Haley, M. M. "Aryl C-H...Cl(-) hydrogen bonding in a fluorescent anion sensor" *Chemical Communications* **2013**, 49(65), 7240-7242.
246. Desiraju, G. R.; Steiner, T. *The Weak Hydrogen Bond: in Structural Chemistry and Biology*; Oxford University Press: Oxford, New York, 1999.
247. Taylor, R.; Kennard, O. "Crystallographic evidence for the existence of CH.cntdot..cntdot..cntdot.O, CH.cntdot..cntdot..cntdot.N and CH.cntdot..cntdot..cntdot.Cl hydrogen bonds" *Journal of the American Chemical Society* **1982**, 104(19), 5063-5070.
248. Wood, P. A.; Allen, F. H.; Pidcock, E. "Hydrogen-bond directionality at the donor H atom—analysis of interaction energies and database statistics" *CrystEngComm* **2009**, 11(8), 1563.
249. Sheldrick, G. M. "A short history of SHELX" *Acta Crystallogr A* **2008**, 64(Pt 1), 112-122.
250. Summerville, D. A.; Jones, R. D.; Hoffman, B. M.; Basolo, F. "Chromium(III) porphyrins. Chemical and spectroscopic properties of chloro-meso-tetraphenylporphinatochromium(III) in nonaqueous solutions" *Journal of the American Chemical Society* **1977**, 99(25), 8195-8202.
251. Bonomo, R. P.; Dibilio, A. J.; Riggi, F. "Epr Investigation of Chromium(Iii) Complexes - Analysis of Their Frozen Solution and Magnetically Dilute Powder Spectra" *Chemical Physics* **1991**, 151(3), 323-333.
252. Pedersen, E.; Toftlund, H. "Electron spin resonance spectra of tetragonal chromium(III) complexes. I. trans-[Cr(NH₃)₄XY]ⁿ⁺ and trans-Cr(py)₄XY]ⁿ⁺ in frozen solutions and powders. Correlation between zero-field splittings and ligand field parameters via complete d-electron calculations" *Inorganic Chemistry* **1974**, 13(7), 1603-1612.